THE UNIVERSITY *of* EDINBURGH

A broad-band study of the evolving emission-line properties of galaxies

João Pedro de Jesus Ferreira

A thesis submitted in fulfilment of the requirements
for the degree of Doctor of Philosophy to the
University of Edinburgh
March 2017

Lay Summary

When we peer deep into the Universe, we see the universe as it was thousands of millions of years ago and can witness all the changes the universe has undergone since the earliest times until today. The young universe was also smaller, so light from once blue stars arrives stretched into infrared light and can only be seen with special cameras. To study these far away galaxies, we need telescopes that can provide images of the universe detailed enough to spot a fly from a kilometer away and as faint as a candle on Pluto, telescopes like the Hubble Space Telescope.

In particular, a fraction of the primitive galaxies observed in the young universe are still under construction, they contain large bursty nebulae (stellar nurseries) which emit light at three very particular wavelengths (emission lines): red (corresponding to Hydrogen) cyan and deep violet (both corresponding to different Oxygen ions). This is very useful, because these types of regions can only be studied in detail in the nearby universe, so their growing visibility makes it easier to see what environments are forming stars, which would be impossible to see for an otherwise normal modern galaxy that far away.

Usually, these galaxies would be studied in small numbers, but in great detail, using spectra. What this thesis shows is that they can also be studied by using broad filters in the infrared, just like the human eye does to see in red, green and blue for visible light. This way, it is possible to measure the strengths of these emission lines for the tens of thousands of galaxies found in these surveys, from a tenth of the mass of our galaxy to a thousandth of that.

Finally, these lines indicate that the 10 times younger universe had 100 times more intense star-forming activity per star and that the conditions in which those stars formed were more extreme and had only a third of the Oxygen and Carbon in today's universe. All this is done with a relatively simple program which can be easily applied to other deeper, or wider galaxy surveys.

Abstract

This thesis describes a new approach to the study of high-redshift star formation and its environments that can be applied to large high-redshift surveys. Instead of relying on spectroscopy or narrow-band photometry to study galaxy line emission in detail, the properties of large emission line galaxy (ELG) populations are estimated from broadband photometry by measuring colour residuals against colours drawn from a set of line-free stochastic burst models based on (Bruzual & Charlot, 2003).

Simulated star-formation histories drawn from semi-analytic and adaptive-mesh-refinement codes were converted into mock galaxy colours, but neither could span the range of observed galaxy colours at high redshift. Instead, an existing set of exponentially declining star-formation models with stochastic bursts was used, because it closely spanned the range in observed galaxy colours in the bands that were line-free at each redshift. Small colour offsets were measured between the models and the observations, corresponding to the equivalent widths (EWs) of Hα, [OIII] and [OII].

In this way, I measure the rest-frame Equivalent Widths of the Hα, [OIII] and [OII] emission lines as they are redshifted through all filters from CANDELS (near-continuous U to 4.5μm coverage) for a large sample of galaxies from z=0.1 up to z=5. This approach relies solely on the line-free models, a set of existing reliable photometric redshifts, and a colour cut (B$-$K$<$2 or equivalent) to select only the dust-free young objects (the majority of identified emission-line galaxies). Once correctly identified, I apply this method to the CANDELS-UDS photometry to characterise the properties of Emission-Line Galaxies (ELGs) through these lines.

I find that in this sample the Hα and [OIII] ELG fraction with EW$>$150Å rises from $<$5% at z$<$1 up to 40% at z$>$2. The co-moving ELG density rises

from 5 to 30 $\times 10^{-4}$/Mpc^{-3} at z=2.3. The evolution of median Hα EW with redshift is consistent with results from HiZELS and 3D-HST yielding median EW $\sim$ M$^{0.25}$(1+z)$^{1.75}$ up to z=2.3, from which it departs to values of 450Å at z=4.3. [OIII] remains weaker than Hα for z<3 and matches its values above that redshift. [OIII] also displays a larger fraction of extreme EWs than Hα. [OII], while correctly identified, never becomes as extreme as the other two lines lines, even when corrected for the evolving continuum.

This is evidence of an increasing [OIII]/[OII] ratio with increasing z throughout this sample. While these results agree with spectroscopic and narrow-band surveys, the use of the deeper broadband filter coverage enables a systematic measurement of the increasingly prevalent high EWs (>500Å) in galaxies at every redshift spanning the 10^8 to $10^{10.5}$ M$_\odot$ range. Subsequently, this method was applied to all the other CANDELS fields (GOODS-South and North, COSMOS and EGS) and further corroborates these results. These results further show that EW dependence on mass is steeper for [OIII] than for Hα.

Line EWs are then converted into luminosities for the three lines and fitting formulas are obtained, displaying $L_{H\alpha}\sim(1+z)^{3.2}M^{0.45-0.6log(1+z)}$, with similar results for the other lines. $L_{H\alpha}$ is converted into star-formation rate and specific star-formation rate (sSFR). sSFR at low-z aligns approximately with the main sequence (with a steeper dependence in mass), but at high-redshift sSFR remains above the main sequence by a factor of 2 and rising towards median sSFR=100/Gyr around log(M/M$_\odot$)=9, showing a departure of the main sequence of star formation at lower masses log(M/M$_\odot$)<9.5. The SFRD of ELGs is 1% at low redshift, but rises to 30% at z=4.5. The $L_{[OIII]}/L_{H\alpha}$ ratio is used to estimate $L_{[OIII]}/L_{H\beta}$ and the ionization parameter q, for which the median at z>0.5 stays approximately constant at 10^8 cm/s, and increases with mass. Using the $L_{[OIII]}/L_{[OII]}$ ratio and q, median metallicity is shown to be subsolar, and can be tentatively estimated for z>0.5 to be Z/Z$_\odot\sim$0.3. The errors are large, but this could also mean a large range in metallicity from Z$_\odot$ to 0.1Z$_\odot$. $L_{[OIII]}/L_{[OII]}$ rises with sSFR as shown in the literature. This method shows great potential to survey emission-line-derived physical quantities for large galaxy populations with a low computational footprint, which could be particularly useful for pixel-by-pixel EW imaging. It is also flexibile, which allows it to be applied to any future deep multibroadband fields.

Declaration

I declare that this thesis has been composed solely by myself and that it has not been submitted, either in whole or in part, in any previous application for a degree. Except where otherwise acknowledged, the work presented is entirely my own.

Joao Pedro de Jesus Ferreira
March 2017

Acknowledgements

I would like to start by thanking everyone who listened to my wild thoughts and enjoyed bouncing back ideas, everyone who I have had interesting discussions with, astronomy related or not, it can really liven up a day sometimes. I specifically thank Becca, Esther, Jovan, Derek, Emma, Richard, Marco, Marika, Victoria, Alice, Fergus and at least a few more that I am missing as I finish writing up for their help and for being supportive colleagues. I thank FCT for fully funding my PhD project, the ROE for hosting me and python/numpy and matplotlib for the tools I used in my computing.

I express my gratitude to my supervisors for their guidance and infinite patience and especially Jim for believing in me and never letting me give up, even when it all felt like groundhog day and I didn't believe that I could make it.

I thank my grandma and my aunts Alda, Ana Luisa and Susete and my sister Lena for always welcoming me with open arms, after all the months of unreplied messages and worrying about my chronic terminal procrastination.

Finally, I am extremely lucky to have my mother Ilda, who was tireless in her presence and called me every day at 7 am for two years, just to keep me on track from 2000km away, and love my girlfriend Valentina for our bond, who kept me sane and happy through the toughest months of the PhD.

Thank you to all for believing in me, even when I don't.

Contents

List of Figures

List of Tables

Chapter 1

Introduction

Cosmological Context

The Einstein field equations (Einstein, 1915) determine the metric tensor of space-time $g_{\mu\nu}$ for an energy-momentum density field tensor $T_{\mu\nu}$, including the Ricci curvature tensor $R_{\mu\nu}$, a scalar curvature R and integration constant Λ also known as a dark energy, with c the speed of light and G the gravitational constant

$$R_{\mu\nu} - \frac{R}{2}g_{\mu\nu} + \Lambda g_{\mu\nu} = \frac{8\pi G}{c^4}T_{\mu\nu}. \tag{1.1}$$

Assuming that at large scales the Universe is homogeneous and isotropic, the Friedmann-Lemaitre-Robertson-Walker (Friedmann, 1922) metric parameterizes the family of metrics that describe space-time through a time-dependent scale factor $a(t)$ and a space-time curvature term k, describing a metric element $d\tau$ or proper time in terms of general metric coordinates a(dt,dr,dθ,dϕ)

$$-c^2 d\tau^2 = -c^2 dt^2 + a(t)^2 \left(\frac{dr^2}{1-kr^2} + r^2(d\theta^2 + sin^2\theta d\phi^2) \right). \tag{1.2}$$

Introducing the FLRW metric into 1.1, and requiring $T_{\mu\nu}$ to also be homogeneous and isotropic at large scales, the scale factor evolution is determined: the time component yields an energy balance equation and the space components a momentum balance equation, with ρ as energy density (T_{00})and p as scalar pressure or momentum flux (T_{x0}=T_{0x}):

$$\frac{\dot{a}^2}{a^2} + \frac{kc^2}{a^2} - \frac{\Lambda c^2}{3} = \frac{8\pi G}{3}\rho, \tag{1.3}$$

$$2\frac{\ddot{a}}{a} + \frac{\dot{a}^2}{a^2} + \frac{kc^2}{a^2} - \Lambda c^2 = -\frac{8\pi G}{c^2}p. \tag{1.4}$$

These equations resemble the Newtonian solution for a gravitational homogeneous, isotropic system (McCrea & Milne, 1934) with extra terms for curvature and vacuum energy.

In a Universe that is changing scale, light emitted when the Universe was smaller will have to increase wavelength in order to keep moving at c (the vacuum permittivity ϵ_0 and permeability μ_0 are constant in space and time and $c = \frac{1}{\sqrt{\epsilon_0 \mu_0}}$), so redshift is defined:

$$(1+z) = \frac{1}{a} = \frac{\lambda_{obs}}{\lambda_0} \tag{1.5}$$

Taking 1.3 and defining the Hubble parameter H:

$$H^2(t) = \frac{\dot{a}^2}{a^2} = \frac{8\pi G}{3}\rho - \frac{kc^2}{a^2} + \frac{\Lambda c^2}{3} \tag{1.6}$$

For Λ=0 and k=0, the critical density of the Universe is defined:

$$\rho_{crit} = \frac{3H^2}{8\pi G} \tag{1.7}$$

And from there, ρ has a radiation (γ) and matter (M) components:

$$\frac{\rho}{\rho_{crit}} = \Omega_\gamma + \Omega_M \tag{1.8}$$

The known components of energy density in the Universe are radiation (scales as $\sigma \mathrm{T}^4$) and matter (scales as $\rho_M = \mathrm{MR}^{-3}$), so rearranging:

$$H^2(z) = \left(\frac{\dot{a}}{a}\right)^2 = H_0^2(\Omega_{0\gamma}(1+z)^4 + \Omega_{0M}(1+z)^3 + \Omega_{0k}(1+z)^2 + \Omega_\Lambda) \tag{1.9}$$

Thus, the evolution of the scale of the Universe over time can be traced back from its present-day contents. Hubble (1929) first described measurement of the Hubble constant as the increasing redshift of lines with the distance to a receding galaxy, using the cepheid period-luminosity relation (Leavitt & Pickering, 1912). The resulting conclusion was that the Universe was expanding.

ΛCDM

The Measurement of Cosmological parameters was attempted for more than 50 years, but it was only with the help of the Hubble Space Telescope (HST) that Riess et al. (1998) finally used Ia supernovae as standard candles to measure the Hubble constant out to far enough redshifts to show evidence that expansion was in fact accelerating, so a cosmological constant was not only necessary, but dominates the energy content of the Universe. From then on, other methods of measuring cosmological parameters have been added and a consistent picture of concordance and precision cosmology was set, the most recent of which is provided by the PLANCK cosmological survey of the cosmic microwave background radiation (Planck Collaboration et al., 2016) (byproduct of the recombination of Hydrogen, now redshifted to 2.7K). These measurements showed that the Universe is flat (Ω_k<-0.0005), with H_0=(67.8±0.9)km/s/Mpc, and has an age of 13.8Gyrs with Ω_M=0.308±0.012.

With these values, one can imagine the post-inflation Universe in three stages, each dominated by one component of the energy density, which can be integrated piecewise, between the times when two energy components are balanced:

$$H_0 t(a) = \begin{cases} \int \frac{da}{a\sqrt{\Omega_\gamma a^{-4}}} = \frac{a^2}{2\sqrt{\Omega_\gamma}} & z > 3000 \\ \int \frac{da}{a\sqrt{\Omega_M a^{-3}}} = \frac{2a^{3/2}}{3\sqrt{\Omega_M}} & 0.75 < z < 3000 \\ \int \frac{da}{a\sqrt{\Omega_\Lambda}} = \frac{ln(a)}{\sqrt{\Omega_\Lambda}} & 0 < z < 0.75 \end{cases}$$

As each of the energy terms is diluted by the expansion of space-time, the vacuum energy background term, which is expansion-independent, is uncovered and starts to dominate the energy density of the Universe. For the full energy, this can be integrated numerically, but if the radiation term is small enough at small redshifts, there is an exact solution:

$$H_0 t = \frac{2}{3\sqrt{\Omega_\Lambda}} asinh\left(\frac{\Omega_\Lambda}{\Omega_M} a^{3/2}\right) = \frac{2}{3\sqrt{\Omega_\Lambda}} ln\left(\frac{\Omega_\Lambda}{\Omega_M} a^{3/2} + \sqrt{1 + \frac{\Omega_\Lambda}{\Omega_M} a^3}\right) \quad (1.10)$$

So this solution for the Hubble flow combines the accelerating exponential component and decelerating power-law component of the expansion. This is useful to convert observable redshift into comoving time and comoving space

(using a null geodesic for the metric):

$$R = c \int \frac{dt}{a(t)} = \frac{c}{H_0} \int \frac{d(1+z)}{\sqrt{\Omega_\Lambda + \Omega_M (1+z)^3}} \tag{1.11}$$

From here, all other quantities, like luminosity distance and distance modulus, angular distance and comoving volume are computed for this cosmology (shown in Fig. 1.1) to convert from observed quantities into restframe quantities. Most importantly, Flux is converted into luminosity using D_L, the luminosity distance:

$$F = \frac{L}{4\pi D_L^2}, D_L = R(1+z) \tag{1.12}$$

Cold Dark Matter

With the Hubble flow defined for a homogeneous Universe on large scales, now perturbations can be done over that solution to peer into the smaller scales. Dark energy is a constant of space-time, so it does not show structure or cluster, but matter can interact gravitationally with itself. From a census of baryonic matter observed in the Universe, adding up the mass of all observed galaxies plus the maximum estimated for dark cold gas can only provide 20% of all the matter in this cosmology. The conclusion is that most matter is dark and has very small interaction cross-sections, only interacting through gravity, and baryons cannot cluster until most dark matter clusters itself.

The current Cold Dark Matter model (Blumenthal et al., 1984) addresses this issue by making dark matter a slow-moving particle which can cluster.

If dark matter locally has a significant excess of energy density, it will decouple from the Hubble flow at a turnaround radius where gravitational contraction matches cosmic expansion. This delimits dark matter halos. So the turnaround radius defines a gravitationally bound halo that evolves independently from cosmic flow, with a final potential well with a gas supply. As the Universe expands, dark matter overdensities locally behave like closed Universes against the background Hubble flow and at a turnaround radius and time begin collapsing. The overdensity contrast necessary for turnaround is 178 times the critical density (Peacock, 1999).

The mass distribution of random density fluctuations should be scale-free (fractal), because there are no interactions from cosmological scales down to kpc

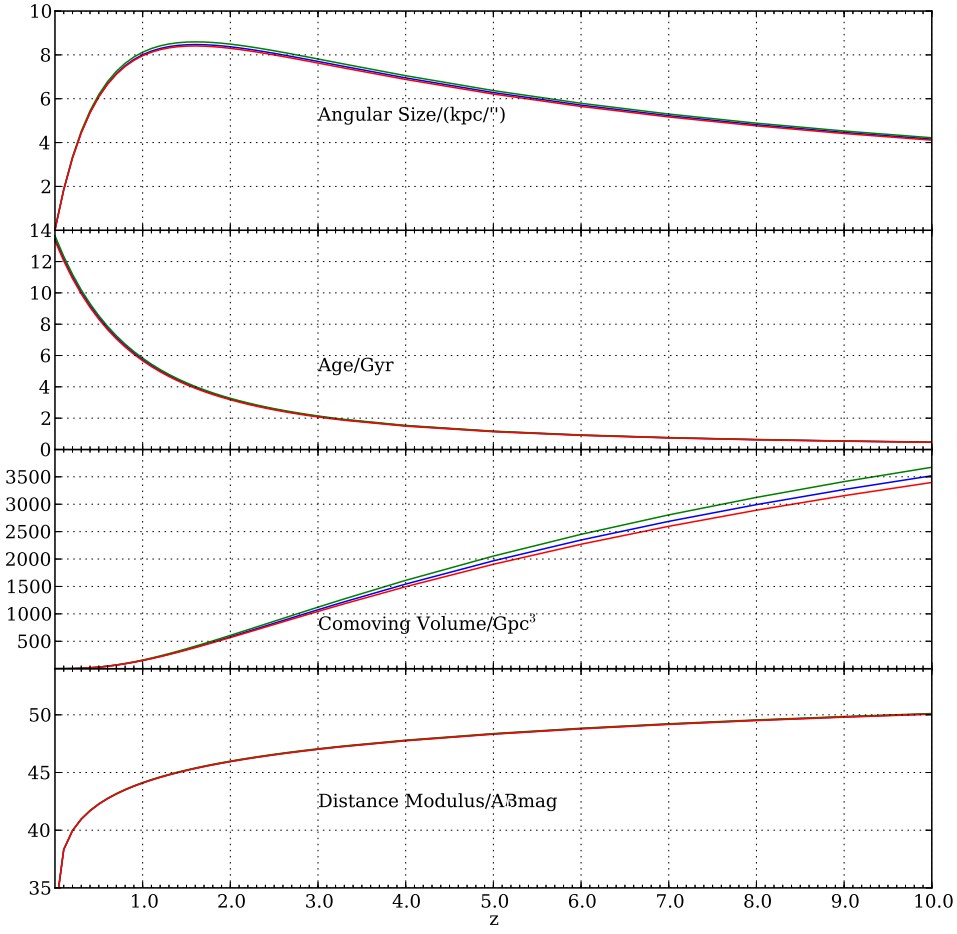

Figure 1.1: Dependence of cosmological quantities used in this work as a function of redshift: angular size, age, comoving volume and distance modulus. The blue line corresponds to the standard H_0=70, $\Omega_{0\Lambda}$=0.7 and Ω_{0M}=0.3. Green: H_0=69. Red: Ω_{0M}=0.31,$\Omega_{0\Lambda}$=0.69

scales, where gas pressure starts to introduce physics. Starting with a Gaussian field of density perturbations, a threshold for structure formation is $M*$ and spectral index n_s and assuming linear growth. By recombination, galaxy seeds of mass $10^7 M_\odot$ are already present and their distribution relates to the original spectrum of density fluctuations (Press & Schechter, 1974).

$$N(M)dM = (1 + \frac{n}{3})\frac{\rho}{M^2 dM x e^{-x^2}}, (M/M^*)^{(3+n)/6} \tag{1.13}$$

The resulting galaxy mass function is important for three reasons: it is statistical link between the spectrum of fluctuations of the CMBR, the distributions of masses drawn from simulations (which can be used to test hypothesis like cold vs hot dark matter and merging within halos) and the luminosity function, which folds in the M/L ratio and feedback and links the actual observed distribution of galaxies with models. For this reason, it can be a point of contention between theory and observations.

A further refinement of the Press-Schechter formalism for the mass distribution including hierarchical merging is described in Bower (1991) (Extended Press-Schechter) and applied as an early semi-analytic galaxy formation and gas accretion model in Somerville et al. (2000), which eventually develops into the concept of the merger tree (Somerville & Kolatt, 1999). From producing merger trees semi-analytically, N-body simulations became the standard method to track mass growth, from large scales (Springel et al., 2005) to the sub-Mpc scales of halos(Navarro et al., 1997).

This unifies cosmological dark matter with the galactic dark matter responsible for the flattening of galaxy rotation curves discovered by Spitzer (1942) by tracing the cosmic web in detail from halo scales down to galactic scales. Other intermediate-scale evidence for dark matter comes from X-ray measurements of the temperature of gas in the intergalactic medium of a common dark matter halo, consistent with larger masses than suggested by the luminous matter by using the virial theorem and hydrostatic equilibrium 3kT/2=mMG/R.

However, at first look, if dark matter cannot radiate, how does it cool without evaporating stars or mass segregation, how can it cluster? The answer is given by (Lynden-Bell, 1967), by defining a fourth type of equilibrium statistics for collisionless DM (along with Maxwell-Boltzmann for stars, Fermi-Dirac for fermions and Bose-Einstein for bosons) and violent relaxation, a process of fast

speed redistribution that only stops when the halo relaxes and reaches its virial temperature.

Dark matter clustering is very favourable to simulations, because its clustering amplifies primordial overdensities to create detached bound galaxy halos (closed island-Universes) apart from the Hubble flow, smooth (non-collisional) and only interacts gravitationally. It sets the stage for galaxy formation and the contnuum between galaxy major merging, minor merging and gas accretion.

Baryons and Radiative Cooling

With a unified cosmological framework and the dark matter halos as seeds for galaxy formation, it is time for collisional gas physics to kick in. Gas in a halo starts out at a constant temperature and then heats isothermally in hydrostatic equilibrium. Gas at a certain temperature will radiate through collisionally-induced excitation (CIE):

$$P = \Lambda(Z, T)n^2 \tag{1.14}$$

This is a two-body process and the Λ term combines all types of de-excitation processes (from Hydrogen recombination to free-free emission at high T) into a cooling rate shown in Fig. 1.2. The cooling function, at first metal-free and then progressively more efficient because of CIE metal cooling. The cooling function describes the time and processes gas must go through after being shock heated to be accreted in the form of cold gas, the ingredient necessary to form stars. However, gas heated above 10^7K will take longer than the age of the universe to cool. Metals ejected by stars may accelerate cooling rates.

An alternative to accretion for low-mass galaxies on such long timescales would be cold streams (Kereš et al., 2005), (Dekel et al., 2009), through which galaxies grow through minor mergers (1:10 or even larger mass ratios), so gas accretion is not purely cosmological, it may vary from galaxy to galaxy, depending on the surrounding structure. This requires not only semi-analytic modelling (subgrid recipes), but mainly a hydrodynamical treatment of gas cooling and steady accretion onto galaxies, unlike major mergers, to keep galaxies from going read and dead prematurely.

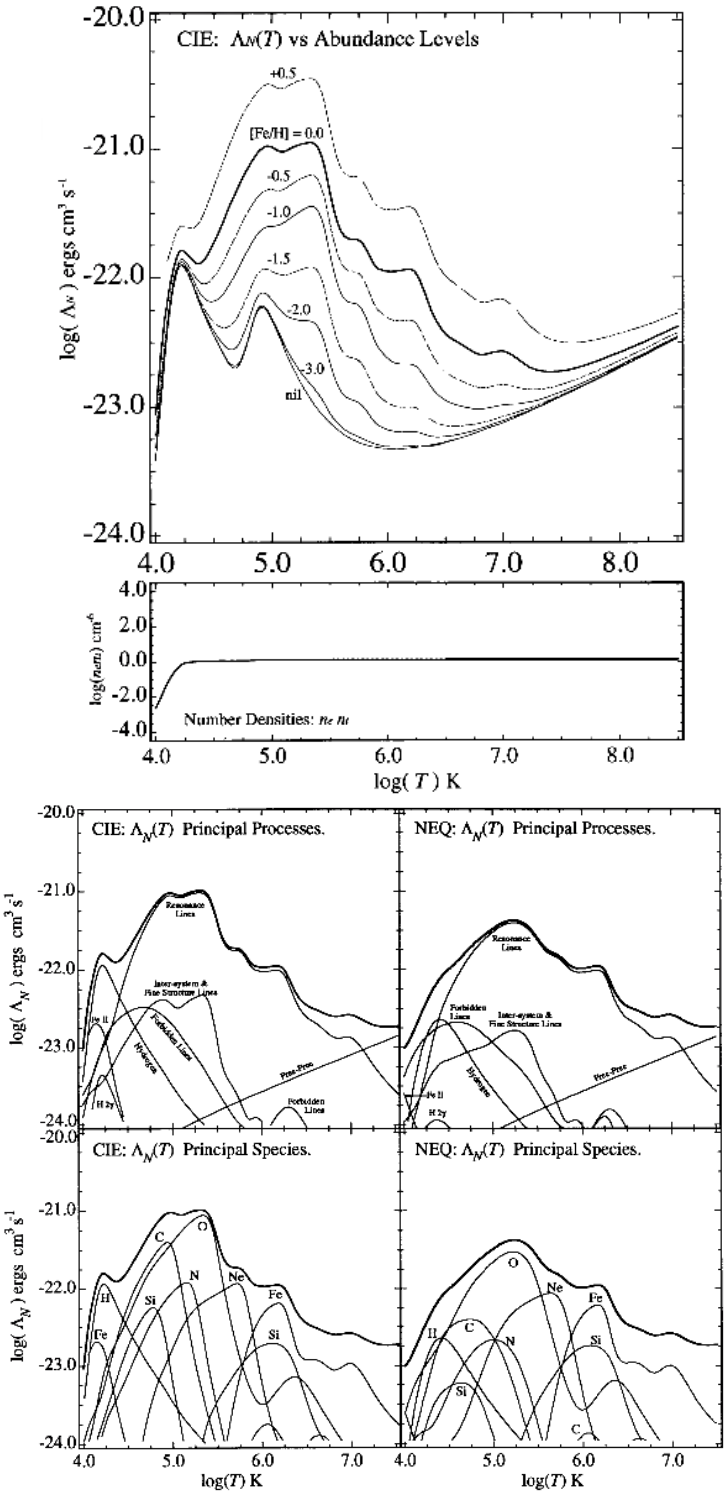

Figure 1.2: The cooling function as a function of temperature for gas at different metallicities, showing below the contribution of each element and physical process towards cooling. Above 10^7K, free-free emission dominates, below $10^{4.5}$K, Hydrogen recombination dominates and in between the resonance lines of C,N, and O dominate. Metals increase cooling efficiency by two orders of magnitude. Adapted from Sutherland & Dopita (1993)

Galaxy Evolution

Accreted gas clouds further cool to become molecular hydrogen and undergo fragmentation to form individual stars as described in McKee & Ostriker (1977) and Silk (1977). However, star formation taps into the extra energy reservoir of the strong nuclear force and energy is generated that halts the cooling process and keeps gas pressure inside the galaxy (Murray et al., 2005). Stars also create chemical elements through nucleosynthesis, which once dredged-up or actually exploded into the interstellar medium (Matteucci & Greggio, 1986) will make cooling and further star formation even more efficient, through the more complex spectra of higher atomic number elements and especially molecular vibration-rotation spectra (Goldsmith & Langer, 1978).

So from recombination, the history of the Universe is one of gas cooling until stellar emission reionizes the Universe (Barkana & Loeb, 2001).

Self-regulated Star Formation

So far I have presented how dark matter halos form and from there how galaxies get their gas, either through hot (slow, steady-state and isotropic) or cold accretion (fast, episodic and directional). At the cores of the potential wells, where gas density is highest and cooling is most efficient, stars will start to form, establishing a dynamical system of the form:

$$\begin{cases} \dot{M}_*(t) = \epsilon(\rho_g, Z, ...)M_g(t) \\ \dot{M}_g(t) = A(t) - \dot{M}_*(t, Z) \\ \dot{M}_Z(t) = \mu\dot{M}_*(t, Z) \\ M(t) = M_Z(t) + M_g(t) + M_*(t) \end{cases} \tag{1.15}$$

Stars form from gas with an efficiency ϵ that depends on initial gas density and metal cooling. Gas accretion is the balance between inflows, which are just a forcing parameter with time, and the sum of gas lost to star formation and gas outflows from stellar winds and supernovae, also proportional to star formation. All of these effects are added in the A parameter. The μ parameter reflects the yield of metals from different types of supernovae and stellar winds.

The form of these combined equations ensures that after an initial period of rapid unchecked star formation, once stellar feedback sets in, star-formation

and outflows rise at a steady state to match the accretion rate over redshift. If the accretion signal is irregular, the system of equations will dampen it and display a delayed reaction on the part of feedback, which takes 10Myrs to react to an increase in star formation. Stellar winds also depend on metallicity, which regulates stellar atmosphere opacity. For subsonic winds (which don't have the galactic escape velocity), ejected metals will pollute the halo of a galaxy and be re-accreted. Beyond the semi-analytic approach (Somerville et al., 2015), detailed simulations today include simultaneous processing of dark matter and gas: OWLS (Schaye et al., 2010), EAGLE (Schaye et al., 2015), ILLUSTRIS (Vogelsberger et al., 2014). Episodic star formation caused by perturbations in time and space around a mean given by the steady-state galaxy equations (secular evolution).

A number of results come simply from the form of these equations and can be addressed analytically, as described in equations 1.15. One is the main sequence of star formation, the other is the mass-metallicity relation, which are all relations that a simulation must reproduce to begin testing more ellusive galactic properties.

The Main Sequence of Galaxy Formation and fundamental plane

While tracing the many effects over galaxy formation at different scales and the influence of different forces, there is emergence of a mean-field behaviour: the "main sequence" of galaxy formation, described by Brinchmann et al. (2004), Daddi et al. (2007), Noeske et al. (2007) and Elbaz et al. (2007). Originally, this name was given in comparison with the main sequence of star formation where stars spend most of their lifetime in relative stability fusing Hydrogen. The analogy ends here, because the main sequence of star formation is a statistical concept to refer to the specific star formation that most galaxies have due to their gas inflow and star formation balance. Here once galaxies reach high enough masses, they build most of their mass at relatively modest specific star formation rate (sSFR), buffered by the structure already present. The main sequence is known to evolve over redshift, following the decline of gas supplies with cosmic time. Speagle et al. (2014) provides a compilation of results from different studies.

The Mass-Metallicity Relation

The mass-metallicity relation, as described in section 2.3, emerges from the fact that star formation produces stars, which themselves synthesise and eject. As such, exposing a galaxy to prolonged intense star formation is bound to increase its mass and metallicity in tandem. The another approach to this relation is to imagine that metal pollution of the ISM very quickly increases the efficiency of star formation, which would decrease the necessary amount of gas to produce the same number of stars and feedback to balance accretion (self-regulation), so metal production, while increasing star-forming efficiency, might actually be responsible for the decreasing star formation since z=2, along with the consumption of gas reservoirs. This would produce an evolving mass-metallicity-SFR surface (Mannucci et al., 2010).

Both the mass-metallicity relation and the main sequence of star formation have an intrinsic thickness, made of galaxies which temporarily form more or less stars, only to return to the main sequence (if they are still accreting gas). This may be due to perturbations of the equilibrium solutions for self-regulated star formation due to oscillations in the accretion rate or mergers, but it can also be due to the inherent stochasticity of secular star-formation.

Theoretical Star formation: the Jeans Mass

On a microscopic level, star-formation is also self-regulated. Any gravitational perturbation in the gas is counteracted by gas pressure, because gas clouds are in hydrostatic equilibrium. Therefore, a perturbation must be large enough to lead to a runaway contraction. This happens when the free-fall time (t_{ff}=$(G\rho)^{-1/2}$) for a density perturbation is lower than the speed of sound (c_s^2=$dp/d\rho$, related to T as c_s=$\sqrt{k_B T/\mu}$ for an ideal gas), known as the Jeans instability criterion. The consequence of this is that for masses greater than

$$M_J = 3 \times 10^4 \left(\frac{T^3}{n} \right)^{1/2} \tag{1.16}$$

A gas cloud region will start collapsing and fragmenting to form stars. This threshold requires a combination between gas temperature and density. Once the individual $M_\odot$ clouds that will be forming individual stars form, the gas cloud contract at the same rate that it cools, but when density becomes high enough,

the cloud will become optically thick, so the rate of star formation will depend on cooling mechanisms. At these temperatures, molecular rotational-vibrational cooling is the most efficient method to take energy away from the cloud, especially for molecules with a dipole, like carbon monoxide or particles with even more degrees of freedom to radiate, like dust. This mechanism is responsible for the effect that metallicity has in increasing the efficiency of star-formation (Dib et al., 2011).

On larger scales, another intermediate-scale criterion to take into account is the Toomre parameter (Toomre, 1964).

ISM pressurization and turbulence

In practice, star formation will not happen passively, but will also react to the dynamical state of the ISM and where there are convergent flows of gas or supernova trigger gravitational collapse by Jeans instability (McKee & Ostriker, 1977). When gas cools, its dynamics spans 20 spatial and temporal orders of magnitude from Mpc to atomic reactions in gas clouds that make H_2. Star formation occurs in the middle of this scale and effectively becomes a black box where all the sub-pc physics emerges as a set of empirical laws measured in the local Universe in a diversity of environments, albeit not as well sampled in the parameters common at high-redshift. An important subgrid parameter that may lead to delayed star formation is the turbulence cascade and ISM cooling.

Examples of the detailed treatment of the ISM and turbulence with an impact on star formation are given in (Bournaud & Elmegreen, 2009), (Bournaud et al., 2011a), (Elmegreen & Falgarone, 1996), (Elmegreen, 2000), (Elmegreen & Scalo, 2004), (Bournaud et al., 2010), (Bournaud et al., 2011b).

Empirical Star Formation: the SK-law

Star formation is a complex process that spans many scales, but like many systems, on large scales it has a simple emergent behaviour. The Schmidt-Kennicutt law (Kennicutt & Evans, 2012, and references therein) is a good example, where it was empirically determined that the surface density of star formation depends on the surface density of molecular gas (H_2+HI) as:

$$\Sigma_{SFR} = \Sigma_{gas}^{1.4\pm0.15} \tag{1.17}$$

This result is robust for different galaxies, scales and is one of the main semi-analytic recipes (or a requirement that another recipe needs to fulfill). Luna et al. (2006) and Misiriotis et al. (2006) study this result for the atomic and molecular components of gas. Recently, Bigiel et al. (2008) has found a departure from the SK-law at low gas densities.

Feedback

Stellar

The main effect of star formation on the properties of galaxies, besides spreading metals and speeding up cooling, is to inject energy into the ISM in the form of supernova winds. These winds pressurize the ISM and may trigger or quench star formation. However, their main effect on galaxy properties is to reduce gas supplies by ejecting gas out of the galaxy through supersonic winds Hopkins et al. (2014), Dalla Vecchia & Schaye (2012), Martizzi et al. (2015), Hopkins et al. (2012b), Hopkins et al. (2012a).

AGN

An alternative source of energy for feedback is the gravitational energy dissipated by infalling matter onto supermassive black holes in the nucleus of galaxies, known as Active Galactic Nuclei (AGN), which can change galactic systems when it becomes dominant at high masses, because it bypasses star-formation and makes feedback proportional to gas accretion, which it regulates through heating. There is ample literature on the SF-AGN connection, which may just be an indirect consequence of SF responding to accretion. AGN can effectively suppress star-formation by nearly cancelling accretion. AGN is a local feedback effect, whereas SF is a global effect

Cosmic Star Formation History

Tracking the complex interplay between the complex systems that are galaxies, star-forming systems and the forcing from gas accretion and minor merging along galaxy filaments, obtaining cosmological star formation from first principles is a hard problem to solve. However, with the few emergent recipes observed for star-forming systems, star-formation rate can be measured from today using a variety of methods (measuring the UV flux, the IR flux, emission lines, or differentiating the mass function), in the local universe all the way to very high redshifts and its evolution can be interpreted. Madau & Dickinson (2014) and Dunlop (2013) wrote very complete reviews on the subject, detailing three main eras of cosmic star formation.

Redshift 5 and above - Early Galaxy Formation

From the first metal-free population III stars that reionized the universe, this era is one of rising star formation, high gas densities and strong gas inflows, which in the absence of very strong feedback can build galaxies almost up to modern sizes very quickly.

Intermediate Redshifts - the Peak and decline of Star Formation

At intermediate redshift, a number of competing effects start to show and galaxies start to have higher metallicities and to stabilize on high masses to main sequence. There is a transition from the gas-rich, strongly star-forming Universe to the quiescent metal-rich Universe we know, with a dominance of AGN feedback at the high-mass end for $z<0.7$. This involves major transformations in galaxy dynamical, radiative and density structure, the rise of elliptical galaxies, etc.

Local Universe: Resolved Stellar population Archaeology

The local Universe is very rich in archaeological information, resolved stellar populations, age dating of clusters, but it cannot say anything about the full range of instantaneous conditions all over the Universe. Maybe through archaeology it is possible to know what the conditions of the early Milky Way and Local group could have been, and produce valuable constraints. The local universe is also the laboratory for calibrating many of the relations used at high-redshift (some of

them are purely physical and remain unchanged, some are empirical and depend on the conditions of the measurements).

Stellar Population Synthesis Modelling

To produce observables from simulations, galaxy star-formation histories need to be converted into light. This is done by taking sets of stars and evolving them simultaneously. This last step is called population synthesis modelling, where one deals with sets of single-age and metallicity star "clusters", rather than individual stars. So far, galaxy evolution has only focused on how stars form: attempt was made to separate the theory of galaxy formation and gas cooling from the observable Universe, which is another layer of complexity added to the star-formation histories and which effectively erases much of the information that simulations are capable of providing. This is the step where a galaxy simulation needs to be adjusted to the available observable quantities, because a model with many degrees of freedom and too little data cannot constrain a model either. Another important point to make is about luminosity functions and the importance of colour. Usually the field of galaxy simulation focuses on mass and luminosity functions (converted using a M/L ratio that depends on an initial mass function) to compare among simulations and between simulations and observations. However, what is most important for the galaxy physics is the difference between bands or colours, because these small differences are where how intensive properties (independent of galaxy mass) like ISM temperature and metallicity manifest themselves.

Stellar Evolution Tracks

The first component of a population synthesis model are the stars and their evolution. This encapsulates all of stellar evolution along the main sequence, along the red giant branch and includes many minor refinements, like stellar winds, metal mixing, rotation, pulsation, pre-main-sequence physics and produces luminosity and temperature for a set of isochrones (stars of constant age as a function of stellar mass) or stellar tracks (stars of a given mass as a function of age) for different metallicities. This requires a computation of the hydrostatic and thermal equilibrium of the plasma inside a star. Different metallicities will affect opacities, changing energy transport mechanisms from convection to radiation. An example of such tracks is the commonly used Padova tracks (Bressan et al., 2012) (PARSEC), which are shown in Fig. 1.3. Stars of different mass ranges have different structures and energy transport mechanisms, so they display different

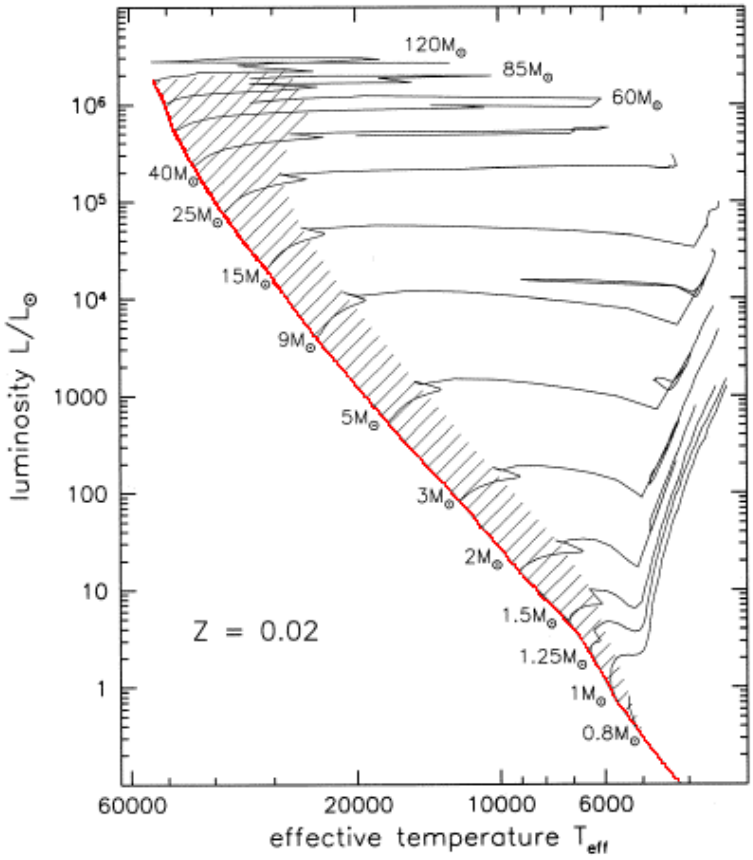

Figure 1.3: Padova Stellar evolution tracks for different masses (Bressan et al., 2012). As Hydrogen in the core runs out, their cores contract and their atmospheres expand almost adiabatically (almost constant L) until their cores reach the right temperature to fuse Helium.

dependencies of luminosity on mass (M/L ratios).

The Initial Mass Function

The next assumption to consider is how many stars of each mass are produced. This is a continuation of the cloud-instability problem and connects to turbulence, with Hopkins (2013) providing a scale-free description. This is a justification for using power-law initial mass functions. The two most commonly used IMFs are the original Salpeter IMF (Salpeter, 1955), with a powerlaw slope of $N(M)dM=M^{-2.35}$ and the log-normal IMF by Chabrier (2003). There are many studies showing that a different slope could fit observations better, e.g. Wilkins et al. (2008), but a change in the IMF is a change to make only when all other options to model a stellar population are exhausted, so this is not usually invoked.

A way to test these models in detail is a survey of local young star clusters like FLAMES (Evans et al., 2011). The initial mass distribution of stars can be simply described as a function of log(m), because mass spans many orders of magnitude

The IMF also influences the M/L ratio, by increasing the number of stars with specific M/L ratios, increasing the M/L ratio for bottom-heavy (dominated by low-mass objects, steeper than Salpeter) IMFs and decreasing it for top-heavy (dominated by high-mass objects, flatter than salpeter) IMFs.

Galaxy SED

Using the IMF and the stellar tracks, a set of atmosphere templates are obtained (either from observations or for the rarest objects from models like Kurucz (1993)) and summed for each of the stars included in the stellar template. Different templates exist, notably: GALAXEV, known as BC03 (Bruzual & Charlot, 2003), the Maraston models (Maraston, 2005) and PEGASE (Fioc & Rocca-Volmerange, 1997). The SHARDS survey (Pérez-González et al., 2013), which combines highly detailed multi-medium-band photometry for large numbers of galaxies compares the merits of these different sets of models.

Dust

The final ingredient to add to simulate stellar populations is a treatment of dust. The calculated galaxy SED is further changed by dust in the line of sight between stars and the observer. This may be due to attenuation (A_V) or reddening E(B-V). The two are usually related by the constant R_V=A_V/E(B-V)=3.1 for the Milky way and higher for stellar birth clouds.

The addition of the effects of dust can be done in a very detailed manner, using ray-tracing equations which calculate the attenuation and emission at each point, they can take into account energy balance and multiple scatterings.

A useful quantity to define at this point is the optical depth τ, the integrated total opacity:

$$\tau_\lambda = \int \rho a_\lambda dz \tag{1.18}$$

Such that

$$I = I_0 e^{-\tau_\lambda} \tag{1.19}$$

Where τ=1 is equivalent to the probability of a photon to be absorbed of 63%. In magnitude space:

$$A_\lambda = -2.5log_{10}(I - I_0) = 2.5log10(e)\tau\lambda = 1.08\tau_\lambda \tag{1.20}$$

So in the magnitude system, $A_V \sim \tau_V$

A simple model of the application of dust is to define a screen with an optical depth defined in the V band and a reddening slope:

$$\tau_\lambda = \tau_V \left(\frac{\lambda}{\lambda_V}\right)^n \tag{1.21}$$

Other more sophisticated reddening laws include Calzetti et al. (2000).

Nebular Emission Lines and HII regions

More direct than looking just at stars, looking at the process of star formation as it happens is what is most important to understanding galaxy properties. However, at high redshift this is simply impossible to resolve, so one must use indirect ways to probe the physical conditions of nebulae where stars are forming, mainly optical emission-line spectra and mid-infrared spectra to probe dusty regions.

Theory of Nebular Emission

Young stars produce line emission by ionizing the surrounding atomic hydrogen, which is eventually followed by a recombination cascade. For the system to be in a steady state, the ionization rate must balance the recombination rate (Osterbrock & Ferland, 2006):

$$n_H \int_{\nu_0}^{\infty} \frac{F_\nu}{h\nu} a_\nu(H^0) d\nu = n_e n_p \alpha(H^0, T) \tag{1.22}$$

The left side shows the rate of ionization of Hydrogen atoms with number density n by UV photons above the ionization frequency threshold (for Hydrogen 13.6 eV or λ=hc/E=1216Å) with an a_ν cross-section. The left side shows the later spontaneous recombination of the resulting photons and electrons with recombination coefficient α.

After recombination, a series of level de-excitations occurs, which emits a spectrum of lines. The different possible pathways for this cascade are given by a set of quantum mechanical selection rules.

If the gas cloud is not very dense, optical depth will be below 1 and this process will only happen once for each ionizing photon without further absorption of re-emitted photons. This is called case A recombination and is not very common in gas-rich star-forming nebulas. When the gas density is high (>100 atoms/cm^3), there is a chance that the re-emitted photon can be reabsorbed by the reverse transition that gave origin to it. This is the case of the resonant transitions to the ground state (Lyman series). Higher energy levels are only temporarily populated before they spontaneously de-excitate to the ground state, so the opacity for the Balmer series is much lower, as can be shown using the Boltzmann factor:

$$\frac{p_1}{p_0} = \frac{g_0}{g_1} e^{\frac{hc}{k_B T}(\lambda_1^{-1} - \lambda_0^{-1})} \tag{1.23}$$

At 10^4K, the ratio between the level populations of the 1S and the 2S (hc/6563Å-hc/1216Å) orbitals is p_{2S}/p_{1S}=0.0077, so the chance to absorb a Balmer series photon is 0.0077 times that of a Lyman series.

In this situation, all transitions finishing in the ground level are effectively blocked by gas absorption and reprocessing until they are re-emitted in other non-optically thick lines, effectively making level 2 the lowest energy level to which emission can be observed. This is called case B recombination. In practice, real-world nebulas will be a linear combination case A and B recombination, so some objects will display Lyα emission (Charlot & Fall, 1993) in some viewing angles (if the gas density is not homogeneous). The escape fraction of Lyα (Kuhlen & Faucher-Giguère, 2012) is a useful parameter to measure how close a nebula is to case B.

To obtain the line ratios between Hα and Hβ, the Boltzmann factor is used again and forbidden transitions are computed taking into account that the emitted photon carries a helicity of ± 1 and that spin does not change. The resulting line luminosity ratios are shown in Osterbrock & Ferland (2006) for case A (page 79) and case B (page 84). For example the Hα/Hβ ratio remains around 2.85 in both case A and B, increasing to 3 for T=5000K and decreasing to 2.7 for T=20000K. The following lines in the series decrease in intensity as Hγ/Hα=0.16, Hδ/Hα=0.09, with the Paschen series Pa_n/H$\alpha\sim$0.11 and the Brackett Br_n/H$\alpha\sim$0.05.

So in case B, for metal-free dense gas, 47% of the UV luminosity of the nebula will effectively be re-scattered and forced to leave through Hα (35%) and Hβ (12%). If the hot O and B stars ionizing the gas are considered blackbodies, the ionizing flux is given by Planck's law:

$$F_\lambda = \frac{8\pi c^2}{\lambda^5} \frac{1}{e^{\frac{hc}{k_B T \lambda}} - 1} \tag{1.24}$$

And the fraction of the flux that is ionizing is:

$$\frac{F_{ion}}{F_{total}} = 1 - \int_{\lambda_{min}}^{\infty} \frac{8\pi c^2}{\lambda^5} \frac{1}{e^{\frac{hc}{k_B T \lambda}} - 1} / \sigma T^4 \tag{1.25}$$

For case B λ_{min}=1216Å and a 10000K star, the ionizing fraction of flux is 15%, but it can rise to 95% for the 50000K O stars responsible for HII regions.

The ionizing flux fraction is given by integrating (below 912Å for case A,

below 1216Å for case B).

So with case B recombination, an estimate of the maximum possible equivalent width (EW_0) of a line is F_{line}/F_λ=0.95*$\sigma T^4/F_\lambda$, so $F_{H\alpha}/F_{6563\mathring{A}}$ = 0.35*0.95*$\sigma T^4/F_{6563\mathring{A}}$=578Å, for the theoretical limit of a 10000K star. This is the theoretical highest equivalent width observable for Hα, if a galaxy was only composed of nebula heated only by O-stars, but it is a good indicator of the maximum expectable equivalent widths of a galaxy dominated by line emission and above all it explains how line emission can easily be dominant over the continuum in a strongly star-forming galaxy like those at high redshift. Higher values could be obtained for stars with higher surface temperatures, notably, Wolf-Rayet stars (Crowther, 2007), even though their prevalence increases with metallicity (Brinchmann et al., 2008), so for the highest redshifts and low-metallicity another type of massive star may be necessary, possibly with treatment of rotation and magnetic fields, possibly population III stars (Matteucci & Calura, 2005).

Other Chemical Species

When considering additional elements, temperature has additional importance, because it determines which ionization stages of each element are most abundant in a nebula. According to the Saha equation, which assumes a Maxwellian distribution in particle speeds:

$$\frac{n_{i+1}n_e}{n_i} = \frac{2}{\lambda_e^3}\frac{g_{i+1}}{g_i}e^{-\frac{E_{i+1}-E_i}{k_BT}}, \lambda_e = \sqrt{\frac{h^2}{2\pi m_e k_B T}} \tag{1.26}$$

In the presence of other elements, the electronic energy level computations become more complicated, due to the added energy terms and selection rules from interactions between the multiple electrons. A simplifying case here is to refer to Hydrogen-like cases of ionized species where there is only one electron and a nucleus with charge Z. This is the case for HeII;

$$E = -13.6\frac{Z^2}{n^2} \tag{1.27}$$

The only reason HeII does not display line emission as strong as Hα is that its equivalent transition occurs at $6563/Z^2$=1640Å, which puts it in the UV, where it can be absorbed by Hydrogen ground-state electrons. The Paschen-equivalent

(Fowler lines) fall at 4686Å, but are weaker than the balmer-equivalent lines by a factor of 10.

The next most abundant elements in the Universe are carbon and the by-products of the CNO cycle: O and N. In these cases, the electron on the outer orbital can be considered as isolated if a screening term is applied to the electronic charge of the nucleus. As such, the CII, NIII and OIV are comparable to Hydrogen as well and the same happens as with Helium, but their strongest transitions happen even further into the UV.

For systems with two (CI, NII, OIII, SIII) and three (OII, NI, SII) outer-shell (2p) electrons the situation becomes even more complicated, but the high ionization states generally only make energies rise. The key here is that atoms with complex orbital structures exposed to collisional excitations can place electrons in levels from which the natural decay probability is very low. The probability is low because this would require a quadrupole term instead of a dipole term, which increases the transition timescale beyond the timescale for dipole emission. This is important for case B recombination because if all strong OIII transitions are in the UV, then the levels with the greatest populations above the ground states will be the meta-stable levels, responsible for the forbidden transitions. Furthermore, the nebula is always optically thin in these forbidden transitions, as the cross-section for a quadrupole transition is very low.

Oxygen displays two doublet transitions: [OIII] 5007Å+4959Å [OII] 3729+3726 as described in pages 64 and 132 of Osterbrock & Ferland (2006). Analogous to these through electron screening are [NII] and [SIII] for [OIII] and [SII] for [OII]. For example, [OIII] with total charge 6583Å+6548Å. The case [SII] to [OII] the difference will be caused by a stronger nuclear charge screening term. Through a combination of Balmer lines and forbidden transitions, a complete visible emission-line spectrum is obtained, as shown in figure 1.4.

To quantify the importance of the Balmer lines to the forbidden lines (sensitive to electron pressure), the ionization parameter is defined:

$$q = \frac{Q_0}{4\pi R^2 n_{H^0}} \tag{1.28}$$

Where Q_0 is the rate of ionizing photons produced by stars.

This quantity can be interpreted as the speed at which the ionization front of the Stromgren sphere of ionized gas is expanding (in which case U=q/c gives it

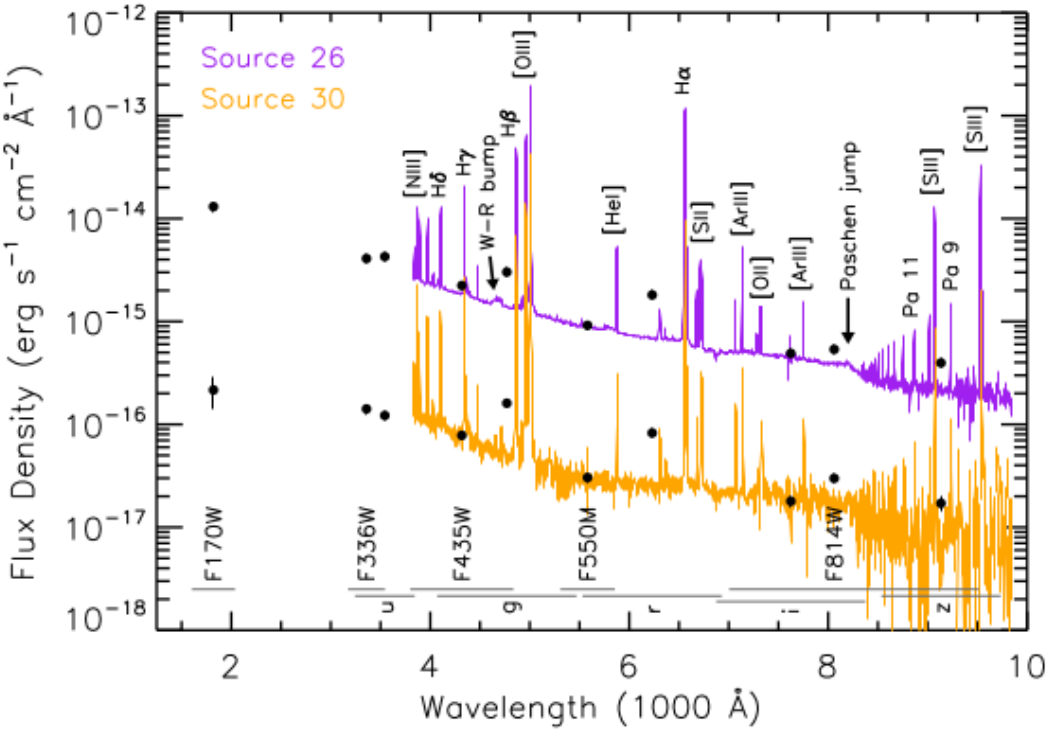

Figure 1.4: Spectrum produced in Reines et al. (2010)

a a fraction of the speed of light). It can also be interpreted as the ratio between the number of photons and the number of HI atoms.

From equation (1.22), q could be converted into a rough estimator of the ionized fraction for Hydrogen:

$$q = \left(\frac{n_e}{n_{H^0}}\right)^2 \frac{\alpha}{a} \tag{1.29}$$

So q reflects the weight of collisionally-induced forbidden transitions over the less electron-density dependent Balmer lines. In practice, is much more going on in the nebula other chemical species, each one with their ionization stage, so this is also going to be sensitive to the ratios between ionization stage populations, like [OIII]/[OII].

Dust Processing

In practice, for gas-rich regions with metals, dust will be the most efficient way for a star-forming region to cool. Each dust grain in thermal equilibrium with incident radiation will re-emit:

$$\frac{4\pi R_{star}^2 \sigma T_{star}^4}{4\pi d^2}\pi r^2 = 4\pi r^2 \sigma T_{dust}^4 \tag{1.30}$$

with d the distance of the dust particle to the star and r the radius of the dust particle, which cancels to yield:

$$4\left(\frac{T_{dust}}{T_{star}}\right)^4 = \left(\frac{R}{d}\right)^2 \tag{1.31}$$

Photons of an original radiation temperature T (through Wien's law) will be re-emitted at a temperature T=$T_0\sqrt{R_{star}/2d}$) at a distance d from the source. Because high temperatures will vaporize carbon-based dust, this will only happen far from the star, so for a 50000K O star with radius $30R_\odot$, dust within the nebula at 1 pc will be re-emitting at 30K, or 100μm.

This is why it is so important to observe star formation in the restframe mid-infrared as well, especially at high redshift.

A final problem to address is that of the nebular continuum. The set of infinite long-wavelength low-probability higher-order transitions for a variety of elements and ionization stages can add up to a considerable amount of nebular continuum, which will increase observed line equivalent widths over the stellar continuum (when this is known), but will decrease the observed equivalent widths (when ignored), because the measured continuum will include a large nebular component Reines et al. (2010).

ELG modelling

Given the complexity of the problem, simultaneous detailed modelling of all these processes is necessary. This has been done by Charlot & Longhetti (2001), Zackrisson et al. (2001), Schaerer & de Barros (2012), Anders & Fritze-v. Alvensleben (2003), Pacifici et al. (2015), etc. The CLOUDY code (Ferland et al., 2013) includes all the recipes described in these references. Modelling needs to be adapted to the available data. Simple datasets must be fit with simplified models. Fitting with emission lines may prove successful but for large data sets it can systematically shift the data in ways that can be unpredictable for unknown samples.

Emission Line Diagnostics

Star Formation Rate

The most important line measured at high redshift is Hα, because its luminosity is directly proportional to the instantaneous SFR (not a mass-averaged quantity) for ages up to 10Myr. The conversion is done through an empirical calibration by counting the rate of ionizing photons above the ionization energy threshold (Q(H^0)=$\int L_\nu/h\nu$), defined as (Kennicutt, 1998):

$$\frac{SFR}{M_\odot/yr} = \frac{1.08 \times 10^{-53} Q(H^0)}{s^{-1}} = 7.8 \times 10^{-42} \frac{L(H\alpha)}{\mathrm{erg/s}} \tag{1.32}$$

The number of photons thus computed uses a Salpeter IMF from 0.1 to 100 M$_\odot$ at solar metallicity.

Line Ratios

Line ratios are used to estimate their underlying physical properties. For example, as mentioned before the [OIII]/Hβ ratio is affected by both metallicity and ionization parameter. The reason it is so important is because these are two adjacent lines which can be measured simultaneously with spectroscopy and any dust reddening or flux calibration issues will have the same effect on both lines, so it is dust-independent and requires no flux calibration. Whereas the Hα/Hβ ratio should only depend weakly on temperature or dust, so it can be a good A$_V$ indicator. Depending on how many emission-lines are available, more detailed diagnostics can be achieved.

The BPT diagram, named after the paper Baldwin et al. (1981) by authors Baldwin, Phillips and Terlevich, combines two pairs of adjacent forbidden and Balmer lines, [OIII]/Hβ and [NII]/Hα to give a very detailed picture of the galaxies emitting these lines. A very complete analysis of these indicators is given by Kewley & Dopita (2002) and Kewley et al. (2004). Whereas the [OIII]/[OII] ratio depends on simultaneously on metallicity and ionization parameter, as described in Fig. 1.6, [OIII]/Hβ (Fig. 1.5) is most sensitive to ionization parameter at low metallicities and at super-solar metallicities it becomes more sensitive to metallicity.

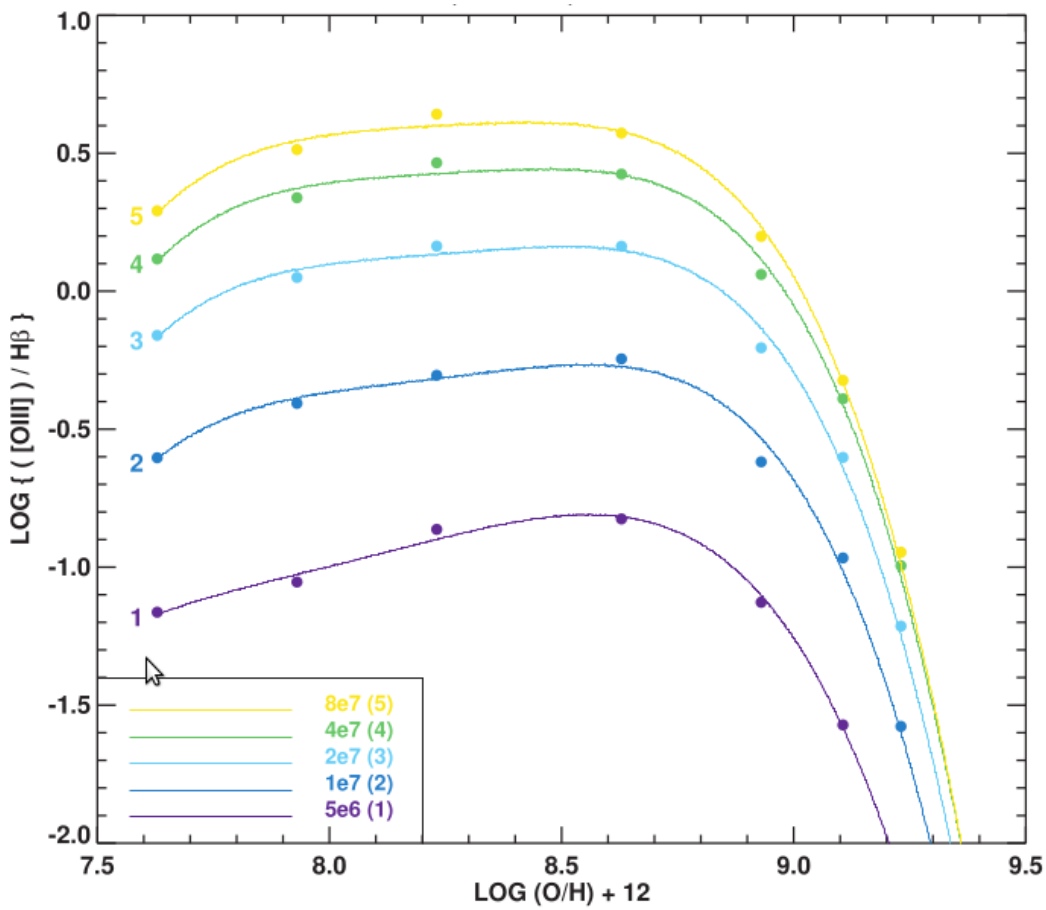

Figure 1.5: [OIII]/Hβ dependence on metallicity and ionization parameter from Kewley et al. (2004)

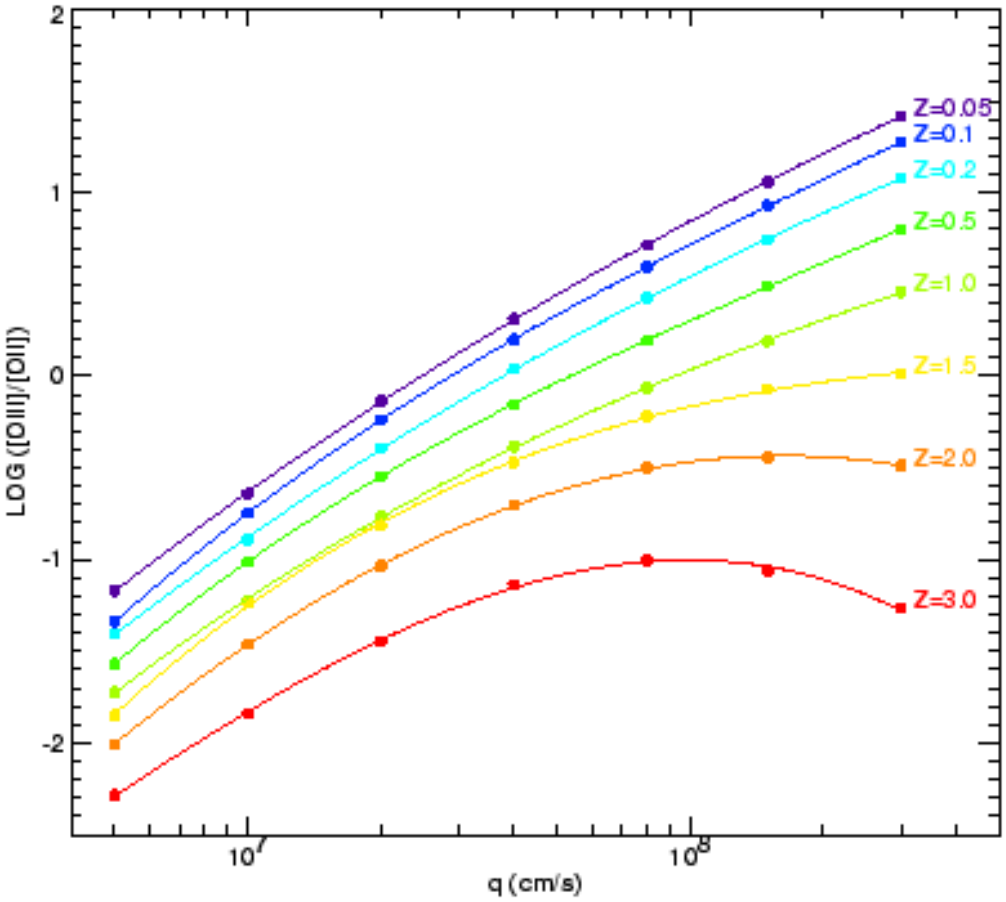

Figure 1.6: [OIII]/[OII] dependence on metallicity and ionization parameter from Kewley & Dopita (2002)

Spectroscopic Surveys

To measure these line ratios and learn precious information about the star-formation state of galaxies at high redshift, it is necessary to obtain large numbers of deep spectra at high redshift. This is an expensive process in terms of observing time, but multi-object-spectrographs, like KMOS in VLT (Sharples et al., 2013), MOSFIRE in KECK (Steidel et al., 2014) can direct this observing time to preselected objects of interest, like the VUDS survey (Le Fèvre et al., 2015) using VIMOS on VLT; integral field units, like MUSE (Bacon et al., 2015) can extract the full spectral and spatial information with that observation time and grism spectra surveys such as WISP (Atek et al., 2010) and 3DHST (Skelton et al., 2014) can obtain a large number of spectra by placing a grism in the light path already in place for photometry.

Narrowband Surveys

What can be done when there are no available spectra, or when spectra need to be surveyed? It is not efficient to take spectra for all galaxies, especially because many of those pixels are not bringing in new information. A more efficient way to survey the sky for emission-line galaxies without obtaining spectra is to take a number of narrow-bands and to compare their flux with the underlying continuum. The most prolific of these surveys have been HiZELS (Sobral et al., 2009), with results in Hα, [OIII] and [OII] and combinations of these (Sobral et al., 2013; Stott et al., 2013; Sobral et al., 2014) and NEWFIRM (Ly et al., 2011).

Broadband Studies

The narrow-band method can only be used at the redshifts where the line is in the filter. This reduces the available volume of the survey per filter to dz=0.1, so to compensate this, large sky areas are surveyed. This works very well for the higher-mass objects, but cannot capture the low-mass end, especially at growing redshifts. It is biased towards high-luminosity EWs and may miss low-luminosity EWs. The final point is that when a narrowband is used, it analogous to using a slit-spectrum in wavelength and many other galaxies that could be measured are not observed at all, as in slit spectroscopic surveys. On the other hand, the broadband approach is analogous to taking a grism spectrum: all the information

is there, only it is hard to extract and in some cases some information about the continuum is erased by emission lines. An example of this is [OIII]/Hβ, which cannot be deblended to obtain the contribution of each line, so that information is lost. In the cases where dust is present, it is also necessary to make assumptions to account for continuum reddening and differential line reddening, because any two emission lines are to be far apart. Then it is difficult to find bands which are line-free. The study of ELGs with broadband colours is more difficult and requires very deep observations to minimize the errors in the continuum. This can be done simply by placing two broadbands bluewards and redwards of the intended line (where they are line-free) to bracket the estimate of the continuum flux at the line wavelength.

The first time that galaxies with large EWs (spectrsocopically confirmed) were found to affect broadbands colours was in the green peas, galaxies up to z=0.3 with excess [OIII] line emission that makes them look green in RGB photometry (Cardamone et al., 2009). At high redshifts, the first usage of broadband colours to actually measure EWs (for [OIII]) was performed in van der Wel et al. (2011). Ever since, the popularity of the broad-band approach has grown with the new large samples of deep photometry, as shown in works like Smit et al. (2014b), Marmol-Queralto et al. (2015). A more detailed review of ELG measurement methods will be presented in the introduction of chapter 3.

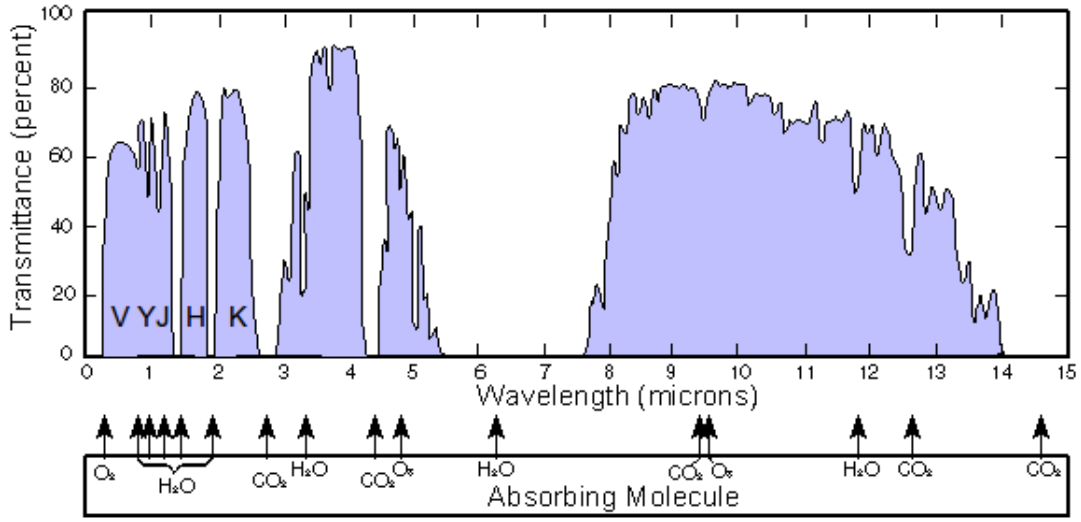

Figure 1.7: Wavelength windows for ground-based observation due to water vapor and CO_2 in the atmosphere of the Earth. The positions of the J, H and K bands are shown. The two subsequent peaks of transmission (L and M bands) roughly correspond to the 3.6 and 4.5 μm IRAC bands. Telescopes at higher altitudes can mitigate this. (from Wikimedia, public domain: https://upload.wikimedia.org/wikipedia/commons/1/1c/Atmosfaerisk_spredning.pdf)

Instrumentation and Data Processing

Observing the high-redshift Universe so far has required a combination of ground and space-based telescopes. Ground-based telescopes have a large (and growing) collecting area and can go very deep. However, the redshift of visible wavelengths by (1+z) places the well-understood restframe visible in the near infrared, in which the sky coverage is limited to the visibility windows shown in Fig. 1.7. Going to space is necessary to have a continuous wavelength window and diffraction-limited spatial resolution is possible, however, collecting surfaces are smaller than those possible from the ground. For observations from 5.5μm to 7.5 μm (and the gaps at 1.4, 1.9, 2.8, 4.3 μm), there is no ground option (see figure 1.7), so a large infrared space telescope must be employed. This explains the need for the James Webb Space Telescope (JWST). However, the 3.4 to 4.1 μm window looks like it could be promising for deep observations with a large ground-based telescopes, to complement the bluer bands of JWST. Photometric surveys in multiple bands are the best resource for finding the furthest/faintest ELG galaxies.

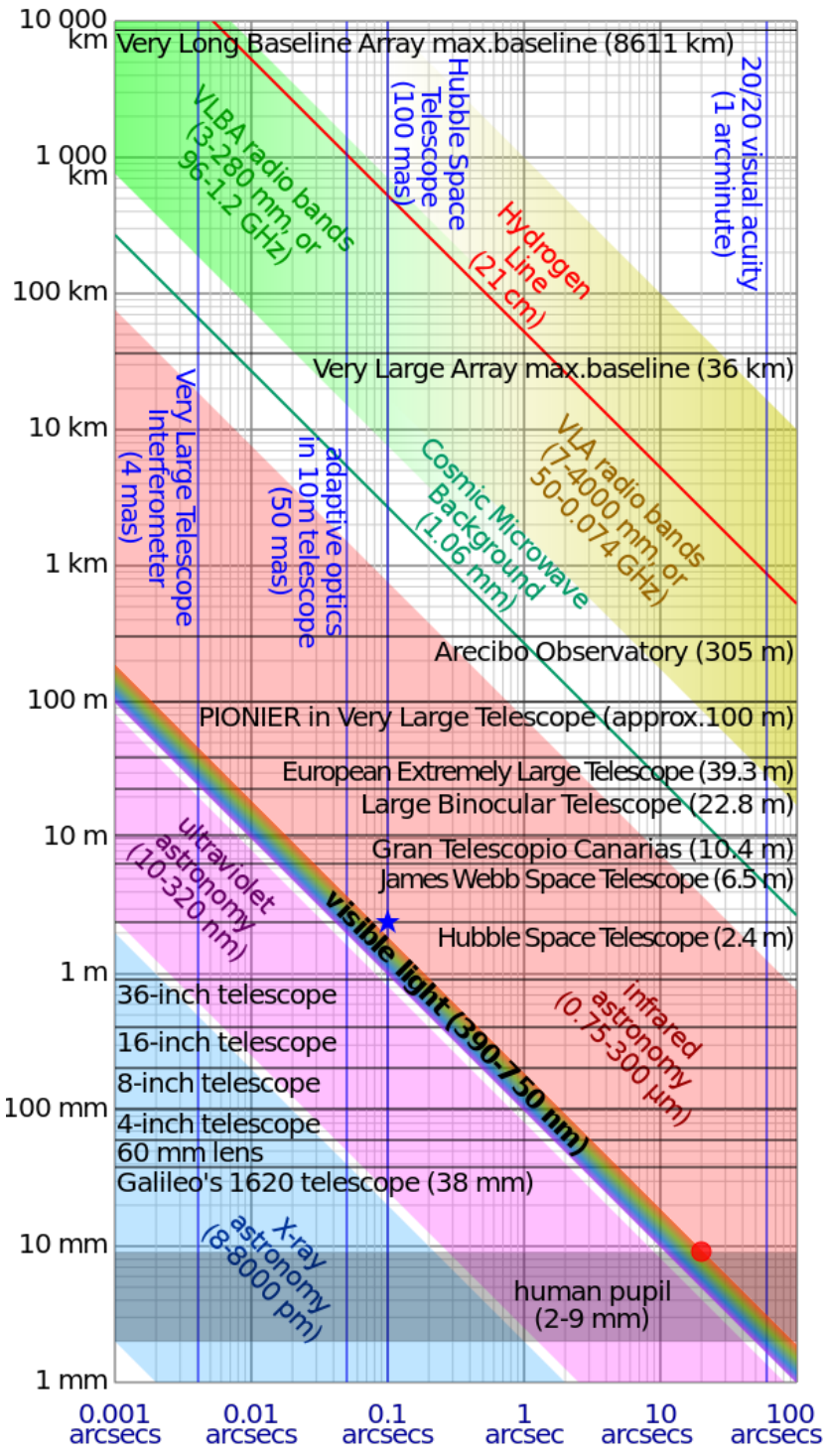

Figure 1.8: Summary of diffraction limits for ground and space-based telescopes with diffraction limit in the x axis and diameter (or baseline for interferometers) in the vertical axis. Wavelength ranges from the X-ray to the radio are shown in colour. (Wikimedia creative commons)

HST - WFC3

HST revolutionized astronomy. It started in 1995 by providing the deepest aperture-limited resolution imaging of the Universe at the time (the Hubble Deep Field) and giving epoch information of SNIa for usage as standard candles to measure the Hubble constant as mentioned in section 1.1 and ever since has been the go-to telescope for visible near-IR sub-arcsecond imaging. The primary mirror is 2m wide and it has a focal length of 57.6 meters. Its main advantage is that spatial resolution is diffraction-limited and as such it can deliver 103184*λ/D=0.08 arcsec resolution in the H band (check Fig. 1.8 for a summary of telescopes in wavelength and resolution). It has an array of sensors, notably the Advanced Camera for Surveys (ACS) CCD and the WFC3.

The Wide-Field Camera 3 is a fourth-generation Teledyne HgCdTe FPA (Beletic et al., 2008) with a plate scale of 0.13 arcsec/pixel and FoV of 123x136 arcsec. The available infrared filters range from 900 to 1700 nm (no cooling): the wide filters F105W (here Y_{105}), F125W (here J_{125}), F160W (here H_{160}) F110W, F140W, the medium filters F098M (here Y_{098}), 127M, 139M, 153M and additional narrow-band filters (more at www.stsci.edu/hst/wfc3/ins_performance/throughputs/IR_filterthru.html).

SPITZER - IRAC

Spitzer is also a space-based telescope with the InfraRed Array Camera (IRAC) (Fazio et al., 2004) focusing on NIR wavelengths on 4 simultaneous channels on two 5.2'×5.2' fields: 3.6+5.8μm (InSb detector) and 4.5+8 μm (Si:As detector), with pixel size 1.2'×1.2', with a PSF 10 times wider than HST NIR, which creates confusion problems when cross-matching neighbouring resolved sources from high-resolution H imaging. The first two channels are still active, but channels 3 and 4 at 5.8 and 8 μm can only observe high signal-to-noise objects because it has run out of coolant.

In some cases, going to space is inevitable, but ground-based photometry can outperform space telescopes in collecting area as shown in Fig. 1.9, field of view and essentially, time: much more observation time is available for deep and wide surveys.

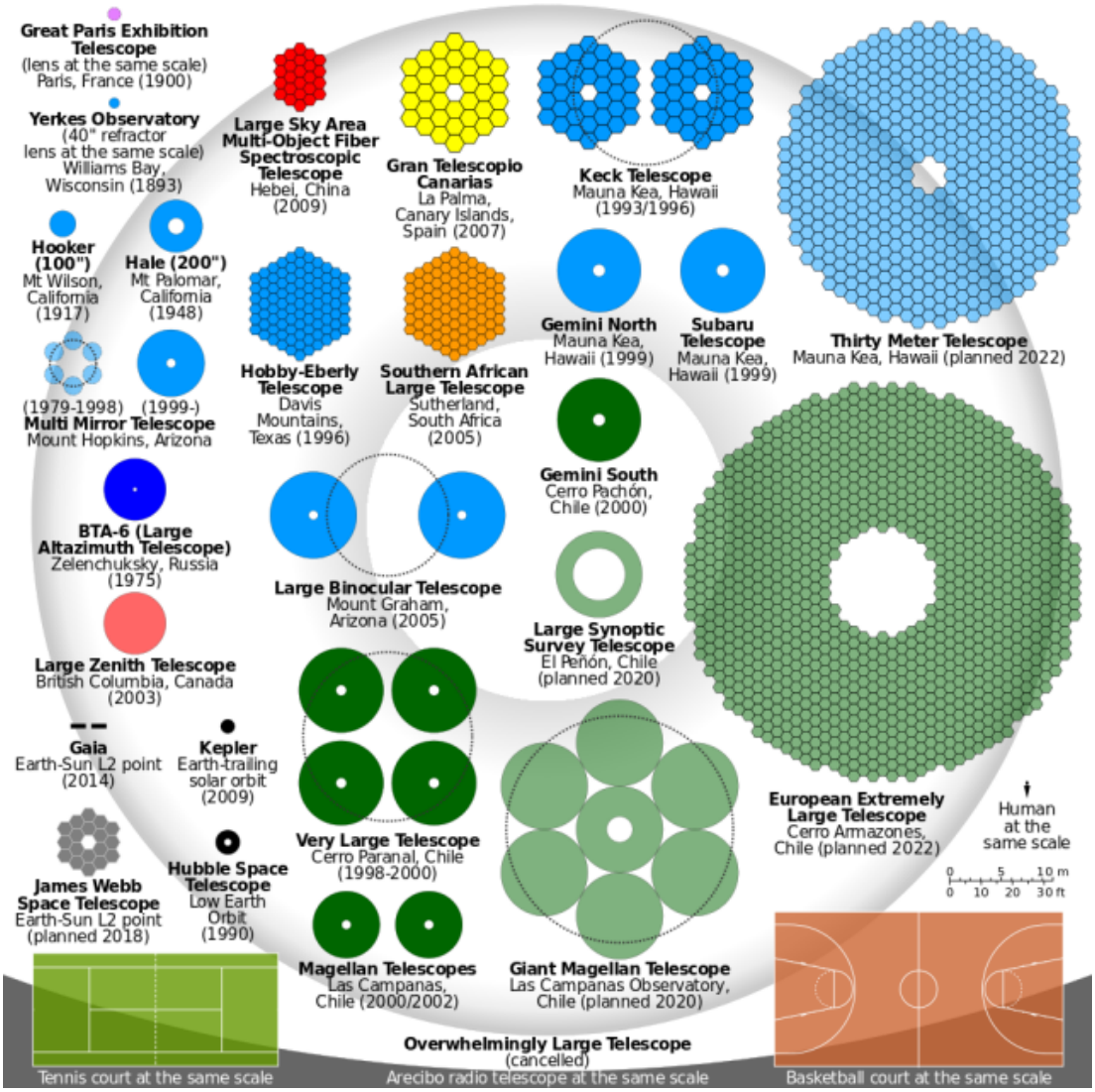

Figure 1.9: Description of the mirrors of present and projected telescopes, notably HST, Subaru, VLT, and JWST. Notice the large advantage ground-based telescopes have over space telescopes when the atmosphere is transparent. (Wikimedia creative commons)

SUBARU - SUPRIME CAM

Subaru is an 8.2m telescope on Mauna Kea and when the Suprime-Cam was comissioned in 2000 (Miyazaki et al., 2002), it had the highest sub-arcsecond survey speed: field of view × photon collecting area, so very deep wide-area surveys in the visible-NIR (B,V,R,i,z) could be performed, including the Ultra Deep Survey (UDS, Lawrence et al., 2007) and COSMOS (Scoville et al., 2007). More recently, the Multi-Object Infrared Camera and Spectrograph camera has been comissioned (MOIRCS, Suzuki et al., 2008), with a K_s band that can reach a 5σ limiting magnitude of 22.3 mag in 1 hour. As for all ground-based observations, resolution is seeing-limited due to atmospheric effects.

CFHT - MegaCam/WIRCam

The Canada-France-Hawaii telescope (CFHT) is a 3.6m survey telescope that provides analogous bands (U,G,R,i,z+) to the Subaru bands with the MegaCam detector (Boulade et al., 2003) plus K_s coverage with the WIRCam NIR camera (Puget et al., 2004). Resolution is also seeing-limited.

The K and Y bands

The VLT High Accuity Wide-field K-band Imager (HAWKI, Pirard et al., 2004) includes a K_s and Y-bands, which complete the wavelength-wide coverage from HST, IRAC and SUBARU. Additional K_s coverage is provided by other telescopes, such as the 4.1m VISTA (Dalton et al., 2006)

Photometric catalogs and magnitudes

The imaging in each band is then converted into catalogues: lists of objects with RA and DEC sky positions and photometric fluxes at different bands cross-matched from different instruments (Multi-band photometry). This is done by identifying galaxies and counting photons within an aperture for each of those objects, for example with the software Source Extractor (Bertin & Arnouts, 1996). This is a complex process, because apertures between observations of different wavelengths have different spatial resolutions, so they have to be aperture-matched. In the case of HST, the reddest band is H, which has the highest wavelength and the widest point-spread-function (lowest resolution), so catalogues extracted from the CANDELS survey use that band to set the aperture. However, when adding photometry from other telescopes, care has to

be taken to re-match the apertures and Point-spread-function (PSF) centroids, otherwise artificial differences in magnitudes might arise between bands. This is why it may be necessary to perform zero-point adjustment corrections between filters. Then, a photometric catalogue is compiled with the observed fluxes in each band (normally in units of μJy=10^{-29} erg/s/cm^2/Hz, roughly 23.9 ABmag) and the errors, which for a uniform sky background would just depend on the magnitude of each source, but in practice depend also on how the errors vary.

From there, the fluxes can be converted to magnitude using:

$$m_{AB} = -2.5log_{10}(F_\nu/(erg/s/cm^2/Hz)) - 48.6 \tag{1.33}$$

The CANDELS Survey

The Cosmic Assembly Near-Infrared Deep Extragalactic Survey (CANDELS) is a major HST-based survey covering five regions of the sky with deep multiband photometry. The science case and survey design are described in Grogin et al. (2011) and the data reduction and data products are described in Koekemoer et al. (2011). The survey provides deep HST near-infrared photometry in five fields in a wedding-cake approach (CANDELS wide: all fields, CANDELS deep: parts of UDS and GOODS and the ultra-deep HUDF) either close to the galactic poles or pointing away from the galactic center (COSMOS), and has a strong extragalactic survey focus (low field star counts). Each field was chosen to overlap with sky areas already widely covered in previous surveys to cross-match objects and produce extensive mutiwavelength coverage from X-ray to Radio. Over time, new deeper subregions have been added to the surveys, creating near-continuous deep broadband coverage from UV to IRAC.

To study the well-known visible spectrum of galaxies at high redshift, it is necessary to probe the visible wavelengths of 4000Å-6000Å at z>1, implying observed wavelengths of λ>8000Å-18000Å, which places most familiar galaxy physics at high-redshift behind the H2O and CO2 absorption of the earth's atmosphere. There are gaps in the absorption, where the UKIRT J ($\sim$ 12500Å), H ($\sim$ 16000Å) and K ($\sim$ 22000Å) filters were placed (analogous to BVR at z$\sim$2), but the difficulty in subtracting sky emission limited the depths then reachable in the infrared. A key goal of the refurbished Hubble Space Telescope (HST) was to obtain the deepest NIR photometry in J and H using the WFC3 NIR camera.

When HST's spherical aberration was corrected, the Extended Groth Strip (Groth et al., 1994) and the Hubble Deep Field (Ferguson et al., 1995) were percursors to modern coordinated multiband surveys, of which CANDELS is a refined example. I refer to the EGS in this way, because Groth first defined the compromise between depth and sky area to go deep while mitigating cosmic variance (using a strip geometry) which characterizes the wedding-cake approach taken today. I refer to the HDF because it set a trend for surveys of extreme depth, despite limited sky coverage. Furthermore, at the time it was essential to combine Chandra X-ray observations with HST NIR photometry and ground-based visible photometry, because this was one of the most reliable ways to identify high-z galaxies, through AGN X-ray and Radio emission. Later space telescopes filled important wavelength gaps unavailable from the ground but essential to study the restframe visible above z>4, like SPITZER (the IRAC bands) and Herschel. From the ground some NIR gaps can be filled, like the K band from HUGS (Fontana et al., 2014), the deepest K-band survey so far, but due to CO_2 and Water atmospheric absorption, the Infrared bands require a large space telescope, which JWST will be the new generation of. With a large number of photometric bands and dynamical range in wavelength, SED fits become possible to obtain redshifts, masses and emission line luminosities up to z=5.

CANDELS was designed to supply a number of regions in the sky with deep V606, i814, J125 and H160 imaging. These fields have complementary characteristics (fortuitously and by design): COSMOS was designed to be wide area in a variety of bands, UDS has the largest number of deep NIR photometric bands (takes advantage of SUBARU visible ground-based photometry), GOODS has the deepest observations (it is mostly space-based HST ACS and WFC3 bands with a strong focus on SPITZER IRAC coverage) in two nearly opposite sky areas to compensate for the small area (the price of going deep) and EGS/AEGIS is a precursor field, having been the first to combine multiband observations as commonly used today. The HST WFC3 and ACS coverage maps for the 5 CANDELS fields are shown in Fig 1.10

The CANDELS photometric catalogs used in this section were originally available on the private CANDELS wiki website, but those officially released are now also available on the MAST website: https://archive.stsci.edu/prepds/candels/.

The GOODS-North multiband photometric catalog have not yet been officially released.

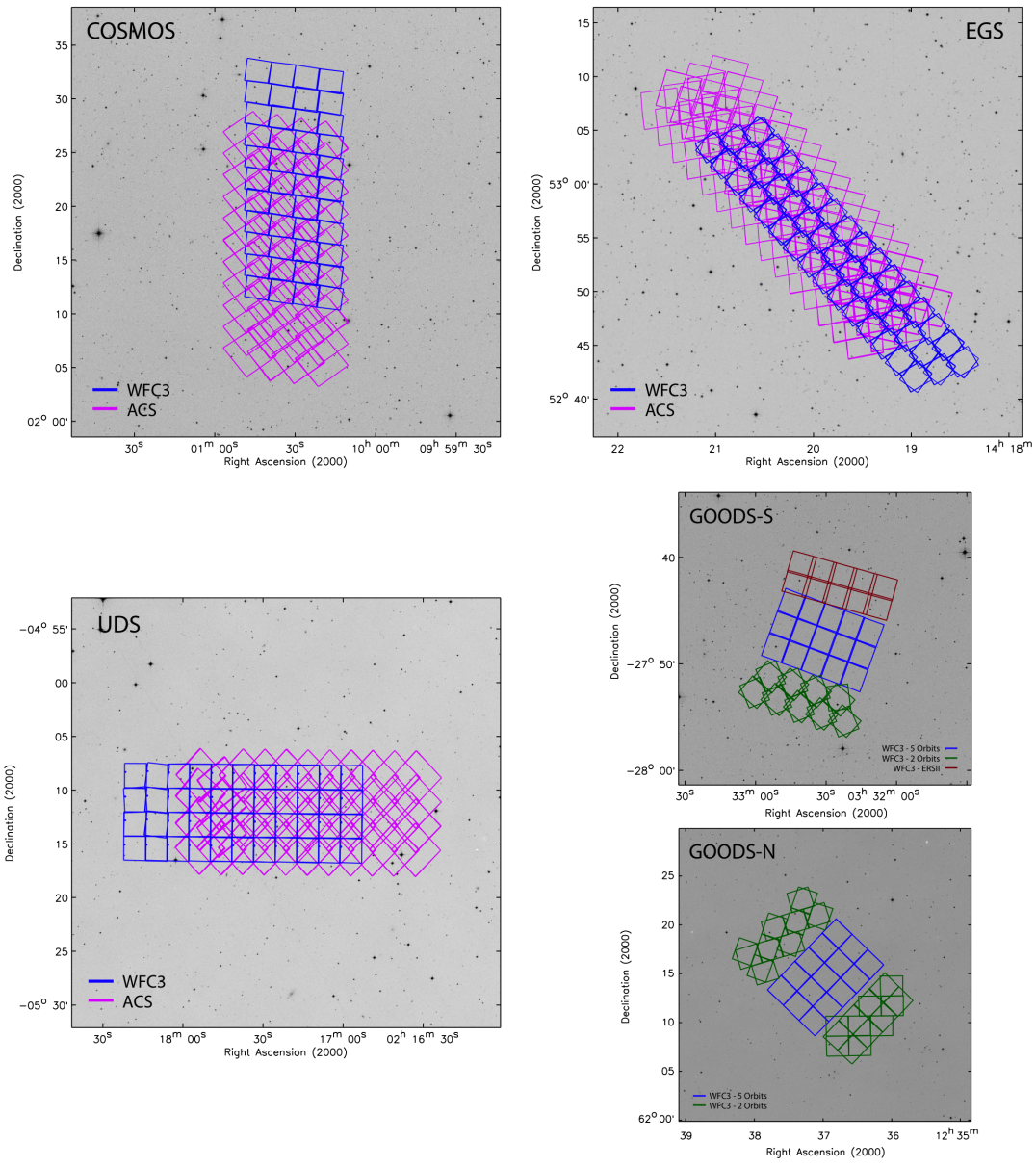

Figure 1.10: Maps of the deep HST WFC3 and ACS pointings in the five CANDELS survey fields (http://candels.ucolick.org/survey/Field_Maps.html)

Aims and Overview of the Thesis

After presenting this context, in the following chapters I will describe how an efficient new technique to measure the strengths of emission lines in galaxies over redshift was developed to trace their star-forming properties using broadband photometry from the restframe ultraviolet to the near-infrared. This method has the advantage of not requiring assumptions about emission lines (other than their expected wavelength) to measure their strength, by only measuring residuals against a set of simpler stellar-continuum models (with assumptions described in chapter 2). This method is able to simultaneously obtain equivalent widths for the three strongest lines: Hα, [OIII]+Hβ and [OII] up to z=5 down to the lowest available masses for large numbers of galaxies in surveys like CANDELS. Some drawbacks of this approach are that the values of EW it produces have large errors and so is not ideal for measuring equivalent widths of individual galaxies, for that spectroscopy would be more reliable.

This thesis attempts to bridge the current gap in understanding between the very high redshift parameters of cosmological models (and their consequences and their observable consequences for the earliest galaxies) and progressively higher redshift observations, driven by instrumentation and galaxy modelling to reach the highest possible redshifts. The method I will describe in Chapter 3 is ideal to explore this gap, because it focuses only on the most strongly star-forming galaxies and the values of EW measured become easier to measure towards higher redshifts, as the familiar low-redshift old stellar populations becomes less dominant towards higher redshift. This is done in three chapters, each addressing a different question.

In chapter 2, I seek to understand how simulated galaxies and their star formation histories are converted into observed broadband fluxes using a set of spectral synthesis models and what parameters we can reliably expect to know from spectral fitting of multi-band photometry. From here, I attempt to show what quantities are recoverable from broadband photometry, using colours and principal component analysis and end with a set of stellar stochastic burst models that align well with observed CANDELS colours.

Chapter 3 addresses the fact that some of the colour discrepancies observed in Chapter 2 cannot be described by stellar emission alone and whether these discrepancies between the simulated galaxies and the CANDELS observations

are consistent with nebular emission. After proving this, a set of colour baselines is constructed to generalize the measurement of line equivalent widths systematically from z=0 to z=5 for Hα, [OIII] and [OII] in the Ultra-deep Survey.

Finally, chapter 4 addresses whether it is possible or not to use this method and the corresponding line luminosity ratios to trace the evolution of physical parameters over mass and redshift and describes how each CANDELS field was adapted to the analysis described in Chapter 3, how line luminosities are obtained for each line and how these can be used to survey star formation rates, ionization parameter and metallicity as a function of redshift and mass. I finish with a summary of results and possible ways forward for developing and using the method.

Chapter 2

Linking Theory and Observables with Simulations

This chapter briefly describes a number of approaches to galaxy growth modelling, and the techniques used to compare deep multiband photometry from CANDELS (through colours and principal component analysis) with mock observables obtained from different types of simulations (semi-analytic, adaptive mesh refinement and exponentially declining with bursts). Originally, the work described in this chapter was intended to have described in detail how different parameters (like star formation efficiency, supernova yields) in semi-analytic galaxy modelling can influence colours and to attempt to recover some of those parameters (like age and stellar metallicity). However, in trying to match the colours through simulated galaxy star-formaton histories, it was found that a consistent population of galaxies had colours which could only be described through emission-lines and that an independent way to measure them would be necessary.

Star Formation History Models

Star Formation Histories (SFH) describe the rate at which stars are formed in a galaxy as a function of age. The grid of stellar mass produced as a function of time can be constructed with regular time steps or on a logarithmic time scale, to provide improved time resolution for recent star formation and, in particular, the short-lived populations of O and B stars. Furthermore, star formation history tables also detail the stellar metallicity of each burst of star

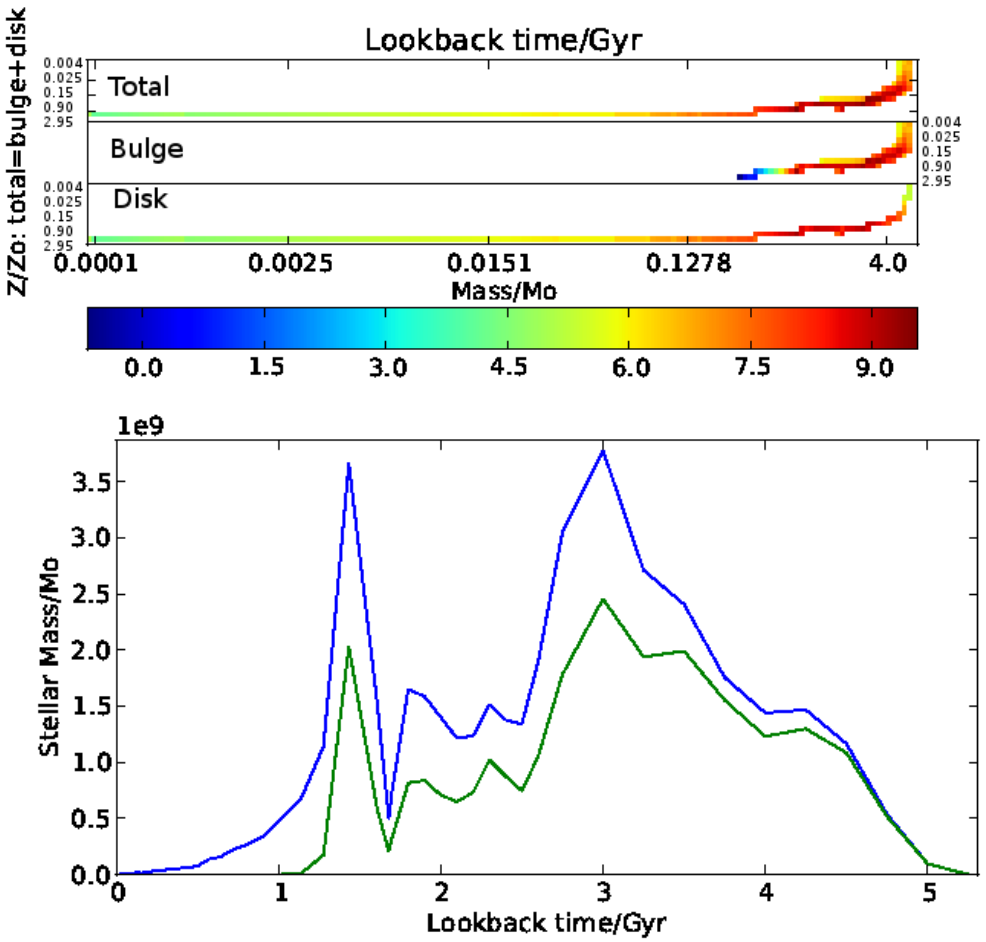

Figure 2.1: Upper panel: Example of a detailed star-formation history table for a z=1 galaxy from a semi-analytic galaxy catalogue (Somerville et al., 2008). Time and stellar metallicity are binned in a logarithmic scale and the vertical scale shows metallicity values for the galaxy (top third of the scale) bulge (middle third) and the disk (lower third). The colour shows the $\log_{10}$ stellar mass formed in each bin. This example shows strong early low-metallicity star formation (on the right) localized in the bulge, which increased metallicity and quenched star formation. The disk shows a gentler evolution of star formation, with an exponentially-declining SF. Bottom figure: Total mass of stars produced in each age bin in blue (bulge in green). Masses can be divided by age bin width to show star formation rates. This galaxy displays a rising SFR which peaks after 2Gyrs and a second burst of star formation (probably due to a merger), after which the bulge SF is rapidly quenched and the disk forms stars passively (exponentially declining SF) with the remaining gas.

formation (an example is shown in Fig. 2.1). In modelling the mass assembly of galaxies, the SF history at different metallicities is the essential output from any simulation. From this, other physical quantities such as star formation rates, metallicity evolution, luminosity-weighted age and mock photometry can be calculated. It is important at this point to distinguish between stellar and gas metallicities. The metallicities of stars formed in a simulation correspond to the gas metallicities at the time of formation of those stars. From star formation onwards, the metallicity of stars is locked in, whereas gas metallicity evolves independently of existing stellar metallicity depending on star formation rates and the corresponding supernova rates as well as the gas inflows that dillute the metal concentration in the interstellar medium (ISM).

Single-Age Models and Colours

From the star-formation history, the final observables extracted that can be directly compared with observations are multiband photometry. From here one can construct a single-band luminosity function (LF), but colours hold information which the LF by itself cannot convey and which is essential for model discrimination and refinement. In other words, even if one obtains the right numbers of galaxies at each magnitude in multiple bands, it is still possible to get incorrect colours. The average colours of galaxies needs to be correctly reproduced for a model to be considered viable, but the variance of these colours reveals other properties of galaxy populations, like intrinsinc burstiness and frequency of other off-equilibrium processes like minor-mergers.

To produce simulated colours, a spectral library is used to translate the SFH tables into an integrated spectrum, by assigning each age and metallicity bin a single-age and single-metallicity spectrum template. These are then integrated and weighted by mass to produce a mock spectrum of that galaxy, which is then convolved with the filter response functions to produce mock photometry.

Spectral libraries are extremely important, because any inaccuracies will be propagated and potentially dominate the information coming from the star-formation history. Even though these libraries contain accurate spectral observations of the most common stars, there are generally not enough of these spectra to properly represent rare objects, short-lived stages of stellar evolution, UV and infrared parts of the spectrum and generally how stellar evolution is affected by lower metallicities expected to be prevalent at higher redshifts. For this, a set of theoretical stellar evolution tracks is used to estimate the stellar interiors of low-metallicity stars and, most importantly, stellar atmosphere modelling of AGB stars and their thermal pulsation behaviours and infrared luminosity.

Of the spectral libraries available, the most reliable and widely used are those of Bruzual & Charlot (2003) (hereafter BC03), which produces the (R-i,i-z) colours shown in Fig. 2.2. More recent spectral libraries include more sophisticated treatment of the infrared, but do not seem to produce the right colours. In this work, the models of Charlot & Bruzual (2007) (CB07) were tested but ultimately abandoned due to an unreliability of the infrared spectrum due to the treatment of Thermally-Pulsating AGB stars, which produced redder

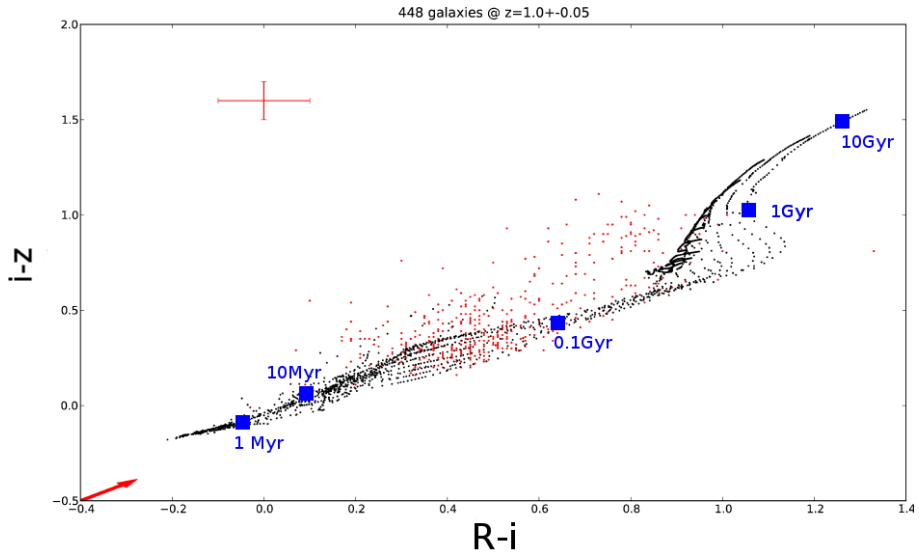

Figure 2.2: BC03 single-age/single-metallicity population colours (black dots) vs CANDELS-UDS (Galametz et al., 2013) observations (red dots) in colour-colour space (R-i, i-z) at z=1. The red cross shows the median scatter in observed colours. The blue squares mark the ages along the solar-metallicity track for reference. This figure shows that a majority of galaxies at z=1 can be approximated by a young 100Myr population rather than older 1Gyr populations. A number of objects lie in between the young and old models. While this could be caused by strong dust attenuation of young galaxies, it can also be a combination of old and recent star formation.

galaxies than observed (shown in figure 2.3).

From the single-age colours shown in Fig. 2.2 it is already possible to see that a majority of galaxies selected to be at z=1 seem to lie along single-age population tracks, especially the blue ones younger than 100Myrs. However, many of the other objects are expected to be composite (multi-epoch star formation, with a recent burst over an old stellar population) and include at least two major components in their SFH, so they sit in between the recent SF and the old stellar populations, with an average colour. With the BC03 colour catalogue, the observed colour of any possible simulated SFH can be computed: perform a mass-weighted sum over the SFR of the flux ratios corresponding to the colours

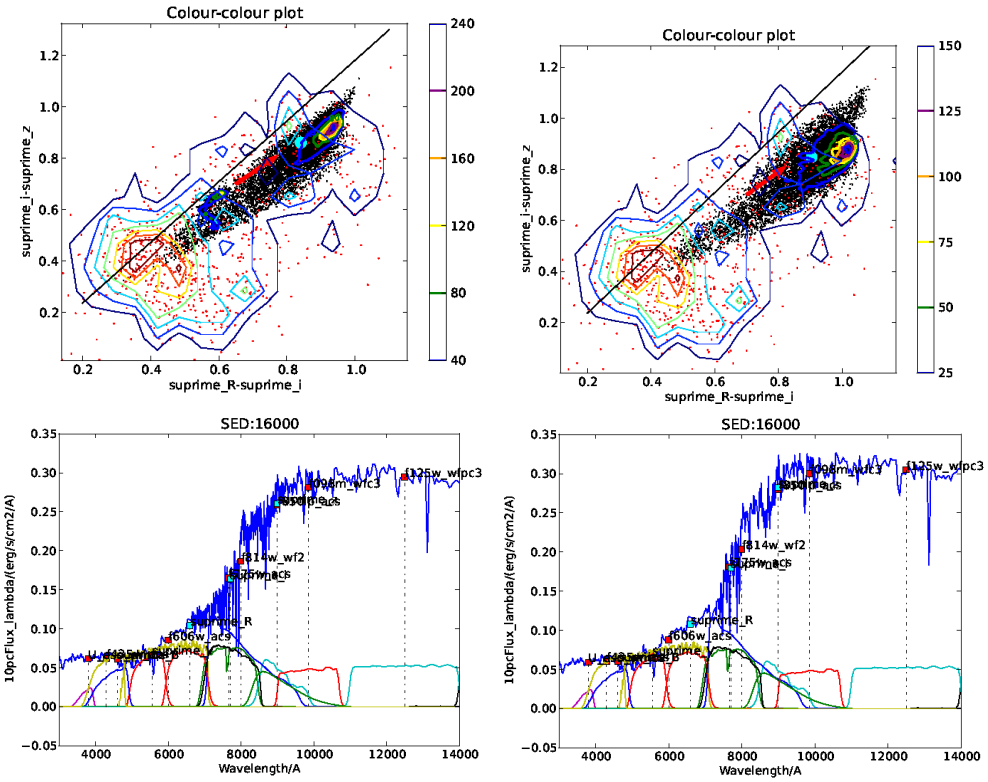

Figure 2.3: Top: Comparison of BC03 (left) and CB07 (right) colours for Somerville et al. (2008) models (black dots and respective density contours) with CANDELS observations (the red dots and their density contours). Bottom: respective observed spectrum for the galaxy represented by the cyan circle close to colour (0.8,0.8). The CB07 model displays enhanced flux redwards of the 4000Å break, while keeping the bluer bands the same. None of these changes seemed to improve the match with the observations, in fact making it worse in the reddest colours.

shown.

Dust absorption, UV processing and emission lines

Other effects to include in modelling galaxy photometry are dust reddening and emission lines. A simplified way to add the effects of dust is to add a dust screen (independent of the spatial distribution of light sources in the galaxy) by multiplying the galaxy spectrum by a shallow powerlaw of index n=0.7 (from R_V=3.1) and normalization given by an optical depth. This is shown in Figure 2.2 and other colour-colour figures in this thesis for A_V=1 as the reddening vector, showing the effects of a dust screen with an optical depth of 1 in the V band on

the colours. An example of the effect of dust on a spectrum is shown in Fig. 2.4. In a more detailed approach to the screen model, the dust law can be made steeper (n=1.3) for age bins below 100Myrs. This affects very young galaxies with a large amount of dust, but the direction of the reddening vector does not change enough to provide a different interpretation of results in colour-colour space due to degeneracies between the direction of age effects and reddening effects on colour.

A galaxy with a fraction of its total stellar mass made of young (age<100Myr) stellar populations can be described by a linear combination of one steep (-1.3) one shallow (-0.7) reddening laws. μ indicates the fraction of attenuation that comes from the ISM, while the remainder 1-μ coming from steeper birth cloud attenuation. For old populations μ=1.

$$\tau_{lambda} = \tau_V[(1-\mu)(\lambda/\lambda_V)^{-1.3} + \mu(\lambda/\lambda_V)^{-0.7}], \lambda_V = 5500\mathring{A} \tag{2.1}$$

However, another effect with real potential to change the observed colours in a way that is distinguishable from the natural colour range of the single-age models is line emission. The very high numbers of ionizing photons in starbursts combined with gas densities large enough to make Lyα optically thick is enough to excite Hα and the forbidden oxygen lines [OII] [OIII] to very high luminosities compared with the faint continuum in visible wavelengths.

Adding these lines for a combination of ionization parameter, density, metallicity, temperature, and a consistent λ <912Å ionizing photon rate it is possible to make predictions about line contamination (especially if Av is low and differential attenuation is negligible). This is an active field of research: Pacifici et al. (2015), Wilkins et al. (2013), Zackrisson et al. (2008) and Schaerer & de Barros (2012). However, this involves adding a number of parameters which increase degeneracy even more when simulations output these quantities for each star particle. As such to minimise the number of assumptions in measuring emission line equivalent widths, a choice was made to measure off of the line-free models and expected line-free colours to assume as little about these mechanisms as possible (just enough to get the redshifts and masses right).

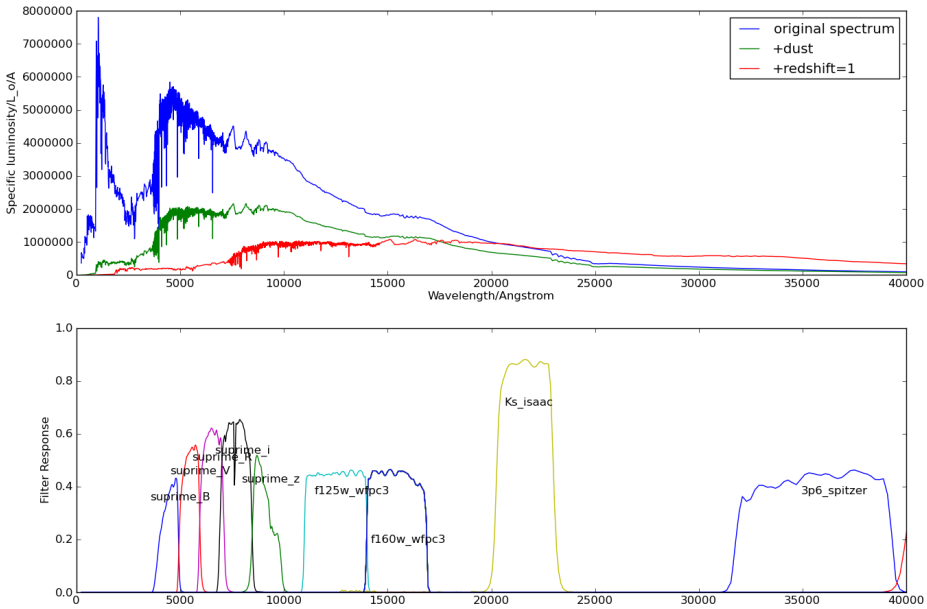

Figure 2.4: Top: A dust-free integrated galaxy rest-frame spectrum, with very strong Balmer and Lyman breaks (blue) and a blue continuum; when the effects of dust reddening are added (green) the major UV features are damped; the same spectrum is then redshifted to z=1 (red) and integrated over the filters shown in the lower panel.

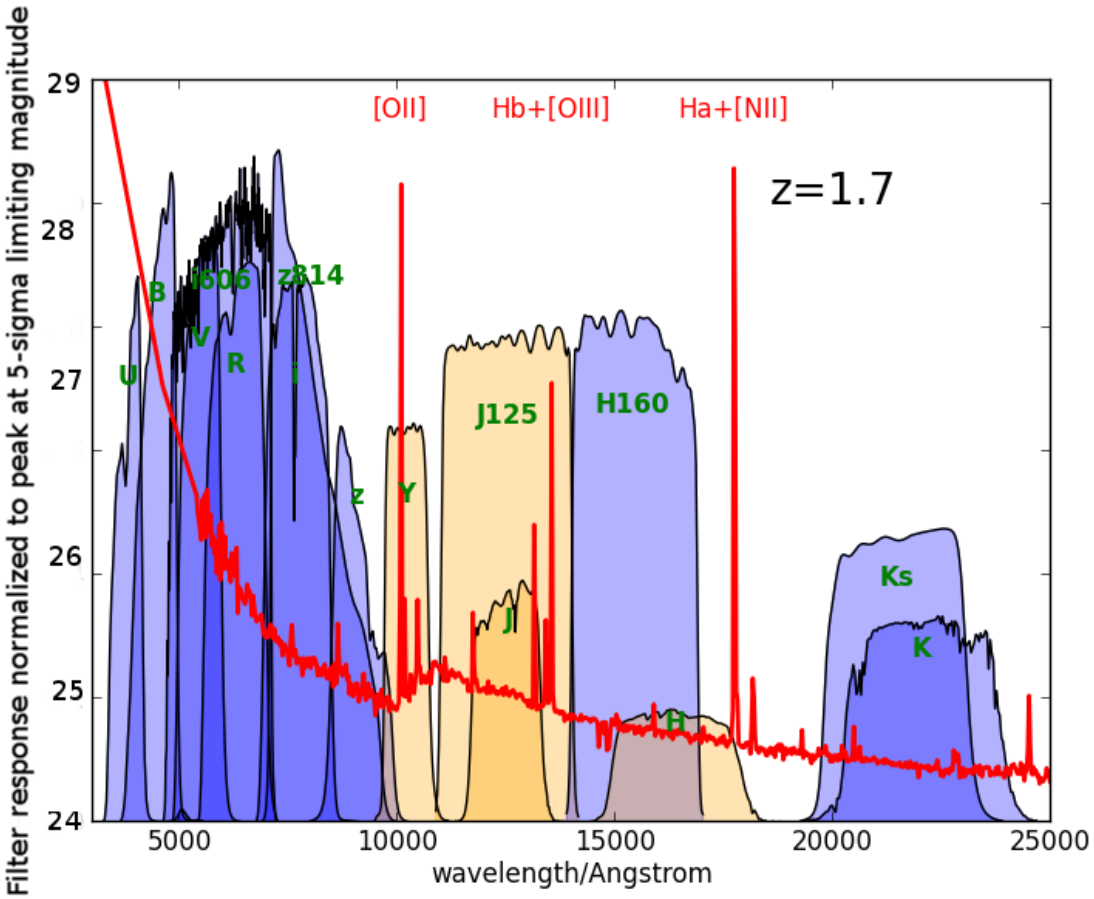

Figure 2.5: Example of how optical emission lines are present in broad-band filters typically used in ground-based and space-based observations of galaxies at z=1.7. It is difficult to ensure that adjacent bluer and redder filters are line-free to attempt to estimate a measure of the lin-free continuum by averaging the flux in those filters. Due to uncertainties in redshift, some objects may still display an ehanced H-band flux because their real redshift may be lower and fall in the H band, so baseline filters must be chosen far from emission-line contaminated bands.

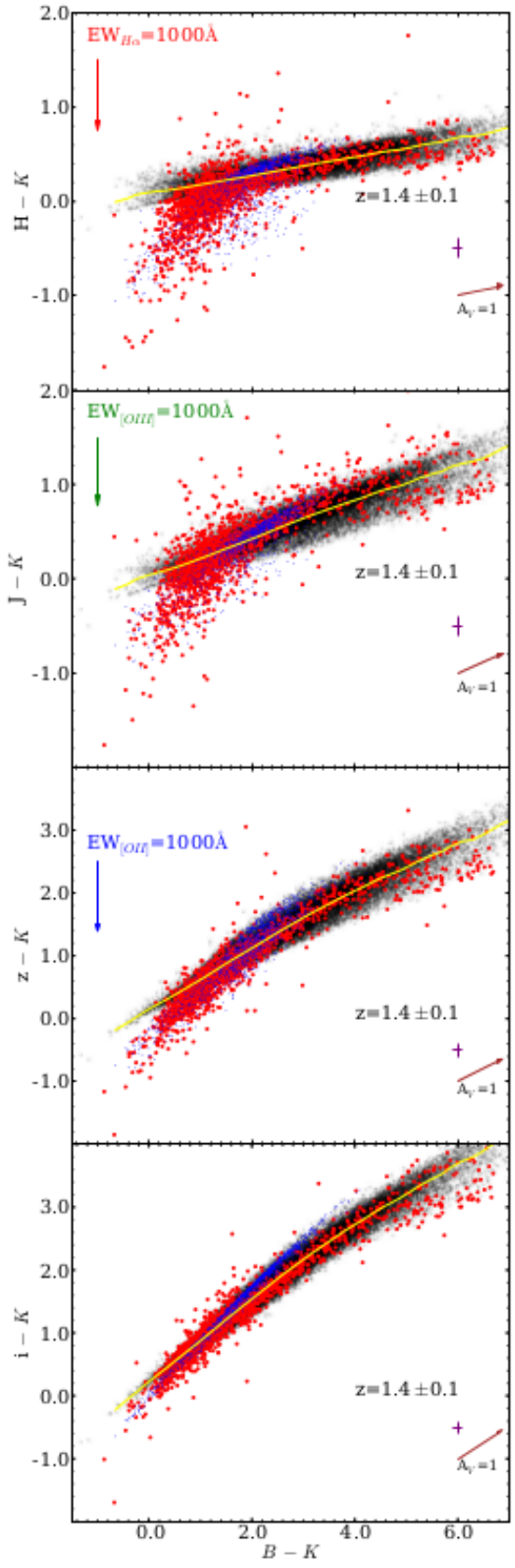

Figure 2.6: Mock colour-colour diagrams drawn from models including line contamination computed using CLOUDY as described in Pacifici et al. (2015)) including line emission for a range of ionization parameters. Black: line-free stellar models. Blue: models with emission lines. Red: CANDELS-UDS observed colours (redshifts are photometric). The top three panels show colours where contamination at z=1.4 is expected by the line indicated (Hα in H, [OIII] in J and [OII] in Y). The bottom panel shows the agreement between line-enhanced, line-free models and observations when using the line-free i-band. The yellow line shows the median of all simulated colours (the black points) in each colour bin.

Somerville Semi-Analytic Models

After describing how star-formation histories are converted into colours using the BC03 spectral library, in this section I will show the first set of realistic SFHs used in this thesis, drawn from a simulation described in Somerville et al. (2008). This semi-analytic model was created to describe the co-evolution of galaxies and AGN through AGN feedback prescriptions. It was chosen because of its level of detail, as it contains galaxies over a range of redshifts, with an age-metallicity grid and bulge-disk decomposition. Figure 2.7 shows results, with examples of individual galaxy SFHs at each of these redshifts and their location in colour-colour space.

These models seem to predict redder colours than the observations suggest, possibly due to their focus on AGN feedback and bulge growth, all effects which are most pronouced towards the high-mass end and lower gas densities. More recently Somerville et al. (2015) improves on the previous models and employs better SFH prescriptions. Historically speaking, AGN feedback was the major problem to solve at the time Somerville et al. (2008) was published and the low-mass gas-rich samples of galaxies unveiled by surveys like CANDELS were not available yet. Since then, however, the focus has shifted to the bursty star formation seen in deep high-z observations, which this thesis addresses.

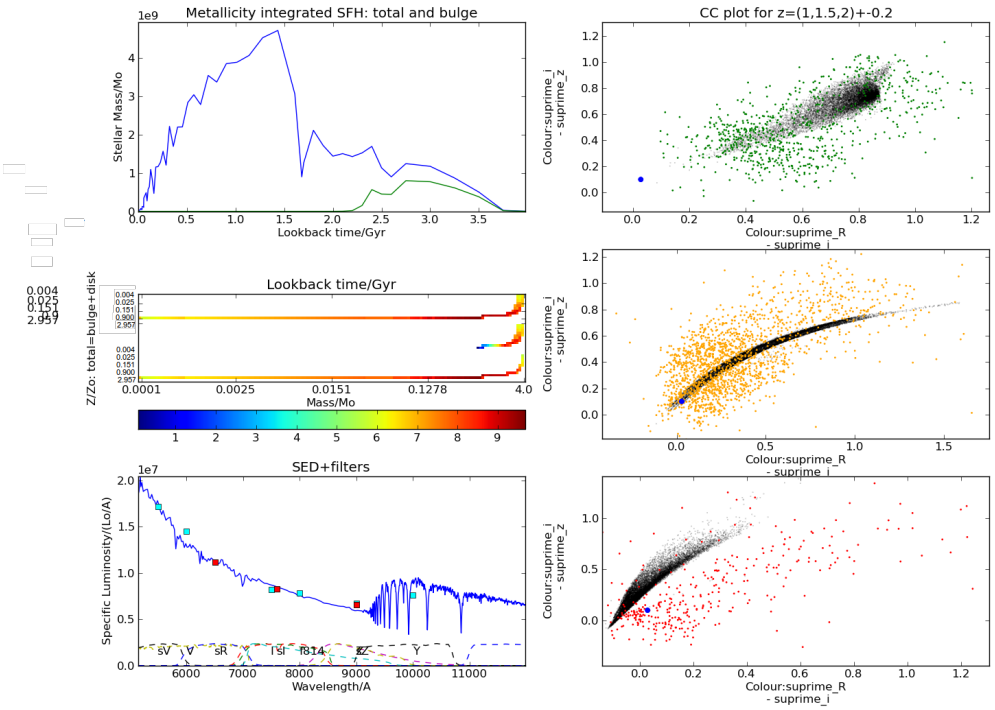

Figure 2.7: Somerville et al. (2008) semi-analytic mock observations in (R-i, i-z) colour-colour space (right panels) for z=1, 1.5 and 2 (top, middle, and bottom respectively). The black dots represent the Somerville models at each redshift and the coloured dots show CANDELS-UDS observations. The blue data-point in each of these panels shows the colours of the same galaxy at z=1.4 with the SFH shown on the top left panel (blue line) and its bulge (green line). The metallicity-SFH table is shown on the left-middle panel, with tracks for the disk, total and bulge coloured by mass produced in that age bin. The bottom left panel shows the spectrum of that galaxy.

GALICS

Given that the range of colours produced by the Somerville models was not appropriate for the CANDELS galaxy sample, a custom set of semi-analytic models was used: a simplified version of the GALICS code, which is described described in Hatton et al. (2003).

This is also a semi-analytic model running accretion over a set of simulated merger trees. It could be used to test the effect of semi-analytic recipes on the general outcome of accretion and feedback models: self-regulation and potentially recurrent SF behaviour due to the structure of the differential equations being solved. In the end, semi-analytic models are a testing tool that can be used to rule out mechanisms or quantify their prevalence, but due to degeneracies they cannot really capture the physics.

The way this model was used was to check the impact of SFH on observables. One conclusion was that the model templates and the implementation of the age grid can strongly affect the colours of the very young objects that are essential for model refinement, but it can be relaxed for objects without recent SF.

An example of how numerical implementation in semi-analytics is critical to the production of reliable observables is shown in Fig. 2.8: the age grid can affect the output colours by up to 0.025 magnitudes. An example of powerful insight provided by semi-analytics is shown in Fig. 2.9, where constant accretion and an enhanced inflow during 1Gyr are compared. Star formation responds to the additional gas by increasing to match the new equilibrium SFR at a higher accretion rate. When accretion ends, SFR decreases exponentially to match its original SFR at a lower constant accretion rate. Galaxy luminosity increases quickly as a response to enhanced accretion and stays high for almost 2Gyr, when it converges with the constant accretion model. Finally, metallicity responds by decreasing sharply at first, but quickly the metal output catches up and after the accretion inflow is over is when a metallicity surge is observed, for 4Gyr, at which point the galaxy metallicity stays constant. This is very important when considering the mass-metallicity relation, because it works for settled systems. Violently starforming systems may show some of these metallicity-reversal effects, or delayed response (due to the fact that pristine gas lowers metallicity, but after supernovae leading to higher metallicity), which may at first look counter intuitive in observables, like a brighter high-metallicity, low-star-formation object (a post-

starburst). A global picture of integrated galaxy properties or mean properties of a galaxy population are well tracked by semi-analytics, especially when testing how individual model prescriptions respond to self-regulation processes.

Another problem with simple semi-analytic codes is that the system of equations is solved effectively through the Euler method, which quickly amplifies errors. This is problematic when what is precisely being tracked are instabilities in the SF. This is why this model was ultimately abandoned by a collaborating group providing the dark-matter merger trees in favour of a spatially-resolved adaptive-mesh simulation (see Section 2.3).

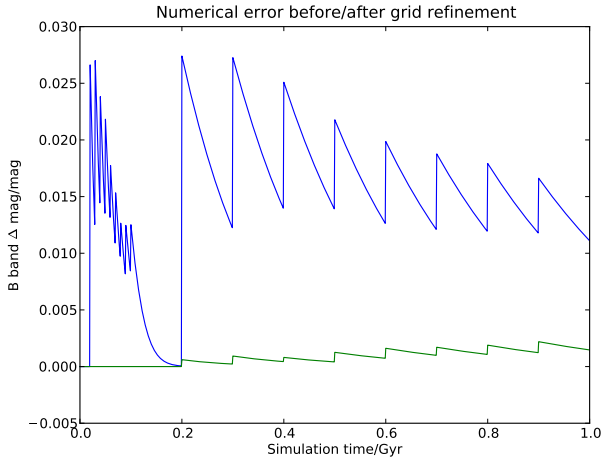

Figure 2.8: This figure shows an example of how the age grid refinement influenced the B band magnitude over simulation time. To reduce simulation errors, a finer age grid was used to improve photometric accuracy. Stellar masses created at age 0 of the star-formation table are shifted progressively right to higher ages by the simulation. Due to irregular binning, sometimes a mass bin will be distributed between two bins as mass is shifted to higher ages along the age grid. The end result is that for a single strong burst no bin which it enters is left empty, but drains exponentially. This is a major problem because a very small fraction of age-0 stars can substantially affect simulated spectra. The difference is shown here between the blue coarser grid and the finer grid (green). Even though it is computationally heavier to use the finer grid, photometric errors are minimized before 0.2Gyr and after that the effect of that burst of star formation is minimal on galaxy colours.

Another problem with semi-analytic models is that because the gas position and properties are not tracked, it is difficult to realistically simulate spontaneous

bursts (non-merger induced) of star formation (active star formation), unless a recipe for random bursts is introduced ad-hoc. Semi-Analytic models average accretion and bursts in space (prescriptions can be added in time), so they can make good predictions for quenched high-mass galaxy populations (where AGN feedback dominates anyway).

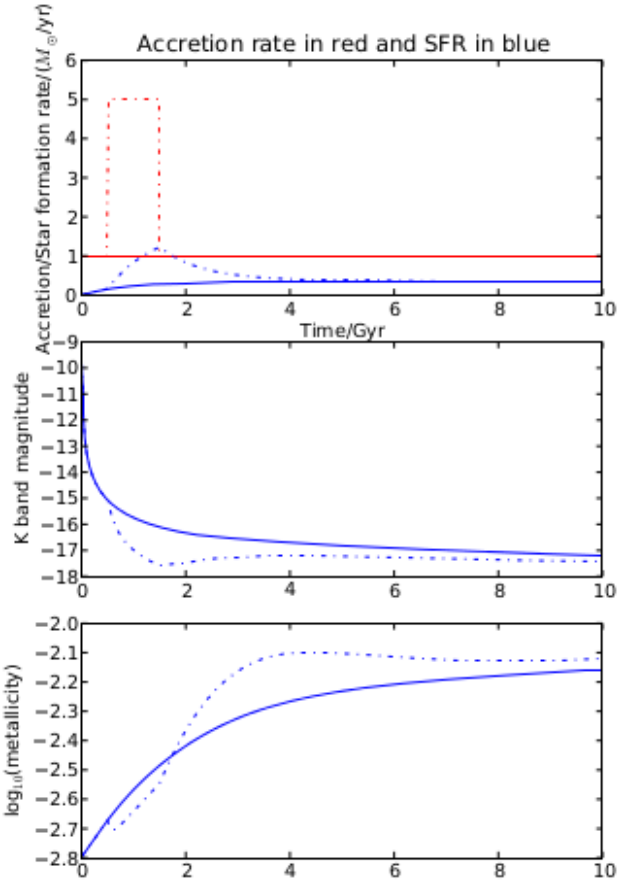

Figure 2.9: This figure shows the effect of a temporary increase in the accretion rate. The red solid line shows a constant accretion rate with the corresponding SFR in solid blue. The dashed lines show the effects of the perturbation in accretion and how equilibrium was restored. In the top panel, SFR increases linearly throughout the duration of the enhanced accretion, to match the equilibrium SFR of the new accretion rate. However, when the accretion stopped, the SFR exponentially returned to the original values. The middle figure shows the K-band magnitude of the galaxy. When the accretion is enhanced, the enhanced SFR immediately impact on the galaxy's brightness, but when the accretion stops, the galaxy remains brighter than without added accretion for 2Gyr. Finally, the bottom panel tracks total stellar metallicity and illustrates the oscillatory/self-regulating nature of galaxy formation: when accretion increases, the metallicity is instantly decreased, due to the higher amount of pristine gas which is not immediately consumed due to feedback. However, as SFR increases to match accretion, metallicity increases and even surpasses the original values (due to the extra metals produced in the SF burst). In fact, this amount of gas is enough to completely change the metallicity history of the galaxy, making it reach its final metallicity 7 Gyr earlier.

RAMSES AMR Simulations

A complementary approach to semi-analytic modelling is to actually track gas and star formation in space. This requires very large volumes in order to simulate galaxies at cosmological scales and high resolution to keep track of gas properties, especially at high densities, where most of the star formation takes place. A way to make this more efficient is to adapt the mesh in which gas is tracked to the densities, and to refine the grid only where required (Adaptive Mesh Refinement, or AMR). The advantage is that the gas physics is well simulated, including gas streams and perturbations in the gas density within the galaxy. Both factors are essential to producing the more bursty starforming galaxies, like the ones observed at z>1.

The results described in this section come from an adaptation of the AMR code RAMSES (Teyssier, 2002), which tracks gas physics, star formation, includes stellar feedback and is generally adaptable to test an array of different astrophysical models and recipes, from galactic winds (Dubois & Teyssier, 2008a), magnetohydrodnamics (Dubois & Teyssier, 2008b), and trace scales from Mpc-scale accretion to resolve kpc galaxy cores (Teyssier et al., 2013). The simulation box used to produce the galaxies described in Fig. 2.10 had a volume of (20 h^{-1}Mpc)^3 (with h_0=0.702).

From the code outputs, a set of galaxy halos was identified and each galaxy was produced as a set of simple stellar populations with age of formation, mass, metallicity, and position, which can be used to produce star formation histories and mock galaxy morphologies and spatial parameter distributions.

The great advantage of this approach was that, along with the unresolved information like age of formation, mass, SFH-metallicity, it also provided the spatial distribution of star particles and gas that gave clues about the source of disturbances in the SFH. Simulations show well-defined disks and clumps at z=1, while at z=2 the disks are more diffuse.

This was done for two redshifts, at z=1 and z=2, where z=1 required a much larger computational effort (7 days for z=1 on a University of Lyon Cluster). This is not only because from z=2 to z=2 the simulation time steps double, but there are also more detailed structures and interactions to trace at high resolution from z=2 to z=1 than from z=10 to z=2. In fact, this redshift range is challenging because it is low enough that it is hard to simulate in detail, but high enough to

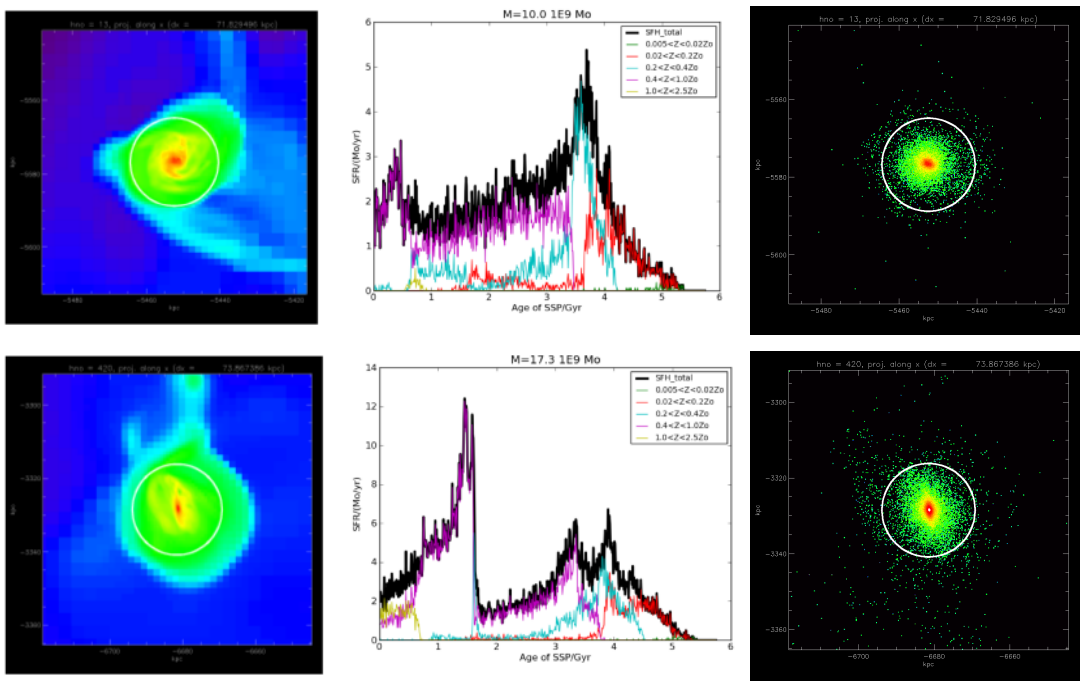

Figure 2.10: AMR matched SFH and galaxy samples. On the left, total gas density shows accretion streams and evidence of occasional mergers at z=1 for two different galaxies. Their SFHs are shown on the middle plots (solid black shows total SFR and each colour shows SFR at a given metallicity bracket). The top galaxy shows the typical exponential rise of SF, then a plateau to balance a constant accretion rate, followed by a recent burst, possibly a minor merger; most stars after the peak of SF are of solar metallicity. The bottom galaxy shows a more convoluted history, with the initial rise, a dip in SF and a decrease leading to what looks like it could be a major merger (and there is evidence of major gas disturbances). The right panels show the corresponding distribution of star particles (the effective morphology in broadband photometry)

make detailed observations difficult to perform.

These simulations produced a wealth of information, but ultimately had a major bug that cast doubts over the analysis of some of the most interesting features, such as the major starburst shown in Fig. 2.10. The Hubble flow makes the smallest resolution element expand, so whenever this element doubles in scale, the simulation needs to divide the spatial bin into 8 bins. The problem is that doing this redistributes the star particles and gas in an ad-hoc way which systematically induces starbursts. This is visible in the cosmological star formation history plot in Fig 2.11. Each of the discontinuities shown happens

at the grid refinement timesteps. This is unfortunate, because the global SFHs look like they are in broad agreement with the star formation rate density in the literature, with a peak of cosmic average sSFR at 0.5/Gyr just after z=2 and decline down to 1/5th of that at z=1 (subtracting the SFR discontinuities) in line with Cucciati et al. (2012).

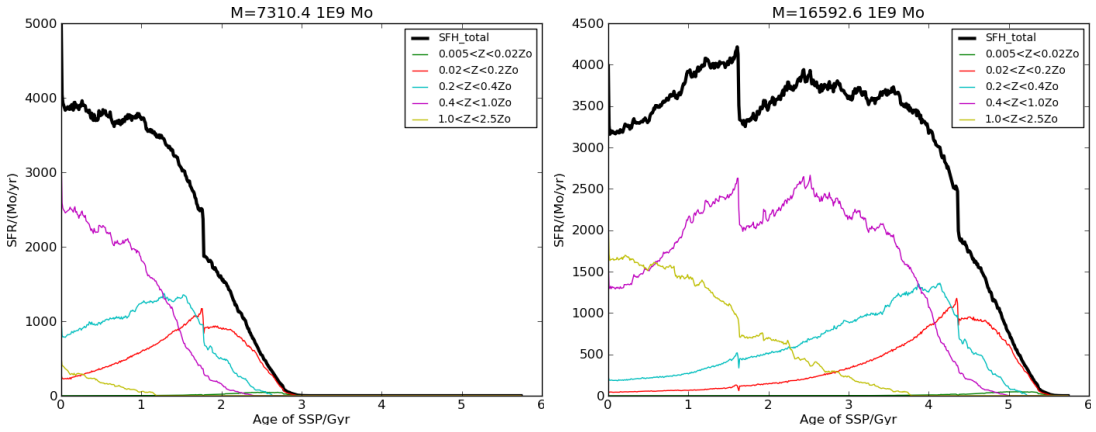

Figure 2.11: These plots show an integrated SFR of all the galaxies in the simulated volume (left at z=1, right at z=2), an attempt to produce a cosmic SFR and the contribution of different metallicities. At first look, there is a rise and plateau of SFR, but a closer look shows that there are discontinuities in the SFR. This is a bug in the implementation of the code. Due to the hubble flow, every grid in the simulation expands according to ΛCDM, however, when the grid becomes too big, it is subdivided to keep a fine resolution. It seems that it is this subdivision which triggers these sudden cosmic starbursts of what would be an exponentially increasing, peaking around z=2 when the universe was 3Gyr old and declining thereafter. The peak of the cosmic SFR is at subsolar metallicity, but not below $0.4Z_{\odot}$. Different regimes of star formation due to low metallicities would only have dominated star formation 1Gyr after the Big Bang. The problem is that peaks like that in Fig 2.10, bottom panel coincide with this grid rebinning and could not be used.

To test the smaller scales, I also verify that the galaxy population reproduces the mass-metallicity relation up to z=1 (Fig. 2.12). The mass-metallicity relation is tight and shows the intrinsic scatter of bursty galaxies (Peeples et al., 2009) and irregular accretion (which can quickly shift metallicity without significantly changing mass), due to the detailed treatment of gas. For quantities as similar as the mass-weighted age (what time most of the mass was formed) and the age of the oldest star, the gradients of these two quantities seem to be orthogonal in M-z

space. Whereas the age of the oldest star depends both on mass and metallicity (all three quantities increase as stars form, die, and metals are produced), the mass-weighted age still increases with metallicity, but decreases with mass. This is because:

$$\mathrm{Age_M} = \frac{\int \mathrm{Age(M)dM}}{\mathrm{M}} = \frac{\int \mathrm{Age(M)}\frac{\mathrm{dM}}{\mathrm{dt}}\mathrm{dt}}{\mathrm{M}} = \frac{\mathrm{SFR}}{\mathrm{M}}\frac{\mathrm{T}^2}{2} =< 2\mathrm{sSFR}^{-1} > \qquad (2.2)$$

So, for constant SFR, the average age is inversely proportional to the sSFR. This is what the fundamental M-SFR-Z relation describes (Mannucci et al., 2010). Furthermore, if SFR is not constant and there is a peak at any time, the average sSFR is shifted to that value and age, so this further explains the scatter around M-SFR-Z, because recent bursts will increase average sSFR and push galaxies down in the diagram (Fig. 2.12). Finally, the last panel in the figure shows the ratio between the mass-weighted age and the oldest star age. This ratio indicates the fraction of the age of the galaxy since the burst when it formed most of its mass. While the low-sSFR objects show that their mass-weighted age is half of their total age (which means a constant sSFR), most objects have formed their stars more recently, indicating an increase of sSFR with time, possibly a recent burst.

Apart from these problems, the focused brute-force approach of AMR simulations is still limited when ultimately trying to track gas properties down to the very small scales and eventually requires some subgrid recipes as well (e.g. to include the effects of AGN). This is also the case with Supernova Feedback, so as with semi-analytics the value of these simulations resides primarily in excluding certain dominant physical mechanisms that control discrepancies between simulations and observations. The galaxy population produced was mostly blue as required, but the lack of red galaxies was due to the need for an ad-hoc AGN or mass-quenching mechanism and the need for a higher simulation volume. Since the aim was to get the burstiness, these simulations included a smaller volume, whereas larger volumes would lead to lower resolutions and potentially redder galaxies due to a coarser treatment of gas.

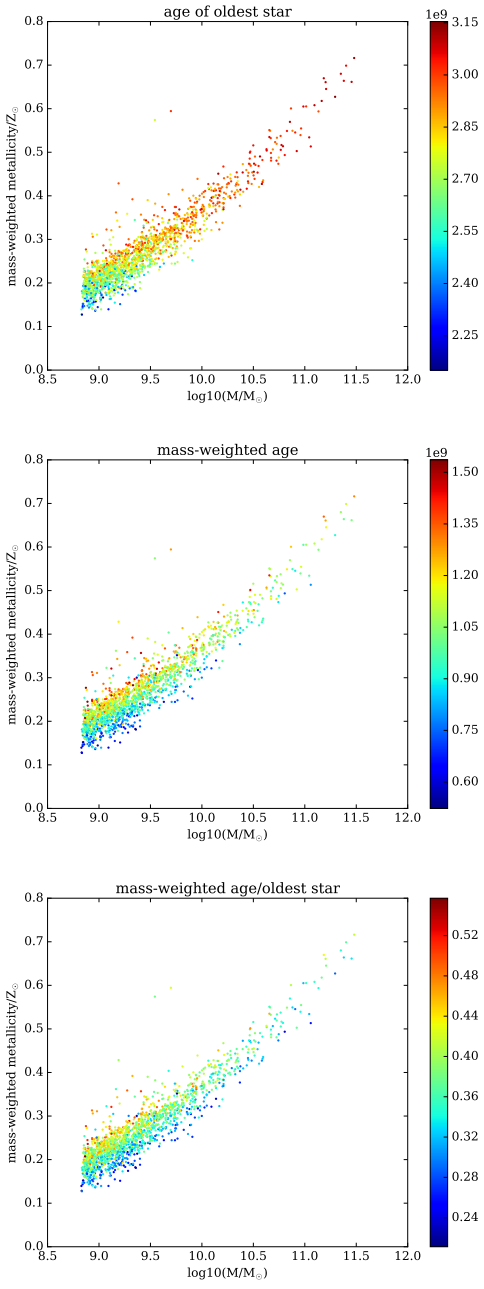

Figure 2.12: Mass-metallicity relation colour-coded by the age/Gyr of the oldest star (left) and the mass-weighted age (right) for simulated AMR galaxies at z=2. These Figures show that, while many of the galaxies in the relatively tight sequence started forming stars early on, their mass-weighted ages show that most galaxies are younger than that (no significant star formation quenching or exponentially declining SF). The age gradients also show that the oldest star is correlated with metallicity (due to ongoing continuous star formation), and anti-correlated with galaxy mass (the gradient is orthogonal to the M-z line). On the other hand, for mass-weighted age the gradient becomes orthogonal to the mass-metallicity relation.

Stochastic Burst Models

Given the difficulty in finding a simulation that can at least span all the colours observed, especially at the blue end, a different strategy was adopted. An array of 43993 different star formation histories was produced following an exponentially-declining SFR over a range of τ indices, age of formation, and metallicity ($0.1Z_{\odot}$ to 2 $Z_{\odot}$) (galaxy metallicity does not evolve in time for these models). Most importantly, the SFRs include stochastic bursts of star formation in the last 100Myrs. These star-formation histories are somewhat artificial (they are not produced from first principles) but once converted into colours are very good at covering colour-colour space. For this reason, these are originally the same models used to derive the eigenvectors in Wild et al. (2014) due to their wide coverage of n-colour space, as I will show later in this chapter. Alternatively, the range of colour covered by the array of BC03 single-age colours could have been used, but actually drawing colours from a set of realistic parameterized SFHs shows how the properties of the star-formation histories translate into the output colours, rather than rare single-age galaxies.

Originally, these models were only intended to serve as a diagnostic tool, a way to keep track of the original properties of the models that produced each colour and a way to see if any colours were easy to separate for a given age and metallicity. Some populations, like post-starbursts, are easily identified in these circumstances, because there is no age mixing and they show the strongest Balmer breaks.

The mock spectrum of each galaxy is then integrated under the z, J, H and K filters. Figure 2.13 includes three colours to show how close models are to the observations and BC03 tracks are shown for guidance.

At z=1.4 and z=1.6, an example of the resulting colours is shown in Fig. 2.13. At this redshift, the R filter falls bluewards of the 4000Å break, and K is line-free. In Figs. 2.14 and 2.15, z is once again bluewards of the 4000Å and Hα is just entering the K filter, but is otherwise clean (unless [SII] becomes strong, but that is assumed to be a much weaker effect). This will be a recurring pattern of using well-understood colours with line-free Ref−N (e.g. B-K) colour on the x-axis, where Ref is the reddest band bluewards of the 4000 Å break and N is a normalizing band that is usually picked to be the bluest redwards of Hα. On the y-axis a line-contaminated band will be shown normalized by the same band

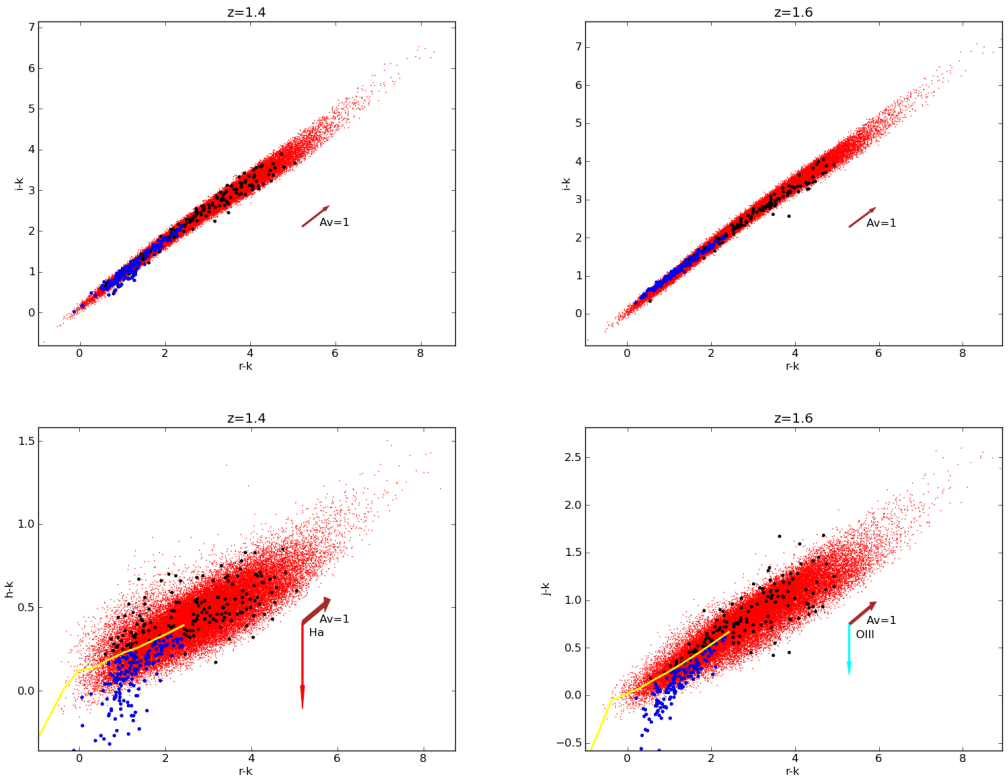

Figure 2.13: Colour-colour plots showing $r-$K vs i$-$K H$-$K and J$-$K colours from CANDELS photometry (black dots) at z=1.4$\pm$0.05 and z=1.6$\pm$0.05 with errors below 0.4 on both colours. Stochastic Burst Model galaxies at z=1.4 and z=1.6 using BC03 (red), objects with potential emission-line contamination due to recent star formation in J and H are delimited below the yellow line (median of the models in red) and coloured in blue. The models shown are dust-free, but the reddening vector shows the expected effect of A_V=1 for these colours. This figure shows that the models (red) encompass all the observed colours (black) closer than any other models obtained through other methods except for the blue points, offset by emission-line contamination.

used to normalize the x-axis (e.g. J-K). The distance between the two bands is an advantage, because it contains the global variation of the spectrum (robust against minor variations in these bands) without going too far into the more uncertain UV. For redshifts above 2, an IRAC bands will have to be used as the normalizing N band.

Fig. 2.13 shows that the Stochastic Burst Models (SBMs) accurately predict the colour distributions of the observations, except in the case where emission-

lines are present.

The observations closely cover the SBM colours for all colour and redshift combinations across a range of values where emission lines are safely out of the filters, only limited by the lack of very old (limited by redshift) and very young (low-mass) galaxies. The limitation here, like with the Single-age models, is that because the distribution is not based on a mass-function (theoretical or observed), the spread mostly shows the range of colours available with combinations of available parameters for simplified SFHs.

Interpreting SBM Colours

With a set of SBMs produced using a range of metallicities, bursts and exponentially declining star formation rates, I now show how these parameters map onto different colour-colour planes in Fig. 2.14 and where individual SFHs from RAMSES fall in this colour-colour space (Fig. 2.15).

The z=2 RAMSES simulations seem to have bluer R−K colours, which broadly match observed colours in CANDELS-UDS (upper left panel of Fig. 2.15) and are bluer than the Somerville et al. (2008) simulations (apart from the J excess caused by [OII]). Overlaying constant star formation tracks (CSF) (middle left panel of Fig. 2.15) and exponentially-declining tracks (lower left panel of Fig. 2.15) star-formation tracks for different average metallicities, the colours show that the simulations tend to have subsolar metallicity and can be interpreted as mid-age (100Myr) closest to exponentially-declining star-formation histories, but is also degenerate with old stellar populations (>1Gyr) from constant star-formation rate tracks. Looking at the actual properties of the models, the simulations occupy sub-solar metallicities and metallicity increases with R−K(upper right panel of Fig. 2.15), so the bluer objects with most recent star formation and higher sSFR have higher metal content. The models seem to have a <100Myr mass fraction of up to 0.1 for the bluer objects (middle right panel of Fig. 2.15), so an sSFR=1/Gyr for R−K=0.5 and 0.3/Gyr for the reddest objects at R−K=1.5. When considering sSFRs over a longer timescale, the <1Gyr mass fractions range from 100% to 40% (lower right panel of Fig. 2.15), so again 1/Gyr and 0.4/Gyr, no major shifts due to the bursts. The major problem here is that doing this exercise in simple colour-colour space is highly degenerate in age, metallicity and dust reddening, so multiple colours have to be analysed at once to separate different spectral features (n-dimensional colour space). These

degeneracies can be lifted through principal component analysis, which reduces the dimensionality of the n-colour space to up to 3 components and shows the strongest signals from the global colours, as will be shown in section 2.5.

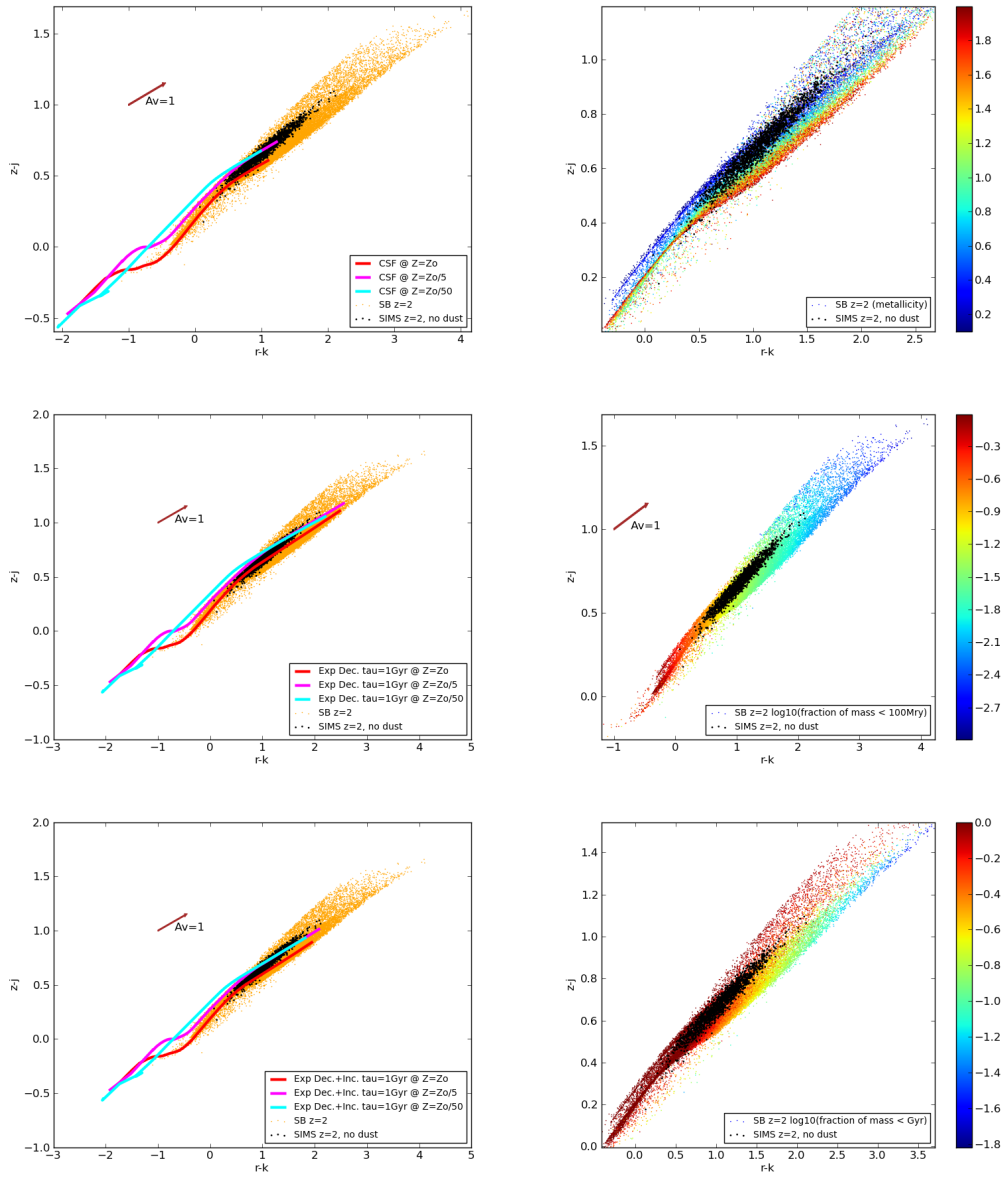

Figure 2.14: R-K vs z-J colours for SBMs at z=2 (in orange, colour-coded on the right) and the AMR simulations (in black): the simulations only cover a bluer side of the SMBs. The left panels show star-formation tracks for different parameterizations of star formation at the metallicities indicated. Top left: constant SFR, middle left: exponentially declining and lower-left: exponentially declining plus increasing SFR. Only the bluest AMR-simulated galaxies are possible with constant SFHs since the big bang, the rest are too red. The middle left panel shows exponentially declining SFHs and in this case the tracks completely cover the AMR simulations, but some of the redder galaxies are missing, whereas adding some exponentially increasing SFR keeps all galaxies bluer than R-K=2 as the AMR simulations. The right panels show a colour scale for metallicity as a fraction of solar (top), the mass fraction of young stars (middle) and the $\log_{10}$ mass fraction of stars with ages below 1Gyr (bottom). Almost all the AMR-simulated galaxies have subsolar metallicities. The young population fraction is spread between 0.1 and 0.03. In contrast, all AMR-simulated galaxies formed most of their mass 1Gyr ago.

Comparison with simulated SFHs

Since the AMR simulations provide complete SFH information for individual galaxies and SBMs have the potential to describe this information in a parameterized way, the SMBs can be used to show how mapping the detailed SFHs from AMR simulations onto colour-colour space only allows the recovery of a few parameters of the SFH. In Figure 2.15 I show z-J at z=2 along with single age models, SBMs, CSFs and observations along with specific SFHs (the coloured dots). Even if the SBMs only explore a fraction of the possible Single-age colours, they encompass all the line-free observations at z=2. This comparison is done ultimately to verify how detailed SFHs need to be (compared with the simple parameterization of SMBs) when the observations used to constrain them rely only on broad-band colours.

To check what colours were associated with individual SFHs (and which major features of SFHs can be recovered), Fig. 2.15 shows what colour values the individual SFHs displayed in Fig. 2.16 have in z-K, z-J space. The bluest simulated galaxies (see galaxy IDs 1214,740,406 and 152), tend to have exponentially increasing SFHs, which the SBMs emulate with their recent bursts, while the oldest, reddest, galaxies (see galaxy IDs 1362 and 950) seem to have flat SFHs, so the galaxies in the AMR models are not old enough to actually have an exponentially declining SFH.

The variety of simulated bursty SFHs does not show in colour-colour space because colours effectively respond to stellar age over logarithmic bins. The consequence is that the mass formed at a small number of low-age bins is what really matters and short-bursts will only matter if they are very frequent and thus add up in the old bins or if they are recent. Otherwise, bursts older than 1Gyr should not be visible from photometry unless the galaxy is quenched afterwards, effectively becoming a post-starburst galaxy. This sample does not have many exponentially declining or quenched SFHs because it was effectively run at z=2, where gas abundances ensure that if a galaxy entered an exponentially declining SF stage, it can still be rejuvenated by streams of gas, for example in galaxies 0 and 87 of Figure 2.16. Additionally, AMR simulations might need to include the semi-analytic treatment of AGN feedback to actually get some of the red quenched galaxies, shown as the red scatter plot in the top left panel of Fig. 2.15, but this could be achieved with dust reddening of up to A_V=5. In the latter case,

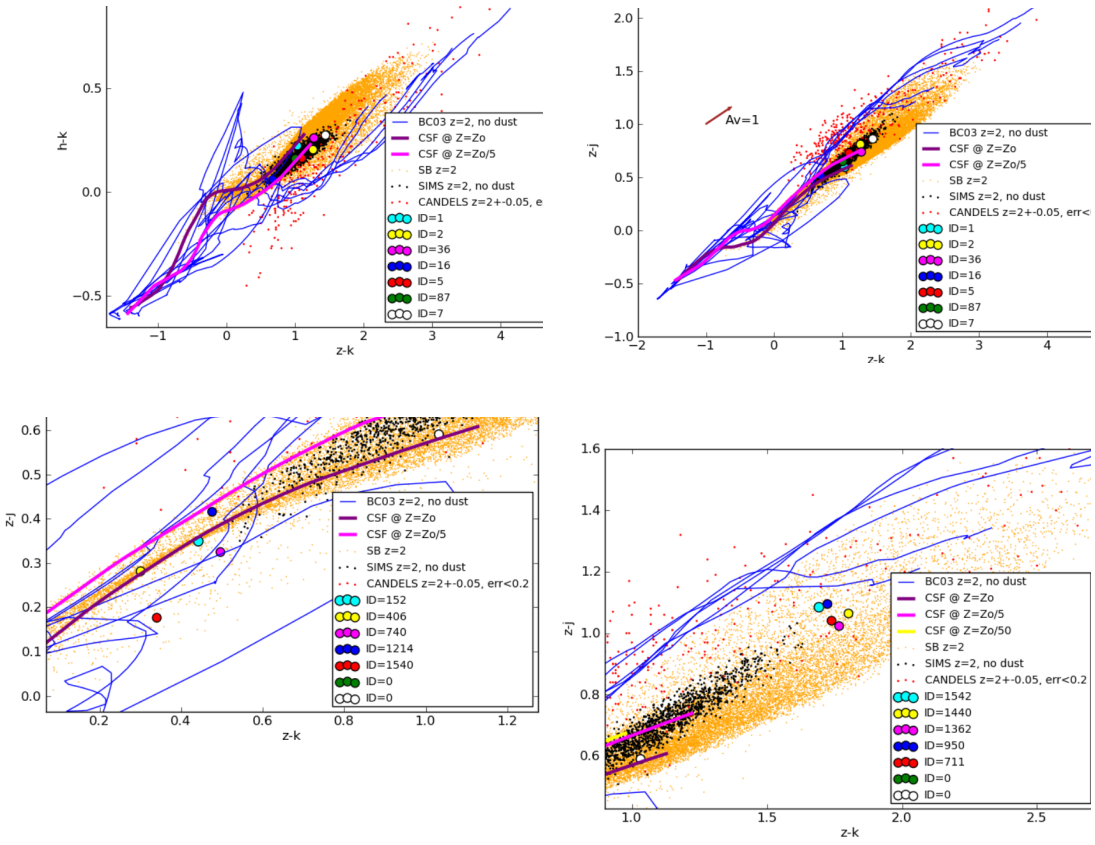

Figure 2.15: Panels showing z-K vs z-J colours with CANDELS observations at z=2 (red), SBMs (orange), single-age BC03 tracks for different metallicities (blue), constant SF tracks at different metallicities, AMR models (black) and the IDs for individual galaxies. The top panels show the same objects for H-K (left) and z-J (right). The lower-left panels show the bluest galaxies simulated: 152,406,740,1214,0 and lower-right panels show the reddest galaxies simulated: 1362,950. If the SFHs are compared: the reddest galaxies shown here have almost flat SFHs and the bluest galaxies have exponentially increasing SFHs. In the sequence of colours from bluest to reddest, looking at the SFHs reveals that the bluest galaxies are the ones with recent bursts, rather than the rising SFHs, further confirming not only colour degeneracy, but also SFH degeneracy.

75% of star-forming galaxies at z=2 would be virtually dust-free. These are the same galaxies that display line emission, whereas the reddened ones do not.

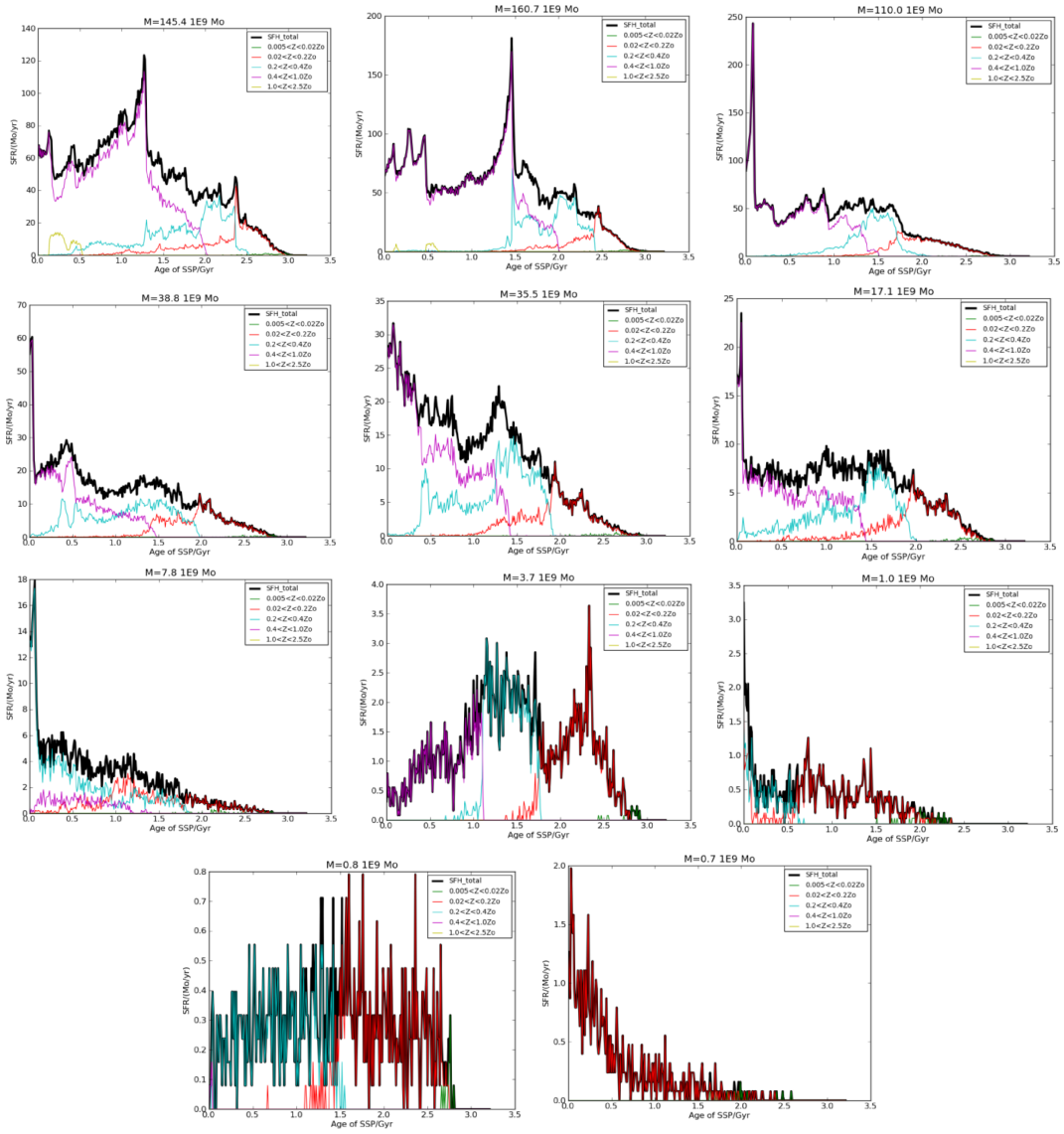

Figure 2.16: Set of Star Formation Histories at z=2, corresponding to galaxy IDs: 87,0,94 (first row), 740,147,130 (second row),152,1362,406 (third row),950,1214 (last row). Galaxies are ordered by mass (identified at the top of each plot from $1.6\times10^{11}M_{\odot}$ to $0.7\times10^{9}M_{\odot}$. The different colours show the metallicity ranges in the labels. The galaxies in the bottom panels display display more low-metallicity star formation, up to $0.2Z_{\odot}$ (later formation) and appear burstier due to the resolution limit of the simulation, however this parallels reality, since frequent $10^{7}M_{\odot}$ starbursts can easily shift the SFR of a low-mass galaxy. Most importantly, very few of these SFRs are exponentially declining like the SMBs expected to emulate them.

Principal Component Analysis

Given the importance of colour in comparing galaxy mock observables (essentially colours) with real observed samples, multi-band photometric surveys offer extended wavelength coverage from the UV to IRAC. However, apart from breaks and lines in the underlying galaxy spectrum, many of the observed colours of these galaxies will provide primarily the same information: the age of the stellar population though the fraction of blue, steep-powerlaw emitters vs flatter-spectrum redder or dust-attenuated stars in the SED. This dominance of age over broad-band colours makes it difficult to masure other weaker signals in the spectrum, like weak Balmer breaks and the 4000A break associated with stellar absorption by [CaII], the H and K Frauenhofer lines.

Principal Component Analysis basics

One way to extract such spectrum-wide features optimally from multiband data is to construct a linear combination of band magnitudes, a generalization of the B−R concept of colour (hence the usage of the term supercolours).

To achieve this, a set of rest-frame models is produced in N-colour space. Then a basis is created using the axes of greatest variance of this data. These eigenvectors will constitute the Principal Components over which the data shown in observations will be projected.

PCA is only statistical insofar as the covariance matrix is used to optimize the colours. Everything else is a diagnonalization of that matrix and projection onto the resulting eigenvectors. This is the reason why there is no physical information in the components, it is a data compression method (higher principal components include increasingly faint signals, even noise).

As a first example, let us pick 4 modelled galaxies (the blue points in figure 2.17) and some realistic example colours B-K and R-K, the $\vec{M}$ model colours matrix. The reason colours and not magnitudes are used is that in practice this method is applied to normalized fluxes (colours are essentially the flux in one band normalized to the value in another band) to remove mass dependence, which would be a natural component, sometimes considered as PC0, so every value used is in fact a colour. First, all model values need to be referred to the mean B-K and R-K values, the origin of the new base onto which the photometry is going to be projected. This ensures that all the values shown are normalized

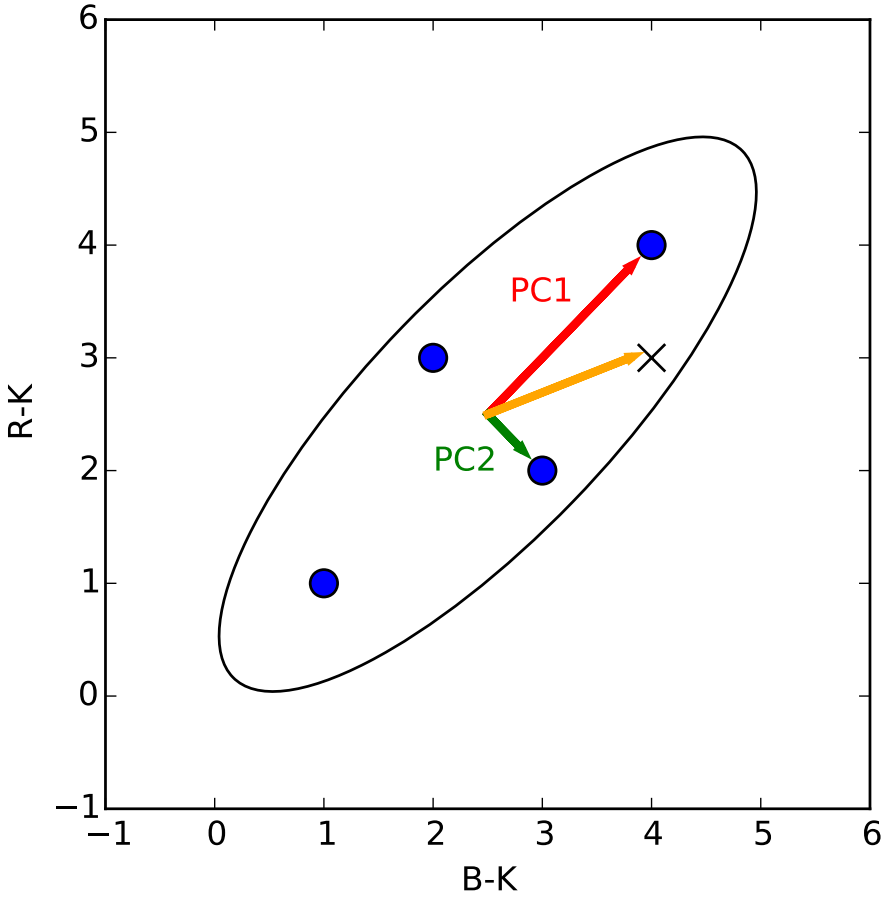

Figure 2.17: An example of PCA in 2D using 4 model galaxies (blue points) that are a subset of a larger background set of models. Despite the spatial distribution of the models, the usage of the covariance matrix will average outliers and produce results for the models as if they were an n-dimensional ellipse of which the PCs are the major axes.

and independent of mass. In the following example 4 by 2 matrix M_0 contains the colours of 4 galaxies, shown in Figure 2.17:

$$cov(M_0) = M_0^T M_0 =$$

$$\left(\begin{bmatrix}1&2&3&4\\1&3&2&4\end{bmatrix} - 2.5\begin{bmatrix}1&1&1&1\\1&1&1&1\end{bmatrix}\right).\left(\begin{bmatrix}1&1\\2&3\\3&2\\4&4\end{bmatrix} - 2.5\begin{bmatrix}1&1\\1&1\\1&1\\1&1\end{bmatrix}\right) = \begin{bmatrix}5&4\\4&5\end{bmatrix}$$

Now if the covariance matrix is diagonalized it will produce a normalized basis of normalized eigenvectors (P) and a diagonal matrix with eigenvalues that set the weight of each component (in this case only B and K):

$$cov(M_0) = \sqrt{2}/2\begin{bmatrix}1&-1\\1&1\end{bmatrix}\begin{bmatrix}3&0\\0&1\end{bmatrix}^2\sqrt{2}/2\begin{bmatrix}1&1\\-1&1\end{bmatrix} = P^T D P$$

The outcome is the second matrix PC1=$0.7B + R$ (total 2-band magnitude) and PC2=$0.7B - R$ (a colour), which are the natural directions in which the data points are spread and the magnitudes of the variance in each direction (3:1). Finally, to obtain any principal component amplitudes (PCa) in each PC, any point can be projected onto this base, say the cross (point X):

$$P\vec{C}a = P\vec{X}_0 = \sqrt{2}/2\begin{bmatrix}1&1\\-1&1\end{bmatrix}\left(\begin{bmatrix}4\\3\end{bmatrix} - 2.5\begin{bmatrix}1\\1\end{bmatrix}\right) \approx \begin{bmatrix}1.4\\-0.7\end{bmatrix}$$

Figure 2.17 shows this example works almost in a trivial way in a simple bidimensional plane. However, in practice, this method is applied to a covariance matrix produced from a matrix with ≈40000 galaxies and multiple colours. If it was just in the rest-frame, this matrix would have 19 columns, one for each filter. However, since multiple redshifts are involved, this diagonalization is performed over all wavelengths covered by redshifts in steps of z=0.1:

$$[\mathrm{B@z} = 0.0, \mathrm{V@z} = 0.0, ..., \mathrm{B@z} = 0.1, \mathrm{V@z} = 0.1, ...3.6@\mathrm{z} = 2, 4.5@\mathrm{z} = 2] \quad (2.3)$$

So in practice the M matrix has 40000×380=(19 bands @ 20 redshifts from z=0 to z=2 for example) and the covariance matrix is large (380 by 380). The resulting principal components (the lines of the P matrix in order of decreasing variance eigenvalues) are shown in Figure 2.18. PC1 shows the dominant source of scatter (its shape coincides with the negative powerlaw slope of blue galaxies) and the higher components show decreasing levels of variation and therefore

lower levels of available information. For this, only the three first components were used, effectively reducing the dimension of the colour problem to 3: PC1: global blueness/β slope, indicating sSFR/light-weighted age, PC2: balmer break, indicating the age of the older stellar populations, and PC3: Balmer Break/4000A break discrepancies, probably related to metallicity. All PCs are by design orthogonal and normalized, so their self-dot product is 1 and the dot-product between any 2 PCs is 0. In practice there may be small deviations from these values due to the fact that diagonalization of large matrices in practice is performed numerically and is more akin to a multidimensional least-squares fitting of the datapoints than exact diagonalization. This is because exact diagonalization involves characteristic equations of degree equal to the dimensions of the matrix and no general exact solution exists for polynomials of degree 5 or higher.

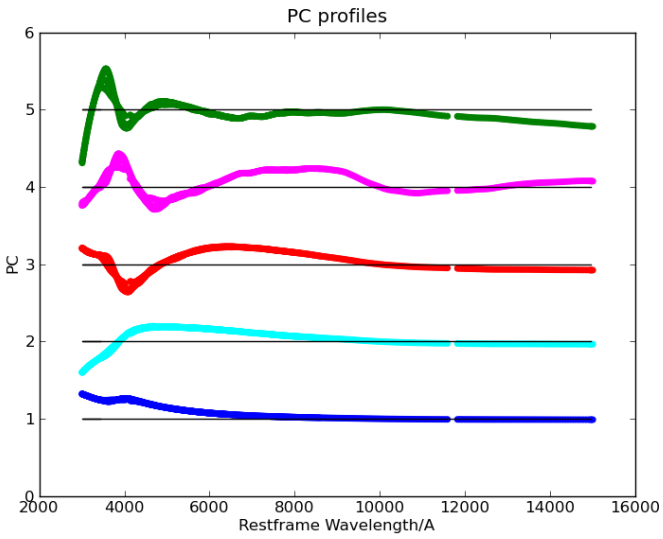

Figure 2.18: PCA components: projecting colour-colour space into the colour combinations with the highest variance over wavelength. Principal components from PC1 at the bottom to PC5 at the top have a decreasing amount of information and increasingly capture random scatter. PC1 shows a typical young galaxy spectrum with high sSFR, PC2 shows a typical old redder galaxy spectrum with a Balmer Break. Higher components include signals which may not be of physical significance

As this subsection shows, PCA is a method that reduces the dimensionality of multi-redshift multiband space into a small number of dimensions with almost

all the physical information needed to interpret the evolution of galaxy mass assembly. However, since PCA is just an optimized projection method the capacity for PCA to decypher the physical information on the data depends on which models (or rest-frame spectral observations) were used in first place and thus still requires either a simulation like a SAM or AMR or a heuristic model like SBMs to create the principal components. In the following figures I will use principal components derived from SBMs due to their effective coverage of all colour space. Once the PCA basis is set, then simulations and observations can be projected onto the redshift-independent PC1-PC2 plane for example. Line emission for example is hard to capture in PCA since it does not produce a spectrum-wide signal and only contaminates specific bands at a time. Some observations may be captured by some PCs with spikes where the lines should lie, but since the PC eigenvectors were drawn from line-free models this will not have any physical meaning. Producing a set of PCs from models with emission lines could prove effective in capturing the relation between line emission and colour, but this would only show the observational consequences of the recipes used to produce the models, which would serve to interpret observations, not to use the observations to inform the modelling.

Interpreting PCA space

Once a set of PCA eigenvectors is determined it can be applied to the models themselves to drastically reduce the dimensionality of the colour space to search for underlying spectral features linked to age and metallicity. Additionally, it takes as input several redshifts, but the PCa outputs are relative to the rest-frame spectra for which the covariance matrix was computed, so PCA space is a way to compare the physical properties of galaxies at different redshifts. This means that the comparisons in colour done in the previous section can be efficiently performed for all galaxies and all bands. The drawback is that the PC amplitudes are require some interpretation: they are further from observational quantities and depend on the models used.

PCA space visualization is advantageous, because all colours are treated simultaneously with minimized degeneracies. The problem is that for a general population the effects of dust, which are simple to visualize in colour-colour space, are non-linear (Fig. 2.19). This is shown in Fig. 2.20 as well, where single-age minimum metallicity tracks for various A_V cover very different amounts of PC1-

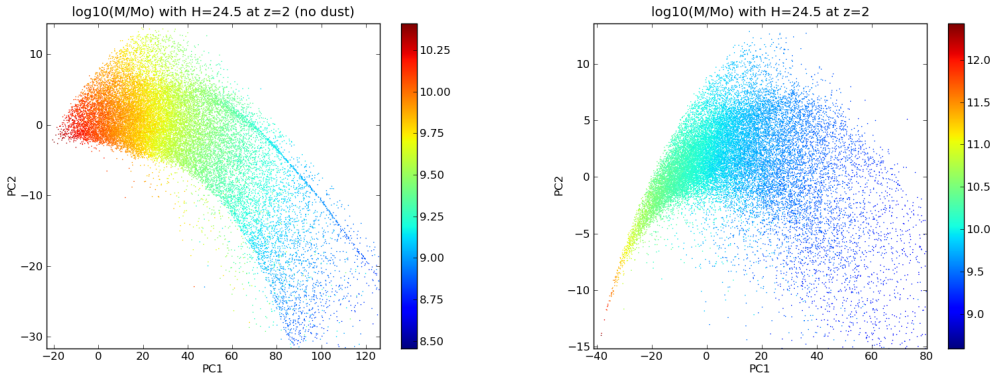

Figure 2.19: SMBs in PC1-PC2 space colour-coded with $\log_{10}(M/M_{\odot})$ if each model has H=24.5. On the left is the dust-free version. On the right the added effects of dust are shown. The gradient of mass is antiparallel to PC1, showing that PC1 is an indicator of M/L ratio and sSFR (all included in PC1 information). Massive old objects have PC1=0 and a positive value of PC2 (balmer break), so old stellar populations. On the right is the same figure with added dust. Since the dust screen does not have a principal component and its effects are multiplicative (a dust screen can not be added to a galaxy as a linear combination of stellar components), strong dust effects can simulate a strong negative PC1 (subtract blueness) and add to the balmer break (redden stars).

PC2 space, with high-A_V being the most degenerate and turning the blue cloud into a red-sequence-like proportionality between PC1 and PC2. The Somerville et al. (2008) models (dust-free) cover only a small fraction of the blue cloud and a number of objects seem to be outside the maximum allowable blue cloud (the group of blue star-forming objects occupying a range in colour-colour space defined in contrast with the red sequence).

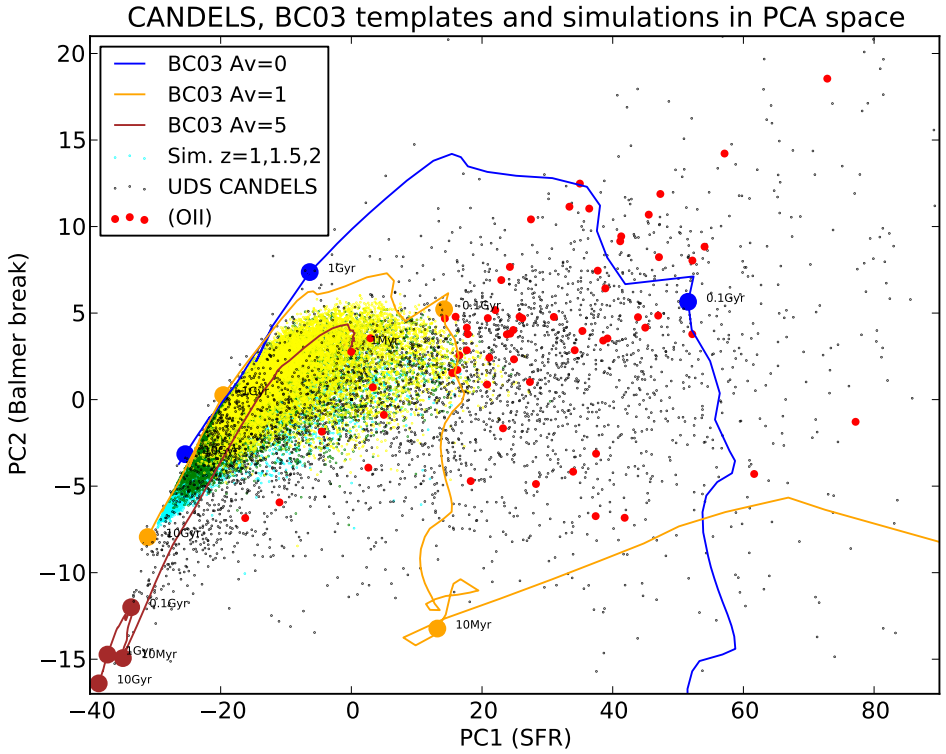

Figure 2.20: PC1 vs PC2 showing CANDELS-UDS observations (black), single-age BC03 tracks for A_V=0 (blue) A_V=1 (yellow) and A_V=5 (brown) to show how dust influences the outer locus is the single-age models and all the other SFHs produced from linear combinations of points on these tracks. The yellow, green and cyan overlapping scatterplots show Somerville et al. (2008) models respectively at z=2,1.5 and 1 (dust-free), showing that they do not cover most of the blue cloud, but cover the red sequence and evolve along it. The red objects are the CANDELS-UDS galaxies with potential [OII] contamination, in an attempt to explain the number of objects with fall out of the blue locus.

PCA Results with RAMSES simulated galaxy colours

The AMR simulations provide a better coverage of the blue cloud, which is shown in Figure 2.23 for various A_V values, but only for a thin strip. This is further detailed by looking at how the AMR simulations cover the SBMs in PC1-PC2 space (Fig. 2.21), while mapping time of formation and metallicity. These quantities (t_{form} and metallicity) turn out to be orthogonal in PCA space and very well recover the two original quantities for the colours of RAMSES simulations, with $\log_{10}(t_{form}/\mathrm{Gyr})=9.15\pm0.15$ and $Z/Z_{\odot}=0.4\pm0.3$. Fig. 2.22 shows the how PC3 is indeed a metallicity indicator (the third strongest signal in spectra).

Even using the effects of dust, there is a portion of the observations which is not covered by the simulations (Fig. 2.23). To investigate which parameter may be necessary to enhance, Fig. 2.24 shows the metallicity and mass for each of the simulated galaxies, with the gradient of metallicity being able to cover the rest of the observations in PC space. Therefore, metallicity was artificially increased (multiplied by 5) to explore that empty space (Fig. 2.25). With a combination of dust and metallicity most of the observations can be covered using the RAMSES simulation (Fig. 2.26). This is shown for CANDELS-UDS data, which is wider and has a stronger post-starburst signal, which is not reproduced. That is to be expected, because they are mostly a single-age population, of which there was none in the RAMSES simulation. On the right panel of Figure 2.26, only the z=2 galaxies are shown and metallicity tends to be lower. The lower panels show the same for CANDELS, which has lower-mass objects. The post-starburst signal is much weaker, due to the reduced volumes, and there seem to be many more of the recurrent outliers, so emission-line contamination comes only from bluer (high PC1) low-mass galaxies. This will be explored further in the next chapter. Ultimately, addition of dust is just exploiting a degeneracy and does not solve all problems with the SFHs, since it may actually be that the older, more massive redder objects are missing from the simulation due to its low volume. However, as far as the line emitters go, they seem to be coherent with dust-free models.

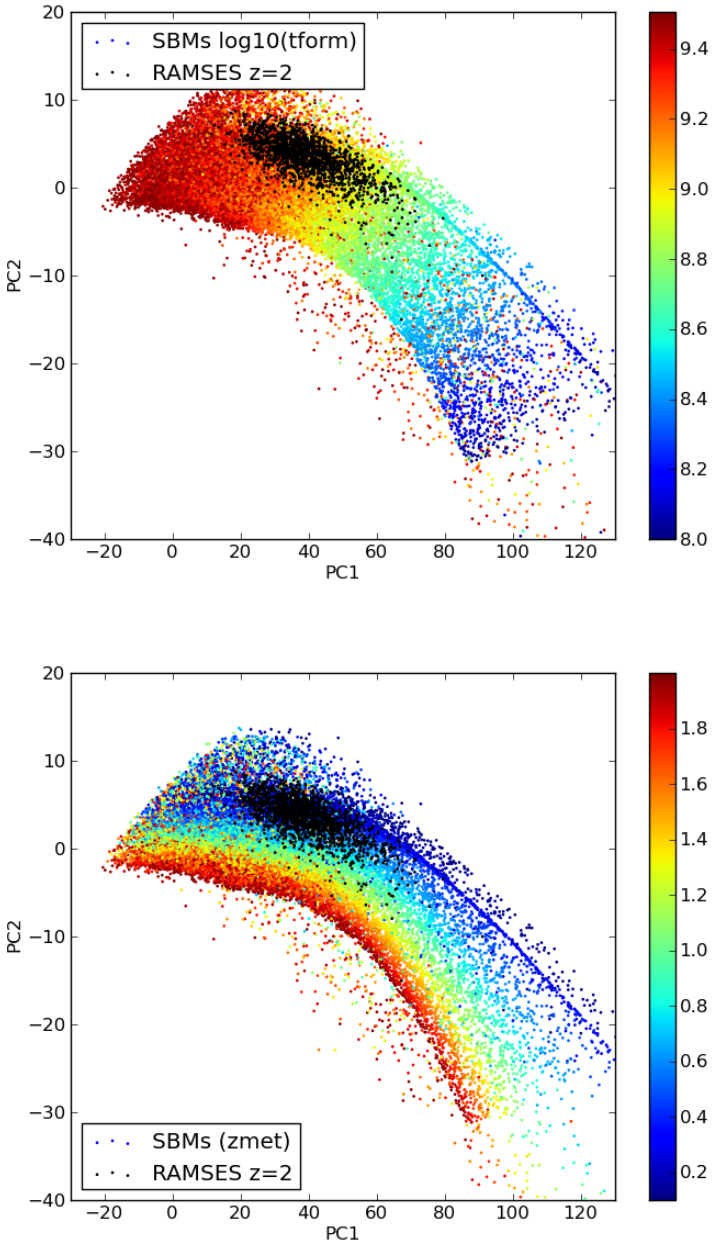

Figure 2.21: This figure shows PC1-PC2 space colour-coded with log10(age of formation) on the top and metallicity on the bottom. In black are overlaid the AMR-simulations at z=2. These provide a much better coverage of the blue cloud, even if they seem to only cover lower metallicities. These figures also show that metallicity shows a clear gradient towards -(PC1+PC2), which is orthogonal to the age gradient -(PC1-PC2).

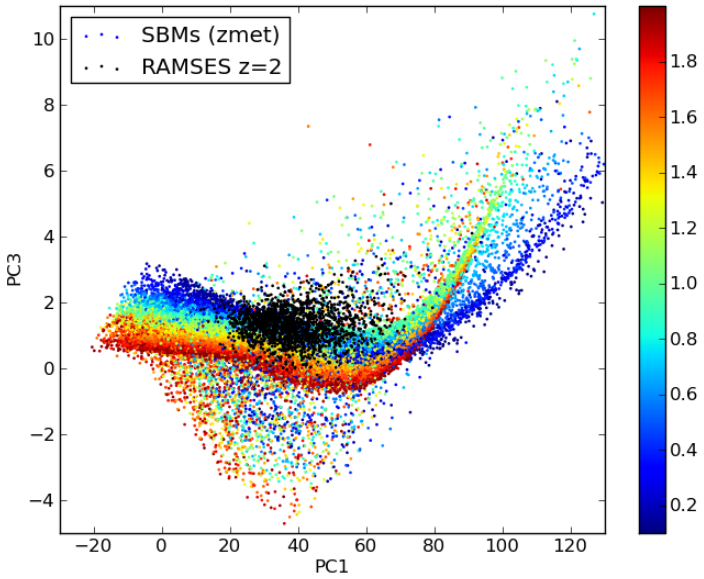

Figure 2.22: This figure shows PC1-PC3 space colour-coded with $Z/Z_{\odot}$. In black are overlaid the AMR-simulations at z=2. The gradient of metallicity is almost vertical, so PC3 is likely capturing the 4000Å break.

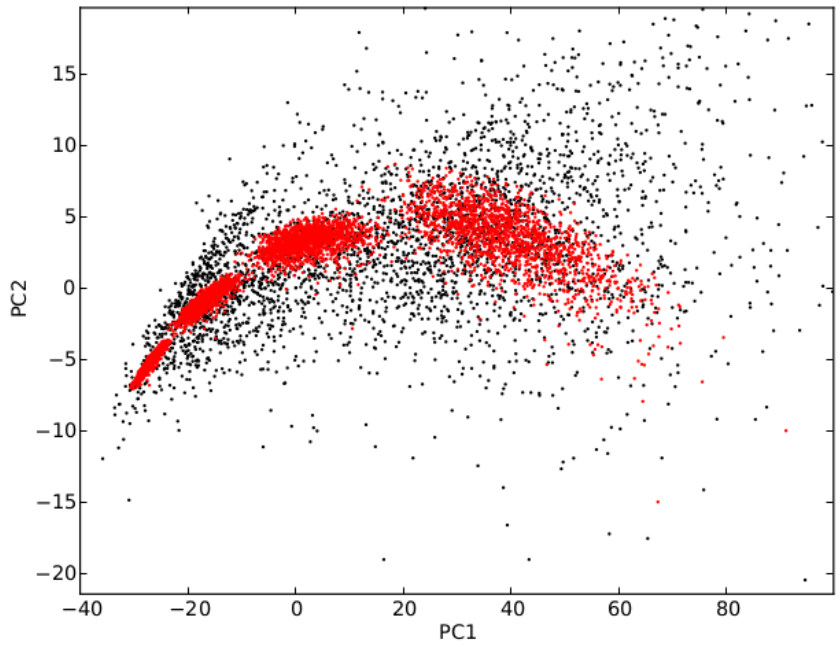

Figure 2.23: This figure shows observations at z=2 in black and in red the simulations for 4 different values of A_V: 0,1,2,3 from right to left. Strong amounts of dust could produce an artificial red sequence, but not the sequence of post-starbursts (the black plume at PC1=-20 and PC2=5), since these closely approach single-age/truncated CSF populations.

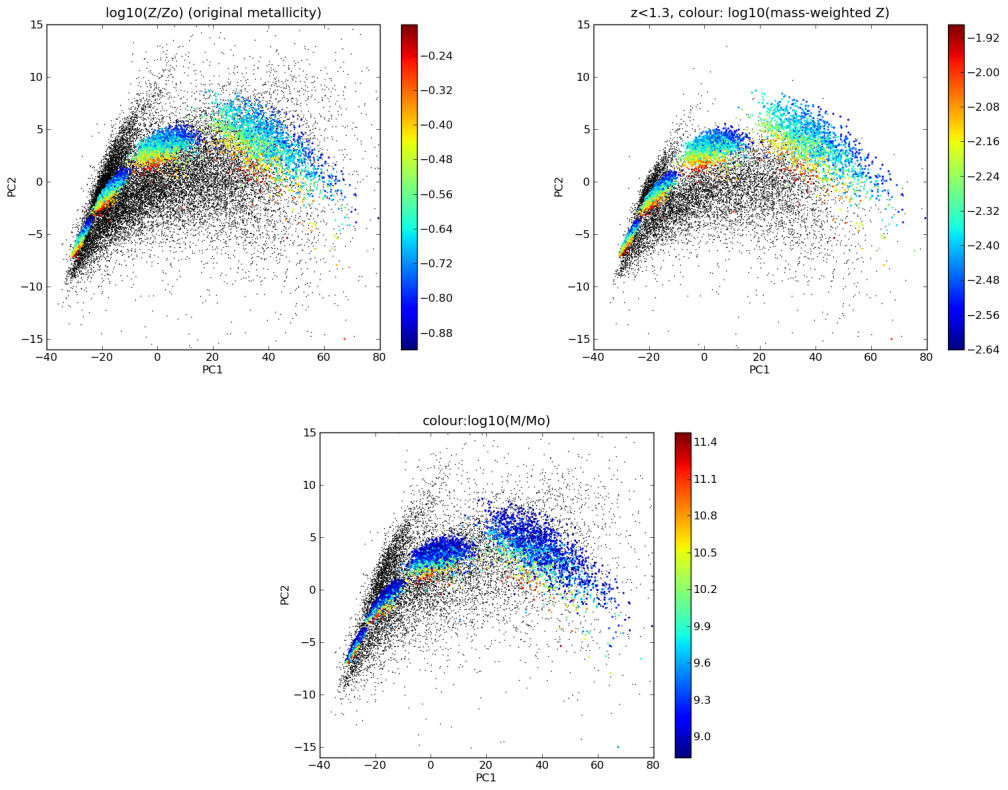

Figure 2.24: These plots show CANDELS-UDS galaxies (black points) (only at z<1.3 on the upper-right panel) and overlay metallicity ($\log_{10}$(Z)) and mass (lower panel) for the AMR-simulated galaxies on PCA space under the influence of 4 different amounts of dust (A_V=0,1,2,3), with age and mass and metallicity gradients still following PC1 and PC2

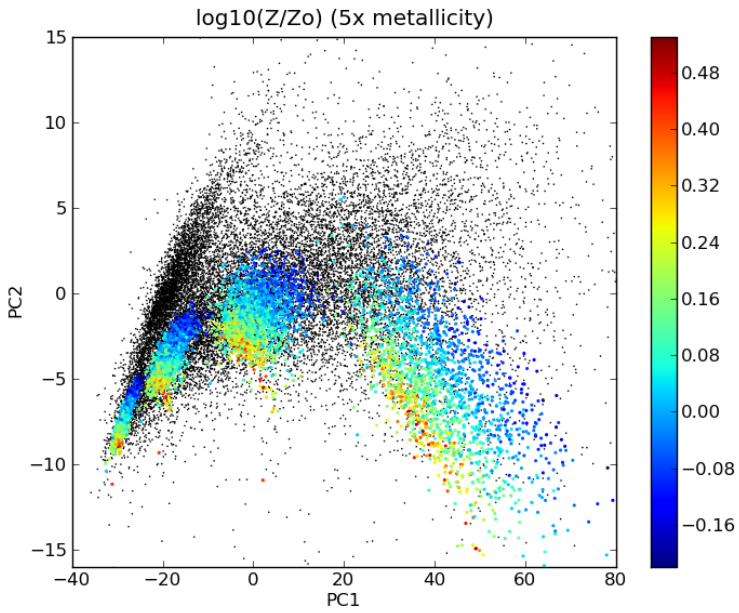

Figure 2.25: An attempt to cover the lower-PC2 blue cloud with the simulations by multiplying the metallicity of the AMR simulations by 5 and then computing the photometry and PCa. The result is as expected from figure 2.21 where the metallicity increased towards lower values of PC2.

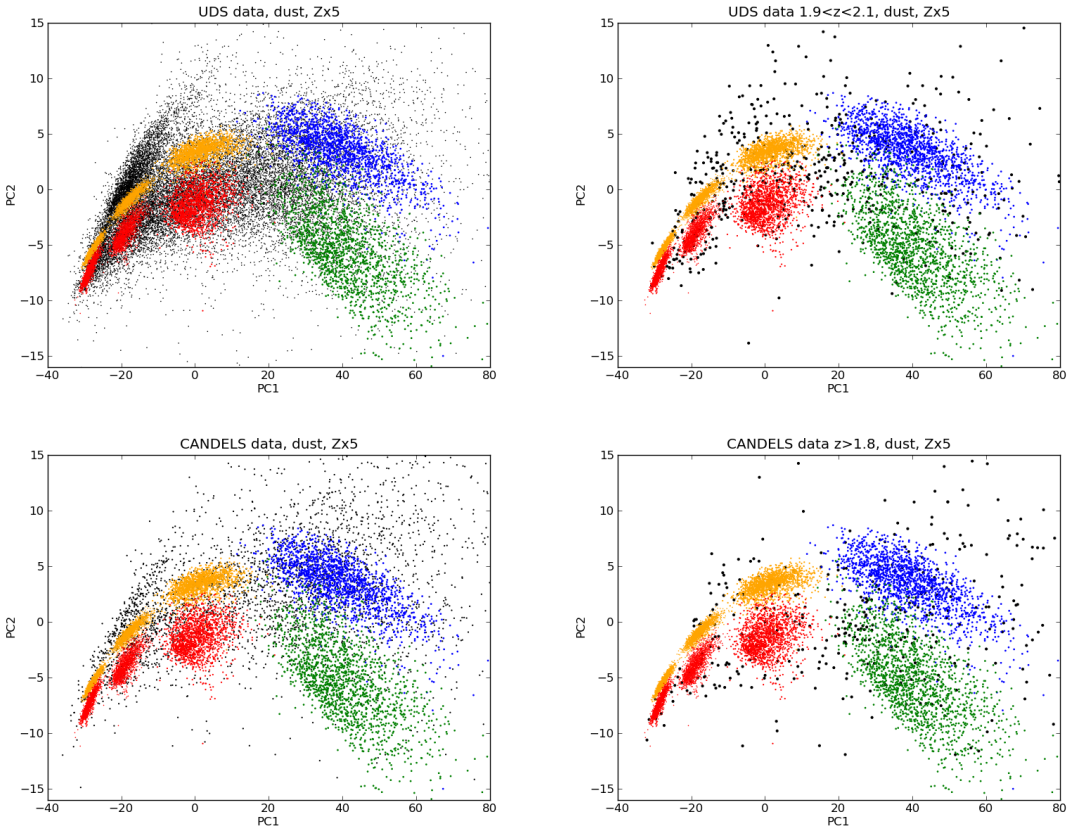

Figure 2.26: An array of possibilities to change the simulations in order to better cover the observations at z=2. Blue: original AMR simulations. Green: 5x metallicity. Red: adding dust to 5x metallicity. Yellow: adding dust. Top left-panel: black points show all UDS observations, with many features present only at lower redshifts, like the red sequence and the post-starbursts. Top-right: UDS at z=2. Bottom-left: only CANDELS-UDS data, bottom-right: CANDELS-UDS at z=2. At z=2 the post-starburst sequence is absent in both CANDELS and CANDELS-UDS, with CANDELS-UDS showing less red objects due to the lower volume clipping the mass function to lower masses.

Photometric Redshifts and Masses

All previously described interpretations of observations depends on an accurate estimation of redshifts. For this, I have attempted to estimate photometric redshifts taking advantage of all of the bands available in the CANDELS-UDS catalog (U,B,V,R,i,z,Y,J,H,K,3.6μm,4.5μm). This is principally a job of identifying the Lyman (912Å) and Balmer (3646Å)breaks in the colours (H-band magnitude may also be used as a prior, since higher-z objects tend to be dimmer), while taking into account any eventual emission lines that may be causing a colour excess.

How this is achieved differs for different codes, of which EAZY (Brammer et al., 2008) and LePHARE (Arnouts & Ilbert, 2011) were used. EAZY produces linear combinations of a small set of templates and is more efficient at reaching a redshift estimate. LePHARE constructs an exhaustive template library consisting of a grid of models over age, metallicity, redshift, and dust attenuation. For more details, Dahlen et al. (2013) provides a comparison of photometric redshifts obtained using different codes and spectral template libraries from CANDELS photometry. When using the latter code, the model grid must be kept simple, because degeneracy between dust, age and metallicity may lead to model over-fitting, especially when emission-lines are involved: natural variations from errors (especially for dim galaxies) in photometry may be occasionally fit by a model with a very fine parameter space or more parameters than necessary (especially those affecting only one band of the photometry like an emission line).

The setup that yielded the best redshifts in this case used LePHARE (as is shown in Fig. 2.27) and used the AVEROI spectral template library: a CWW-derived library, described in Coleman et al. (1980), plus 4 emission-line templates (with optical line emission at solar metallicity at 4 different luminosities), a total of only 32 templates. However, this ensures that the models are not over-fit due to an excess of degenerate models like the ones produced using BC03 with emission lines. With the redshifts, rough masses were computed in a very simple way using the photo-zs, the H-band magnitude and an adjustment for the M/L ratio of the ELGs in this work (but usually in other codes use more parameters and are fit simultaneously with redshift and SFR).

These redshift and mass values obtained agree with those using other codes and spectral libraries by members of the CANDELS team. This is shown in

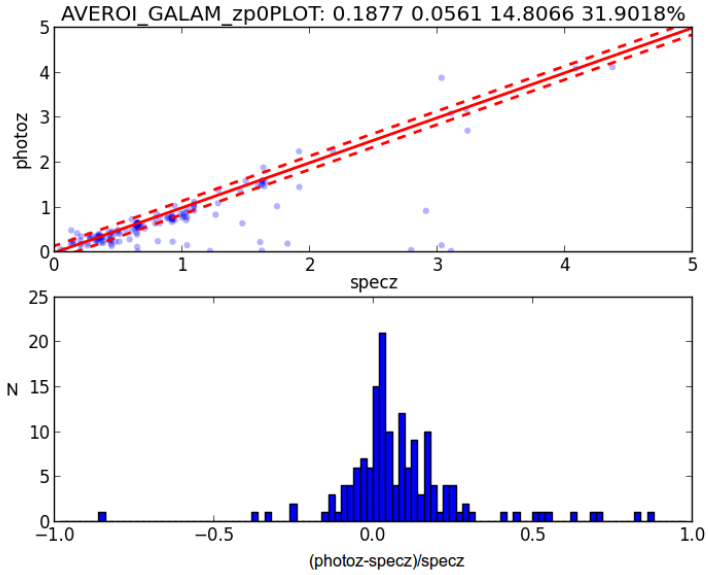

Figure 2.27: Photo-z vs spec-z scatter for CANDELS-UDS (only galaxies with spectroscopic redshifts in the catalogue) for the photo-zs obtained with the LePHARE code and the AVEROI models. There is still a large fraction of outliers and an offset of z=0.18 from the spec-zs. The lower panel shows the distribution of normalized redshift difference.

Table 2.1. Since the photo-zs have to be as reliable as possible to perform all the colour analysis previously described, it was decided to use the concordance optimized median redshifts provided by Santini et al. (2015), which were made public after carrying out these estimates. They combine a number of different approaches, which potentially avoid the caveats of fitting galaxies using templates with emission-lines (also called redshift focusing), and the reverse effect when fitting galaxies which clearly have strong emission lines with line-free models.

To avoid such complications, it would be best to fit for redshift to have a first guess and to re-run the fit without the line-contaminated bands to confirm whether this redshift is reliable. This is less critical for redshift, because the Lyman break is often the most important feature to determine redshift.

A more extensive analysis of derivation of photometric redshifts is given in Dahlen et al. (2013), where the methods used to arrive at the CANDELS-wiki concordance redshifts are described.

dz/(1+z) (ref:average)	average	median	sigma	outlier_frac (+-0.15)
joao	-0.025100	-0.017550	0.321320	0.161640
median	0.004450	-0.002610	0.127270	0.012080
barro	-0.012400	-0.004830	0.162990	0.061850
dahlen	0.041000	0.013420	0.231860	0.031050
finkelstein	-0.022130	-0.003640	0.199060	0.090950
fontana	0.011950	-0.001700	0.191920	0.026020
gruetzbauch	-0.019200	-0.007280	0.113890	0.034370
pforr	0.026620	-0.002950	0.269220	0.061450
salvato	-0.015960	-0.008900	0.156280	0.041910
wiklind	-0.003270	-0.014170	0.212930	0.041670
wuyts	0.009740	0.002450	0.133540	0.014020

d(log10(M)) (ref:wuyts)	average	median	sigma	outlier_frac (+-0.4)
joao	0.260460	0.081320	0.638750	0.347360
barro/FAST	-0.042360	-0.040000	0.081600	0.005740
barro/rainbow	0.113100	0.112000	0.254610	0.137380
finkelstein	-0.439080	-0.310000	0.399230	0.386040
fontana	-0.124000	-0.105000	0.175160	0.076090
pforr	-0.268070	-0.280000	0.154270	0.144380
salvato	-0.106210	-0.108000	0.164970	0.036160
wiklind	-0.184480	-0.193000	0.130100	0.029970
wiklind/delayed-tau	-0.180020	-0.189000	0.136270	0.057160

Table 2.1: Table describing how estimated photometric redshifts and masses using the AVEROI (32 CWW with ad-hoc emission lines) spectral library to compare with other efforts. The results show a larger scatter than many other approaches (the offsets are acceptable), especially in mass, which was done in a very simple way (calibrated proportionality to the corrected H-band flux).

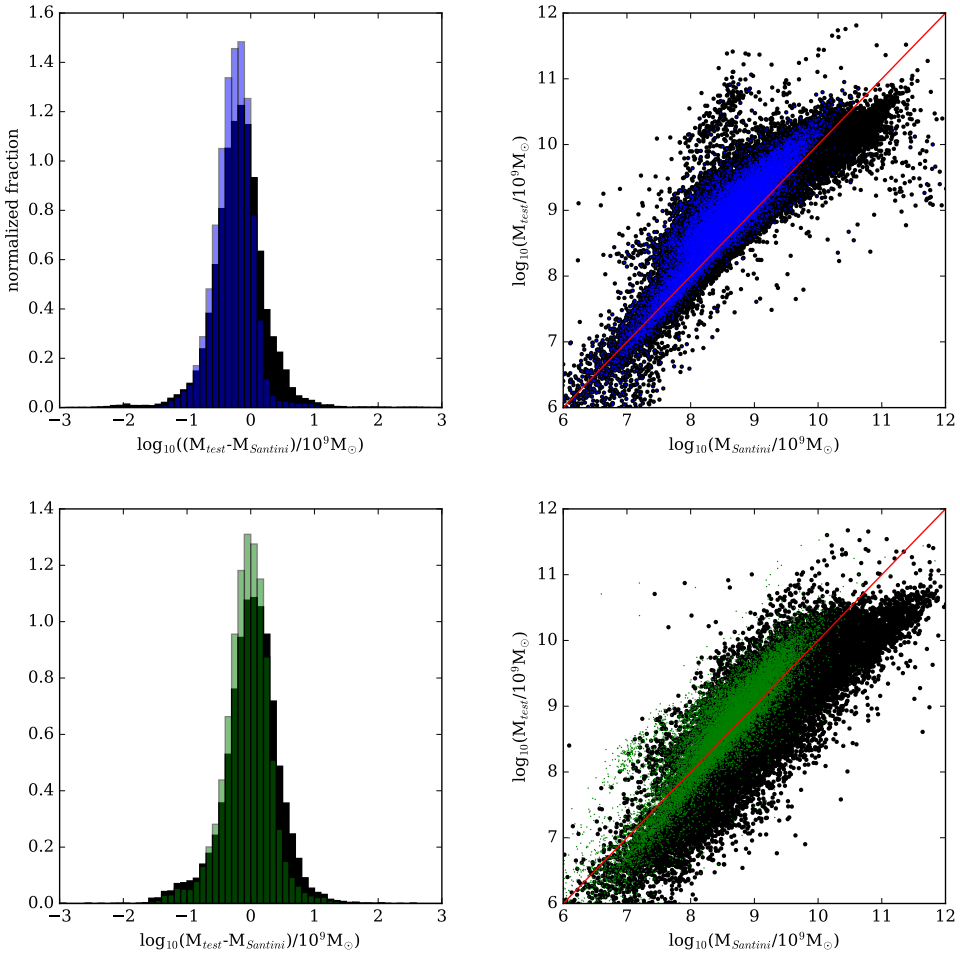

Figure 2.28: Masses estimated for UDS-CANDELS (top panels) and GOODS-S (lower panels). The left panels show the histograms of the mass difference between estimated masses and CANDELS masses (Santini et al., 2015). In black is the full galaxy distribution and in blue/green only the B−K<2 galaxies for which the fit is supposed to work best. This is because determining mass from H-band flux is a very rough method, but if all galaxies have a similar M/L ratio, which is likely if they are all extremely blue, this simple method can be calibrated to produce rough estimates.

Kolmogorov-Smirnov Testing

In an attempt to confirm the coherence of ELG distributions between different redshifts (and confirm that they were different from the control case of line-free bands), the Kolmogorov-Smirnov test (KS-test) was performed.

The way this was tested was to draw a normalized cumulative distribution of EWs and to measure the greatest difference between any two distributions. This offset would then be compared with the KS statistic to provide a degree of confidence that the distributions were similar. This was done for three ranges with [OIII] contamination (in z, J, H) and for three other control cases where no lines were expected.

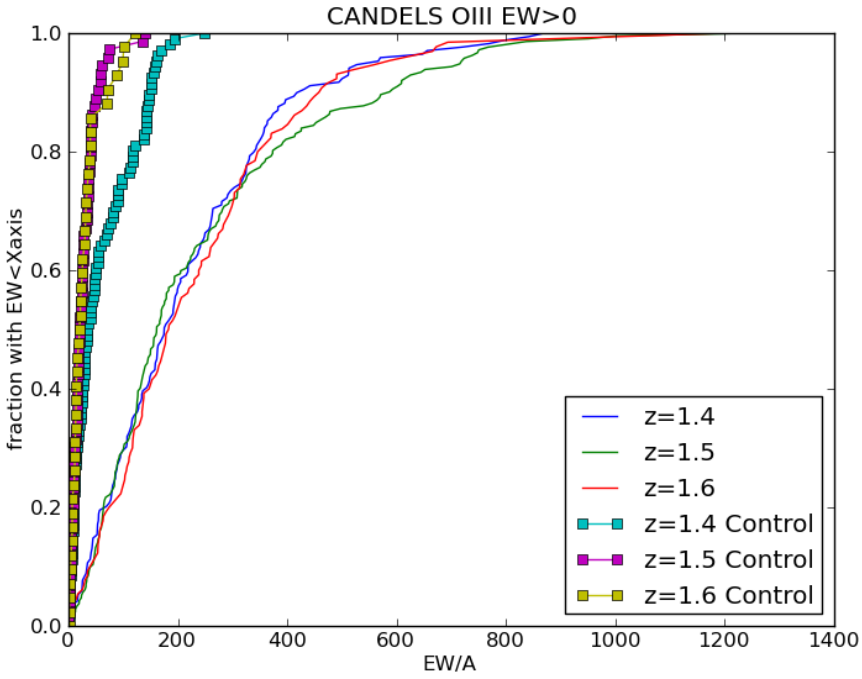

Figure 2.29: Normalised cumulative distribution of the equivalent widths of [OIII] emission lines for three redshift ranges (windows centered around the values shown ±0.1) for the J-band and three other line-free filters used as control distributions. There is a clear qualitative distinction between the line-contaminated and line-free cases.

The maximum distance between the cumulative distributions at any given EW value is compared with the KS two-sample statistic, which takes into account the

sample sizes of the distributions: n and n':

$$D_{n,n'} > c(\alpha)\sqrt{\frac{n+n'}{nn'}}, c(0.05) = 1.36 \tag{2.4}$$

For the window widths used and resulting sample sizes require D>0.2 to conclude that the cumulative equivalent width distributions are significantly different with a 95% degree of confidence. This clearly distinguishes the control samples from the line-contaminated samples and confirmed the consistency between line-contaminated samples by the same line, independently of the underlying distributions.

This approach was abandoned because on the one hand there was no reason to assume that the ELG distributions were not evolving between redshifts and because other methods provided a better verification that indeed it was emission lines that were responsible for colour excesses: comparing colour residuals with a set of models across redshift, which will be described in the next chapter.

Conclusion and Motivation for a New Approach

The methods described in this section were originally aimed at simulating galaxies to obtain SFH tables and produce mock photometry. This mock photometry was then analysed in colour-colour space and redshift-independent PCA space (supercolours) with a set of stochastic burst models that map physical quantities to colour, in order to inform model refinement. Some models were not bursty enough, some did not produce enough metals and the observed colours remain elusive, because they seemed to span the whole range of possible colours, including solar and 1/5th solar metallicity. This was not just a problem with the models, which are general enough to produce SFHs that could eventually be matched with the observed continuum colours. The problem was that a major ingredient was underestimated for the galaxy populations observed in CANDELS: emission-lines. Rather than creating a galaxy evolution model to reproduce line-contaminated colours, which would entail additional ray-tracing, calculation of equilibrium of different chemical species and other nebular properties, it would be better to measure the line emission against a reference which is already well-known: the stellar continuum.

A set of stochastic burst models covering all possible metallicities and ages was used to model this stellar continuum and it showed that the problem was that a

large fraction of the most starforming galaxies were bluer than the bluest models available, which was confirmed to be strong emission-line contamination (up to 0.5 ABmag). This could not be accounted for by dust, which would only make the colour discrepancy problem worse, or by using a different IMF, which would be ad-hoc and affect all other simulated red colours, which seemed to match with observed SBMs colours. As such, the way forward was to keep using the SBMs to model the line-free continuum of high-z young galaxies and to measure the effects of emission lines off of these models to quantify how strong line contamination is.

Chapter 3

Emission Line Analysis in the UDS CANDELS Survey

Introduction

Extreme Emission Line Galaxies (EELGs) are a population of galaxies displaying strong optical emission lines relative to continuum emission, as quantified by unusually large equivalent widths (EWs), above 150Å. Such galaxies were first identified in the local universe by Sargent & Searle (1970) as giant isolated HII regions violent star-forming regions and have since been observed in detail via spectroscopy and narrow-band imaging throughout the local universe (first in Terlevich, 1988; Kniazev et al., 2009; Lagos et al., 2009, in narrowband). The high equivalent widths of lines observed in the spectra of these galaxies require both strong emission line luminosity (i.e. strong present star formation) and a low continuum (i.e. low previous star formation). EELGs are typically low-mass galaxies undergoing young major star formation episodes and therefore are an essential population to survey throughout cosmic history, because they are the most direct source of information about star formation and nebulae at high redshifts.

The characterisation of star formation in ELG populations requires a wide range of wavelength coverage to simultaneously include multiple NUV/optical emission lines, from [OII](3727Å) to Hα(6563Å) across a wide redshift range. Combining this with the fact that the galaxies most susceptible to being EELGs have lower masses, this requires deep observations (H$>$ 24) like those from optical-

NIR-MIR multiband data from CANDELS (Grogin et al., 2011).

A consistent picture has now formed where cosmic star formation rate density steadily rises from very high redshift to z≈2 and then exponentially declines towards quiescence at z=0 (see Madau & Dickinson (2014) and references therein for a comprehensive review). This is likely a saturation (peak) followed by a decline of gas accretion rates, which in turn leads to a depletion of cold gas supplies, but understanding the actual detailed processes at work during this transition, their mass dependence and changes in ISM properties requires detailed simulations of multiscale effects and feedback (e.g. Kimm et al., 2015; Tacchella et al., 2015). Simulations have evolved to minimise the amount of tuning required to produce agreement with observables (Lagos et al., 2015) while making testable predictions about the transition starting from the peak of star formation when cold gas supplies are high up to z=0.7 when these are depleted. This requires dissecting large samples of galaxies over a wider range of mass, redshift and wavelength.

Cosmic star formation rate density can be inferred from the evolution of UV/IR luminosity, assuming a model for photon absorption and reprocessing by dust. When present, optical emission lines are particularly helpful, as they directly probe the instantaneous properties of gas exposed to the ionizing radiation of Wolf-Rayet, O and B stars as they form along with emission nebulae (Schaerer & Vacca, 1998). While not as severely affected by dust as the UV, it is still necessary to correct for differential dust extinction and to quantify the influence of metallicity and the ionization parameter (Kewley et al., 2013; Anders & Fritze-v. Alvensleben, 2003). However, this can be accounted for and used to characterise the nebular component of such a galaxy, especially if multiple lines can be measured.

Major observational steps towards measurement of line emission are underway where growing numbers of wider-baseline spectra of high-z galaxies are being collected through grism spectroscopy (WISP Atek et al. (2010), 3DHST Skelton et al. (2014)), surveys using multi-object spectrographs (MOSFIRE Steidel et al. (2014), VIMOS Le Fèvre et al. (2015), KMOS) and new integral field units like MUSE (Bacon et al., 2015) that can characterise line luminosities for individual objects in large samples. Complementarily, to get a comprehensive statistical coverage of the evolution of galaxy properties to high-z it is still

more efficient to use photometry to go deeper, measure the continuum, and take advantage of existing large optical-NIR multi-band photometry surveys like UKIDSS (Lawrence et al., 2007) and CANDELS (Grogin et al., 2011) to obtain photometric redshifts, cover the restframe optical and any line emission up to high redshifts (>5).

A highly effective photometric approach to measure star formation rate density is to choose an array of available narrow-band+broad-band filter pairs to obtain equivalent widths (EW) directly (and accurately down to 25Å) at specific redshifts by subtracting the broad-band continuum flux from its narrow-band counterpart: (e.g. HiZELS by Sobral et al. 2009 and NEWFIRM by Ly et al. 2011). Nevertheless, redshift slices containing a line in each narrow-band have dz≈0.01 and miss the majority of the objects otherwise present in the broad-band, so this method is indicated for large sky areas.

This picture began to change in the survey age with the first large high-z narrow-band surveys (Ly et al., 2007; Sobral et al., 2009; Ly et al., 2011) showing an evolution of star-forming activity from emission lines and the first high-z grism survey data with HST-WFC3 (Straughn et al., 2010), which shows large numbers of strong line emitters (Atek et al., 2011), most recently pushing down to dwarf galaxy territory in Atek et al. (2014). Further progress from the grism approach has yielded accurate enough line luminosities to derived metallicities at z>2 (e.g. Cullen et al. (2014)).

A third method has developed from the traditional colour-colour characterisation extensively used to select high-z samples of LBGs in wide redshift windows for spectroscopic follow-up. An early example is using UGR colours to detect the Lyman break at z>3 (Steidel et al., 1996). This was later extended to use other spectral features like optical emission lines: the BzK method (Daddi et al., 2004) to select starforming galaxies for follow-up, but the objective was never to measure the emission lines themselves until van der Wel et al. (2011), henceforth referred to as vdW11. As the number of photometric bands available grew, multi-colour selection evolved into photometric redshift fitting (spectroscopically calibrated whenever possible) and the effects of optical emission lines became secondary to estimating SFR from UV continuum, Lyα, escape fractions and the Lyman continuum (Vacca et al., 1996) (simply due to the lack of deep NIR spectrocopy/photometry at high redshift).

As deeper ($H_{5\sigma}$ >27) WFC3 photometry was gathered in J_{125} and H_{160} it was noted by vdW11 using these deep broad-bands that galaxies with very high colour excess in J-H and i-J were in fact very strong EW_0 EELGs at z=1.7. More than a nuisance or a subsample for follow-up, ELG colours can be directly converted into estimates of EW_0 for [OIII].

At lower redshifts, known ELGs (from available spectroscopy) were rediscovered in SDSS broad-band photometry as the green peas in galaxy zoo low-density environments (Cardamone et al., 2009). Subsequently there have been various broad-band studies confirming the ubiquity of ELGs at all higher redshifts (Stark et al., 2013; Smit et al., 2014a; Schenker et al., 2013) and their increasing prevalence (e.g. lensed objects in CLASH exhibiting EW>3000Åby Huang et al., 2015), so the question of how to systematically study strong emission lines with broad-band colours across redshift is a pertinent one.

SHARDS, introduced in Pérez-González et al. (2013) provides an insight into this, with very deep (26.5 ABmag) GTC observations in 24 medium bands between 5000Å and 9500Å (roughly covering V,R,i,z) with some early results in Cava & Pérez-González (2013), but as ELG studies go, it will need J, H and K coverage to really probe the peak of star formation and SFR transition. Recent work by Spitler et al. (2012) (ZFOURGE) and Papovich et al. (2015) provides further medium bands, now in the infrared, by subdividing the J band. More recently Faisst et al. (2016) also performs an analysis of emission line EWs using broad-bands throughout redshift.

The multi-mediumband observations from SHARDS (Pérez-González et al., 2013) suggest that Bruzual & Charlot (2003) with a Chabrier (Chabrier, 2003) IMF (henceforth BC03) are the most reliable templates to fit UV/optical continuum. Dust corrections can be applied to the continuum using simple recipes that capture the main observable effects of differential extinction: a patchy dust-screen with birth clouds (Charlot & Fall (2000),Wild et al. (2011)). Other corrections deliver progressively smaller gains in fits, but for high redshifts emission-line EWs are expected to be enhanced by a factor of (1+z), the ratio between observed and rest-frame EWs.

A number of papers (Schaerer, 2002; Zackrisson et al., 2008; Wilkins et al., 2013) have drawn attention to the importance of considering the effects of high-z extreme emission-line contamination (and nebular continuum), increasingly

towards higher-z (both due to increased sSFR/EW_0 and EW enhancement by a factor of (1+z)) and their impacts on SFR and mass estimates, so when fitting at high-z it is essential to include emission lines in a fit.

A natural answer to this is to add emission lines to the models, and codes like LePHARE (Arnouts & Ilbert, 2011) typically add this in an ad-hoc manner (detailed computation would require applying e.g. CLOUDY to each spectrum used in a spectral library), but as their effects increase with redshift, very strong lines can progressively contaminate the broad-band photometry for low-mass galaxies in what is already degenerate information coming from broad-band photometry, so adding 1 or 2 extra parameters for emission lines can easily over-fit the limited number of bands available. Pacifici et al. (2012) show that fitting colours with carefully built emission line templates can still reliably recover physical parameters, redshift, SFR and mass.

As progressively higher-z galaxies are yet to form most of their mass, stronger than usual nebular emission from frequent star-bursts will not be buried in continuum as compared to z=0, so it is possible to see higher equivalent widths (EW>500Å). The subsequent questions are: up to which mass is this the case, until which z they are important (a mass-EW-z distribution), and how much do they contribute to CSFR leading up to its peak and its decay. Going deep enough to reach ELG dwarf progenitors of modern L* galaxies or at least witnessing how a large fraction of the stellar mass accreted onto massive galaxies was formed.

In this sense, strong ELGs make emission line SFR measurement even more useful than usual, as nebular star formation becomes a dominant spectral feature of high-z galaxies that can be measured as a primary observable (instead of age and mass, for example). So direct measurements of emission-line evolution would be useful to guide SED modelling.

Given this background, I propose to extend the broad-band colour method to obtain ELG emission-line EWs in as wide a redshift range as possible using the rich near-continuous broad-band coverage of existing surveys from U to IRAC to simultaneously survey all strong (only dust-free) [OII], [OIII] and Hα low-mass emitters from z=0.1 to z=5 in the CANDELS UDS field. This field is used because of its deep, complete NIR photometry (including HST J and H, but also K and IRAC), the availability of photometric redshift and mass catalogs, and the extra Subaru R band of the equally valid CANDELS GOODS South.

The structure of this chapter is as follows: Section 3.2 describes the catalogues, bands and models used. Section 3.3 describes the colour offset signal as observed at redshift 1.7 for the previously explored [OIII] (van der Wel et al., 2011) and how this extends to the [OII] and Hα lines. Section 3.4 describes the signal search strategy for all lines, redshifts and multiple filter combinations. Section 3.5 describes how to convert measured offsets into equivalent widths in each filter and their evolution. Section 3.6 discusses mass cuts and construction of equivalent width (EW) distributions and fractions the evolution of mean EWs and how the results compare with other narrow-band and grism measurements. Section 3.7 summarises the results.

Further conversion of observables and EWs into physical quantities like line luminosities, SFR, sSFR, UV slope (β), line ratios and the respective analysis is deferred to chapter 4, where data from all five CANDELS fields will be used.

All cosmological quantities are derived assuming ΛCDM with Ω_Λ=0.7, Ω_{Matter}=0.3 and h=0.7 (Planck Collaboration et al., 2015). All magnitudes are in the AB magnitude system (Oke & Gunn, 1983).

Observations and Models

All CANDELS-UDS data used in this paper are drawn from the publicly available catalogue described in Galametz et al. (2013). It includes ground-based U (CFHT+Megacam), B,V,R,i,z (SUBARU+Suprime cam) from UDS and the deeper HST-CANDELS subregion in V_{606}, i_{814} (I) (HST+ACS), J_{125} and H_{160} (HST+WFC3). Deep (Spitzer+IRAC) photometry is provided for the 3.6 and 4.5 μm bands from SEDS (Ashby et al., 2013). Finally, two ground-based (VLT+HAWK-I) bands Y and K_s are added from HUGS (Fontana et al., 2014) to create near continuous coverage from U to $IRAC_{4.5}$ over a sky area of 200 arcmin^2. The data yield a sample of 20966 galaxies with $H_{5\sigma}$ <26 from z=0.1 to z=5. Only objects with stellarity below 0.95 are used in this sample. Filter profiles and 5σ limiting magnitudes are described in Fig. 3.3.

The only zero-point corrections applied to the photometry in this catalogue were in the IRAC bands, generally due to the wider point-spread functions in the IRAC bands and centroid offsets ($ZP_{IRAC3.6}$=-0.08, $ZP_{IRAC4.5}$=-0.08).

Two auxiliary catalogues are used, one of photometric redshifts (Dahlen et al., 2013) and one of mass estimates described and released by Santini et al. (2015) in

the context of the CANDELS collaboration. Most of these models use templates with emission lines, but it is possible (and indeed necessary) to reliably recover continuum parameters (redshift, and less robustly, mass) just with modest line contamination. As long as z and M can be determined taking advantage of the large number of bands over the wide wavelength coverage of CANDELS, redshifts can be used as an independently obtained parameter and used as leverage to determine more degenerate parameters like emission-line EWs.

Finally, the method relies on an independent set of simulated colours drawn from a set of pure continuum BC03 galaxy templates convolved with a set of static-metallicity (chosen in the range $2.5<Z/Z_{\odot}<0.001$) exponentially declining star formation histories (drawn from the range 1Myr<Age<10Gyr) with stochastic bursts of star formation, as the models used in Wild et al. (2014) (Fig. 3.2).

Colour Excess at z=1.7

The starting point for this analysis is the colour-colour selection from van der Wel et al. (2011) in $J_{125} - H_{160}$ versus $i_{814} - J_{125}$, shown in Fig. 3.1. In this way it is possible to select only the emission-line galaxies with a J_{125}-band boost by [OIII] (Hβ is included in all the [OIII] emission I will refer to) while i_{814} and H_{160} are mostly clear of emission lines at z=1.7. After selection, it is also possible to measure how strong [OIII] contamination is relative to the stellar continuum or the estimated line-free models. The objects thus selected correspond to objects with 500Å<$\mathrm{EW}_{[OIII],rest}$<1300Å and either $0 < A_V < 1$ or $7 < \log_{10}(\mathrm{Age}/yr) < 8$. Such young objects have correspondingly low masses, estimated in vdW11 and confirmed in Maseda et al. (2013). However, this band combination can only select objects in the very narrow redshift window where H_{160} is line-free (dz=0.1) and, in addition, that [OII] at z=2.6 could potentially produce the same effect.

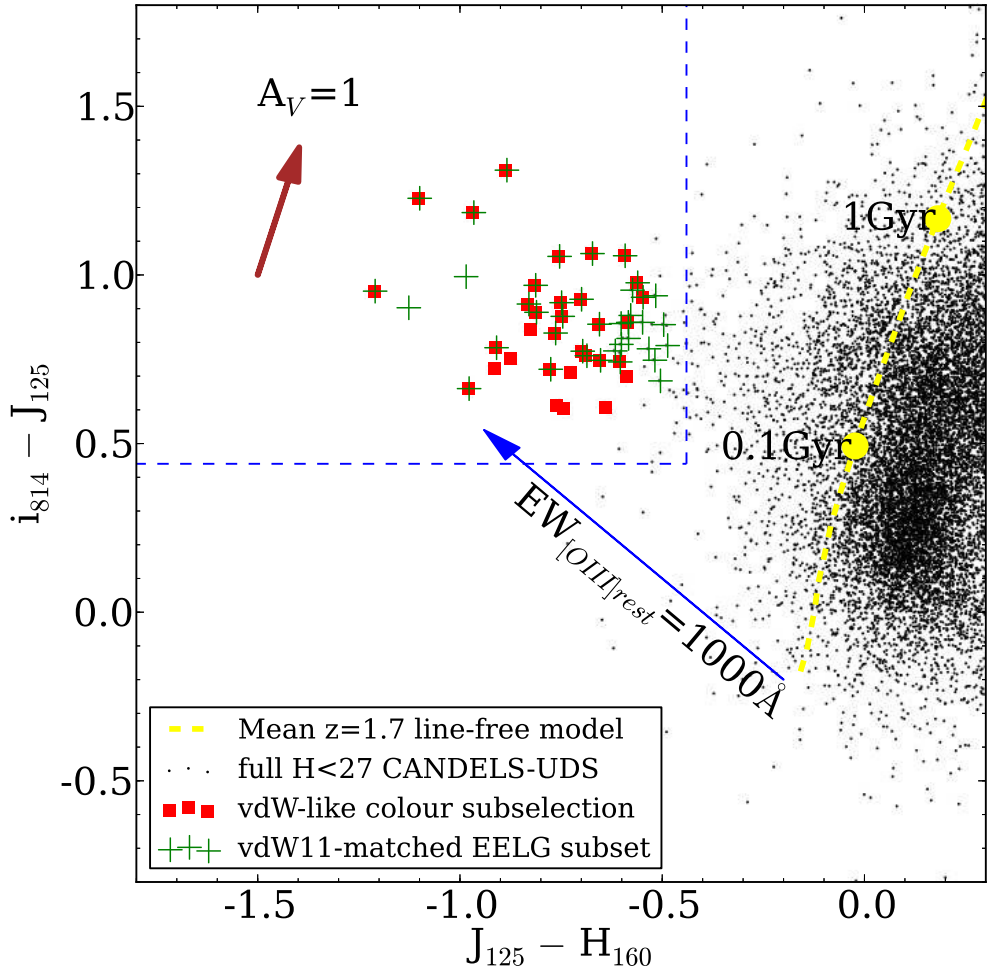

Figure 3.1: $J_{125}-H_{160}$ versus $i_{814}-J_{125}$ colours of objects in the full CANDELS-UDS catalogue for H_{160}<27 and stellarity<0.95 (black). The dashed yellow line shows the median simulated colours of line-free galaxies at z=1.7, with 0.1Gyr and 1Gyr colours marked. The red squares show the subsample of all objects with $J_{125}-H_{160}+\sigma(J-H)<-0.44$ and $i_{814}-J_{125}-\sigma(i-J)>0.44$. The green crosses show the subsample of CANDELS-UDS objects cross-matched in RA-DEC with all the objects selected in vdW11 with the same colour cut (regardless of stellarity). The blue arrow shows the expected magnitude boost in J from EW$_0$ =1000Å of [OIII] present at z=1.7 and the brown arrow the reddening vector. The sample with these colours necessarily has to be boosted in the J band by [OIII] emission from the expected continuum-only colours at 100Myr (with A$_V$=0) or a stellar population with an even lower age and a small A$_V$. The two samples (green crosses and red squares) do not match exactly, the two green crosses on the left due to high stellarity and the rest due to updates to photometry and errors, but the number of selected objects remains approximately the same.

New colours: [OIII] in J and [OII] in Y

To make the colour-colour selection method flexible and cover other redshift ranges, I choose a line-free colour with well-spaced filters (henceforth called a baseline colour) free of any emission lines (e.g. $B - K_s$ at z<2, before Hα enters the K_s band) and use this line-free colour to estimate the expected line-free continuum. Then I use photo-z slicing from an available catalogue of high quality ($\sigma_z \approx 0.1$) CANDELS-UDS photometric redshifts combining fits by multiple groups (Dahlen et al., 2013) in specific (dz=0.2) redshift ranges, which limits data scatter due to photometric errors and photo-z interlopers.

Fig. 3.2 shows how $J_{125} - H_{160}$ and $Y - H_{160}$ colours are enhanced due to [OIII] at z=1.7 (as in vdW11) and [OII] at the same redshift in Y. At z=1.9 the effect of [OIII] is shown now in the H_{160} band and at lower redshifts I show examples of how these colours also capture Hα both in J_{125} at z=0.8 and H_{160} at z=1.4.

There is a generally good correspondence between models and observations on the old, continuum-dominated, red side of the population at $B - K_s$>2 and at line-free redshifts (see extended colour-colour panels 3.5 and 3.6). EWs from BK_sJK_s at z=1.7 agree with those using $JHIJ$ colours. Because it is narrower, the Y band is more sensitive to emission line contamination than H, so the same colour offsets correspond to lower EWs. This already indicates that EW$_{[OIII]}$ is higher than EW$_{[OII]}$. The bottom left panel also shows Hα in BK_sYH at z=1.4, where Y is clear of lines. Hα EWs increase from z=0.8 to z=1.4, but further evidence of this will be provided in the next sections.

However, these colours depend on three bands being completely line-free, which is difficult to accomplish when searching for lines at various redshifts with such broad bands. For example, at z=1.7 the narrow window makes it possible for contaminants from z=1.9 to appear and boost an otherwise line-free band (partly responsible for the observed counterscatter). For this reason, rather than using 4 bands to create two independent colours (baseline colour and line colour), I will use only three bands to create two colours: a blue reference filter for the baseline, a red baseline filter (the normalizer, used in both colours) and a line filter (X) in the baseline colour (e.g. $B - K_s$) and a line colour using the same red baseline filter as normalizer for the X filter (e.g. $Y - K_s$ at z=1.7). This way, wide enough redshift windows can be created to accommodate photo-z scatter.

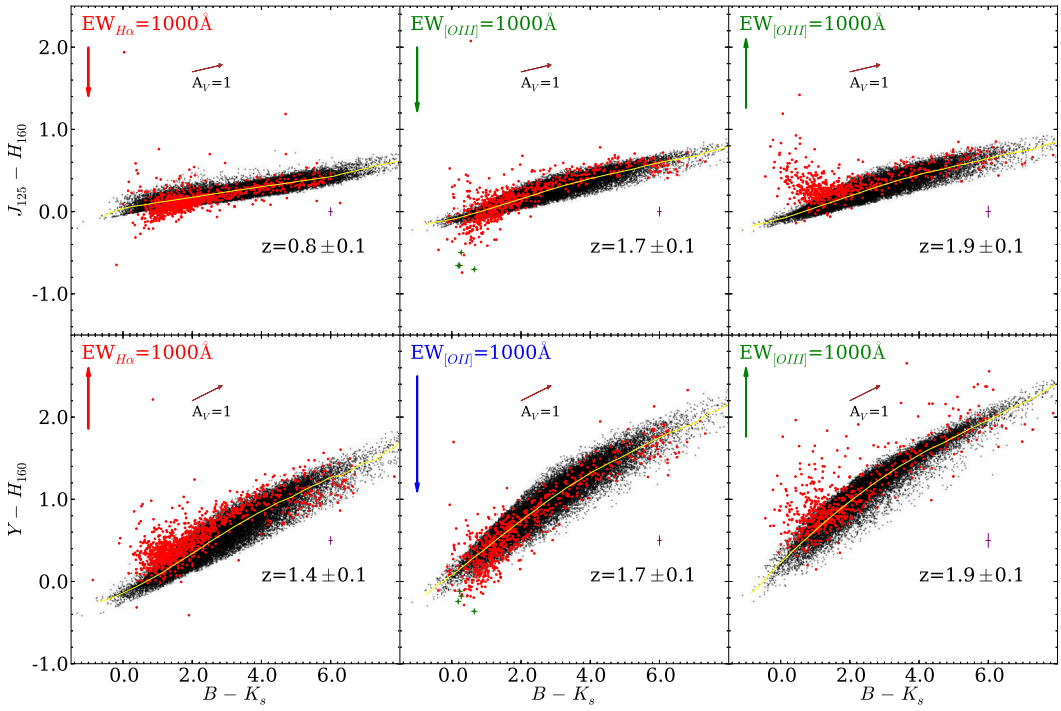

Figure 3.2: Colour-colour plots of CANDELS-UDS photometry (red points) in $B - K_s$ vs $Y - H_{160}$ (bottom) and $J_{125} - H_{160}$ (top) over the indicated redshift ranges for H_{160}<26. The black points show a set of line-free stochastic burst models and the yellow line running through is the average model (binned in $B - K_s$). The coloured vertical arrows show the effect of 1000$\mathring{A}$ in the indicated line for each panel and fold in both the width of the filter where the line is present and the (1+z) EW correction factor. The brown arrow shows the reddening vector for $A_v = 1$ and the purple cross the median colour errors of the plotted observations. The green crosses at z=1.7 in the center plots show the cross-matched vdW11 objects at this magnitude cut. The middle-upper panel shows analogous results to those of Fig. 3.1 with EWs up to 1000Å in $J - H$ and the middle-lower panel shows the [OII] emission for the same sample at z=1.7, with weaker emission. The right-hand panels both show [OIII] in the H band, so the ELG signal goes in the same direction, but the different depths of the J and Y bands introduce different amounts of scatter. The left-hand panels both show Hα in the J band (z=0.8), when H is line-free and then in the H band (z=1.4), when Y is line-free. There is some noise in the middle-upper panel with ELGs scattering opposite to the arrow direction, because the z=1.7±0.1 bracket is contiguous to z=1.9±0.1, so some of the z=1.9 H-band ELGs will leak into the z=1.7±0.1 bin.

Extending redshift coverage, filter coverage and surveyed lines

Using the (B-K_s,X-K_s) colours it is possible to fix B and K_s as safely clean of emission lines and to follow the emission lines as they enter each filter from z=0.3 ([OII] leaves B band) to z=2 (Hα enters K_s). This is detailed in Fig. 3.3, which shows the redshift coverage of the strongest lines expected to be enter each filter: [OII] (3727Å), [OIII] (5007Å+4959Å+4861Å (Hβ)) and Hα (6563$\mathring{A}$+6583$\mathring{A}$) from U to IRAC. [OIII] is always understood to mean [OIII]+Hβ and Hα to stand for Hα+[NII], since these amounts of line contamination are characteristic of high-ionization ([NII]<<Hα and [OIII]>>Hβ in the BPT diagram) regions. To go above redshift 2, it is essential to use the IRAC 4.5μm band as a normalizing filter N, while the best baseline colour to use in this case is i'-4.5, covering z=1.3 to z=4.7, (i'-4.5,X-4.5) colours. Despite the lower signal-to-noise of the shallower IRAC bands, using 4.5μm as a normalizer works because observed equivalent widths scale with (1+z) and this compensates the increased noise levels. For higher redshifts the limiting factor is actually the reduced number of objects, rather than Hα entering the 4.5μm filter. Pushing this approach to a third higher redshift baseline would require at least even deeper 5.8μm and 8.0μm bands to probe ELGs from z=4 to z=9 (H_{160}-8.0,X-8.0) colours, soon to be possible with the JWST MIRI instrument bands F560W, F770W and F1000W (Wright et al., 2008).

The ELG colour excess for (B-K_s,X-K_s) and (i'-4.5,X-4.5) is shown in Figs. 3.5 and 3.6 covering z=0.1 to z=4.9. The models-data correspondence holds. Lines fade in and out consistently with expected line contamination ranges. This is shown in Fig. 3.4, where the distribution of ELG colour offsets is measured relative to the average model as a function of redshift for both BK_sXK_s and i'4.5X4.5 colours. The distributions are drawn only for objects with baseline colour <2. The coherence in the overlap region between z=1.3 and z=2 shows the average colour offsets are robust against changes in baseline.

To bring the line-free regions closer to offsets of 0, the following zero-point corrections were applied in magnitude space: U:−0.2, i':0.05, Y:−0.05, K_S:−0.05, J_{125}:−0.05, 3.6_{IRAC}:0.05, 4.5_{IRAC}:0.1.

ELG subselection at B-K_s<2 and i'-4.5<2 is chosen as the natural limit for the reddest ELG or where observations start to depart from any possible line-free models. The cut remains static in redshift because of the B$-K_s$ colour choice: apart from a power-law background, there are no other major spectral features entering either filter. This cut selects objects with age<100Myr and Av<1 and leaves any dusty/older/more massive objects out of the sample. Due to this, the sample will not contain any potential dusty or old ELGs, but there is no significant evidence to show this will be a large fraction of the sample, from the literature or from the figures in this chapter. In fact, this selection favours young populations with negligible Balmer breaks, where the baseline colour B$-K_s$/i'-4.5 can be used as a direct proxy for the β slope and constitutes a limiting factor to the completeness of this approach.

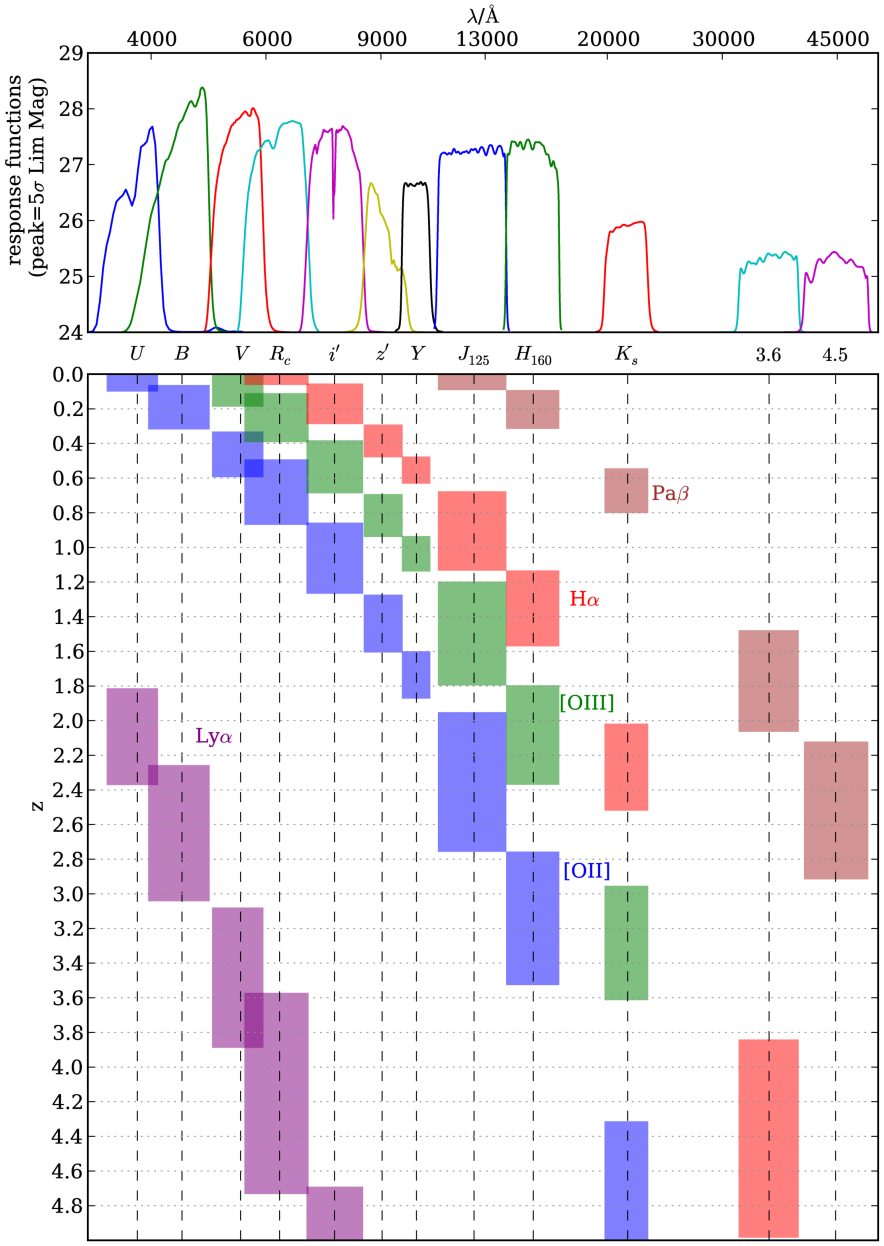

Figure 3.3: Upper panel: Filter profiles for each band used (λ scale is logarithmic), normalised to peak at each respective 5σ limiting magnitude. Lower panel: expected redshift range for line contamination in each filter between its full-width at 40%-maximum for Lyα (purple), [OII] (blue), [OIII] (green), Hα (red) and Paβ (brown) up to z=5.

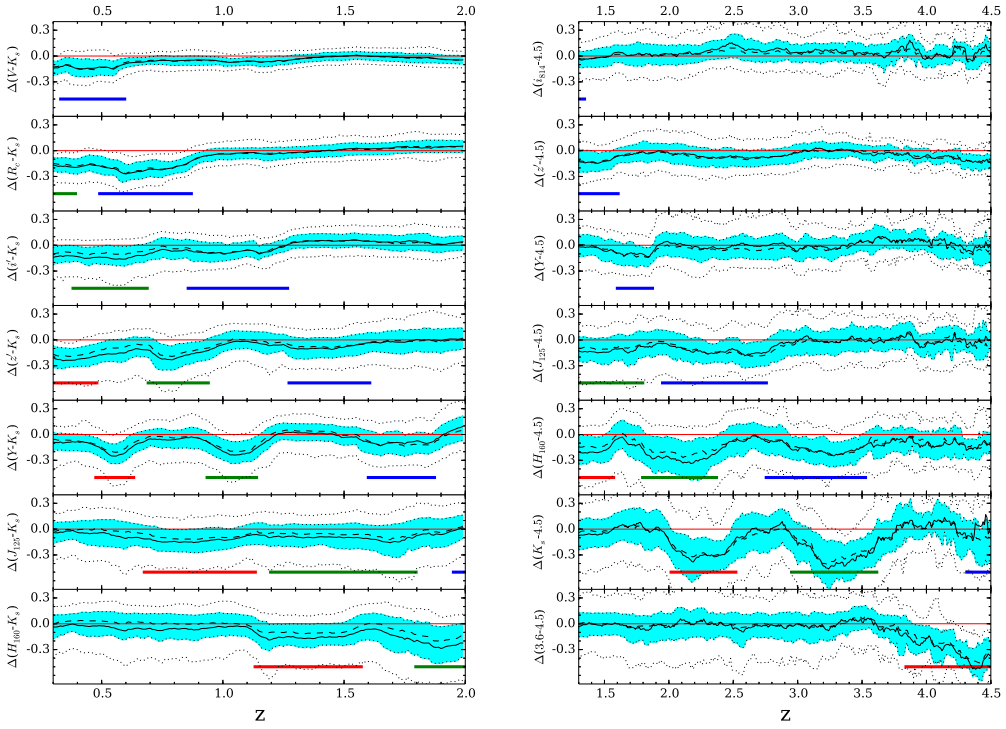

Figure 3.4: Distributions of colour offsets from median line-free model colour as a function of redshift: average (full lines), median (dashed), 25/75th percentiles (blue regions) and 10/90th percentiles (dotted lines). Left: $z < 2$: B$-$K$_s$<2, H<25 selection, X$-$K$_s$ colours. Right: z>1.3, i'$-$4.5<2, H<26 selection, X$-$4.5 colours, with X any filter between the two baseline bands. (Red, Green, Blue) lines show the expected redshift range of (Hα,[OIII],[OII]) contamination.

Full colour signal coverage

This section shows the complete coverage of the raw emission-line signal in colour-colour space in Figures 3.5 and 3.6: 3-band colour-colour signal for each band and redshift and the corresponding inferred equivalent widths in contiguous redshift bins for a magnitude cut of H<25. No mass cuts have been applied at this stage. The yellow lines show the median colour of the SBM line-free colours and as such it represents the line from which equivalent width is measured. Observed CANDELS-UDS colours in red match the black SBM models with consistent discrepancies in the blue when a line is expected to be present (when the downward arrow is coloured). Notice how the Y-band from z=1.3 to z=1.5 matches the line-free models, but outside that range blue galaxies are pushed towards higher values of Y. The same should happen when the H-band is contaminated at z=1.7, but there is still some scatter. Even if this is due to photometric errors, notice how the highest values of H-K for the bluest observations now align with the locus of models, unlike at other redshifts, where they are shifted down. This is the signal that makes Figure 3.4 possible. The two last figures 3.7 and 3.8 show the distributions of colour offsets from the SMBs observed for the CANDELS-UDS sample in the previous figures. At low redshift the distributions do not show very high equivalent widths (>500Å), but after redshift 1 they display larger equivalent widths and [OIII] has a flatter distribution than Hα, while [OII] remains at low values of EW (<300Å). All ranges without expected emission line contamination show only residual spurious values of emission-line EWs, which are indicative of the expectable errors in these distributions.

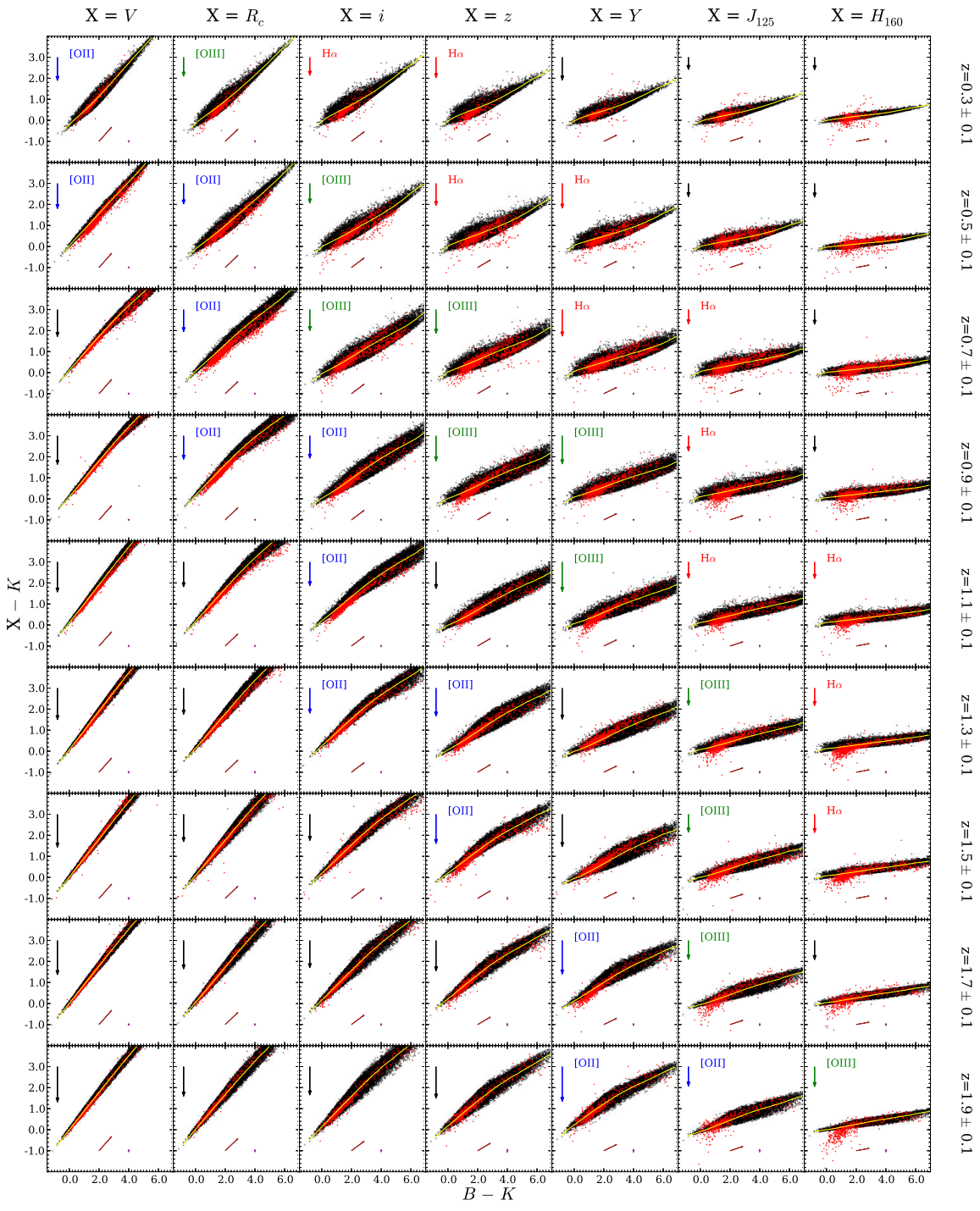

Figure 3.5: Colour-colour (B-K,X-K) plots for X=V,R_c,i',z',Y,J,H filter set from z=0.3 to z=2 in bins of dz=0.2. The black points show the model scatter. The yellow line shows the average model for each B-K value. The red points show the observations in each redshift bin. Wherever line emission is expected, the arrows show the expected effect of rest-frame EW_0=1000Å when Hα, [OIII] or [OII] is present. The dust reddening arrow for A_V=1 is shown in red. Crosses shows median errors in each bin. The magnitude cut applied is H<25, no mass cut was applied at this stage.

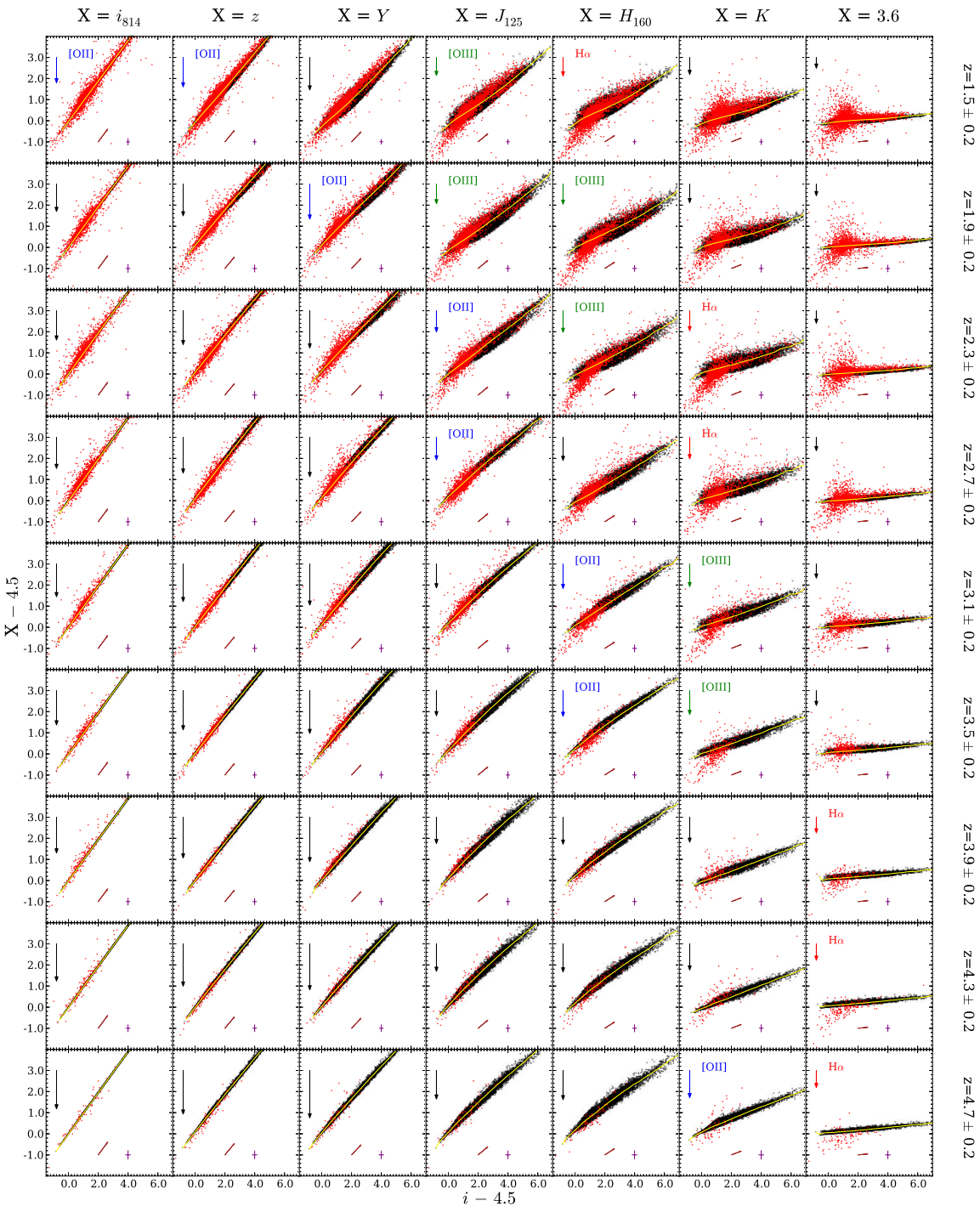

Figure 3.6: Colour-colour (i'-4.5$_{IRAC}$,X-4.5$_{IRAC}$) plots for X=R$_c$,z',Y,J,H,K,3.6$_{IRAC}$ filter set from z=1.3 to z=4.9 in bins of dz=0.4. The black points show the model scatter. The yellow line shows the average model for each i'-4.5$_{IRAC}$ value. The red points show the observations in each redshift bin. Wherever line emission is expected, the arrows show the expected effect of EW$_0$=1000Å when Hα, [OIII] or [OII] is present.Dust reddening arrow for A$_V$=1 is shown. Cross shows median error in each bin. The magnitude cut applied is H<26, no mass cut was applied at this stage.

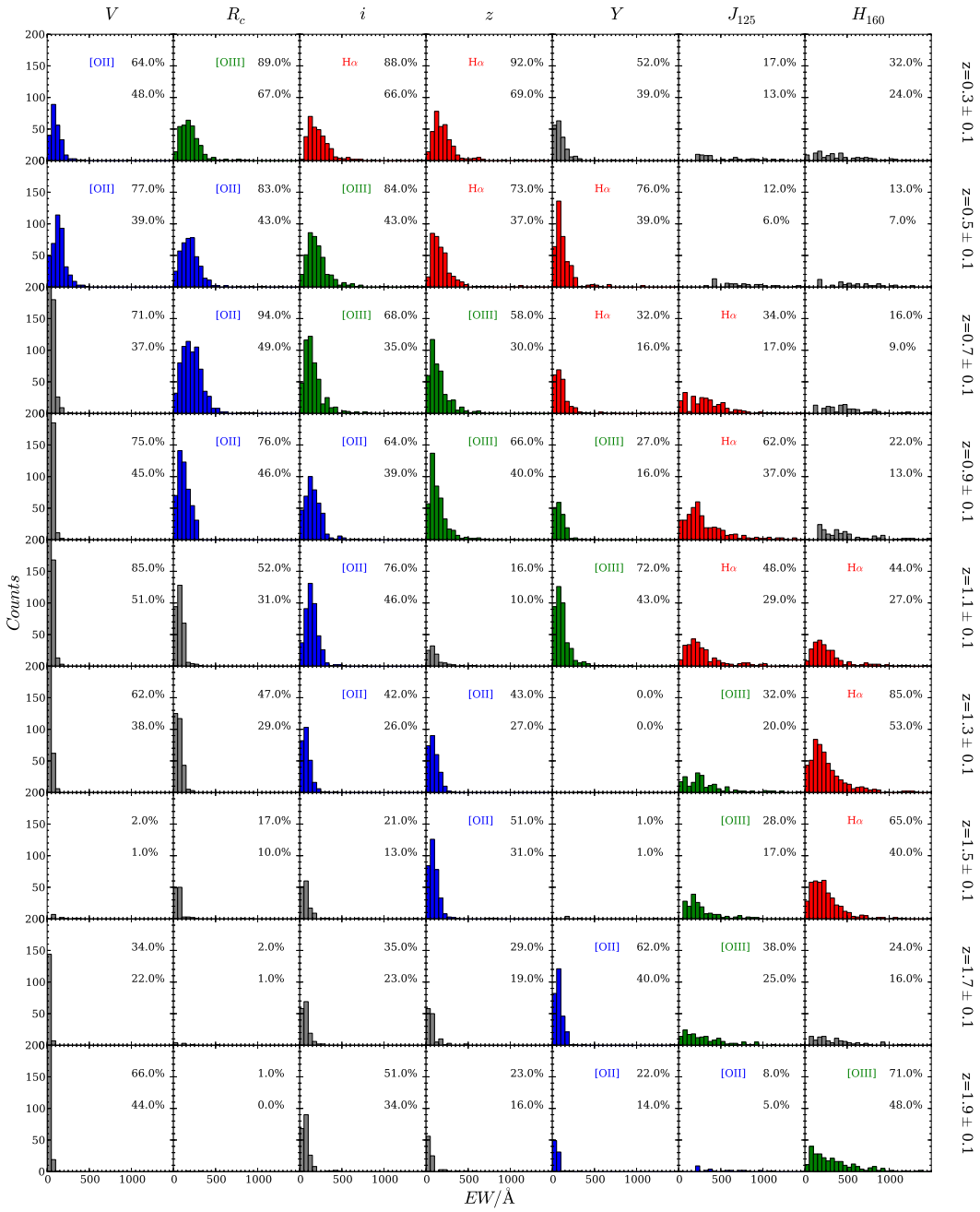

Figure 3.7: Equivalent width distributions drawn from figure 3.5. Where lines are expected to be present the distributions have been coloured in red, green and blue, respectively for Hα, [OIII] or [OII]. The magnitude cut applied is H<25, no mass cut was applied at this stage. The percentages detail what the fraction of shown ELGs is among blue (upper fraction) and all (lower fraction) galaxies in that z range.

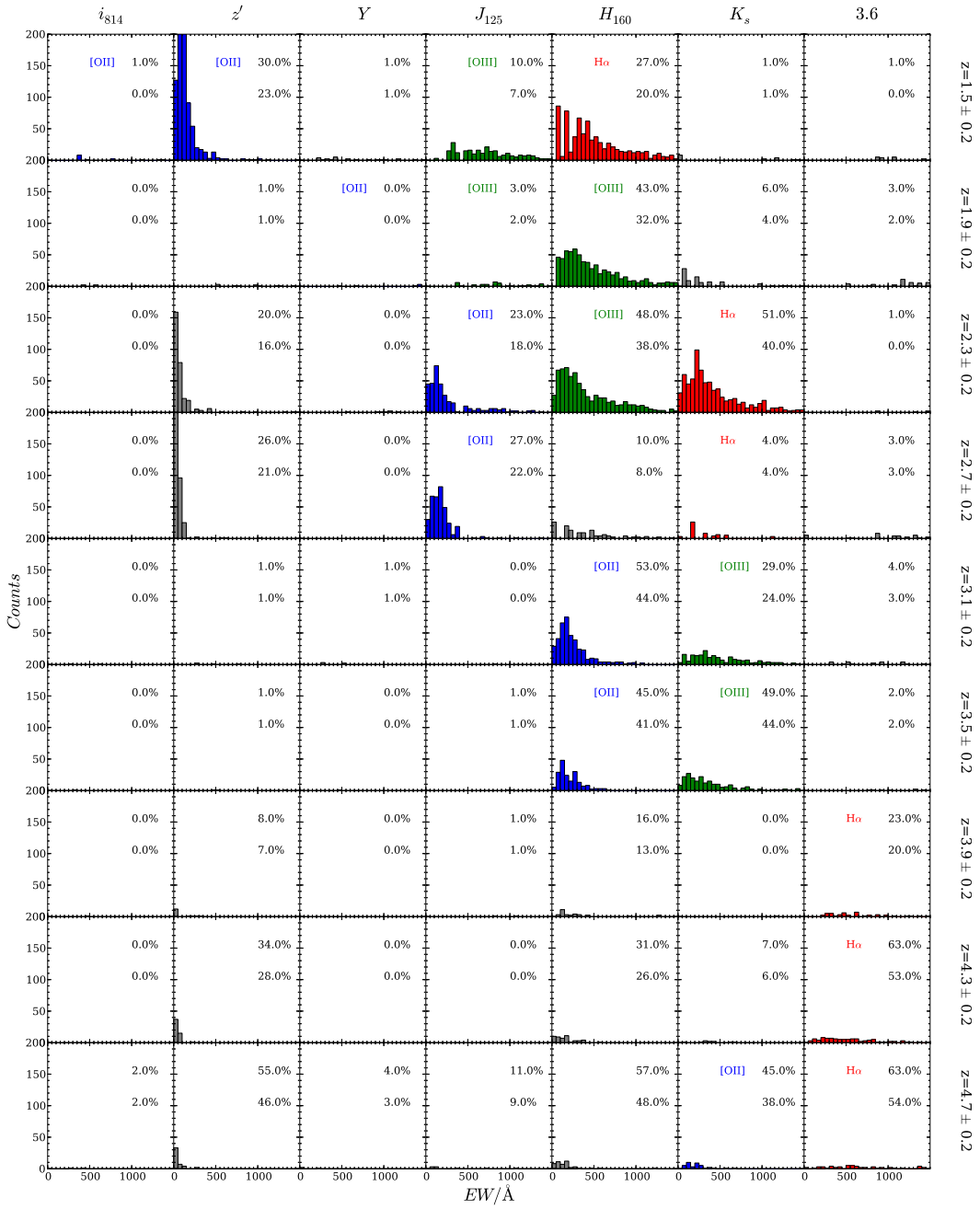

Figure 3.8: Equivalent width distributions drawn from figure 3.6. Where lines are expected to be present the distributions have been coloured in red, green and blue, respectively for Hα, [OIII] or [OII]. The magnitude cut applied is H<26, no mass cut was applied at this stage. The percentages detail what the fraction of shown ELGs is among blue (upper fraction) and all (lower fraction) galaxies in that z range.

Equivalent width Estimation

With an understanding of the colour offsets (X-N, where X stands for any band with a line and N for a normalizing line-free band) and confidence in the ranges where EWs are measurable, one can then estimate equivalent widths from colour offsets using:

$$EW_{obs} = \frac{F_{line}}{F_{\lambda,cont}} = \frac{F_{line}}{F_{cont}} W_X = \left(\frac{F_{total}}{F_{cont}} - 1 \right) W_X \tag{3.1}$$

$$EW_{rest} = \left(\frac{F_{\nu totalX}/F_{\nu totalN}}{F_{\nu contX}/F_{\nu contN}} - 1 \right) \frac{W_X}{1+z} \tag{3.2}$$

$$EW_{rest} = \left(10^{\Delta(X-N)/-2.5} - 1 \right) \frac{W_X}{1+z} \tag{3.3}$$

Where W_X is the line-filter width. If the filter is far from a top hat (e.g. z') one can replace the flat W_X with the normalised response function (but this will magnify Δ X errors near the edges of the filter):

$$W_X = \frac{1}{R_{\lambda X[(1+z)\lambda_{Line}]}} \tag{3.4}$$

Note that for small Δ (X-N)<<1 this approximation holds (if no line is present in N):

$$EW_{rest} \approx -\frac{W_X}{1+z} \Delta(X-N) = -\frac{W_X}{1+z} \Delta X \tag{3.5}$$

So for a normalizing band that is kept line-free, then the median colour X offsets observed are approximately proportional to the EWs of the lines responsible for them.

Applying equation 3.3 on the ELG colour offsets, one can obtain the median EWs (Fig. 3.9) from each band using multiple baselines, along with estimates of data dispersion, in this case the inter-percentile distance (p.d.) between the 50th and 10th/90th percentiles. The 20-50 p.d. should remain constant, because it is expected to be line independent and provides an estimate for the scatter that is not due to emission lines. On the other hand, the 50-80 p.d. shows the same estimate of scatter on the side where the emission lines are present. If the two measures of dispersion match, then the distribution is symmetric and only the

	Reference Band:								
N:	U	B	V	R	i	z	Y	J	H
H	×	×	×	×	·	·	·	·	·
K	×	×	×	×	×	×	·	·	·
3.6	×	×	×	×	×	×	×	×	×
4.5	×	×	×	×	×	×	×	×	×

Table 3.1: Description of all the baseline colour combinations used: × marks each colour (Ref-N) included (N, the redder band picked from one of the rows is also the normalizing band used in the X-N colour in Fig. 3.9.

median value is shifted due to global line emission. However, it is noticeable that the up scatter can be very pronounced, especially for [OIII] and Hα at higher-z, indicating an extended distribution over the ranges containing emission lines (e.g. the most extreme ELGs are boosted by up to 400Å at z=2.3 over the natural scatter caused by errors in the generally shallower normalizing bands).

Variations in the baseline colour

It is useful to compare the measurement of an equivalent width for a band and redshift under a different baseline, to assess how a colour offset varies with the baseline change (e.g. comparing BKXK and VKXK or R3.6X3.6). This works to compute the colours for a large set of baselines, shown in Table 3.1 and to take the median to obtain measurements of EW in individual bands that are robust against the individual systematics for any one chosen baseline. The consistency of the offsets measured between most baselines, the positions of line contamination and the UV desert permit the construction of a final set of combined colour offsets spanning redshift from z=0.1 to z=5 in each band. These offsets were converted into EWs in Figs. 3.9 and 3.10. To apply a homogeneous colour cut (equivalent to B-K<2 for any filter pair), equivalent baseline colour cut thresholds are calculated assuming the line-free continuum to be a power-law.

$$\mathrm{Ccut}_{\mathrm{f1,f2}} = \frac{\mathrm{Ccut}_{\mathrm{BK}}}{\log\left(\frac{\lambda_{\mathrm{B}}}{\lambda_{\mathrm{K}}}\right)} \log\left(\frac{\lambda_{\mathrm{f1}}}{\lambda_{\mathrm{f2}}}\right) \tag{3.6}$$

The EW evolution for each filter in Fig. 3.9 can be further combined, now in rest-frame wavelength, to show directly how the EWs of a median galaxy are

evolving with z (Fig. 3.10), compare agreement between bands and potentially spot any other signal. It shows the dramatic change from z=1 to z=2 in the character of the median emission-line galaxy from the eventual minor line emitter at z<0.5 to a prevalence of Hα and [OIII] above the continuum in the median ELG at z>2.5. However, [OII] does not seem to follow this evolution.

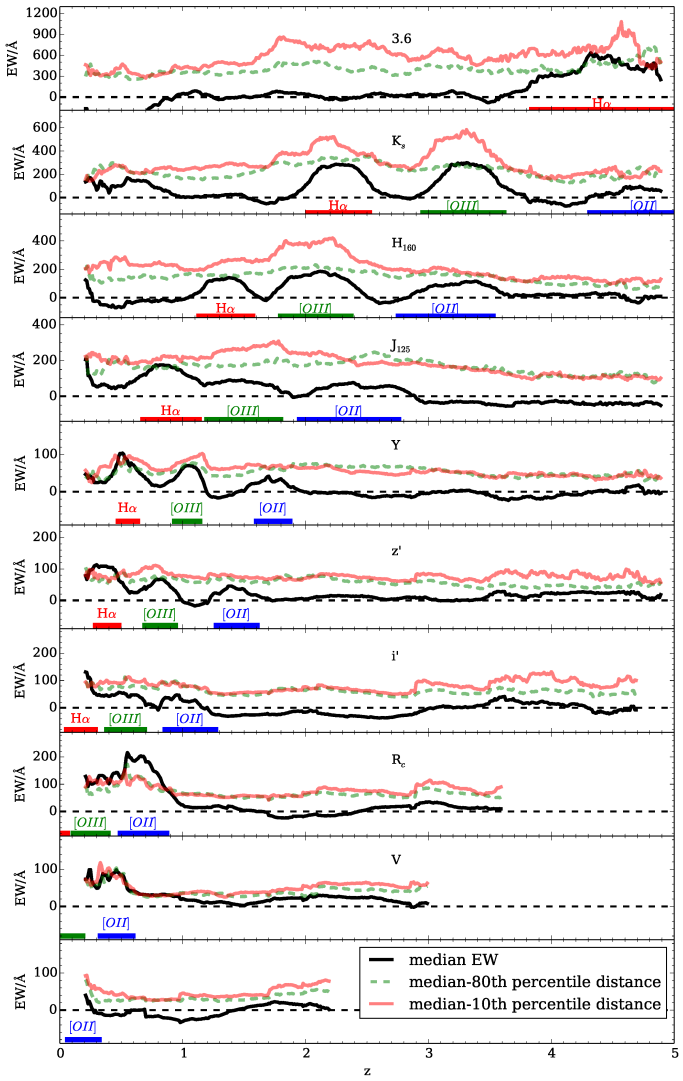

Figure 3.9: Median rest-frame equivalent widths as a function of redshift (black line) drawn from colour offsets using different bands, with expected line contamination ranges marked, for galaxies in the range $8.5<\log_{10}(M/M_{\odot})<11$ and $H_{160}<27$. The green dashed line shows the percentile distance between the 20th and 50th percentiles (negative EWs, only due to scatter) and the red line shows the inter-percentile distance between the 80th and the 50th percentiles (combining scatter and real EWs). Since the 80-50th p.d. gives the scatter naturally arising from the error in the photometry, discrepancies between both inter-percentile distances indicate asymmetries in the EW distributions, which are progressively higher for [OIII] and Hα contamination. The lines in each panel include values derived from the median of different baselines over different redshift ranges (see table 3.1), to reduce the effect of systematic errors from any individual baseline and get a global EW signal.

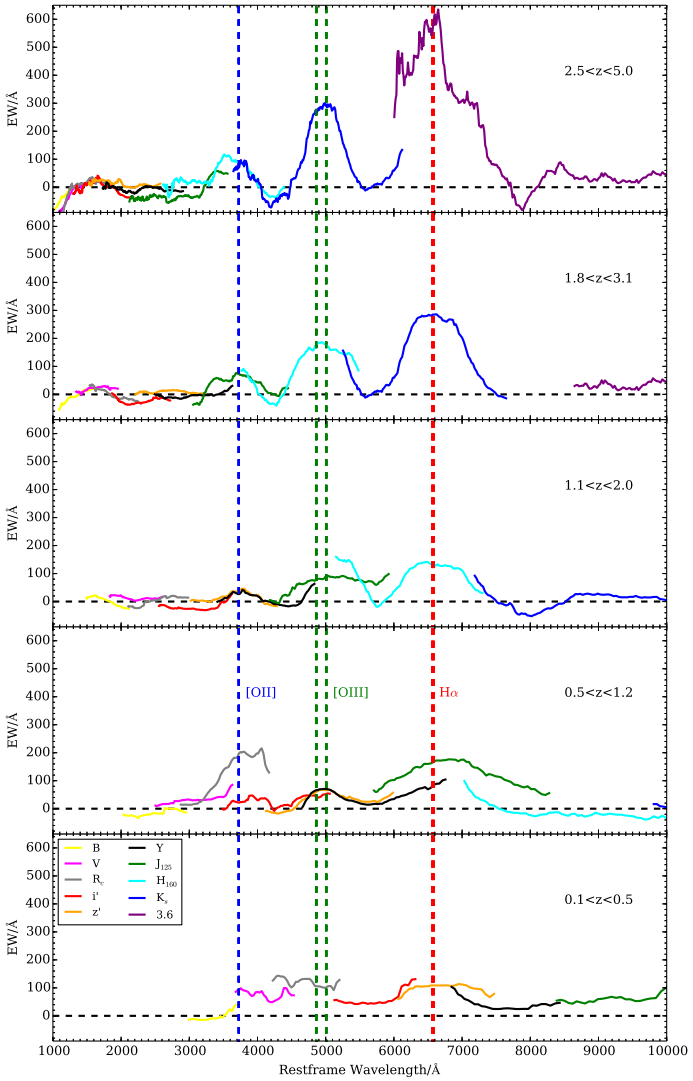

Figure 3.10: Signal of each emission-line as it passes through each filter (Fig. 3.9) now combined in rest-frame wavelength to show the evolution of the EW signal over five redshift ranges from z=0.1 to z=5. The left end of each curve shows the higher redshift values. The Hα and [OIII] lines go from residual (indistinguishable from noise and model systematics) at z<0.5 to being dominant at z>2.

Characterizing ELG Populations

EW evolution with redshift

The evolution of the median Hα EW_0 with redshift is shown in Fig. 3.11. The EW_0 values and evolution obtained with this method for the two different mass ranges presented ($8.5<\log_{10}(M/M_\odot)<9.0$ and $9.0<\log_{10}(M/M_\odot)<9.5$) are consistent with those measured in HiZELS (Sobral et al., 2014) and 3D-HST spectroscopy (Fumagalli et al., 2012) up to z=1.3 and extrapolations in mass and redshift up to z=2.3

$$EW_0 = 100\text{Å} \left(\frac{M}{10^{10}M_\odot}\right)^{-0.25} \left(\frac{1+z}{1+1.3}\right)^{1.75} \tag{3.7}$$

The highest redshift bin seems to depart from this relation, but that is likely due to the saturation of the gas supply and the approach of a maximum specific star formation. The time evolution seems to suggest that the maximum mean EW_0 (extrapolating to Age=0) would be between 400Å and 600Å.

In the second panel in Fig. 3.11 [OIII] shows lower EW_0 than Hα, but an increasing trend of EW towards the values of Hα for z>1.5. However, the median EW_0 of [OII] remains lower than either of the previous measurements, despite a steady increase towards high-z. This is evidence of an evolving [OIII]/[OII] ratio, which is an indicator in the global gas metallicity of ELGs. This would need further interpretation, however, as this ratio is also sensitive to the ionization parameter, which indicates the ionizing photon rate, indicating changes in the pressurization of the ISM or even a top-heavy IMF.

The two mass bins are shown in the time evolution panel, because the distance between the median EWs of the two adjacent mass bins is higher for [OIII] than for Hα, indicating a stronger powerlaw slope for [OIII]. [OII] does not show any mass dependence in the probed range.

A correction of +50 Å in H and -30 Å in J was applied, due to the continuum offset from 0 redwards of Hα (Fig. 3.9)

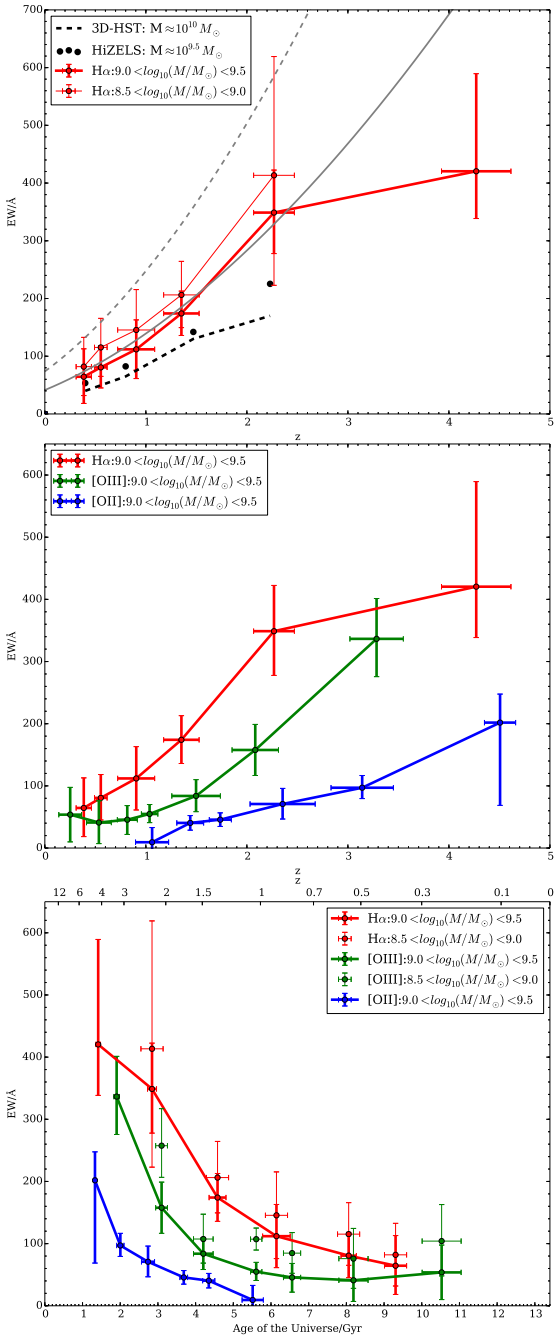

Figure 3.11: Top panel: Evolution of median Hα restframe EWs with redshift for galaxies brighter than H_{160}<27 for the stellar mass bins 9<$\log_{10}$(M/M$_\odot$)<9.5 (thick red line), and 8.5<$\log_{10}$(M/M$_\odot$)<9 (thin red line). Y-axis error bars are estimated from EW variation within a filter and r.m.s. between baselines in and x-axis error bars show redshift ranges used. The black lines show values from Sobral et al. (2014) ($\log_{10}$(M/M$_\odot$)=9.5) (dots) and Skelton et al. (2014) (10<$\log_{10}$(M/M$_\odot$)<10.5) (dashed). The grey lines show the extrapolated z-EW evolution from fits to the HiZELS and 3D-HST data for 10^8M$_\odot$ (dashed), and 10^9M$_\odot$ (full). Middle panel: Evolution of median EWs with redshift for all three lines for 9<$\log_{10}$(M/M$_\odot$)<9.5. Lower panel: Evolution of restframe EW with cosmic time.

ELG Fractions with redshift

Another property of the ELG population seen from the colour-colour plots shown in Figs. 3.5 and 3.6 is that the ELGs described here constitute a very large fraction (40%) of the objects present in CANDELS at z>1. I show the evolution of the fraction of ELGs (i.e. ELGs above an EW_0 of 150 Å divided by the total number of objects in redshift bin) in the top panel of Fig. 3.12 in the $9<\log_{10}(M/M_{\odot})<11$ mass bin from a small part of the galaxy population at low-z up to a prevalence of at least 50% for z>2. The middle panel in Fig. 3.12 shows the blue fraction only. This indicates that a large part of the ELG fraction evolution is driven by the decreasing number of red galaxies, towards higher redshifts. The results still show a much smaller fraction of [OII] emitters than Hα or [OIII], which occur in similar fractions of the sample. The lower panel shows the growing ELG densities up to $3\times10^{-3}\mathrm{Mpc}^{-3}$, increasingly affected by mass incompleteness at this mass range above z=3.5. The grey lines show the same ELG fraction measured for line-free redshifts and filter combinations to account for the background level of spurious ELGs created by redshift interlopers and data errors.

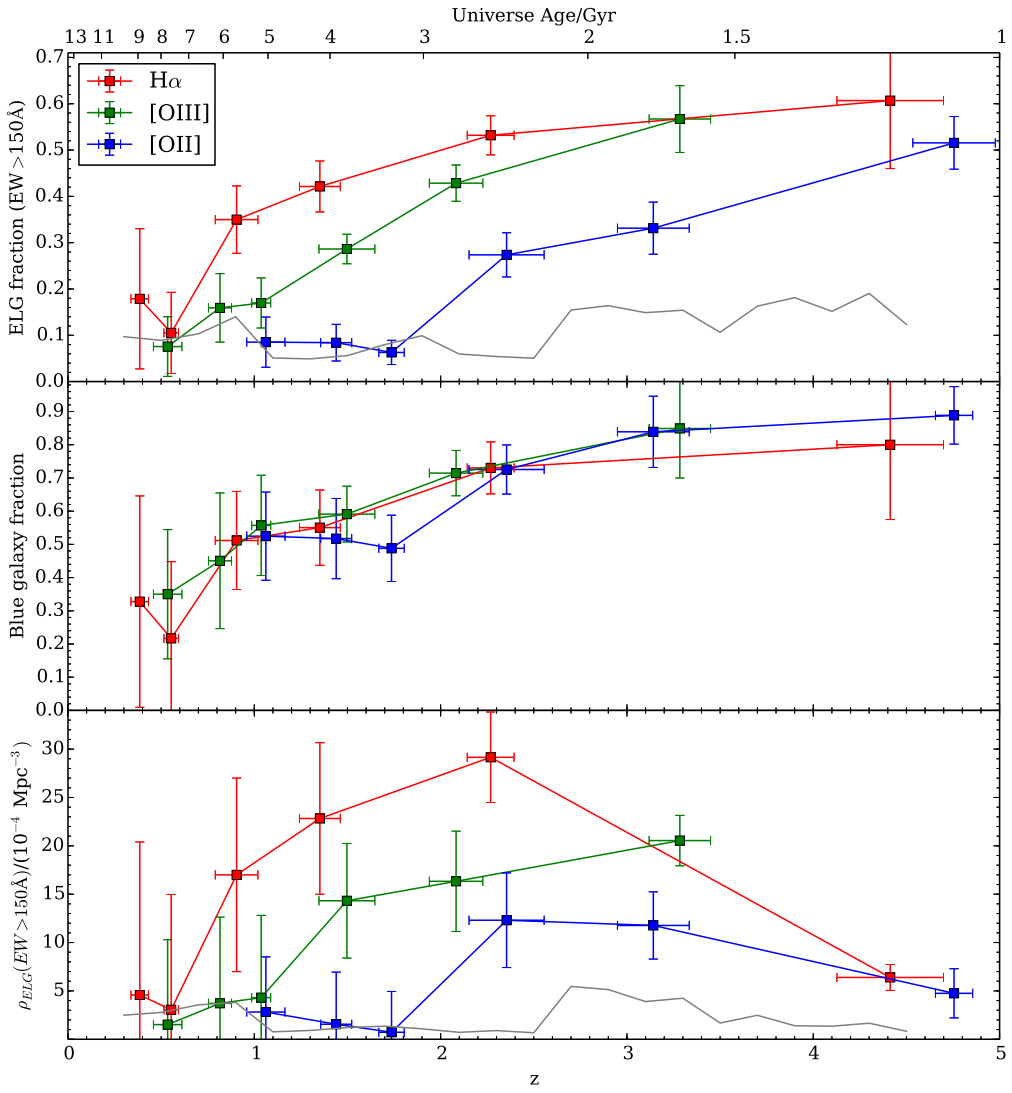

Figure 3.12: Evolution of the fraction of ELGs with EW>150Å (top) and respective co-moving number density of ELGs (bottom) for all three lines studied (red: Hα, green: [OIII], blue: [OII]) for 9<$\log_{10}$(M/M$_\odot$)<11. The ELG fraction was defined as the ratio between all ELGs selected in the z range shown and the total number of objects (regardless of colour) in each of those redshift windows averaged over multiple baselines. The middle panel shows the fraction of blue galaxies defined through the colour cut. Since H<27, the sample used is complete in the mass range to z=2 and declines from there, as the co-moving density plot shows. The grey lines show the fraction of objects also above 150Å but outside any of the expected line contamination ranges, due to errors in photometry or because of redshift interlopers. The full grey line shows the background ELG fraction for ELG-free bands. This figure shows how the fractions and densities of ELGs rise from low-z to high-z for these emission lines.

EW Distributions

A full description of the distribution of ELG EWs and its extreme values is difficult because there is a component of intrinsic colour scatter in the line-free continuum, which difficultates EW measurements below 150Å and there is a diagonal scatter (coordinated errors in the x and y axes) in the colour-colour plots (e.g. Fig. 3.5) introduced by errors in the normalizing band which can mimic extreme EWs for the dimmest objects. To deal with the first, it is useful to note that the colour scatter for objects around EW=0 is approximately symmetric, so one can subtract the negative EW distribution from the positive EWs to obtain a cleaner distribution. The distribution of EWs for line-free bands can be used as an estimate of the line-free distribution of EW errors due to colour errors.

The resulting distributions are shown in Fig. 3.13 ($9<\log_{10}(M/M_{\odot})<11$), which includes all three lines at different redshifts. Hα and especially [OIII] display long-tailed distributions for redshifts above z=1.4. Again the distributions remain at low EWs, with Hα starting to rise and show a tail extending into EW=500 at z=1.4, [OIII] even more extended, with a low co-moving density. [OII] remains lower throughout and never displays values as extreme as the other lines. At z=2.2 and above, the distributions of Hα and [OIII] EW_0 are very extended, well into 500Å, but further beyond that the errors seem to dominate the distribution.

Further evidence of the fact that the [OIII] distribution has a long tail can be seen in Fig. 3.9, where the inter-percentile distance between the 90th percentile and the median is compared with the inter-percentile distance between the median and the 10th percentile and once again there is a significant increase in dispersion towards the high-EW values of the distribution, at lower-z for [OIII], at z$>$ 2 also for Hα.

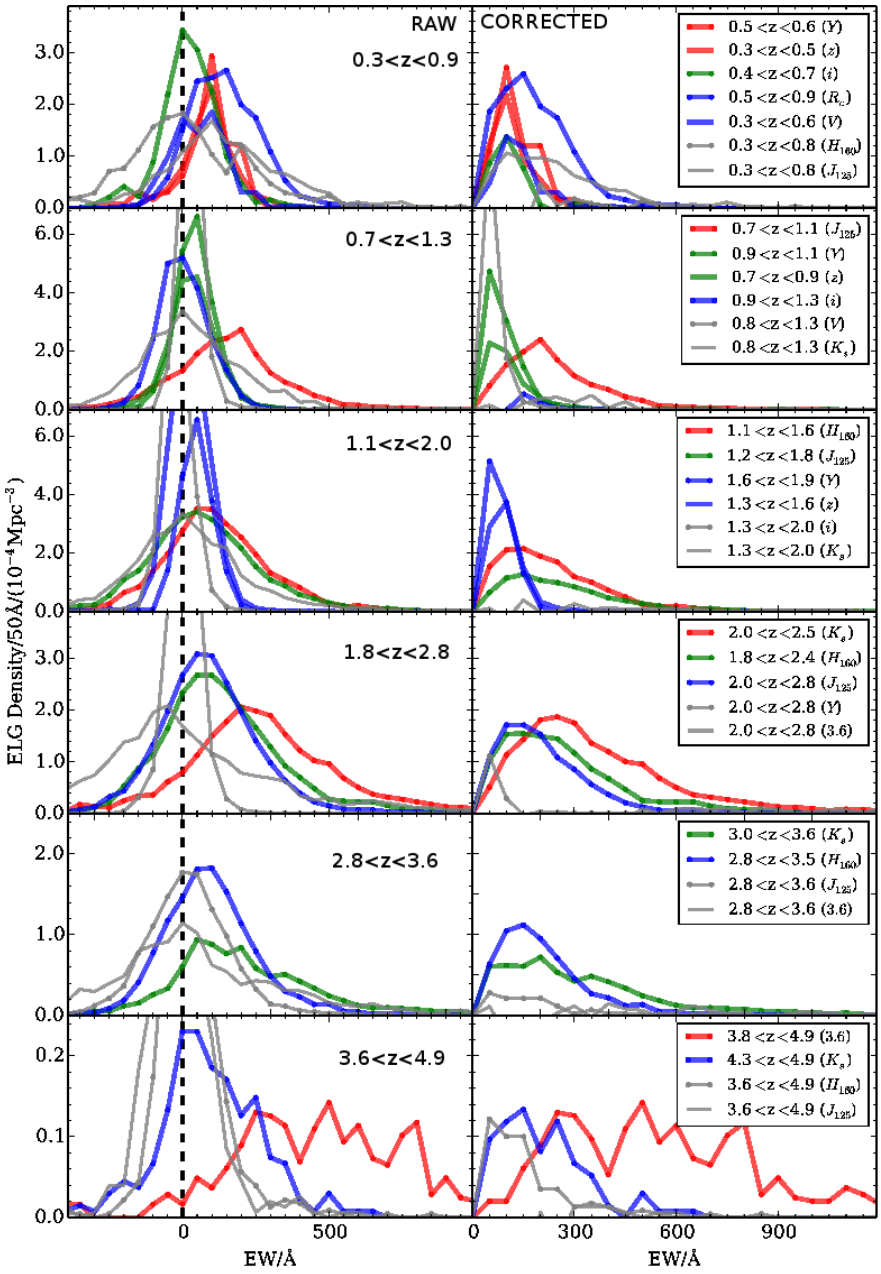

Figure 3.13: restframe EW distributions for different redshift ranges displaying emission-lines, with Hα in red, [OIII] in green and [OII] in blue. The signal expected from photometric errors only is shown in grey from line-free bands. This shows the evolution of strong ELG prevalence up to high-z, especially for [OIII], which tends to be a more extended distribution. The panels on the left show only the raw EW distributions, the panels on the right show the same distributions with the negative EWs subtracted to try to estimate a pure ELG EW distribution. While this figure shows that low-z EW distributions tend to peak at lower values, it is not just the median EWs that are low at low-z, but also the tail of the distribution increases towards higher z, especially for [OIII] (compare with Fig. 3.9).

Equivalent Width Error Distributions

By construction, the individual EWs produced with this method have higher errors than other methods. The errors can come from redshift uncertainty (dz=±0.1), photometric variations (∼0.1 mag), but principally the large dispersion in colour of SBMs (1 mag). If galaxies of a certain x-axis line-free colour may have scattered from any of the colours within the cloud of points of the SBMs, the estimation of the fiducial model from the median colour will create this large error. Therefore, while this method can produce statistical measurements of mean EW across redshift as was demonstrated in Figure 3.4, individual measurements have very large errors and the method as it is implemented now is not indicated for spectroscopic follow-up. A comparison of EWs cross-matched between 3D-HST spectroscopic EWs (Skelton et al., 2014) (uds_3dhst.v4.1.5.linefit.linematched.fits) and the photometric EWs in the present work is shown in Figure 3.14 only for galaxies that have the same redshift in both catalogues (dz=±0.1). It is also noticeable that spectroscopic EWs tend to be higher than photometric EWs, which means that the photometric EWs are not being artificially enhanced by colour errors, but in fact tend to be lower estimates. If this method can be improved to narrow the SBM cloud thickness, the photometric EW approach may still prove useful for spectroscopic follow-up.

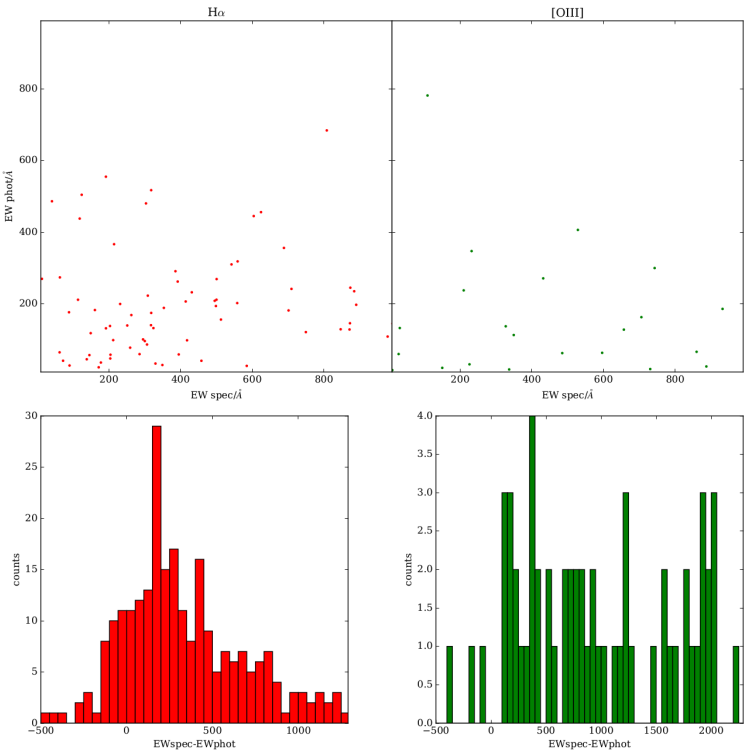

Figure 3.14: Comparison of spectroscopic (3DHST, Skelton et al., 2014) and photometrically-derived EWs (this work) for Hα (265 galaxies) and for [OIII] (62 galaxies). Galaxies are selected only for z>1, M>$10^8 M_\odot$, H¡27 and B-K¡2. The correlation between these values is poor and indicates errors of ±200Å in estimated equivalent widths.

Conclusion

Taking advantage of the fact that an array of exponentially declining SFR models with bursts reproduce well the colours of galaxies from z=0.1 to z=3, we measured the colour offsets between the CANDELS-UDS observations and these models to measure in redshift windows at each filter the strength of the only ingredient left out in the models: emission lines, obtaining the following results:

- This method efficiently traces the evolution of [OII], [OIII] and Hα from colour contamination from z=0.6 to z=5 and I measure the median equivalent widths in excess of 150Å for objects in those windows and their linear increase with redshift.

- The measured fraction by number of high-redshift ELGs is very high, rising from <15% at z<1 to >40% at z>2 for Hα

- The median [OIII] EW_0 increases to match Hα from z=1.5 to 2, whereas [OII] remains low (even after taking continuum evolution into account), indicating a possible evolution of ionization parameter in this redshift range.

- With increasing redshift, lower mass galaxies tend to display stronger emission lines, as expected from previous narrow-band and spectroscopic methods.

- ELG EW_0 distributions are skewed towards extreme equivalent widths for [OIII] for z>1 and for Hα for z>2. [OII] always has a symmetrical EW_0 distribution without extreme values until z=3 and even then they do not match the other two lines.

- This method is easily applicable to any new bands overlapping the field.

- The drawbacks are that individual measurements have poor signal-to-noise, since it works close to band detection limits, but statistical quantities can be recovered for the ELG population. This approach is also heavily dependent on the number and depth of available bands and their contiguity. The method depends on reliable photometric redshifts which require templates with emission-lines.

This systematic method will prove useful in probing the faintest galaxy populations reachable with virtually any deep panchromatic nearly-contiguous UV through MIR coverage for which reliable photometric redshifts have been obtained. It is also thought out to easily accommodate new bands of different widths between the baseline bands to provide extra constraints on high-z optical emission lines. It would also benefit greatly from added depth and coverage in bands from K to IRAC, especially if a very deep ($H_{5\sigma}$ >27) 5μm band was available), well into JWST territory.

Chapter 4

Global Properties of Emission Lines in CANDELS

This chapter shows how the method described in chapter 3 can be generalized and exploited to utilize the full deep multiband photometry provided by CANDELS to measure emission-line equivalent widths, line luminosities and line ratios. Statistical properties are determined and physical properties are derived from the observables to compare with and inform simulations of galaxy formation and evolution.

Multiband Photometry in the CANDELS fields

For this study, the most important factor in each field is how deep the K and IRAC bands are, since these are the limiting factors in determining z>1 EWs. Below z=0.9 the normalizing H band is line-free so the method in principle would capture ELGs better by taking advantage of the very deep HST normalizing band, using equally deep B or U as the reference band. However, the lower equivalent widths observed at z<1 compensate the gains in depth to limit EW measurements to only above 50Å for this method.

UDS

All CANDELS fields are processed in this chapter analogously to the Ultra-Deep Survey (UDS), already described in chapter 3. The UDS combines Subaru ground-based photometry (Suprime-Cam B, V, R, i, z), VLT HAWK-I Y and K_S with CANDELS-wide space-based HST WFC3 J125 and H160 bands and SPITZER IRAC 3.6 and 4.5 μm as described in Galametz et al. (2013), Fontana et al. (2014) and Ashby et al. (2013). The UDS is close to the celestial equator, so it is accessible to telescopes in both hemispheres. The sky coverage of the UDS is shown in Fig. 4.1. The depths at each filter and line contamination over redshift are shown in Fig. 4.2. The median colour offsets caused by emission lines are shown in Fig. 4.3, with zero offset for line-free redshift ranges.

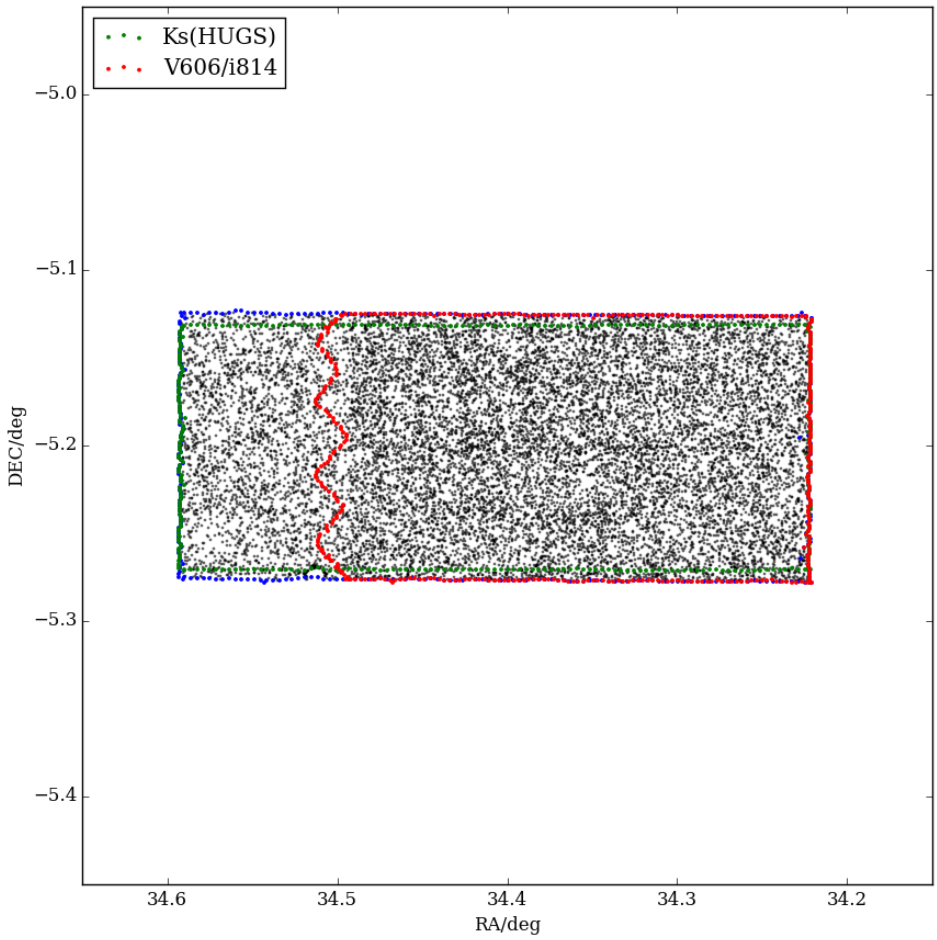

Figure 4.1: The multi-band coverage of the CANDELS-UDS field (201 arcmin^2). The outlines of all filters with consistent coverage are shown in blue. The red line shows the partial coverage of the V_{606} and i_{814} filters, which are not used for EW determination since they are too broad. The green outline indicates the VLT HAWK-I K_s-band coverage provided by the HUGS survey. All objects in the catalog are shown by the black scatter-plot.

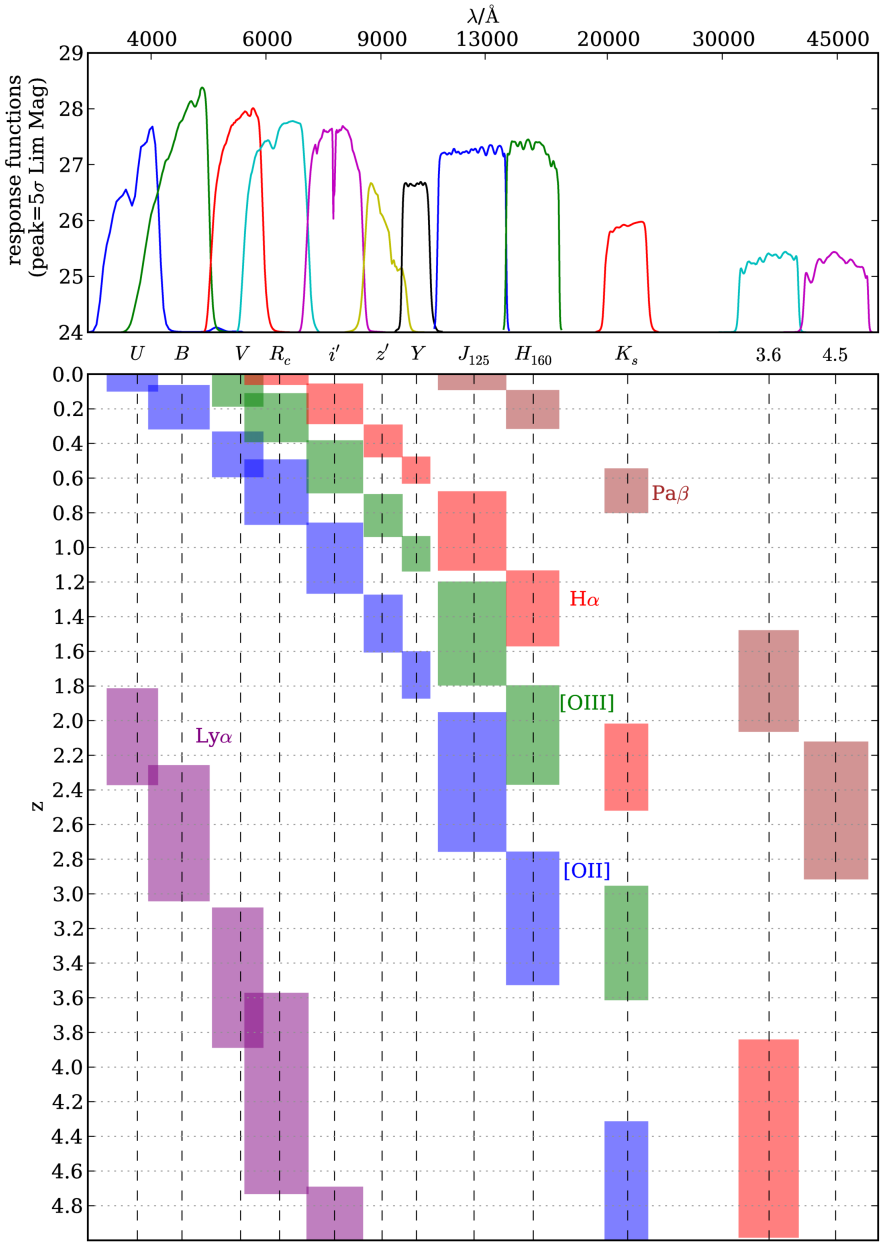

Figure 4.2: Top: Filter profiles for each UDS band used (λ scale is logarithmic) as shown in chapter 3, normalised to peak at each respective 5σ limiting magnitude. Bottom: expected redshift range for line contamination in each filter between its full-width at 40%-maximum for Lyα (purple), [OII] (blue), [OIII] (green), Hα (red) and Paβ (brown) up to z=5.

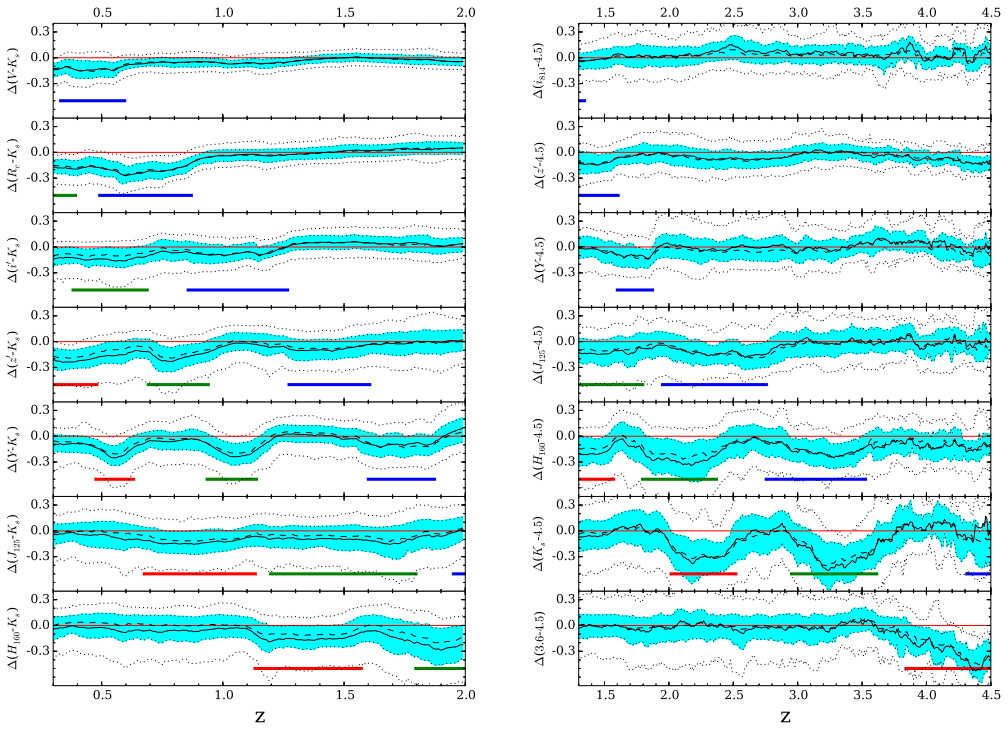

Figure 4.3: Distributions of colour offsets from median line-free model colour as a function of redshift in the UDS: average (full lines), median (dashed), 25/75th percentiles (blue regions) and 10/90th percentiles (dotted lines). Left: $z < 2$: B−K$_s$<2, H<25 selection, X−K$_s$ colours. Right: z>1.3, i'−4.5<2, H<26 selection, X−4.5 colours, with X any filter between the two baseline bands. (Red, Green, Blue) lines show the expected redshift range of (Hα,[OIII],[OII]) contamination.

GOODS

The Great Observatories Origins Deep Survey (GOODS) (GOODS-North and GOODS-South in opposite sides of the sky) relies primarily on the space-based HST photometry: ACS B435, V606, i775, i814, z850, WFC3 Y098 (only for GDS), Y105, J125 and H160, boasting the deepest IRAC 3.6 and 4.5 μm bands. This is complemented by the ground-based VLT HAWK-I K_S band for GOODS-S and SUBARU K_{MOIRCS} for GOODS-N. The galaxy catalog extracted from GOODS-S is described in Guo et al. (2013), also including the ultra-deep HUGS and SEDS photometry. Filter profiles, depths and line-contaminated redshift ranges are described in 4.4

GOODS-South Colour Offsets

The GOODS-S field includes the deepest photometry of all five CANDELS fields. Particularly, the K_s and IRAC bands reach 26 mag, so it is ideal for obtaining model-limited EW errors. This field also includes the HUDF, which provides better statistics at lower masses. For GOODS-S Y098 covers the northern third of the field, whereas Y105 covers the rest of the field (shown in Fig. 4.5). To adapt these fields to the existing analysis pipeline, B435 replaced B, V606 replaced V, i775 replaced i' and z850 replaced z'. These fields have no R band analog. Y098 and Y105 replaced Y_{HAWK-I}. The colour offsets caused by emission-lines are shown in Fig 4.6 for GOODS-S. Comparing with the UDS, the only zero-point adjustments needed were K_s:+0.09 mag, 3.6μm:+0.09 mag and 4.5μm:+0.08 mag. Colour scatter is smaller than for the UDS across redshift, indicating that when the errors introduced by the red bands are reduced, model scatter usually only produces colour scatter up to 0.2 magnitudes.

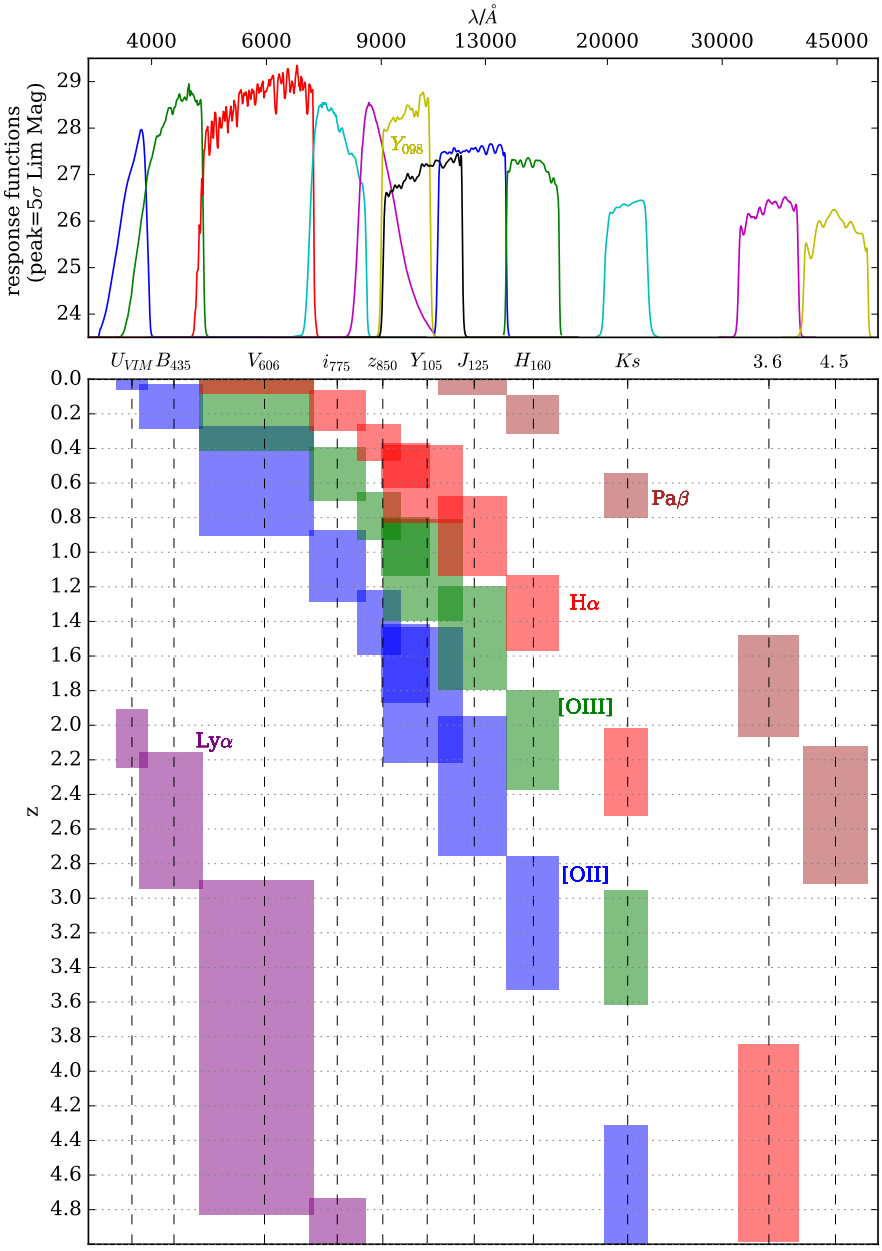

Figure 4.4: Top: Filter profiles for each GOODS band used (λ scale is logarithmic), normalised to peak at each respective 5σ limiting magnitude. Bottom: expected redshift range for line contamination in each filter between its full-width at 40%-maximum for Lyα (purple), [OII] (blue), [OIII] (green), Hα (red) and Paβ (brown) up to z=5. GOODS-South and GOODS-North share the same filters, except for the Y_{098}, and the HAWKI-Ks band in GOODS-S, which is a MOIRCS Ks band in GOODS-N. The available V_{606} and Y_{105} filters are broader than their UDS analogs and so less sensitive to emission lines. The GOODS-S has the deepest photometry in the IRAC bands (even 5.8μm and 8.0μm reach 24 mag).

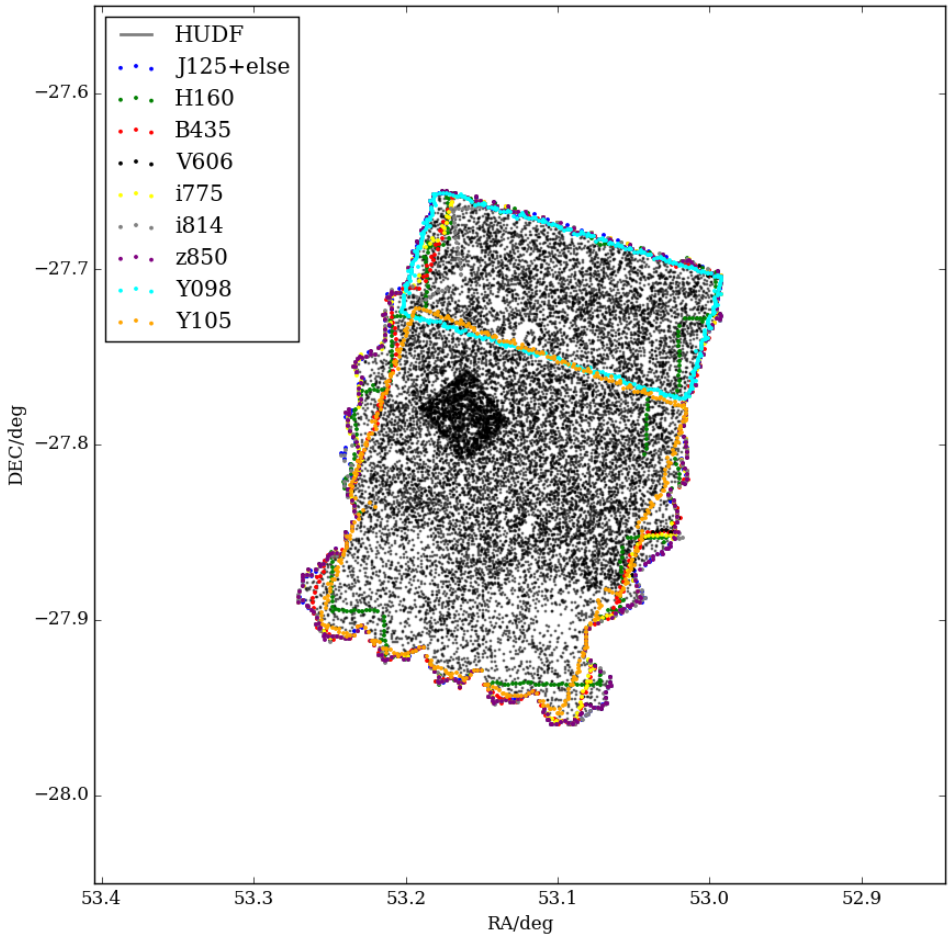

Figure 4.5: The multi-band filter coverage of GOODS-South (177 arcmin^2). There is some variation in the coverage provided by most filters, but generally they coincide. The key features are the complementary Y_{098} (northern 1/3 of the sky area) and Y_{105} (the remaining 2/3) coverage and the HUDF sub-field, which provides extra depth to extend the analysis to even lower masses. Object density is lower in the Southern region due to the shorter exposure time for the CANDELS-wide region. All objects in the catalog are shown by the black scatter-plot.

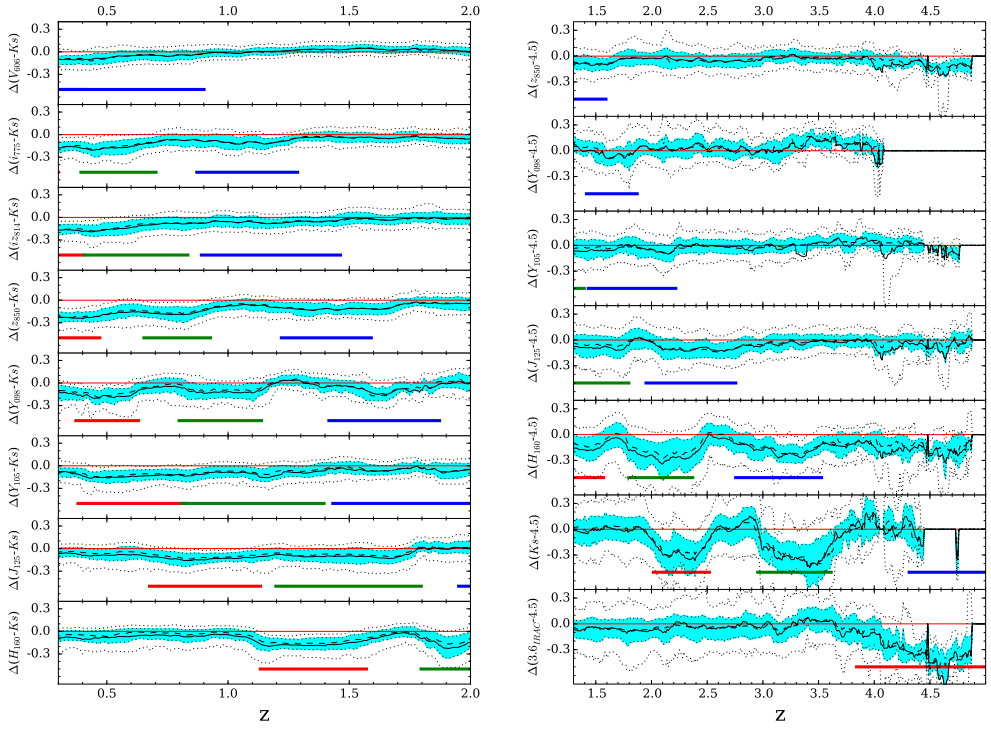

Figure 4.6: Distributions of colour offsets from median line-free model colour as a function of redshift in GOODS-S: average (full lines), median (dashed), 25/75th percentiles (blue regions) and 10/90th percentiles (dotted lines). Left: $z < 2$: B$-$K$_s$<2, H<25 selection, X$-$K$_s$ colours. Right: z>1.3, i$_{775}-4.5<2$, H<26 selection, X$-$4.5 colours, with X any filter between the two baseline bands. (Red, Green, Blue) lines show the expected redshift range of (Hα,[OIII],[OII]) contamination. All offsets are consistent with the ones observed for the UDS and colour scatter is smaller, because of the deeper K$_s$ (0.3 mag) and 4.5μm (1.6 mag) photometry.

GOODS-North Colour offsets

GOODS-N (sky coverage in Fig. 4.7) contains the original Hubble Deep field (HDF) and is generally analogous to GOODS-S, so it should provide good results as well. As Fig. 4.8 shows, this field produces the same ELG signal as GOODS-S and the UDS, but the errors are larger, especially when compared with GOODS-S. No dedicated GOODS-N CANDELS catalog has been detailed in the literature yet, but the 3D-HST description in Skelton et al. (2014) provides a good summary from which 5-sigma depths seem to be shallower than for the other fields. This does not include S-CANDELS (Ashby et al., 2015), which brings completeness up to 70% at 3.6/4.5μm=24 mag Ashby et al. (2015), in line with the rest of CANDELS-wide. The K_s photometry is described in Kajisawa et al. (2011): in the CANDELS-wide region K_s<23 and in the CANDELS-deep region K_s<23.

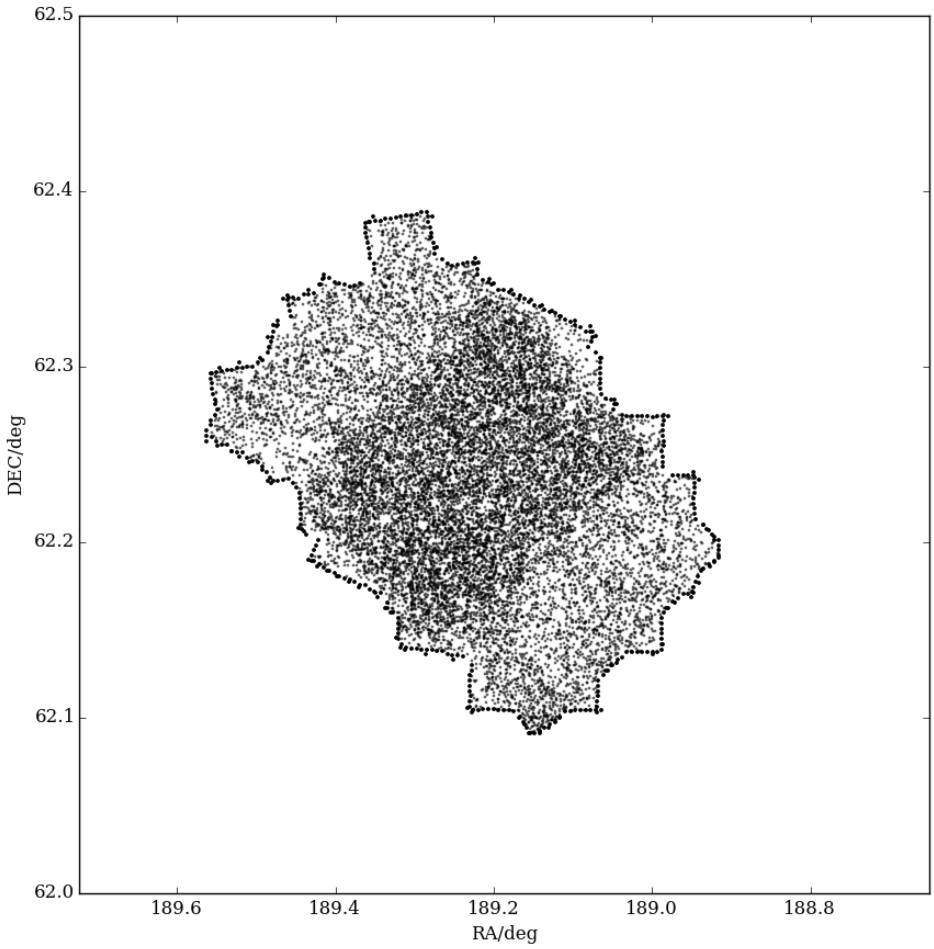

Figure 4.7: The multi-band filter coverage of GOODS-North (164 arcmin^2). There is some variation in the coverage provided by most filters, but generally they coincide. All filters cover the same sky region. All objects in the catalog are shown by the black scatter-plot. As in GOODS-South, CANDELS-deep stands out due to the higher object density against CANDELS-wide.

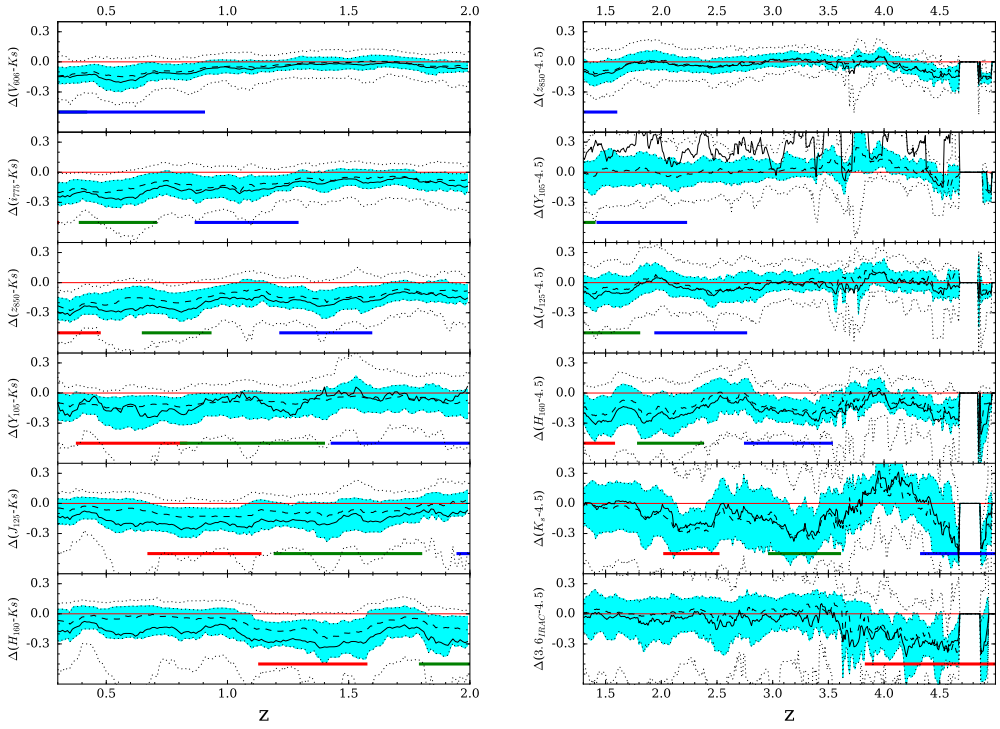

Figure 4.8: Distributions of colour offsets from median line-free model colour as a function of redshift in GOODS-N: average (full lines), median (dashed), 25/75th percentiles (blue regions) and 10/90th percentiles (dotted lines). Left: $z < 2$: B−K_s<2, H<25 selection, X−K_s colours. Right: z>1.3, i_{775}−4.5<2, H<26 selection, X−4.5 colours, with X any filter between the two baseline bands. (Red, Green, Blue) lines show the expected redshift range of (Hα,[OIII],[OII]) contamination. The colour offsets are consistent with the ones observed for the UDS and GDS, with some more scatter due to slightly shallower K and IRAC bands and minor zero-point adjustments.

COSMOS

The Cosmic Evolution Survey (COSMOS) is the field of choice for the deepest observations that require a large sky area (to access high masses, rare, or extreme objects). Its ample multiband coverage makes it ideal for a CANDELS sub-field. COSMOS an equatorial field, like the UDS, which facilitates the addition of coverage in all wavelengths by any ground-based observatory. The CANDELS photometry used for CANDELS-COSMOS is described by Nayyeri et al. (2017). COSMOS-CANDELS includes the same ground (Subaru) and space-based (IRAC, HST) bands as UDS with some additional CFHT/MegaPrime bands and UltraVISTA/WIRCAM Y and K_S (McCracken et al., 2012), with a field map shown in Fig. 4.9. This makes adaptation of the scripts I used to analyse UDS to COSMOS very straightforward, as can be seen by comparing Fig. 4.10 with Fig 4.2 for the UDS. COSMOS is the least useful field for this method as is, especially at z>2. Despite having very deep J and H, it is generally geared towards wide-field studies with the full COSMOS or z<1 studies which generally do not require deep photometry redwards of H. The consequence is that shallow K_s, 3.6 and 4.5μm bands increase errors, even if the signal is still there. z and Y are shallower too, but these have less impact, because they are never reference or normalizing bands. In practice, Fig. 4.11 shows that the colour offsets are measurable and consistent with the UDS and GOODS results, with the inevitable added scatter, particularly at z>3.

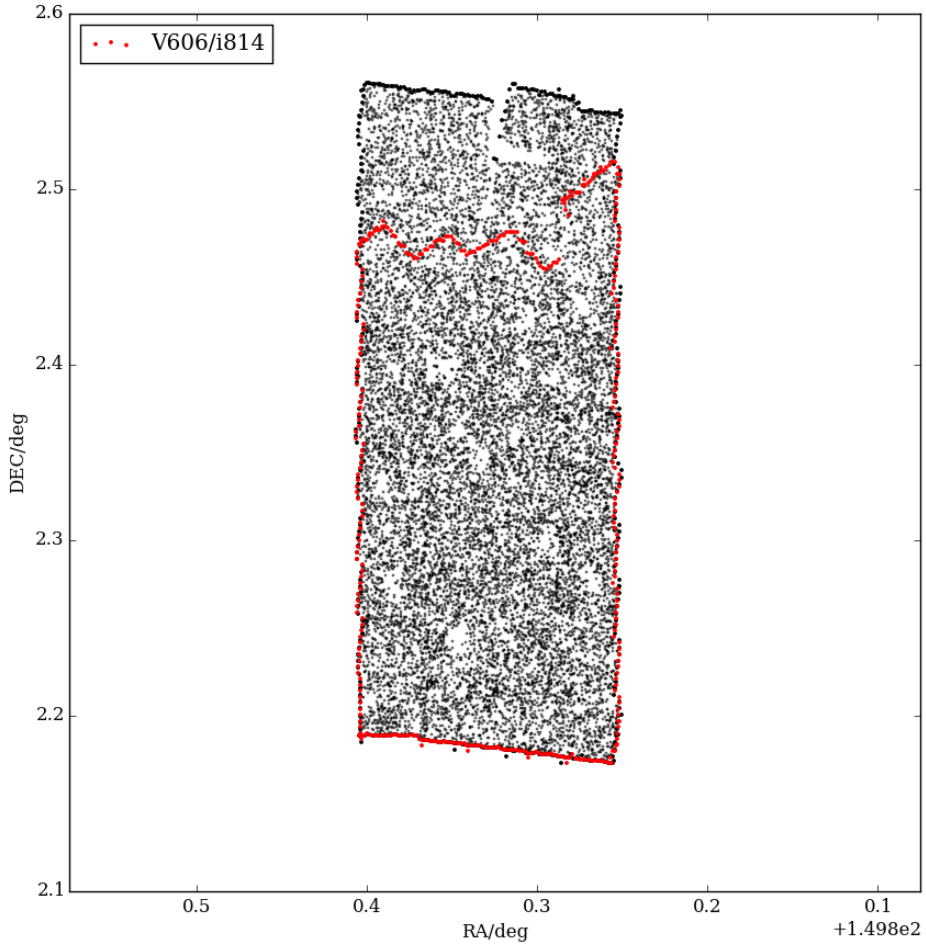

Figure 4.9: The multi-band filter coverage of CANDELS COSMOS (199 arcmin^2). There is some variation in the coverage provided by most filters, but generally they coincide. All filters cover the same sky region. All objects in the catalog are shown by the black scatter-plot. The V_{606} and i_{814} bands have incomplete coverage, but other bands can be used which are not as broad, so more sensitive to EWs, like the B,V,R+,i+,z+ Subaru bands, similar to those in the UDS.

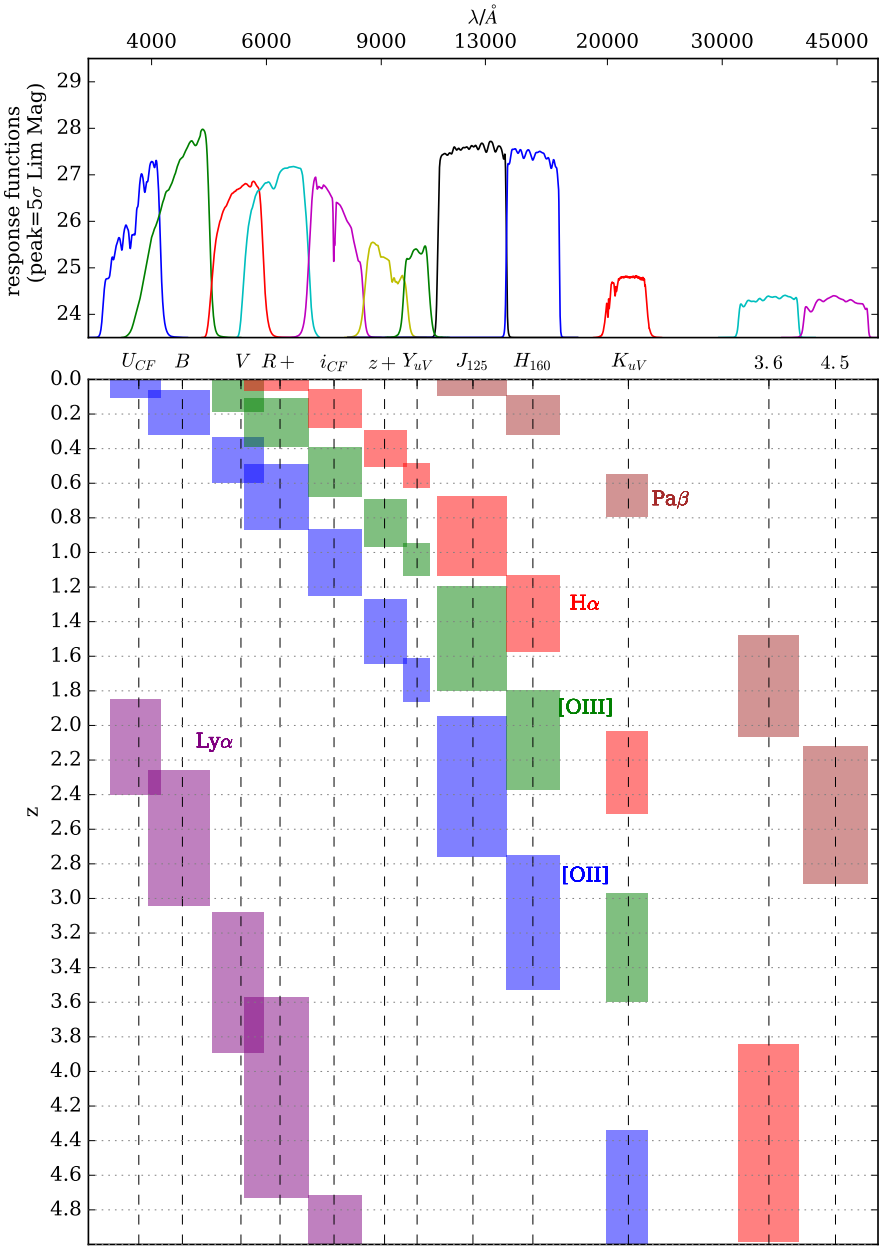

Figure 4.10: Top: Filter profiles for each COSMOS band used (λ scale is logarithmic), normalised to peak at each respective 5σ limiting magnitude. Bottom: expected redshift range for line contamination in each filter between its full-width at 40%-maximum for Lyα (purple), [OII] (blue), [OIII] (green), Hα (red) and Paβ (brown) up to z=5. This field is analogous to UDS but shallower in z, Y, K_s and particularly IRAC.

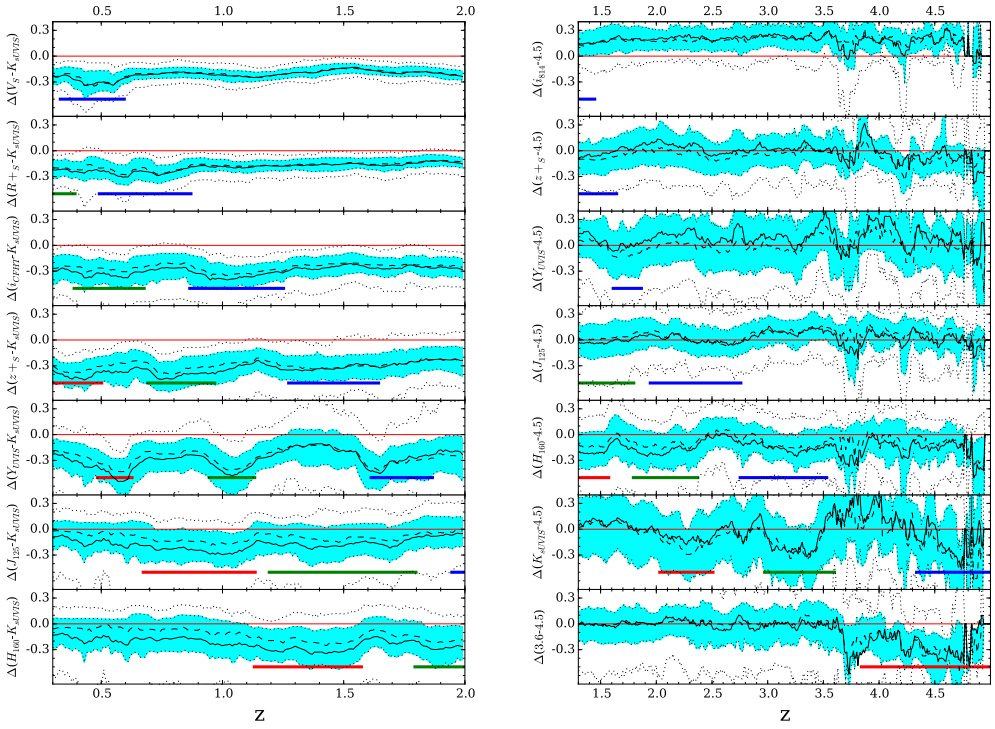

Figure 4.11: Distributions of colour offsets from median line-free model colour as a function of redshift in CANDELS COSMOS: average (full lines), median (dashed), 25/75th percentiles (blue regions) and 10/90th percentiles (dotted lines). Left: $z < 2$: B−K$_s$<2, H<25 selection, X−K$_s$ colours. Right: z>1.3, i$_{775}$−4.5<2, H<26 selection, X−4.5 colours, with X any filter between the two baseline bands. (Red, Green, Blue) lines show the expected redshift range of (Hα,[OIII],[OII]) contamination. Offsets are consistent with the ones observed for the UDS and GOODS, with necessary zero-point corrections in i, Y, J and K and additional noise for z>3.5 due to the lower 4.5μm depth.

EGS

Finally, the Extended Groth Strip (EGS) field includes the early and renewed space-based HST CANDELS bands along with IRAC, ground-based CFHT (G, R, i, z) and WIRCAM K. Of all field geometries, strip geometries are the most efficient at minimizing cosmic variance while keeping volume constant (coverage map in Fig. 4.12). In practice, the volume is still as limited as in COSMOS or UDS, but can stand alone against cosmic variance (spans 30 arcsec), while GOODS (spanning 16.5 arcsec) needs 2 fields (which together would also form a strip). As shown in Fig 4.13, EGS has the shallowest K_s/IRAC bands of all fields, so larger colour offset errors are expected (shown in Fig 4.14). There is no Y band, which not only reduces the number of available ELGs, but can also be decreasing the quality of redshift estimations. Despite all this, like with COSMOS, the median colour offsets remain steady and results are once again comparable to the UDS and GOODS-S with the appropriate zero-point corrections.

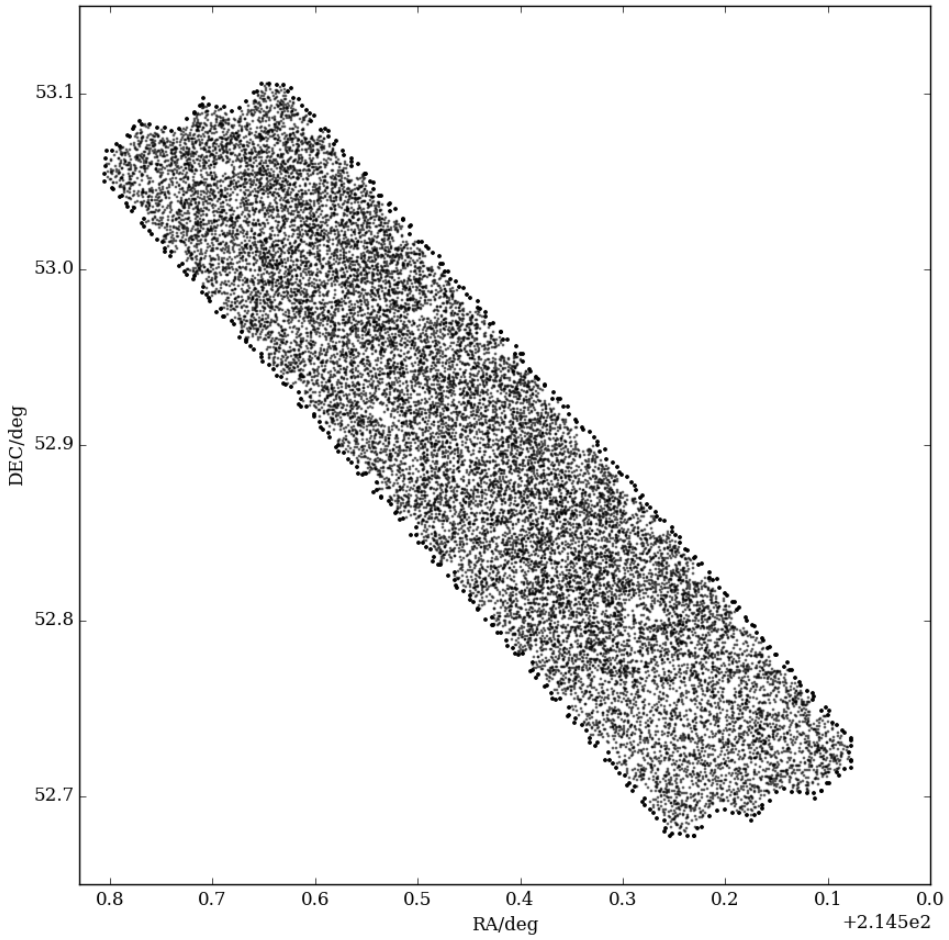

Figure 4.12: The multi-band filter coverage of the EGS (201 arcmin^2). All objects in the catalog are shown by the black scatter-plot. All filters cover the same sky region (trimmed).

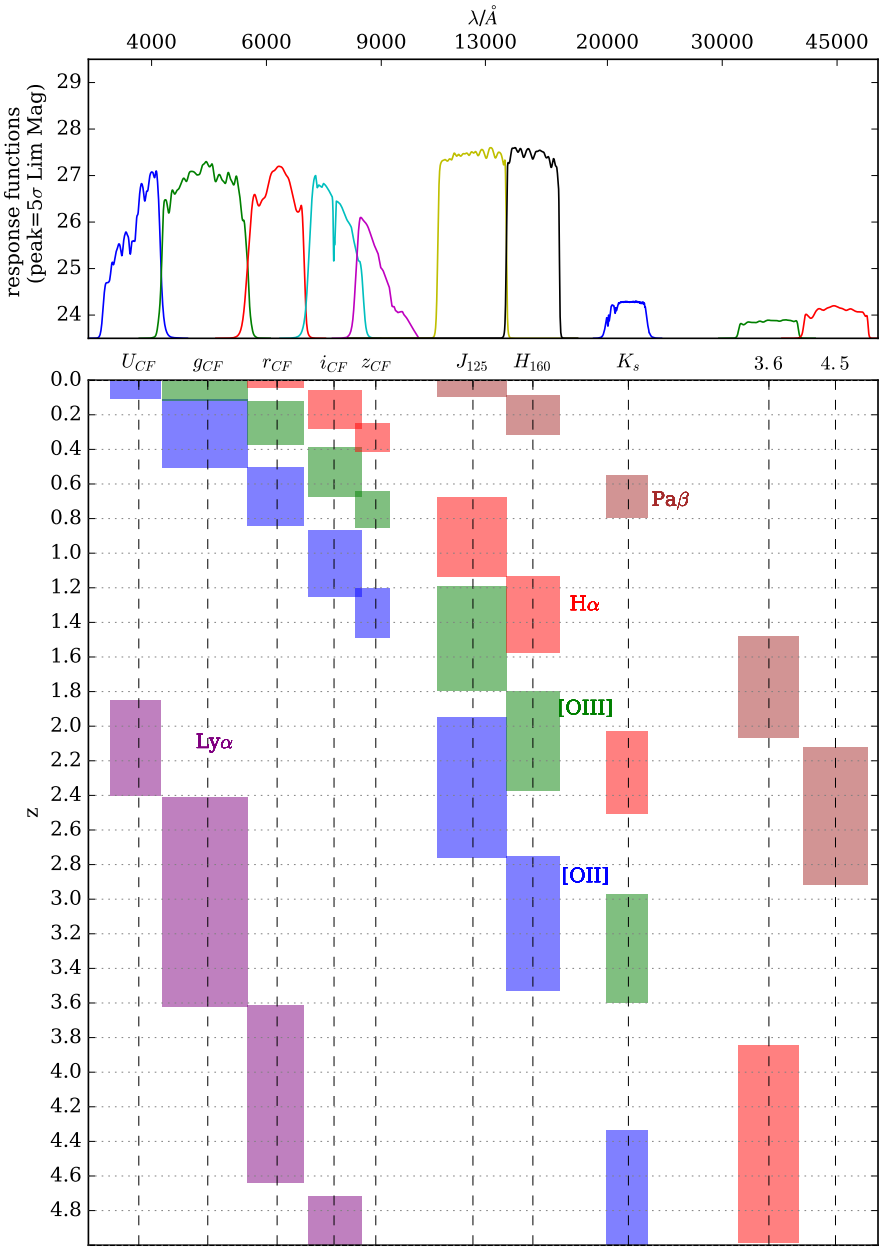

Figure 4.13: Top: Filter profiles for each EGS band used (λ scale is logarithmic), normalised to peak at each respective 5σ limiting magnitude. Bottom: expected redshift range for line contamination in each filter between its full-width at 40%-maximum for Lyα (purple), [OII] (blue), [OIII] (green), Hα (red) and Paβ (brown) up to z=5. The EGS has no Y band or B/V band, so g_{CFHT} was used to replace V. the EGS has the shallowest K_s and IRAC bands, so its scatter is expected to be worse.

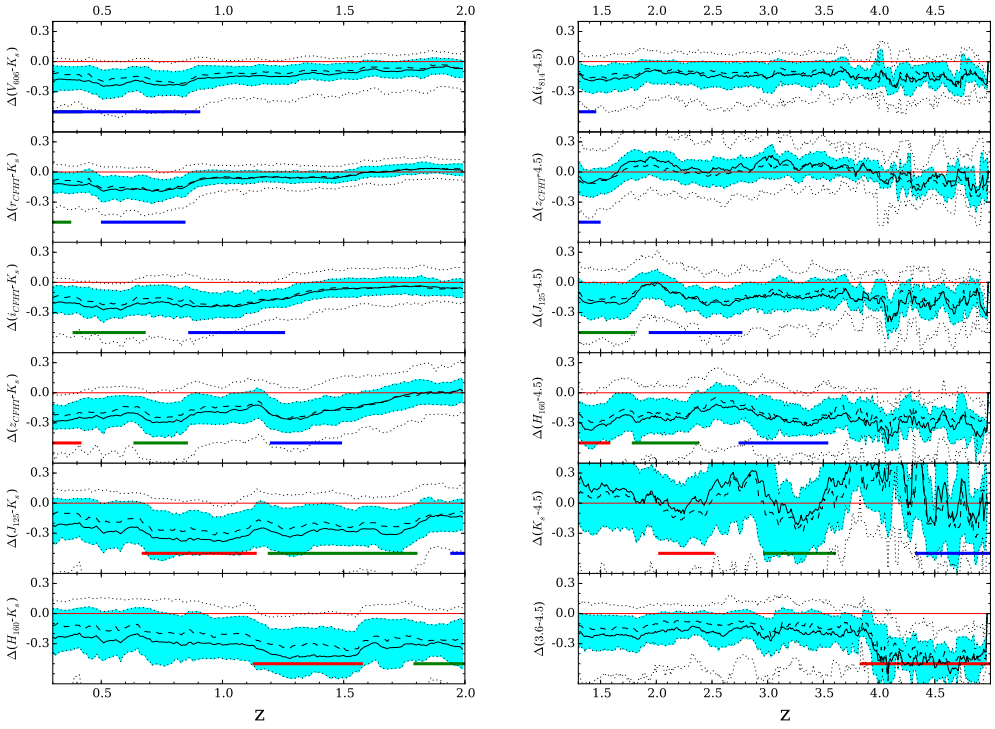

Figure 4.14: Distributions of colour offsets from median line-free model colour as a function of redshift in CANDELS EGS: average (full lines), median (dashed), 25/75th percentiles (blue regions) and 10/90th percentiles (dotted lines). Left: $z < 2$: B−K$_s$<2, H<25 selection, X−K$_s$ colours. Right: z>1.3, i$_{775}$−4.5<2, H<26 selection, X−4.5 colours, with X any filter between the two baseline bands. (Red, Green, Blue) lines show the expected redshift range of (Hα,[OIII],[OII]) contamination. All offsets are consistent with all other CANDELS fields. Redshifts may have a lower quality, which together with the shallow red bands causes the banding of the line emission signal at the highest redshifts in K−4.5, likely because a Y band is not available.

Multi-Field Results

To combine the five fields, I aimed to create analogous catalogs to those achieved in the UDS to apply the same pipeline as in chapter 3 to survey EWs across all the CANDELS fields.

For the sake of simplicity, only analogous filters to the UDS bands were used in this section (other shallower additional bands were available), but the method could be made flexible to include an arbitrary number of filters at various depths to be included in the summed field results, provided they also have deep K_s and IRAC coverage. The filter conversion is described in Table 4.1

Due to its construction, the method is limited by the depth of the reddest broad-bands, so it requires deep NIR/IRAC photometry in the CANDELS fields, especially UDS and GOODS-S).

A drawback of CANDELS is that it has a limited volume and only provides access to masses up to $\approx 10^{11} M_{\odot}$. This also makes individual fields more sensitive to cosmic variance, so the usage of multiple fields can mitigate this. Another problem here is combining the different fields, considering that they all have different characteristics and depths in some critical bands. This is especially the case for K and IRAC, which JWST will provide deep coverage for in the future.

The colour excess figures show that similar colour offsets are produced across all fields. The X-N colours in each field are then converted into EW_0 catalogs for all galaxies for at least the two essential baselines (B−K and i−4.5).

No masses have been provided for these objects, so mass was estimated from line-corrected H-band magnitudes 2.27, while assuming a constant mass-to-light ratio for ELGs. This is a good approximation for making mass cuts.

Each catalog was run through the same data reduction pipeline that was used for the UDS, but there are specifics which change from field to field which need to be dealt with individually. The main adjustment to make is zero-point corrections and in this area there is still room for improvement.

Stellar masses were available for UDS and GOODS-S (Santini et al., 2015). Masses for the remaining fields were estimated from a de-redshifted restframe V band using a constant ELG mass-to-light ratio calibrated to fit the masses in the UDS and GOODS-S (see section 2.6). It does not work for all galaxy colours, but is expected to work in the narrow colour range of ELGs. When a line is known to be contaminating the filter, fiducial colours are used to estimate the continuum.

In practice, the estimated masses were acceptable, but assuming a constant M/L ratio for ELGs can only work for simple sub-populations, so this simple mass estimation method (used to obtain the EGS, COSMOS and GOODS-N masses) was not used to estimate masses per se. It is good enough to make mass cuts (and look at mass-limited quantities between fields), but not to study the relations of mass with other quantities, so in the physical parameters section 4.3, only GOODS-S and UDS photometry was used. The UDS and GOODS-S were the only two fields with photometry redwards of the H-band of sufficient depth to provide reliable EW measurements at z>3.

This section shows the results of processing simultaneously the multiband photometry of analogous filters to obtain results that can be compared between fields and with more robust statistics wherever each field is available.

	UDS	GOODS-S	GOODS-N	COSMOS	EGS
0	U_{CFHT}	U_{VIMOS} (0)	U_{LBC} (0)	U_{CFHT} (0)	U_{CFHT} (0)
1	B_{SUB}	B_{435} (1)	B_{435} (1)	B_{SUB} (5)	G_{CFHT} (1)
2	V_{SUB}	V_{606} (2)	V_{606} (2)	V_{SUB} (8)	V_{606} (5)
3	R_{SUB}		-	R_{+} (7)	R_{CFHT} (2)
4	i_{SUB}	i_{775} (3)	i_{775} (3)	i_{CFHT} (3)	i_{CFHT} (3)
5	z_{SUB}	z_{850} (5)	z_{850} (5)	z_{850} (9)	z_{+CFHT} (4)
(6)	V_{606}	J_{140} (9)	J_{140} (8)	V_{606} (10)	J_{140} (8)
(7)			iz_{814} (4,4,11,6)		
8			J_{125} (8,7,12,7)		
9			H_{160} (10,9,13,9)		
10	Y_{HAWK}	Y_{098}+Y_{105} (7)	Y_{105} (6)	Y_{UVISTA} (14)	-
11	Ks $_{HAWKI}$	Ks $_{HAWKI}$ (12)	Ks $_{MOIRCS}$ (9)	Ks $_{UVISTA}$ (15)	K $_{WIRCAM}$ (12)
15			IRAC 3.6μm (13,11,18,19)		
16			IRAC 4.5μm (14,12,19,20)		

Table 4.1: List detailing the analogous filters used to run a general code to convert the five CANDELS field catalogues into a 12-band equivalent width catalog (U,B,V,R,i,z,J,H,Y,K,3.6μm,4.5μm). The band numbers in the left column are the original order of the UDS bands and the number for each of the bands used to convert the template spectra into colours. The filters used are shown for each field to the analogous band used in UDS. Band 6 is not used (normally V_{606}) so the J_{140} was placed there whenever V_{606} was used as the V band (GOODS). The same happened with Y_{098}. The numbers in parenthesis indicate the original order of those filters for each field when drawn from the catalogs (skipping one U band, if two are available).

Evolution of Equivalent Width with Redshift

Figure 4.15 shows that rest-frame EW can be measured for Hα across all redshifts up to z=5, [OIII] from z=0.3 up to z=3.6 and [OII] from z=0.7 up to z=5. Lower redshifts need models to focus on the strong 4000Å and Balmer breaks for estimating the [OII] continuum, but this work is oriented towards higher redshifts, so that was not attempted.

All lines increase in EW towards high redshift and there seems to be some variation of the equivalent width ratios, which is encouraging, as it indicates that there is some interesting physics to be explored (later in the chapter). This is also plotted with time to show that EWs seem to be converging to a maximum value above 500Å at t=0, which would be of interest to cosmology.

Figure 4.17 shows a comparison of the best-studied line (Hα) EWs in the literature from narrow-band HiZELS photometry (Sobral et al., 2014), 3D-HST spectroscopy (Fumagalli et al., 2012) and CANDELS-(UDS/GDS) excess broadband photometry like this work (Marmol-Queralto et al., 2015), but using spectroscopically-confirmed redshifts for added robustness. Each of these methods offers advantages and disadvantages, the most obvious of which is the depth and mass that they can reach. Spectroscopic methods reach higher masses than broadband methods (because it is difficult to reach the faint continuum in the low-mass objects). Therefore the spectroscopic EWs shown are lower, because they probe higher masses. The same happens for the Marmol-Queralto et al. (2015) sample, because even if it can go to higher redshifts, it still depends on spectroscopy, so the EW values shown are lower, but consistent with the measurements in this chapter at a different mass. Narrow-band methods can go lower in mass than spectroscopy, because the baseline continuum is accounted for by a broad-band, but not as deep as broad-band spectroscopy, because line information comes from a narrow-band, which collects less photons than a broad-band. On the other hand, EW errors are lower for narrow-band methods and even lower for spectroscopy, which requires less assumptions to measure an equivalent width and is adequate for characterizing individual galaxies.

To confirm that the EW drift of Hα is not just due to a loss of quiescent low-mass objects at high redshift, Figure 4.16 shows the mass distribution of each redshift bin for Hα: the low-mass bin $8.5<\log(M/M_{\odot})<9.0$ can only be used up to z=2.2, but the next $9.0<\log(M/M_{\odot})<9.5$ mass bin is reliable and loss of

objects is just limited by volume, not magnitude.

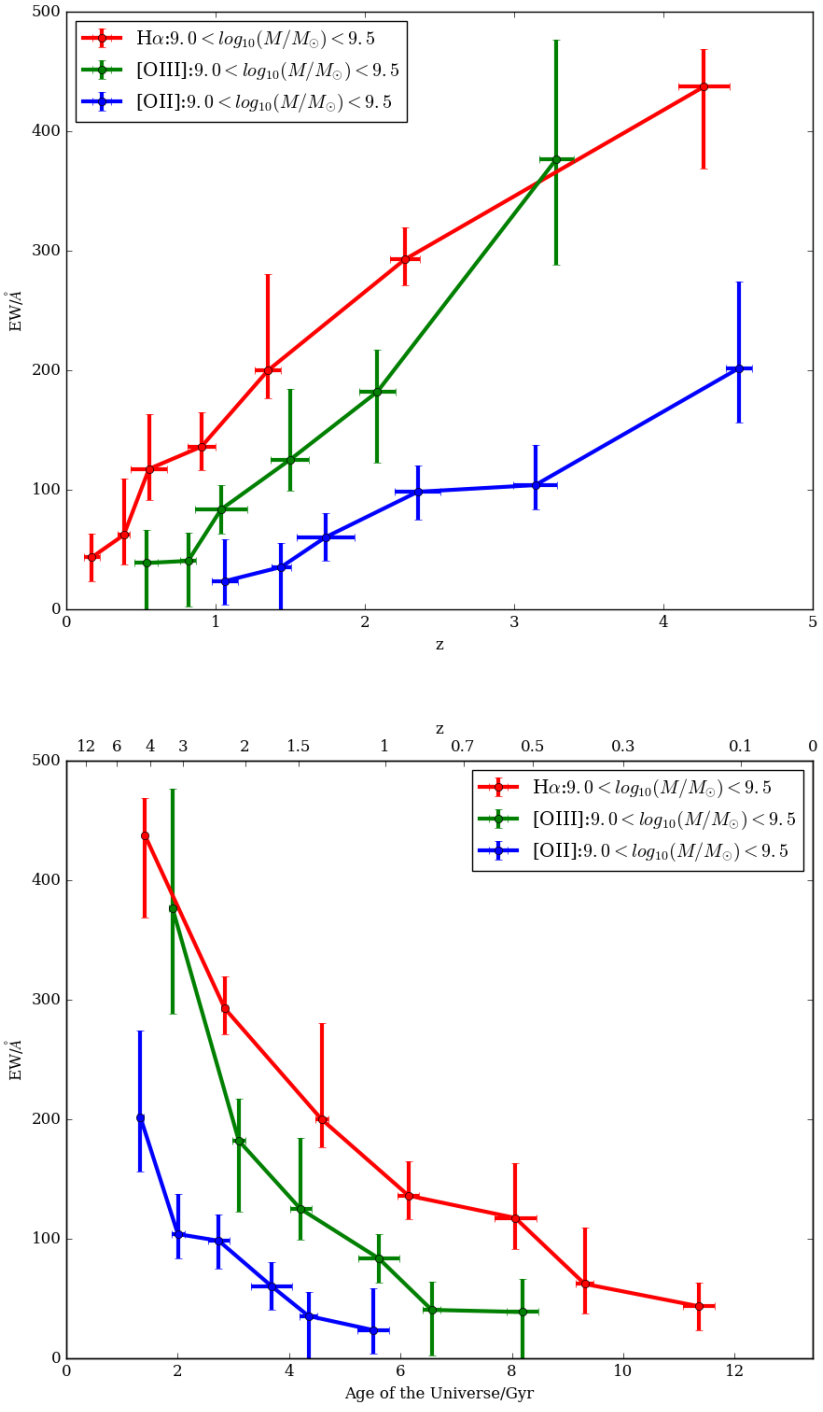

Figure 4.15: Median equivalent widths measured in all redshift windows using all the CANDELS fields to obtain Hα, [OIII] and [OII] equivalent widths, shown as a function of redshift and age of the Universe. The mass range for all bins is 10^{9}M$_{\odot}$ <M<$10^{9.5}$M$_{\odot}$. Vertical error bars are the r.m.s. of the standard deviation for each baseline colour included.

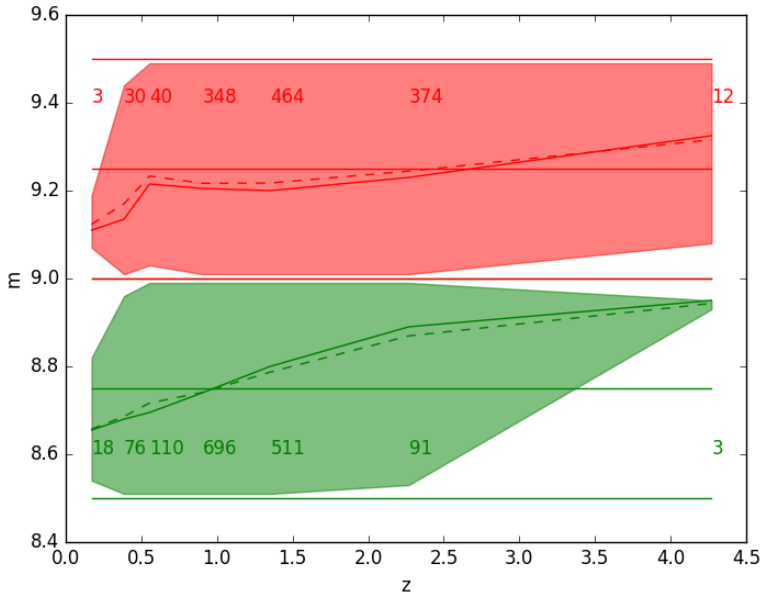

Figure 4.16: The median/average mass from CANDELS-UDS (Santini et al., 2015) in the mass bins selected at each redshift for two mass ranges (10^{9} to $10^{9.5}M_{\odot}$ in red), ($10^{8.5}$ to $10^{9}M_{\odot}$ in green), with the shaded region showing the minimum and maximum mass in the bin. The numbers are the number of galaxies in each bin. Whereas the high-mass bin stays practically complete up to z=4.5, the low-mass bin only goes up to z=2.2, so at these depths, ELGs can only be probed down to $10^{8.5}M_{\odot}$ up to z=2.2. This also shows that, despite having a reduced number of objects in the z=4.5 bin, this is not due to the mass binning, but the limited volume probed.

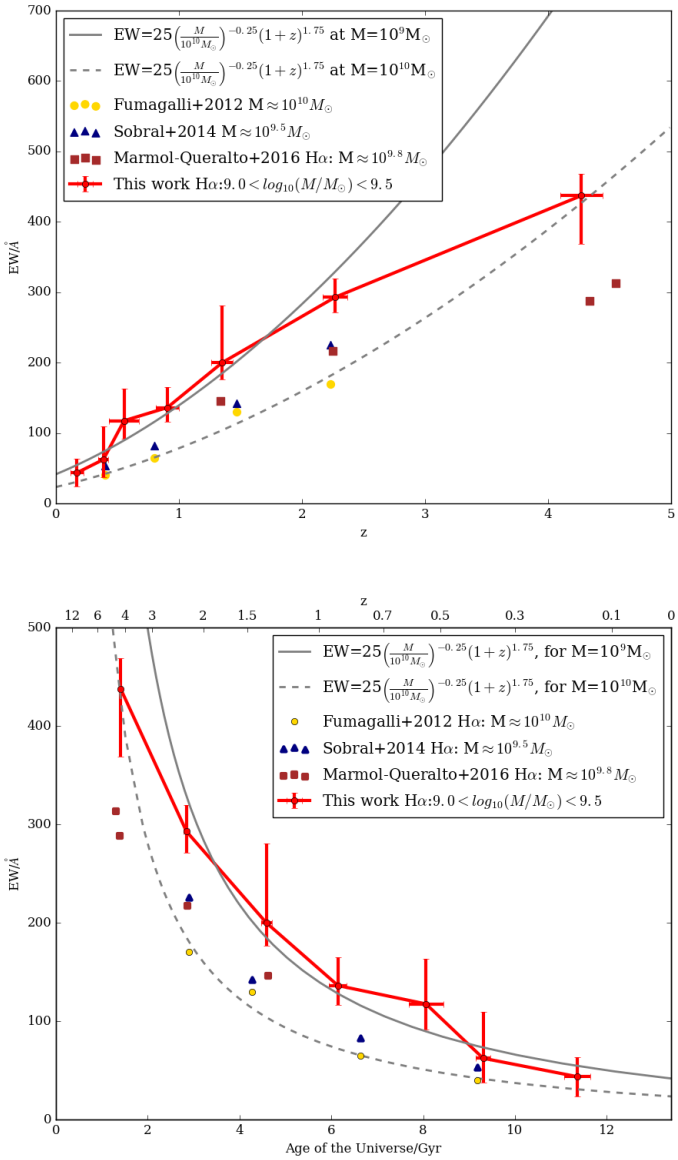

Figure 4.17: Median Equivalent Width of Hα over redshift and time, compared with the EW-z relations in the literature: 3D-HST (Fumagalli et al., 2012), HiZELS (Sobral et al., 2014) and CANDELS-UDS/CANDELS-GOODS-S (Marmol-Queralto et al., 2015). The grey lines show the mass-redshift relations extrapolated from HiZELS and 3D-HST data. The mass range for all bins is 10^9M$_\odot$<M<$10^{9.5}$M$_\odot$. The measured equivalent widths and fits are consistent up to z=2. Above this redshift the published relations break down and favour a slower evolution at higher redshifts. The maximum EW (Age=0) is in the range of 350-450 Å for Marmol-Queralto et al. (2015) for M$\approx 10^{9.8}$M$_\odot$ and 500-600Å for M$\approx 10^{9.3}$M$_\odot$ for this work. Even if there is a departure from z<2 in redshift dependence, these EW ranges can still accommodate the EW-mass dependence $\log_{10}$EW$\approx\log_{10}$M$^{-0.25}$.

Mass Dependence of Equivalent Width

The only fields with released CANDELS stellar masses from SED fitting are the UDS and GOODS-S, so these were used to plot log(EW) vs log(M_*) for all three lines in Figure 4.18. The first column shows Hα EW vs M in the different redshift bins derived from each filter window where the line is detected. Each figure compares for all lines the main coloured Red: Hα, Green: [OIII] and Blue: [OII] lines with the yellow line showing the functional fit EW(Hα)=$23\left(\frac{M}{10M_\odot}\right)^{-0.25}(1+z)^{1.75}$. This is to compare the dependence of [OIII] and [OII] EW dependence on mass with the well-known Hα standard. Hα EW seems to have the same slope in mass as the functional fit; even if the fit breaks down at z>2, the mass dependence is not affected. Still looking at Hα, the dashed line shows the 90th percentiles, in an attempt to understand the properties of the most extreme objects. Constant dispersion would indicate just the usual scatter of EW, increasing dispersion would indicate that the main sequence for which median EWs are measured has objects being boosted to large EWs. These objects converge with the main sequence scatter at large masses and low redshifts, but towards large redshifts there is a plume of bursty objects that progressively creeps to larger masses. The same is done for [OIII] and two results are apparent: [OIII] has a steeper EW-M dependence (especially at higher-z) and larger inter-percentile distances (distance between the 90th percentile dashed line and the full median line). The median [OIII] line EW is not stronger than Hα, but the most extreme objects in [OIII] reach above Hα, so bursty star formation must enhance [OIII]. [OII] looks at times like it is also steeper, but lower than Hα, yet the data look too scattered to be sure in this Figure. To take into account the growing errors from the normalizing band (typically the shallowest), the fiducial models are taken and scatter due to the normalizing band (the redder line-free band) is added to the colours. This produces a number of mock-ELGs and a distribution of N-band-induced errors. Still in this figure 4.18, EWs below the mock (grey) EWs are not reliable (they could still be correct). The same is done for the mock 90th percentiles (the dashed grey line). As a final check that the errors are correctly estimated, mock EWs were estimated from the noise in three line-free control bands. The distributions of errors generally follow those of the mock errors.

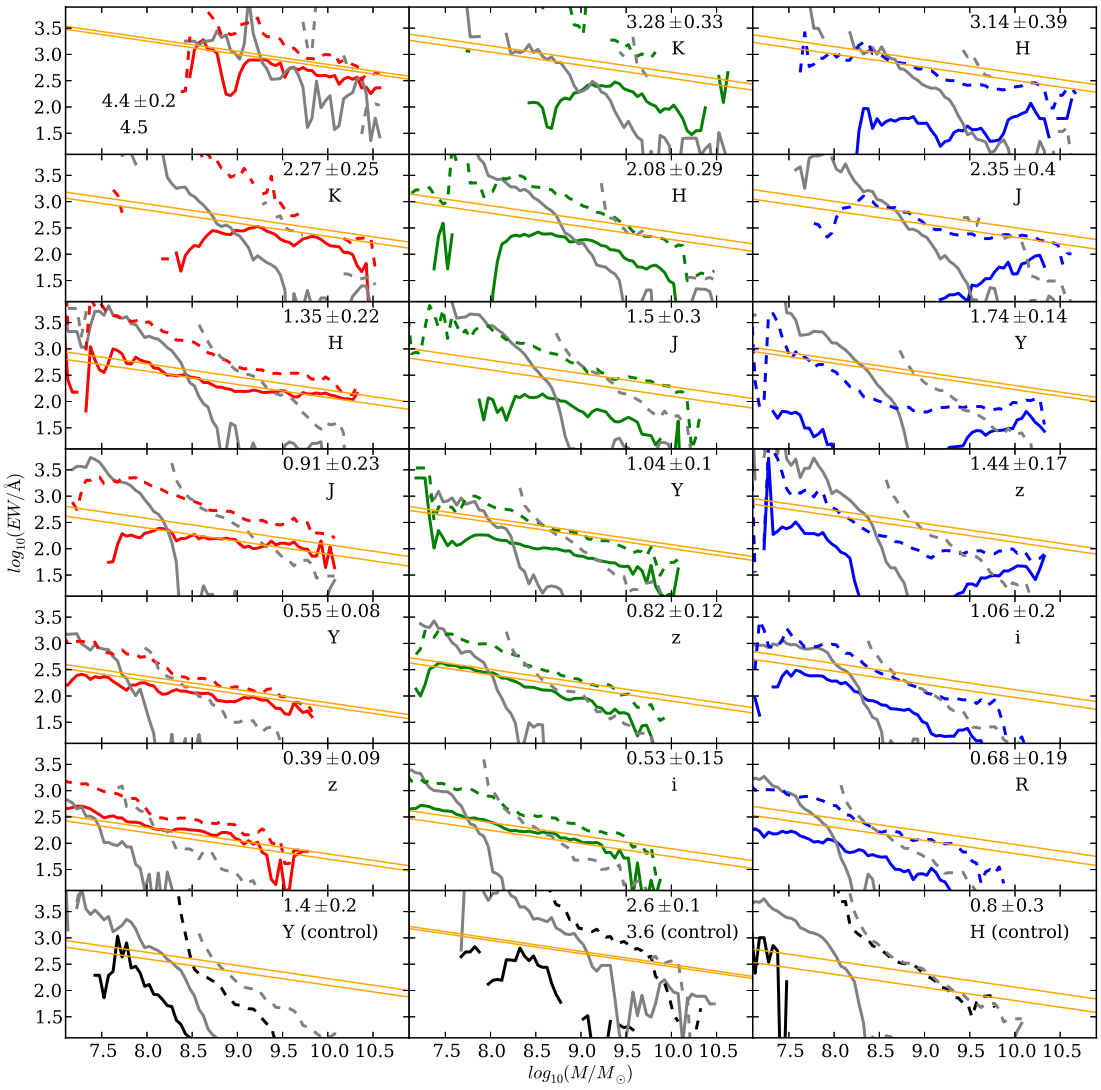

Figure 4.18: The median EWs as a function of mass for the three lines under study (Hα, red), ([OIII], green) and ([OII], blue). Each panel shows an increasing redshift bin upwards (as indicated by the numbers) at the filter indicated by each letter. The dashed versions of these lines show the 90th percentiles as a measure of dispersion. The yellow lines show the expected mass dependence of EW (Hα in all panels, for reference) as derived from a combined HiZELS and 3D-HST extrapolation equation: EW$\approx 23\left(\frac{M}{10M_{\odot}}\right)^{-0.25}(1+z)^{1.75}$. Finally, the grey lines show what the EWs as a function of mass would have been due solely to the errors in the photometry using this method (mainly from the K and IRAC bands). The point in mass where the grey lines (errors) intersect with the coloured lines (EW data) determine the lowest mass for which the EWs are reliably estimated versus mass. The figures show that Hα follows the mass dependence closely up to high redshifts, even if the normalization shifts (because the redshift dependence changes, as shown in the previous section). [OIII] also shows the same slope as Hα at low redshift, but shifts to a steeper dependence on mass at higher redshfits, including a larger distance of the 90th percentiles from the median (dashed line). The method seems to work at low-z for [OII], which seems to be slightly steeper than Hα, but very quickly the dependence on mass becomes at least flat or even negative.

Hubble Ultra Deep Field

Finally, before moving to the actual measurements of luminosity and SFR, a final check has been carried out, shown in Figure 4.19. The HUDF in GOODS is the deepest field of CANDELS and includes about 2000 galaxies (10× the CANDELS density). The unprecedented depth provides much needed statistics on low-mass galaxies to corroborate the results at the low-mass end. Figure 4.19 shows a side-by-side comparison of HUDF and GOODS-S-full (including HUDF), with even more extreme median EWs than GOODS-S, which can be read off and plotted against the existing data to provide an even lower-mass high-z limit ($10^{8.5}M_{\odot}$). Figure 4.19 shows that by selecting only the galaxies in the HUDF larger EWs are obtained, but due to the smaller number of galaxies errors in EW become larger (±100Å). The lower panel shows that the median EWs in the HUDF are on average higher by 50Å in Hα

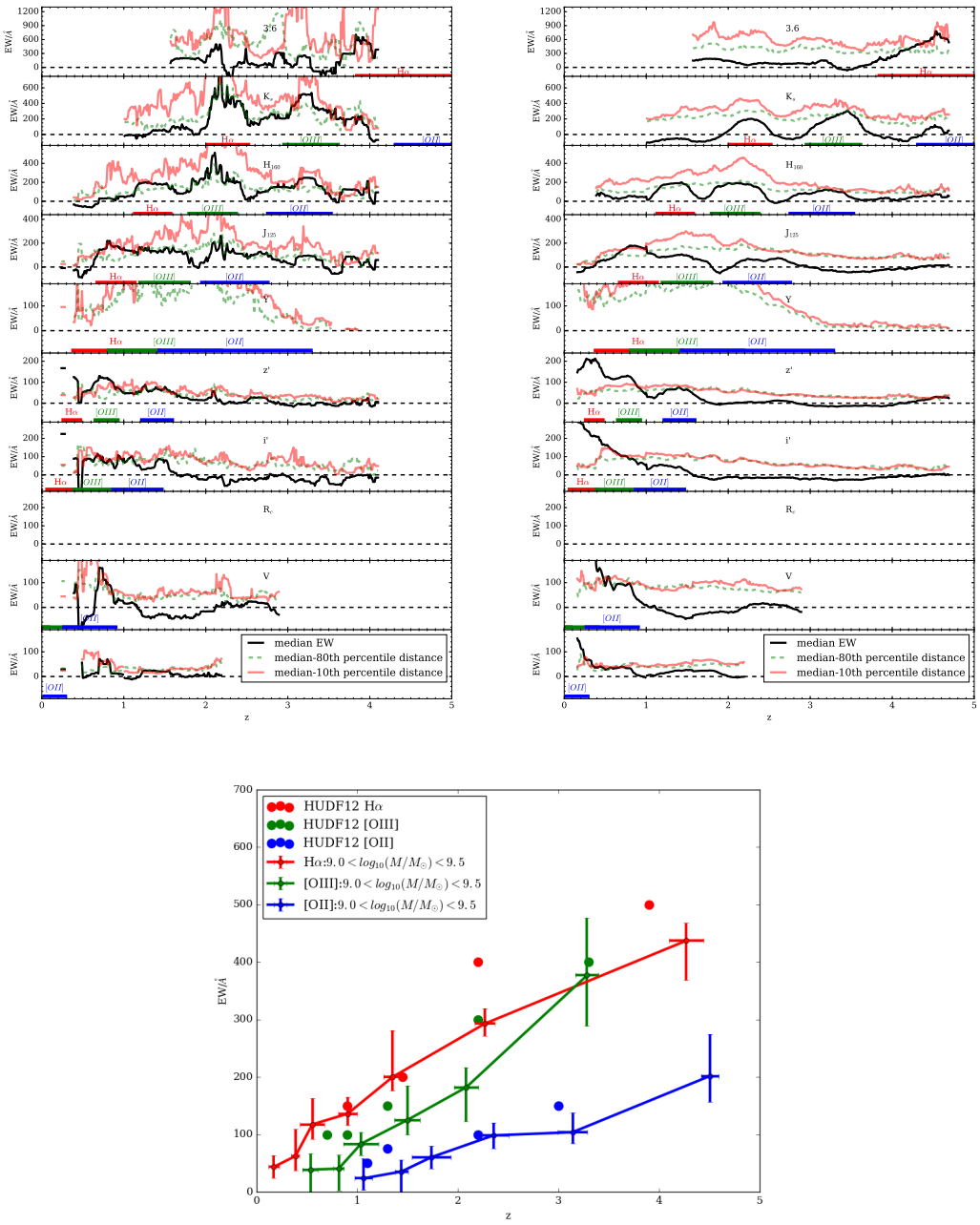

Figure 4.19: This figure shows that the HUDF preserves the same behaviour as its parent field GOODS-South, but produces pronounced ELG features (upper pannels), due to the higher sampling at a lower mass range (down to $10^8 M_\odot$ up to z=2 and $\log(M/M_\odot)$=8.5 at z=4). Note there are no galaxies left by z=4 (this could be due to a magnitude cut which was not used in the GOODS-S figure), but there is enough EW signal to identify the Hα excess at 3.6 μm. Lower-panel: HUDF-only median EW values added to the original EW vs z plot.

Physical Quantities

The objective in this chapter is to take a set of 5 observational quantities (z, Hmag, EW$_{H\alpha}$, EW$_{[OIII]}$, EW$_{[OII]}$) plus B−K colour and combine them to define a set of the same number of independent physical properties: (Age/time, mass, specific star formation, ionizing flux, and metallicity) plus τ_V. Other line-free bands will still contain some information about the stellar continuum, but it is important to note that, when broadbands are used, the visible spectrum boils down to 3 contaminated bands, one for each line, so an equivalent amount of information is available, now dominated by the nebular properties of the galaxy.

To analyse these equivalent widths and extract physical information from them, [NII] is assumed to be weak against Hα (less than 10%) because these two lines can not be separated. The same is done for [OIII] and Hβ, but the evolution of their ratio will be explored further, in section 4.3.5.

Line Luminosity

To convert the Equivalent Widths into rest-frame line luminosities, the total line flux is obtained from the specific line flux, all computed in the observed frame.

$$F_{line,obs} = EW_{line,obs} F_{\lambda,cont.} = EW_{line,rest}(1+z) F_{\nu,Xcont.obs} \frac{c}{\lambda_X^2} \tag{4.1}$$

The line-free continuum can be used directly from the X band if line contamination is weak. However, if the change in magnitude is large, this value must be corrected using the normalizing band N, which is line-free and the line-free fiducial colour X-N:

$$F_{\nu,Xcont.} = \frac{F_{\nu,Xcont.}}{F_{\nu,Ncont.}} F_{\nu,Ncont.} \tag{4.2}$$

The colour correction is better applied in the presence of deep K bands, when the errors caused by the K band are smaller than the magnitude changes introduced by the lines.

The expression for local specific continuum flux (at 10pc) is expressed in terms of apparent magnitude (N) and the distance modulus and the fiducial model galaxy colour:

$$-2.5 log_{10}(F_{\nu,Xcont.10pc}) = N + (X-N)_{fiducial} + 48.6 - \mu(z) \tag{4.3}$$

The total flux in the observed frame is then transformed into luminosity using the luminosity distance (for which a distance modulus μz is used). Redshifted total flux decreases due to photon redshifting by (1+z) and the decrease in the photon arrival rate by (1+z), but both of these (1+z) terms are absorbed into the luminosity distance, such that the usual relation holds:

$$L_{line} = 4\pi {D_L}^2 F_{line,obs} \tag{4.4}$$

Using the distance modulus, the absolute total flux (at D=10pc) is finally converted into luminosity by assuming that line emission is isotropic over a 10pc spherical surface.

ELG Luminosity over redshift

As shown in the previous section, by going deeper in magnitude than other methods, lower mass galaxies can be found, with higher, but similar equivalent widths. This approach is thus also probing lower luminosity objects than can be probed by narrow-band methods.

The luminosities of all three lines are shown in Figure 4.20. The EELG luminosities increase with redshift for each line. The gaps are due to the absence of a filter at that redshift. Near the filter edges there is a loss of objects and luminosity is slightly decreased as the line partially enters and exits each filter's corresponding redshift range. The general trend from the figure is that at z=0 luminosities are similar for all three lines at each mass bin (luminosity decreases with mass, as expected), but the slope of the luminosity-redshift relation increases towards lower masses. $L_{[OII]}$ increases faster than $L_{[OIII]}$, which itself increases faster than $L_{H\alpha}$ only for M$\approx 10^9 M_\odot$. Interpreting the Hα luminosity as a direct result of star formation rate, this is interpreted as a rising mean star formation rate from $0.1 M_\odot$/yr at z=0 for a $10^8 M_\odot$ galaxy, which increases 100 times up to z=4 for all masses and lines. Apart from small corrections discussed later, all lines scale directly with SFR, the source of ionizing photons. Furthermore, the values obtained for luminosity broadly agree with those in the literature (Sobral et al., 2014) for Hα at z=0.7 and z=2.2.

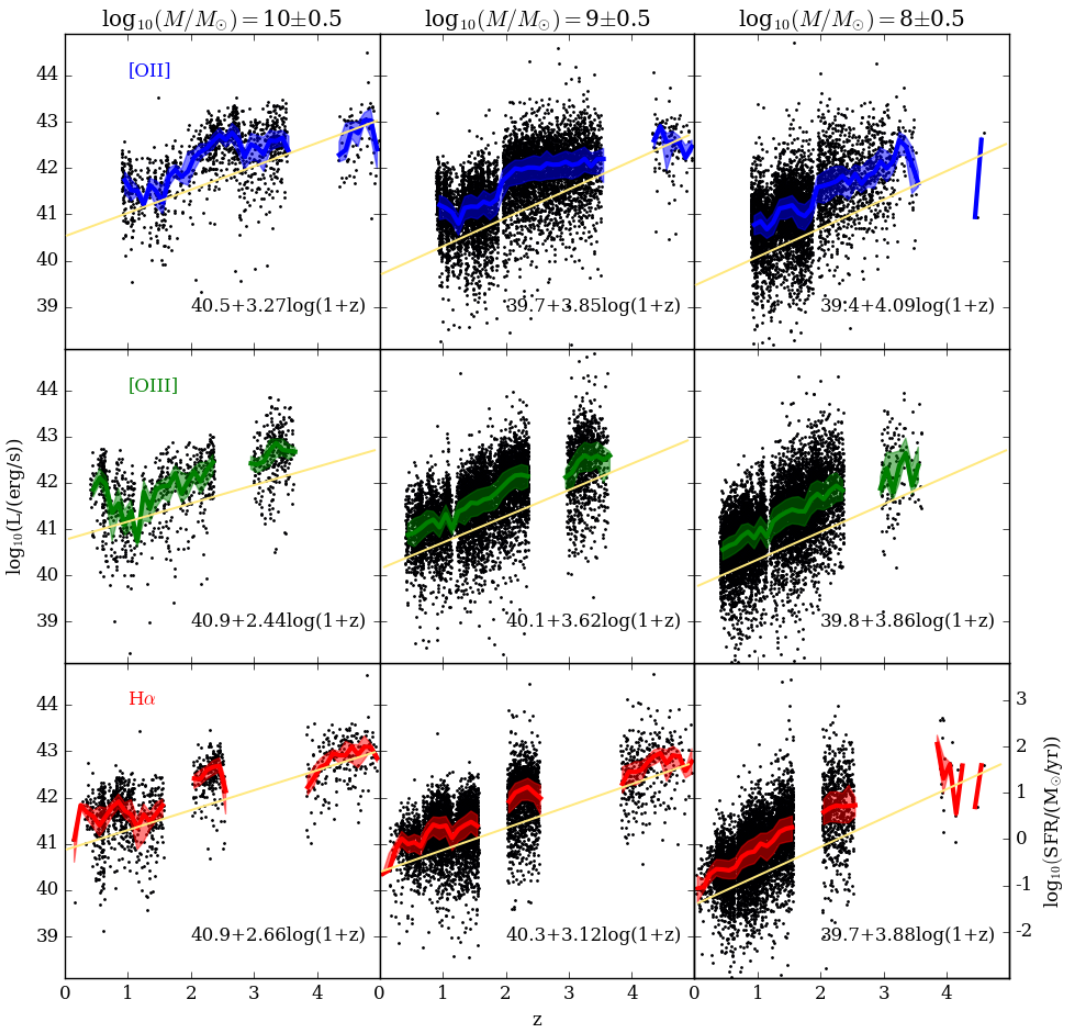

Figure 4.20: Evolution of line luminosity with redshift for Hα, [OIII] and [OII] for 3 mass bins. The central line shows the median luminosity and the shaded regions show the 32nd and 68th percentiles. The values on the graph show an additional (not plotted) least-squares fit in terms of $\log_{10}$(1+z). All luminosities increase with redshift, with a steeper dependence and lower luminosity at lower masses. Comparing lines, Hα and [OIII] have similar z=0 extrapolated luminosities, with [OIII] showing a steeper or similar dependence on redshift than Hα except in the high-mass bin. [OII] always evolves faster, but at all masses it starts out from lower luminosities and starts to catch up by z=4.

Dependence of ELG Luminosity on Mass

To detail how the luminosity depends on mass at different redshift, figure 4.21 shows that median luminosity increases smoothly with mass. This is a manifestation of the main sequence of galaxy formation.

To summarize these results, a functional fit for L=(1+z)$^{a+log_{10}(M)b}$M^{c} for each line (equivalent to a multilinear fit in log(L) vs log(M) vs log(1+z)), as a power-law, with a redshift dependence that increases itself with mass:

$$L_{H\alpha} = 2.0 \times 10^{40}(1+z)^{3.2-0.6log_{10}(\frac{M}{10^9 M_\odot})} \left(\frac{M}{10^9 M_\odot}\right)^{0.45} erg/s \tag{4.5}$$

$$L_{[OIII]} = 1.2 \times 10^{40}(1+z)^{3.6-0.3log_{10}(\frac{M}{10^9 M_\odot})} \left(\frac{M}{10^9 M_\odot}\right)^{0.33} erg/s \tag{4.6}$$

$$L_{[OII]} = 5.0 \times 10^{39}(1+z)^{3.7-0.3log_{10}(\frac{M}{10^9 M_\odot})} \left(\frac{M}{10^9 M_\odot}\right)^{0.45} erg/s \tag{4.7}$$

These fits hold confidently for blue (B-K<2) EELG populations and most favourably at z>0.7 when the lines are the strongest. At low redshifts the continuum spectrum dominates the signal and features like the 4000Å and Balmer break affect [OII] measurements. This could be corrected for low-z by using not the median of all colour models, but a subset of models with strong balmer breaks (selected using PCA) as a continuum estimate.

The fits are used to fill the gaps in data from lack of filter coverage and to track how these quantities will transform into other derived quantities and thus explain possible unexpected behaviour. A more advanced approach to predicting luminosities in regimes outside of the data probed would require a more careful examination and understanding the sources of these values from theoretical expectations. [OII] luminosity seems to depend on mass with some curvature across redshift, so modelling the source of this potential signal would be important for calculating [OII]/Hα ratios for example.

Stellar Mass-to-light ratios and star-burst fractions

Figure 4.21 is related to the EWs in figure 4.19. In logarithm space, using continuum flux as a proxy for mass and the distance modulus μ(1+z), which

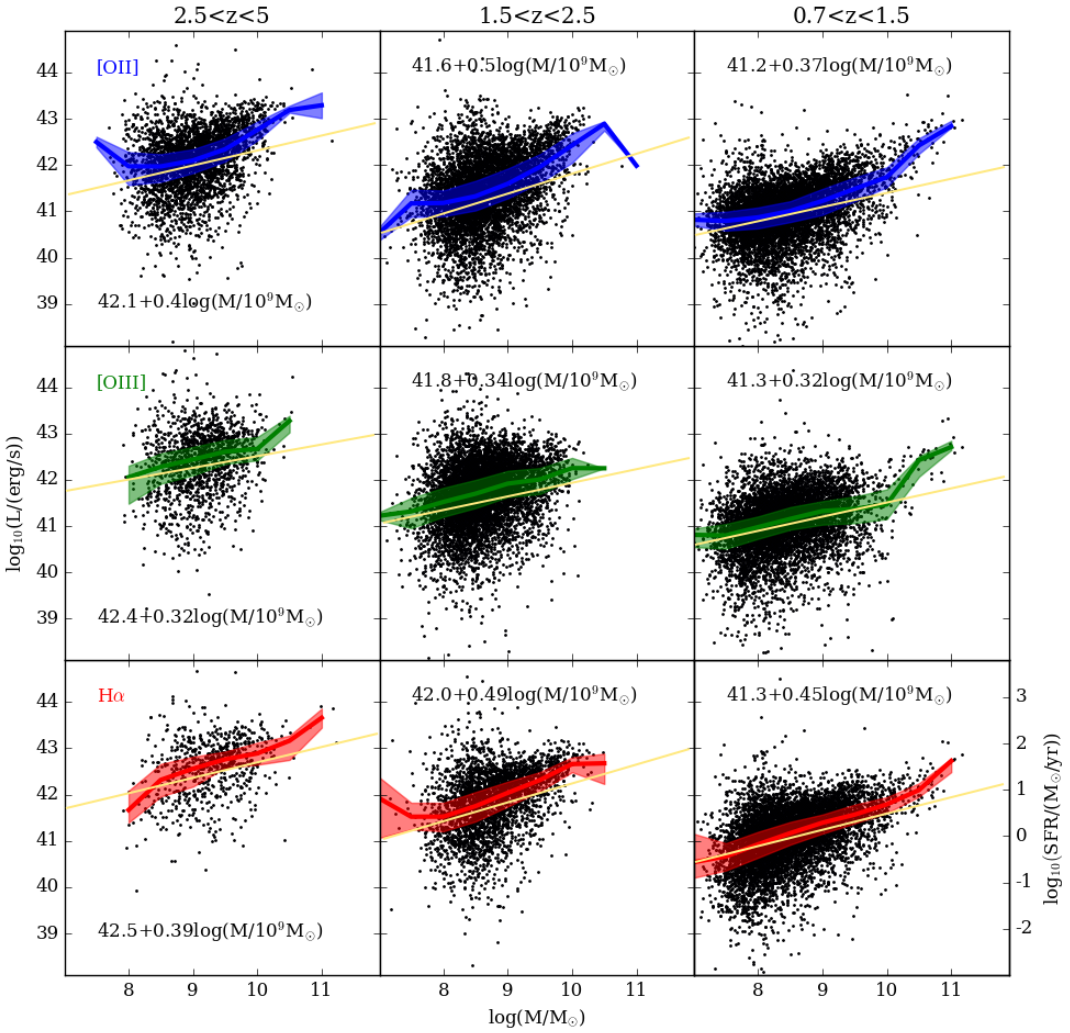

Figure 4.21: Dependence of line luminosity on mass for Hα, [OIII] and [OII] for 3 redshift bins. The central line shows the median luminosity and the shaded regions show the 32nd and 68th percentiles. The values on the graph show an additional least-squares fit () in terms of $\log_{10}(M/M_\odot)$. All luminosities increase smoothly with mass, with similar slopes. Comparing lines, Hα and [OIII] have similar luminosities at $\log_{10}(M/M_\odot)$=9, with [OIII] showing a weaker dependence on redshift than Hα and [OII], which look similar.

scales linearly with (1+z), one can convert the previously used EW dependence on mass and redshift into a luminosity dependence also on mass and redshift:

$$log(L)(EW_0) + log(M) + 2log(1+z) \tag{4.8}$$

and

$$log(EW_0) \propto 1.75log(1+z) - 0.25log(M) \tag{4.9}$$

one obtains

$$log(L) \propto 3.75log(1+z) + 0.75log(M) \tag{4.10}$$

The result is that the predicted dependence of luminosity on mass and redshift differs from L≈3.2log(1+z)+0.45M (from figures 4.21 and 4.20). The discrepancy in the first term can be mitigated by the fact that the 1.75 EW_0 normalization value was set at z=1.5, but for a linear fit the value is lower at higher redshifts, possibly 1.3.

However, for mass the powerlaw dependence index of 0.75 had been found to be in good agreement with observed median Hα luminosities. This seems to be a robust result from the mass plots, so the discrepancy between the dependence of luminosity on mass between values of 0.45 (equation 4.5) and 0.75 (equation 4.10) must have to do with an evolution of the mass-to-light ratio (total light, not just lines of galaxies). I assumed M/L to be constant to convert flux into mass in this calculation (equation 4.8), but this dependence is included in the luminosity via the evolution of observed flux. That would mean that Δlog(L/M)=-0.3log(M) from z=0 to z=2. In this form, one can see that the original M/L, which was considered constant in z must change as

$$L/M = (L/M)_0 M^{-0.6log(1+z)}. \tag{4.11}$$

By changing the base of the mass-dependent part of the redshift index of the Hα luminosity fit, one can obtain (and now interpret it as the M/L ratio.):

$$L_{H\alpha} \propto (1+z)^{3.2-0.6log_{10}(\frac{M}{10^9 M_\odot})} \left(\frac{M}{10^9 M_\odot}\right)^{0.45} \tag{4.12}$$

$$L_{H\alpha} =\propto (1+z)^{3.2} \left(\frac{M}{10^9 M_\odot}\right)^{0.45-0.6log_{10}(1+z)} \tag{4.13}$$

If measuring at z=2, then $\log_{10}$(1+z)=0.5, so the L/M ratio is effectively -0.3.

To further interpret what this value means, consider that for an individual star L scales as $M^{3.5}$. However, giant massive stars (M>20$M_\odot$) scale as M^1. The decreasing M/L ratio means that there is an increasing fraction of giant stars. This could either mean a shift towards a top-heavy IMF, but a simpler

claim would be that towards high redshifts, ELGs, like all galaxies, have a larger fraction of its mass in star-bursts, with enhanced amounts of bright, young O and B stars. As a quick check, I will assume that at z=0 all of a galaxy is modest and $L_0 \propto M^4$. So over redshift the average luminosity dependence on mass will shift towards that of higher-mass stars, described as a linear combination of high and low-mass stars

$$L(z) \propto (1-\gamma(z))M^4 + \gamma(z)M^1. \tag{4.14}$$

γ represents the giant star mass fraction enhancement as a function of redshift. Then:

$$(1-\gamma(z))L_0 + \gamma(z)L(z) = L_0 M^{-0.6log_{10}(1+z)} \tag{4.15}$$

Around $\log_{10}(M/10^9 M_\odot)$ the slope in a log-log plot of a sum of power-laws is another power-law with the average slope. This can be generalized to show that the combined power-law index is obtained by interpolating the two power-law indices with a weight γ.

$$\gamma(z) = -0.6log(1+z)/(1.0-3.5) = 0.24log_{10}(1+z) \tag{4.16}$$

For low redshifts, the average fraction enhancement simplifies to 0.24ln(10)z=0.1z. For z=1 it is 0.07, for z=2 it is 0.11, at z=5 it is 0.19 and at z=10 it is 25%. Even if the z=0 giant star mass fraction is 1%, this number only reaches 50% at z=100 (maybe in the very special case of a population III galaxy, but even there there would be an IMF and the inevitable contribution to low-mass objects). If O/B stars go supernova after 10^7yrs and stellar mass fractions of 0.12 (0.01 minimum + 0.11 enhancement at z=2) of a stellar $10^9 M_\odot$ correspond to $12 M_\odot$/yr, which are very strong star formation rates for such small objects. It must also be considered that giant stars dominate the light, but not the mass, so $12 M_\odot$/yr may already be too high. Would this place a ceiling on sSFR? This will be discussed in the next subsection.

The conclusion here is that even if the EELG objects under study have extreme equivalend widths, it only takes a small fraction of the gas in the galaxy to actively be forming stars to very quickly increase their M/L ratio. Since it is a small fraction, this is consistent with some form of localized star-burst activity and not

necessarily a global star formation enhancement. Looking at the morphologies of line emission would clarify this, but it out of the scope of this chapter.

Deriving Star Formation Rates from Hα

To convert the luminosity into a star-formation rate, it is necessary to refer to the atomic physics of emission nebulae. Even though star formation at high redshift is presumably different from at low redshift (different gas, electron density, temperatures, metallicities), the empirical relation from Kennicutt (1998), which uses a (solar metallicity) Salpeter IMF is:

$$SFR = 7.9 \times 10^{-42} \frac{L_{H\alpha}}{erg/s} M_{\odot}/yr \tag{4.17}$$

Naturally, star formation is an extensive variable, so it is more practical for comparisons throughout a population to use the intensive quantity specific Star Formation Rate (sSFR), which normalizes the star formation rate by the mass of the galaxy in order to get a mass-independent estimate of the intensity of star formation for a given object. It is approximately proportional to equivalent width via the mass-to-light ratio as the ratio of line luminosity (proportional to UV luminosity, as this is the source of ionizing photons) to mass (proportional to the continuum flux).

$$sSFR = \frac{SFR}{M} \propto \frac{L_{H\alpha}}{F_X \times M/L} \propto EW_{H\alpha} \tag{4.18}$$

sSFR comes in units of Gyr^{-1}, an indicative number of the age of the galaxy if it had formed stars at a constant rate (SFR-weighted age of the galaxy). Equivalent widths come in units of Å, which is proportional to Hz^{-1} using the speed of light, so dimensional analysis confirms the interpretation for sSFR as a doubling time (one solar mass is formed per solar mass every Gyr). This is why masses were normalized at 10^9, so that SFR translates directly into sSFR at that mass.

Specific SFR evolution as a function of time and mass

Specific SFR is shown in Figure 4.22 as a function of time for all the EELG objects in the sample and the median value in each redshift bin is shown to increase from 0.1/Gyr at z=0 at $10^{10}\mathrm{M}_{\odot}$ (1/gyr at $10^{8}\mathrm{M}_{\odot}$) to 10/Gyr 1Gyr after the big bang (100/Gyr at $10^{8}\mathrm{M}_{\odot}$).

All values are shown against the M-SFR relation from Speagle et al. (2014), the blue lines, now converted into sSFR:

$$log_{10}(sSFR) = (-0.16 - 0.026T)log_{10}(M/M_{\odot}) - (6.51 - 0.11T) \quad (4.19)$$

This fit represents the evolution of the average galaxy with time and mass, also known as the "main sequence" of star formation (Noeske et al., 2007; Daddi et al., 2007). The ELGs seem to fit well the predicted sSFRs and closely follow the evolution up to z=1.5 (i.e. down to 4Gyr). Local universe sSFRs are around 0.1/Gyr for MW-type galaxies and 1/Gyr for dwarf galaxies. However, for ages below 6Gyr, sSFRs measured in this work depart from the main sequence of SFR. The least-squares fits to the sample predict approximately the same primordial sSFRs, around 10/Gyr. The reason these measurements work for normal galaxies is because they include all the blue galaxies down to $EW_{H\alpha}$=0 and the median EW is computed including that information. However, the median sSFR, which is free to not be linear, seems to reach values 10 times higher for sSFR. There are two reasons for this, one technical, another theoretical. The fact is that this method relies on selecting EELGs, the bluest galaxies (B-K<2) to do the analysis, otherwise the low-dust condition can not be enforced. Furthermore, towards higher redshift and lower ages galaxies are lost due to completeness problems, but the discrepancy is progressively lower. Overall, this departure from the main sequence for times below 4Gyr (z>1.5) is expectable, because this method can only measure EWs for blue EELGs an these are extreme star-formers.

This could be a matter of missing both the low mass and quiescent population, but this could be fixed by estimating SFR from the continuum for the remaining galaxies, since they are line-free. The major problem would be dealing with dust. In fact, the ELG population is not very dusty, with E(B-V) from 0 at very high z up to 0.3 Amorín et al. (2015), so it could provide better sSFR measurements more easily than dusty objects which need to be corrected. The other possibility is that most of these objects may in fact spend most of their time in the main sequence and occasionally flare up as their magnitude increases tenfold. This, combined with the lack of red and low-mass objects could fully explain the discrepancy.

A method for quantifying the episodic star formation would be to look at the distance between the 90th and 50th percentiles of sSFR and see how they scale

with the sSFR itself, provided errors have been accounted for. If galaxies spend 10% of the time in the burst-on stage, that should be noticeable in the percentiles.

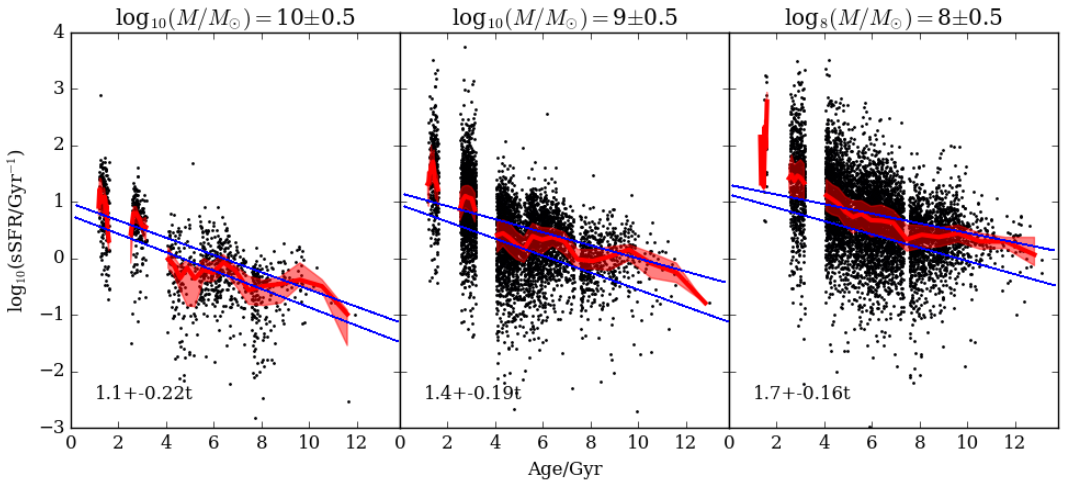

Figure 4.22: The evolution of sSFR with the Age of the Universe for three contiguous mass bins. As usual, the central line shows the median sSFR and the shaded region the 32nd and 68th percentiles. The numbers show the result of doing a linear fit of $\log_{10}$(sSFR) with age. The blue lines show the fit from Speagle et al. (2014) for the higher and lower-mass end of each bin. There is good agreement between the fits and the main sequence. The main discrepancy is caused by the departure of ELGs from the main sequence towards values 10 times higher at t=0.

Alongside the time evolution, like luminosity, specific SFR depends on mass as described in Fig. 4.23 and the fitting formula:

$$sSFR \propto (1+z)^{3.2} \left(\frac{M}{10^9 M_\odot}\right)^{-0.55-0.6log(1+z)} \tag{4.20}$$

Ignoring the mass-to-light ratio (which makes the mass powerlaw index depend on redshift), the mass dependence in each redshift is just around -0.55 as indicated by the fit as expected from transforming the luminosity fitting formula. However, the evolving M/L ratio ensures that the index varies with redshift, so at z=3.75 the index is expected to be -0.66 in the middle of the high-z bin and -0.45 at z=1.1 in the middle of the 0.7<z<1.5 panel, but closer to -0.5 if the sample is biased to higher redshifts due to low volumes. Speagle et al. (2014) yields an index of -0.3. The ELG sample shows a steeper dependence in time, probably because this sample is one dominated by extreme objects at high redshift (while

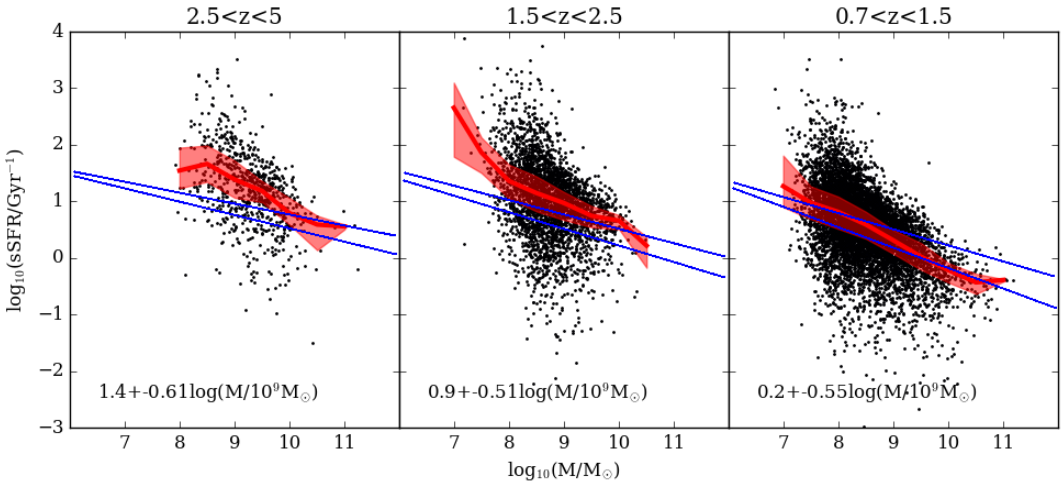

Figure 4.23: sSFR vs $\log_{10}(M/10^9 M_\odot)$ for ELGs. The red line shows the median sSFR and the coloured region shows the 32nd and 68th percentiles. The blue lines show the main sequence prediction from (Speagle et al., 2014). At T>6Gyr the ELG population blends with the main sequence of star formation.

at low redshift, many near-zero EWs with large errors are measured).

Any specific star formation rate above 30/Gyr is exceptional, as it is above the average for most galaxy masses and redshifts. This sSFR can not be sustained for very long, due to supernova feedback cancelling gas accretion and intense star-formation quickly decays in a closed-box situation. There is a way out of this, if cold gas pierces through galaxy winds through cold streaming (Kereš et al., 2005), but even this mechanism may not work due to stream instability at the high wind speeds needed to keep sSFR in such a situation. Either way, extreme star formation (which I have alluded to only involves small fractions of galaxy mass) is not a property, it is a transient state. Therefore, I predict that there must be an upper bound to the main sequence of star formation, the upper star-burst sequence, which is the locus drawn by galaxies shooting up from the main sequence to reach a maximum sSFR. This will be distinguished from the usual scatter around the main sequence (both intrinsic and observational) in that there is a steep gradient of sSFR which has to reach a plateau of sSFR. For an sSFR saturation estimate, imagine forming a single O-star. That has the highest sSFR possible and should provide a safe upper limit to sSFR. That would be $20M_\odot$ over 10^5yr per $20M_\odot$, so that would be an sSFR of 10^3/Gyr when considering the IMF (maybe 10 times more mass would be formed).

So the maximum primordial cluster sSFR would be 10^3/Gyr, which looking at Figure 4.23 would produce galaxy coverage of sSFR-t space from a maximum of log(sSFR)=3 for individual cluster masses of M=$10^7 M_\odot$ at z=0 (extrapolating in mass), and decreasing for higher-mass galaxies because it is more difficult for a major star-burst to dominate the whole galaxy. As accretion rates decrease (this also drives the main sequence), it becomes more difficult to sustain such star-bursts, so the upper star-burst plume reintegrates the main sequence, such that EELGs are very rare at z<1.

Star Formation Rate Density

After showing the behaviour of the sSFR of ELGs, now I will take the SFR for all ELGs of 9<log(M/$M_\odot$)<9.5 (because this is the mass bin that is complete at all redshifts for this sample), sum them and divide by the survey volume at each redshift to obtain a specific star formation rate density (SFRD). A comparison of the values obtained and the dependence in Madau & Dickinson (2014) is shown, where the SFRD of ELGs at z=0 is less than 1%, but rises up to 10% at the peak of SFRD at z=2 and decreases with SFRD, but slowly enough to make up 30% of all SFRD by z=5.

EW([OIII]) extreme behaviour vs sSFR

As shown in chapter 3, the [OIII] EW distribution has a heavy tail (large fraction of high values). This is not just due to errors, because this happens before Hα displays its high-z long tail as well at z=1.5 already. Figure 4.25 shows a description of [OIII] EWs vs sSFR. The area delimited by the blue triangle shows the original population selected at z<1 in Amorín et al. (2015) with an EW cut to select only the EELGs. The presently used sample at z<1 aligns with the most extreme EWs of the starforming galaxy sample, ELGs. At z>2, the trend of maximum EW([OIII]) with sSFR is extended up to 1000/Gyr, with a relation for the maximum EW([OIII])≈50sSFR$^{0.85}$.

It has been assumed so far that Hβ was small when compared with [OIII], so [OIII]≈[OIII]+Hβ. In the next section I will test this assumption.

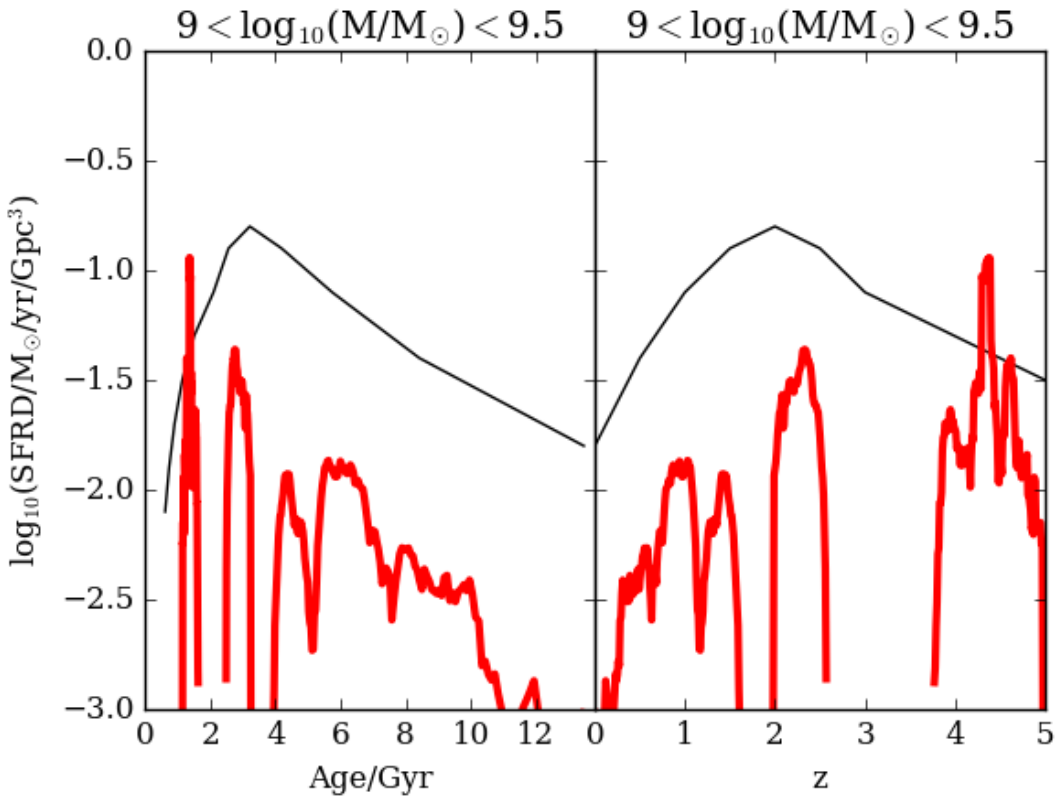

Figure 4.24: Star formation rate density over the age of the Universe and redshift for a mass range that is complete up to z=4.5 (red) compared with the SFRD in Madau & Dickinson (2014) (black line). Note the increasing proportion of SFRD for the low-mass range. This is due to the fact that a $10^{9.5}$ $M_\odot$ cut was taken to keep completeness up to high-z. This means not only that there are more ELGs towards high redshift, but also that the potential progenitors of high-mass galaxies today could once have been ELGs.

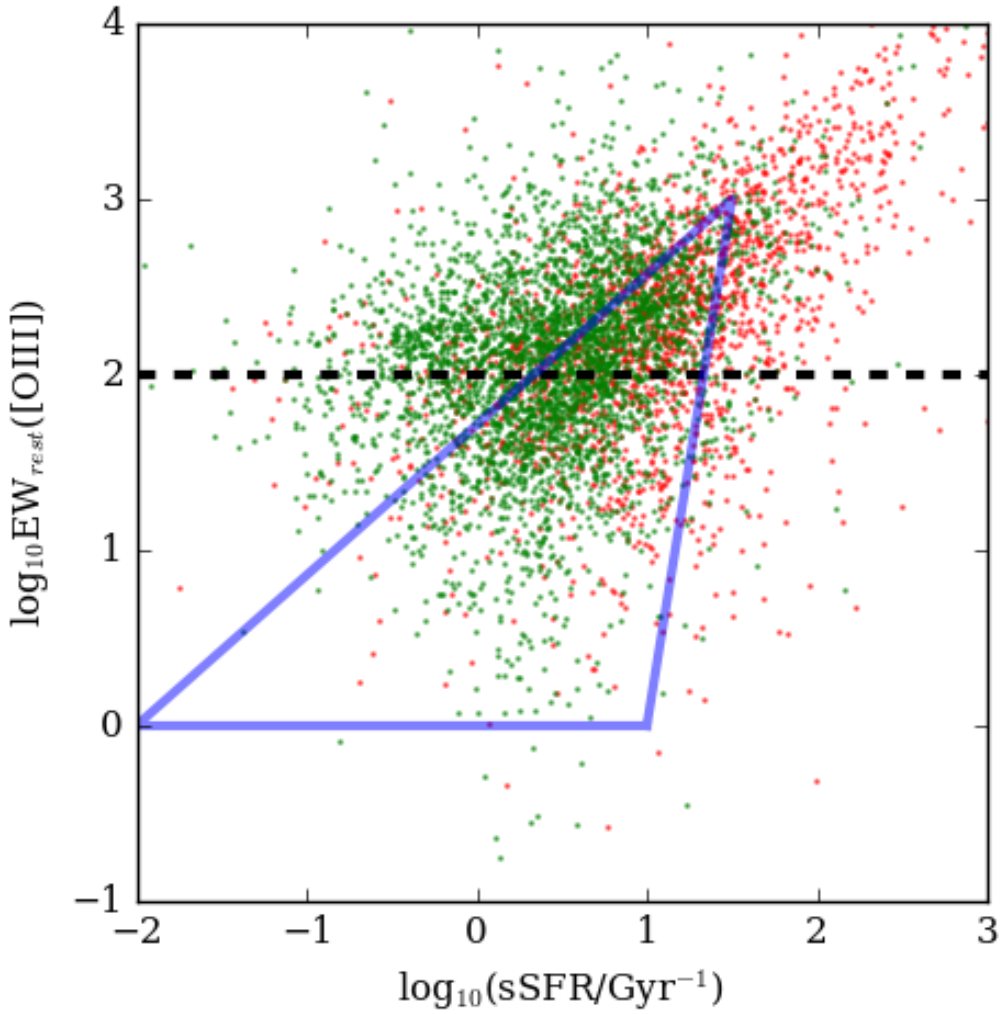

Figure 4.25: This figure combines a physical indicator: sSFR, and an observational indicator: EW([OIII]) to show how their relation evolves from low redshifts up to high redshifts (where both OIII and Hα are available only up to z=2.4). The blue triangle delimits the full star-forming galaxy population selected in Amorín et al. (2015) from the COSMOS-20k Bright Survey Catalogue (Knobel et al., 2012). I define above the grey line at 100Å to be reliable EELGs. The portion of low-z EELGs (green peas) of the COSMOS-20k catalogue is naturally extended to higher sSFRs and $EW_{[OIII]}$. This method unlocks the rest of the EELG population at z>1, while continuing the locus of the upper triangle diagonal that reaches very high EW_{OIII}.

Deriving the Ionization Parameter q from [OIII]/Hβ

Emission line ratios are an essential measurement in high-z diagnostics of the physics of the inter-stellar medium and are usually calculated using two close lines. However, when using broadband photometry there is the problem that one can only use widely separated lines by design. This should not be a problem because these objects are virtually dust-free (A_V<0.5), because of the way they were selected to be blue and have strong lines, dusty EELGs have not been ruled out, but should be a minority of the population, as shown in Figures 3.1 and 3.2. From the atomic physics of emission nebulas, the level populations of HI for case B recombination are such that $L_{H\alpha}/L_{H\beta}$=2.85 at 10000K and this number changes slowly with temperature (Osterbrock & Ferland, 2006). Hence $L_{[OIII]}/L_{H\beta}$=2.85$L_{[OIII+H\beta]}/L_{H\alpha}-1$ is estimated and shown as a function of redshift (Fig. 4.26) and mass (Fig. 4.27)

The median dependence on redshift (from no on $L_{[OIII]}$ always excludes Hβ) is expected to be mild:

$$\frac{L_{[OIII]}}{L_{H\beta}} = 2.85 \times 0.6(1+z)^{0.4+0.3\log(\frac{\mathrm{M}}{10^9\mathrm{M}_\odot})} \left(\frac{\mathrm{M}}{10^9\mathrm{M}_\odot}\right)^{-0.12} - 1 \qquad (4.21)$$

This gives expected values of 0.7 at z=0 and 1.6 at z=2. So from z=1 to z=2.3 there is only a mild increase of 0.1 dex in $L_{[OIII]}/L_{H\beta}$, as is seen in Fig. 4.26. In fact, the increase from 0.7 is almost absent and very modest in the low-mass panel of Figure 4.26. On the one hand, this is because the value of $L_{[OIII]}/L_{H\beta}$ saturates around 0.7 and the previous formula is just a fit. On the other hand, the large errors in $L_{[OIII]}/L_{H\beta}$ obscure the evolution towards the maximum ionization parameter of 3×10^8 cm/s, which spans only 0.5 dex of the line luminosity ratio.

The [OIII]/Hβ ratio is one of the standard BPT diagram (Baldwin et al., 1981) line ratios and looking at Fig. 4.27 it branches out like the spectroscopic BPT diagram. Since AGN are more likely to be prevalent at higher masses (because ELG declines quickly with mass, whereas AGN feedback and mass quenching becomes more efficient), this could be the reason for the rise of [OIII]/Hβ with mass at high masses (>$10^9\mathrm{M}_\odot$) and z<1. The same effect with comparable values and the same decrease of the line ratio with mass on the low-mass end is visible in Fig. 4 of Amorín et al. (2015) (confirming this result for low-z ELGs), in Fig.

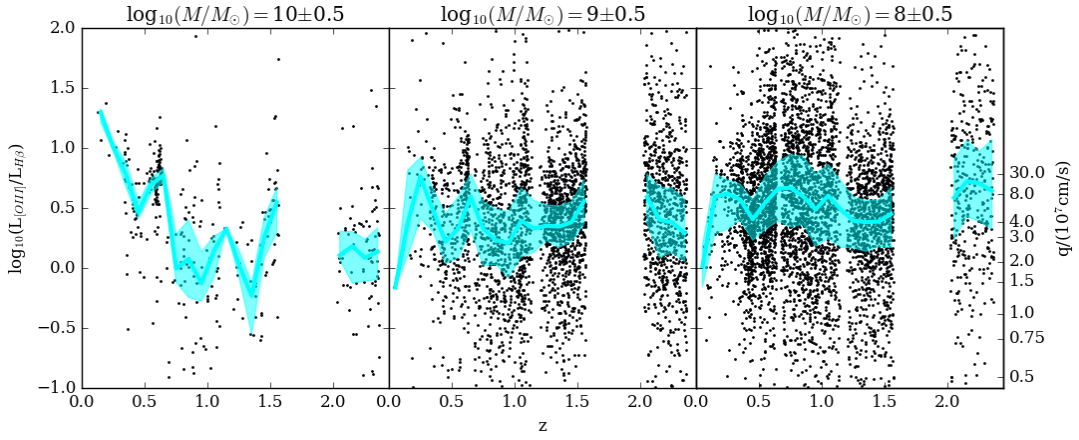

Figure 4.26: [OIII]/Hβ as a function of redshift for three mass bins. From z=0 to z=1 there is a decrease in [OIII]/Hβ for high masses. This can be due to the presence of AGN in the high-mass elements of this sample. For z>1 the evolves slowly and increases with mass up to around $10^{0.5}$. On the right is the scale to estimate ionization parameter q drawn from Kewley et al. (2004) (also shown in Figure 1.5).

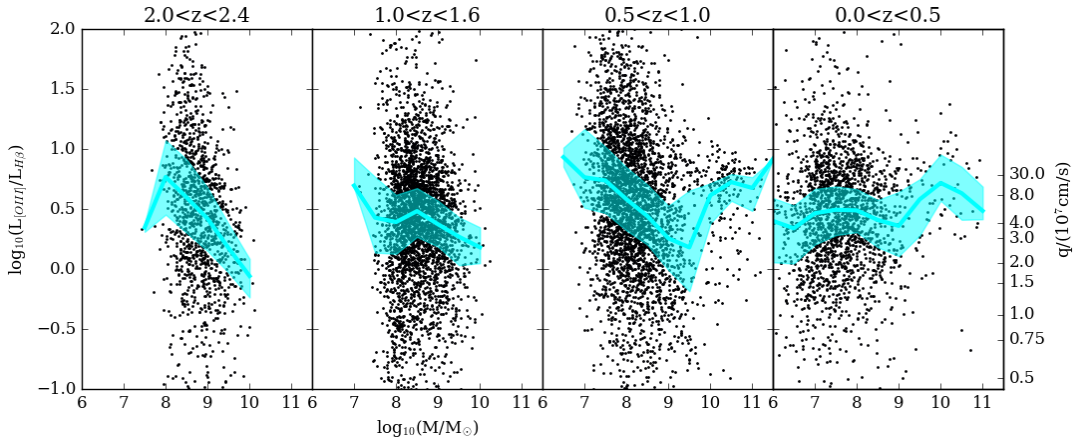

Figure 4.27: [OIII]/Hβ as a function of mass. [OIII]/Hβ generally decreases with increasing mass. For z<1 and log(M/M$_\odot$)>9.5 there is an increase, but this could be associated with some AGN activity in the higher-mass end of the sample. For z>1 the ratio evolves to $10^{0.75}$ or more for the lowest mas bins and remains close to 1 for $10^{9.5}$M$_\odot$. On the right is the scale to estimate ionization parameter q drawn from Kewley et al. (2004).

7 of Holden et al. (2016) and in Fig. 2 of Weiner et al. (2007), where it is also referred to as a pseudo-BPT or MEx diagram (Juneau et al., 2014).

Ionization parameter as a function of time and mass

To estimate q, I use the models in Fig. 11 from Kewley et al. (2004). The majority of [OIII]/Hβ ratios are above 1, so the super-solar branch is ruled out, leaving only the low-metallicity branch, in which [OIII]/Hβ varies very little with metallicity and mostly depends on the ionization parameter q, from where [OIII]/Hβ can be converted into q, as shown in Fig. 4.28:

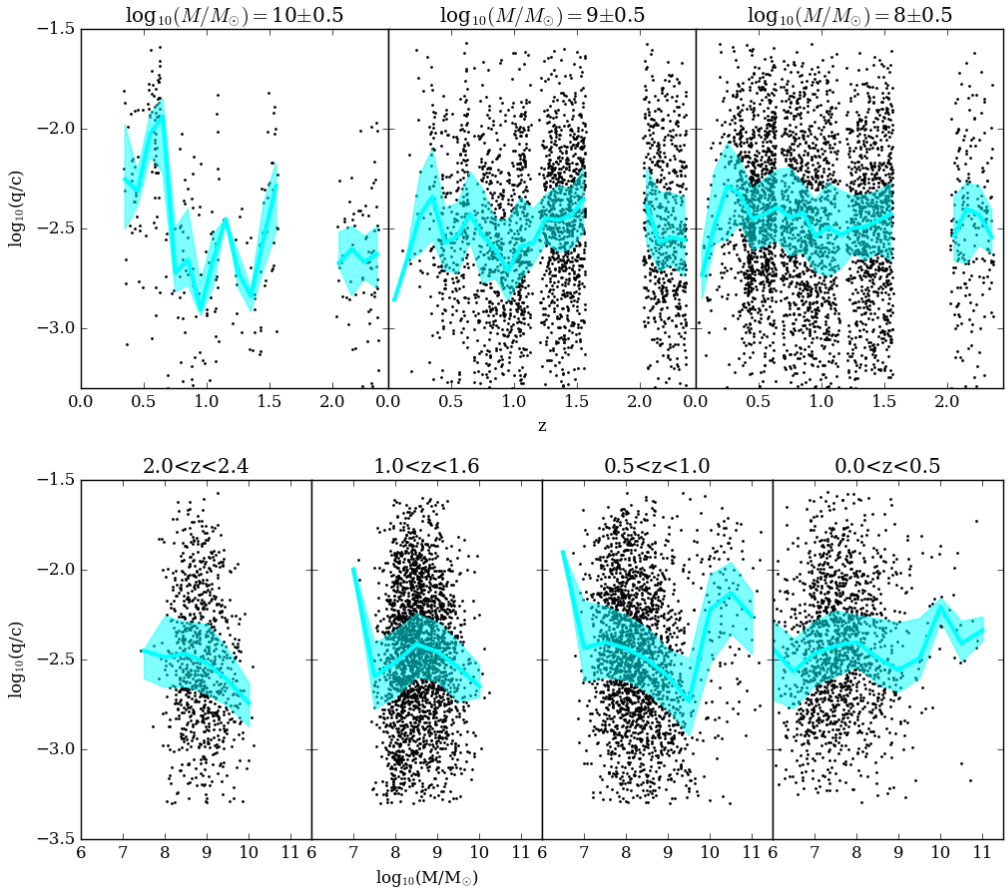

Figure 4.28: Logarithm of the normalized ionization parameter: U=q/c. There is little evolution of U with redshift, with log(U) values remaining around -2.5. Mass dependence is more appreciable and log(U) decreases from 10^7 to 10^9 $M_\odot$ and increases for higher masses.

The values reached by q can be very extreme and reach close to the maximum of the scale used for the models at [OIII]/Hβ=1, a maximum of 30$\times$ 10^7 cm/s (1% of the speed of light, indicating a 100$\times$ higher number of photons than gas), but on average q takes less extreme values around 5$\times 10^7$ cm/s.

For such values of q, the rate of ionizing photons can be estimated from the Hα luminosity: $Q(H^0)=7.3\times10^{10}L_{H\alpha}$.

Taking those values, from the definition of $q=\frac{Q}{4\pi R^2 n_H}$, a gas density can be estimated (provided Stromgren spheres behave in the same way as at low-z): $n_H=646(R/100pc)^{-2}/cm^3$. For a slowly changing ionization parameter, an increase in luminosity will either mean an increased gas density or larger Stromgren spheres. For an ionization parameter that scales with mass as $\log(q/c)\sim M^{-0.2}$ and $Q(H^0)\sim M^{0.45}$ through luminosity, $n_H\sim M^{0.65}R^{-2}$, so higher mass galaxies have higher gas densities or larger Stromgren spheres (probably the latter due to the intense star formation, there is no reason for gas density to be lower than at low-z).

Deriving Metallicity from [OIII]/[OII] and q

Looking at Fig. 1 from (Kewley & Dopita, 2002), [OIII]/[OII] shows an interplay between q and metallicity, but once a value of q can be estimated from [OIII]/Hβ, there is a way to estimate metallicities for the ELG population. The resulting metallicity from interpolating over the [OIII]/[OII]-z-q grid from the literature is shown in Fig 4.29 .

The median estimate of metallicity has a large uncertainty, but its wide range is similar to that found for high-z emission-line galaxies in Amorín et al. (2014), Fig. 2. While the errors on these results are too large to conclusively say that there is a metallicity evolution, it suggests that the median values of metallicity are subsolar for ELGs

[OIII]/[OII] over mass and redshift

Relying on Hα to provide the Hβ value has a drawback: only for redshifts where Hα is present can the correction to [OIII] be measured. What this means for [OIII]/[OII] in practice is that it would only be measurable up to z=2.4 and the last redshift bin would be wasted. However, to push the [OIII]/[OII] ratio to z>2.4, a small value shift due to a non-zero Hβ/[OIII] can be assumed, given how steady the average Hβ/[OIII] ratio is at high-z.

The guide fitting equation here is supposed to be:

$$\frac{L_{[OIII]}}{L_{OII}} = 2.4(1+z)^{-0.1}\left(\frac{M}{10^9 M_\odot}\right)^{-0.12} \text{erg/s} \tag{4.22}$$

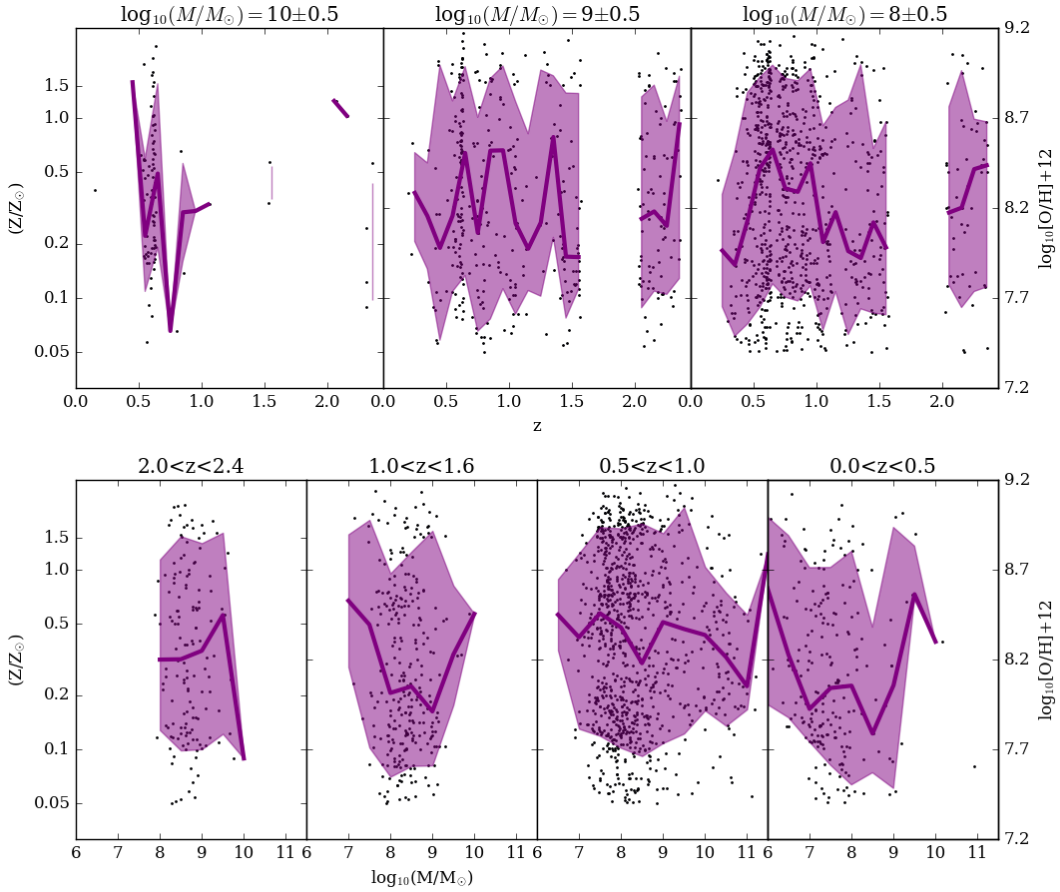

Figure 4.29: Estimated metallicity as a function of redshift (upper panel) and mass (lower panel). The median metallicity is shown by the coloured solid line and the 32nd and 68th percentiles of metallicity in each bin are shown by the shaded regions. Given that all three emission-lines must be measured to obtain an estimate of metallicity, the sample is not significant enough at high-z, but for lower redshifts, the metallicity takes values between $0.1Z_{\odot}$ and $Z_{\odot}$, with a median around $0.3Z_{\odot}$. There are some trends, but none is significant enough over redshifts and mass considering the errors to note a clear evolution in metallicity.

The relation of [OIII]/[OII] with mass follows the same relation as in the literature, for example Fig 2. of Hayashi et al. (2015).

The guide fitting equation fails here in comparison with Figure 4.30, which increases approximately linearly with redshift at a given mass, while it is mass-independent (Fig. 4.31), as expected.

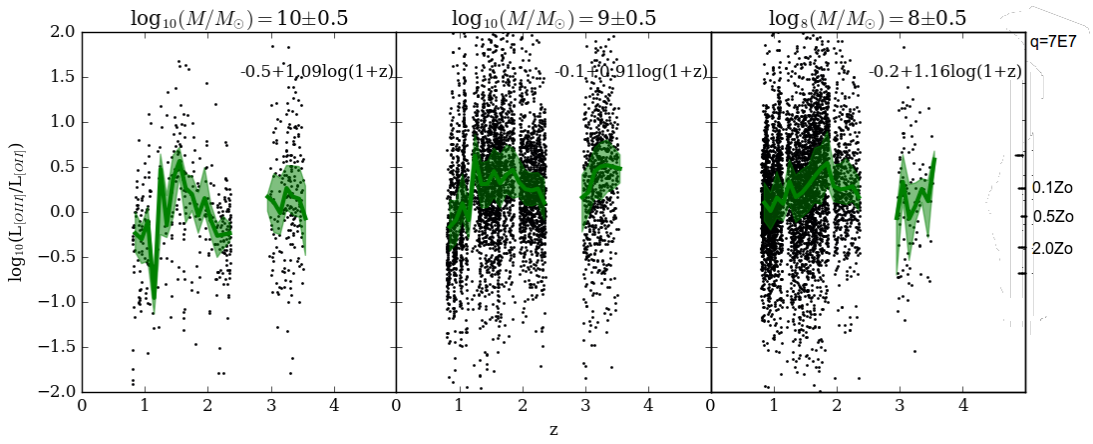

Figure 4.30: [OIII]/[OII] as a function of z at three different masses. The green line and shaded area show the median, 32nd and 68th percentiles. The scale on the right shows metallicity if every galaxy in the sample had a q=7×10^7cm/s (using the table in Figure 1.6 (Kewley et al., 2004)). All metallicities estimated in this way for z>1 are sub-solar. However, the modest evolution from -0.2 to to 0.2 may depend more on the evolution of q than metallicity (Cullen et al., 2016).

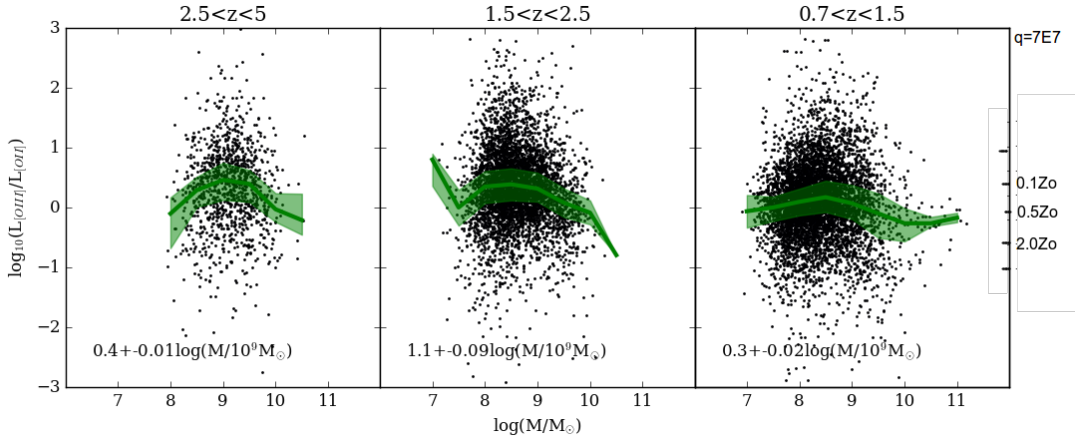

Figure 4.31: Dependence of the [OIII]/[OII] ratio and ionization parameter on mass. The green line and shaded area show the median, 32nd and 68th percentiles. The scale on the right shows metallicity if every galaxy in the sample had a q=7×10^7cm/s. All metallicities estimated in this way for M<$10^{10}M_\odot$ are sub-solar, but there is no evolution of [OIII]/[OII] with mass.

The relation between [OIII]/[OII] and sSFR

After the previous analysis, [OIII]/[OII] is known to be a complex line ratio that depends as much on metallicity as on ionization parameter. However, it is commonly shown in the literature and since it contains only uncorrelated quantities in the x and y axis, any dependences found are more robust than, say, comparing [OIII]/Hα with [OII]/Hα, which should have a linear correlation through the shared errors Hα. It is also useful to look at this figure as the only possible extension of the measurement of metallicity to z>2.4 with the current bands. By assuming that the sample has a median [OIII]/Hβ and a corresponding ionization parameter of q=5$\times$10^{8}cm/s, the ratios shown in Fig 4.32 show a decreasing metallicity (at constant q) with sSFR, indicating that objects (but a maximum star-formation rate dependent on gas accretion) with a lower mass have less metals.

Figure 4.18 had already shown that when extreme, [OIII] can be stronger than Hα, which provides: high sSFR objects, which are extreme, tend to have enhanced [OIII] emission. This claim is corroborated in figure 4.32. However, it looks like the dependence becomes weaker with increasing z, which goes against predictions. It could be that there is a saturation of this relation at high-z, so at any given mass:

The corresponding figure 4.32 shows good agreement with previous measurements which range in sSFR up to 30/Gyr at [OIII]/[OII]=10, the expected extreme regime. So the tendency here seems to be that higher sSFR galaxies have lower metallicities for the same mass and redshift, like what was shown in Fig 2.12.

Conclusion

In this chapter I have applied the method developed for the CANDELS-UDS ELGs in chapter 3 to estimate EWs from all the CANDELS fields. These EWs were compared with spectroscopic and narrow-band measurements in the literature to show that the measured EWs agree and extend the mass range available to estimate EWs from photometric data. Then these EWs were converted into luminosities and I attempted to estimate physical parameters of stellar populations in galaxies across redshift. I identified the main sequence of galaxy formation and found that the median EWs (including 0 values) can

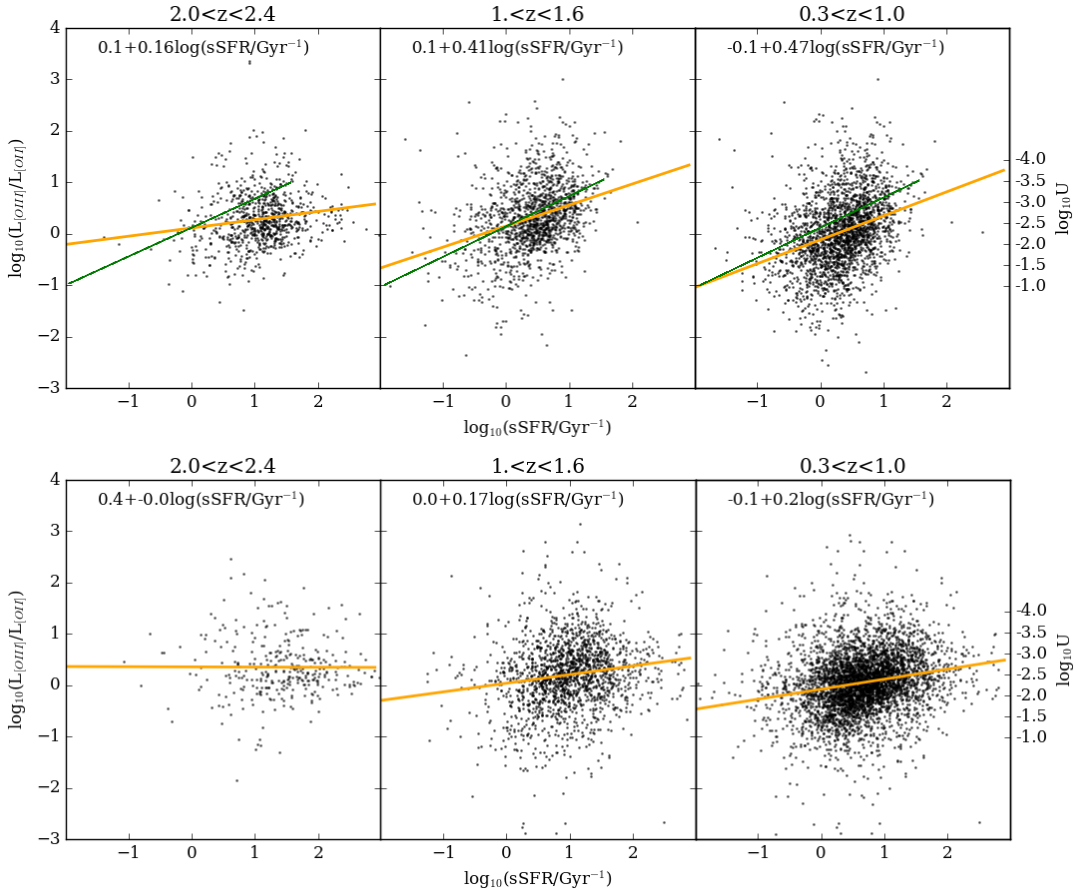

Figure 4.32: The relation between [OIII]/[OII] and sSFR with a linear least-squares fit and the corresponding dependence shown. The observed slopes change smoothly over redshift and mass. The upper panels show $8.5<\log(M/M_{\odot})<9.5$ and the lower panels $7.5<\log(M/M_{\odot})<8.5$. The green line shows a visual fit to the dependence of OIII/OII on sSFR from Nakajima & Ouchi (2014).

replicate the main sequence values up to z=1.5, from where there is a departure to values higher than the main sequence up to a factor of 10 if extrapolated to the big bang. From there, an attempt was made to interpret physically the convergence between Hα and [OIII] seen in Figure 4.15 and the divergence between [OIII] and [OII]. Associating Hα with Hβ, an estimate of [OIII]/Hβ was attempted and while it did not show strong evolution, it was consistent with large values of ionization parameter (7×10^7). Using the ionization parameter, a tentative measurement of metallicity was made, which suggested mean sub-solar metallicity, with very large errors. This is already a hard process to do with spectra and this method has

large uncertainties, but the large number of galaxies surveyed partially mitigated the large errors on estimated quantities. Changes in the method and additional infrared bands that would bring the errors down would make this a viable method for surveying the average physical properties of nebular emission towards the highest redshifts

Chapter 5

Conclusion and Future Work

Summary of Results

In this thesis I have shown that it is possible to study the emission-line properties of galaxies up to very high redshifts using deep broadband surveys like CANDELS and a set of stochastic burst models.

I started by converting sets of star-formation histories drawn from semi-analytic and AMR models into observed colours using the BC03 spectral templates and concluding that only the most recent star-formation history can be recovered. I showed that semi-analytic models are not blue or bursty enough to reproduce the galaxy colours observed in CANDELS. The AMR models used do not produce a significant red population at low masses and z=2 galaxies span a wide range of metallicity, from $Z_{\odot}$ to $0.2Z_{\odot}$. I used a simplified semi-analytic model to show that a small period of enhanced gas accretion can lead to a permanent increase in magnitude and a temporary metallicity inversion. I showed that PCA can very efficiently separate the effects of metallicity and galaxy age in PCA space. Most importantly, in section 2 I show that a set of stochastic burst models have a colour distribution similar to that of high-redshift galaxies and that the only colour discrepancies come from nebular emission lines, which align particularly well in line-free colours with very blue and young objects ($B-K<2$) and seem to be essentially dust-free.

In chapter 3, I use the SBMs and the CANDELS-UDS photometric catalogue, a running-redshift colour cut ($B-K<2$), and auxiliary catalogues of photometric redshifts and masses to measure the offsets between model colours and observed

colours to show that emission-line contamination in Hα, [OIII] and [OII] is prevalent at every redshift from z=0.3 to z=5, producing magnitude and colour offsets up to 0.5 magnitudes. I do this by choosing a line-free baseline colour with a band bluewards of [OII] and a band rewards of Hα, usually K_s or 4.5μm to estimate the line-free continuum in all the intermediate bands. As the emission lines are redshifted through all the bands in between these lines, equivalent widths can be estimated for all three lines.

The equivalent width of Hα shows the highest values from EW_0=100Å at z=1 to EW_0=400Å at z=4.5 for ($9<\log(\frac{M}{M_\odot})<9.5$, with constant median mass). [OIII] has lower EW_0 up to z=3, where it matches Hα or may even surpass Hα. [OII] remains at low EW for z<1.5 and starts rising up to EW_0=200Å at z=0.5. Through redshift, ELG (EW_0>150Å) density rises from 5×10^{-4}/Mpc^3 at z=0.5 to 30×10^{-4}/Mpc^3 at z=2.3 and 5×10^{-4}/Mpc^3 at z=4.5, while the ELG fraction of the sample rises from <5% at z<0.5 to 40% at z>2 and constitute >70% of the blue galaxies at z>2. [OIII] displays an EW_0 distribution with a longer tail and consistently displays more extreme values for EW_0 than Hα or [OII].

In chapter 4, I extend the analysis to all of the CANDELS fields and find that every field shows consistent EW_0 values with those seen in CANDELS UDS, apart from increased errors (due to shallower K_s or IRAC 3.6μm and 4.5μm bands) or lower quality redshifts due to a lower available number of bands. The results obtained using the five fields are robust and compares well with the values expected from extrapolating the EW_0 found in narrow-band measurements from HiZELS and grism spectroscopy from 3D-HST to lower masses:from 3D-HST: $EW_0(H\alpha)=23\left(\frac{M}{10M_\odot}\right)^{-0.25}(1+z)^{1.75}$ and this fit stays consistent down to very low masses. For z>2 there is a departure from this relation to lower EW_0, which extends the results from Marmol-Queralto et al. (2015) for $\log(M/M_\odot)\sim9.8$ to lower masses ($\log(M/M_\odot)\sim9.2$), and is further supported by deeper HUDF values to even lower masses ($\log(M/M_\odot)\sim8.6$). EW_0([OIII]) seems to have a steeper mass dependence and higher values for the distance between the 90th percentile and the median EW_0 over mass than Hα, further confirming that this line more easily reaches extreme values of EW_0.

I convert EWs into line luminosities and show fitting formulas for them as a function of mass and (1+z) from z=0 to z=5 and $8<\log(M/M_\odot)<10$. From here, the increasing slope of the mass dependence of luminosity with redshift

shows an evolving mass-to-light ratio, from which a high-mass star fraction can be estimated to be γ=0.24log(1+z), which shows that only a fraction of the galaxy needs to be a starburst to display these emission-line luminosities.

From there, the SFR and sSFR are computed from the Hα luminosity and their dependence with mass and cosmic time is compared with that of Speagle et al. (2014). For high masses (log(M/M$_\odot$)$\sim$10), the SFRs align with the main sequence of star formation, but for masses below that there is some agreement for the latest 8Gyr (z=1.3), and ELGs are the high-z counterpart of the low-z green peas, also discovered in broadband photometry, but before 8Gyrs ELG EW$_0$ rises up to sSFR=100/Gyr (10$\times$ more than the main sequence) at t=0 for the lowest mass bins. The dependence of sSFR on mass for the low-z bins is steeper than for Speagle14 and for the high-z bins EW$_0$ it is twice that of the main sequence, while keeping its slope. The SDRD of ELGs increases with z as one would expect, with a growing contribution of ELGs from 1% to 30% of the SFRD for the complete mass range 9<log(M/M$_\odot$)<9.5.

Finally, the [OIII]/Hβ ratio is estimated by assuming L$_{H\alpha}$=2.85L$_{H\beta}$, which yields [OIII]/Hβ ratios of $2^{+3.5}_{-0.5}$ at 9<log(M/M$_\odot$)<9.5, corresponding to ionization parameters of 1.5$\times$10^{7}cm/2 to 8$\times$10^{7}cm/s, which is consistent with the literature at high-z. For log(M/M$_\odot$)=9, the median q=3$\times$10^{7}cm/s and for log(M/M$_\odot$)=8 it is q>8$\times$10^{7}cm/s. For high masses, the relation is reversed and the ionization parameter rises with mass, so it is possible that this is evidence of AGN feedback, in a possible serendipitous BPT-like diagram with mass in the x-axis.

Combining q with the Hα-derived Q(H^0) yields a value for n$_H$=646$\left(\frac{\mathrm{R}}{100\mathrm{pc}}\right)^{-2}$ atoms/cm^3, using a 100pc stromgren sphere as a reference value.

The [OIII]/[OII] ratio, which folds in ionization parameter and metallicity stays constant with mass but increases slowly with redshift as L$_{[\mathrm{OIII}]}$/L$_{[\mathrm{OII}]}\sim$(1+z) and increases with sSFR as shown before in the literature.

Finally, a tentative metallicity measurement is made using the [OIII]/[OII] ratio (which rules out supersolar metallicities) and the ionization parameter q. This yields a value with large uncertainty, because it can only use values where all three lines are present and the variable transformations change the error distribution, yet metallicity values are centered around subsolar values (0.3$_\odot$) and span values between between Z$_\odot$ 0.1Z$_\odot$, like the CANDELS-UDS observations seemed to indicate when originally compared with models in section 2.

Through this work I have and provided ample evidence that a photometric approach to the study of line emission is a powerful and efficient tool to study the instantaneous star-forming properties of high-redshift galaxies in deep (K_s>24) surveys down to high EWs with low line luminosities. Individual measurements have high errors, but the rising signal of observed equivalent widths with (1+z) and the sheer number of ELGs in a broadband sample is enough to estimate the properties of the ELG population.

Because it requires no fitting by design, it is computationally cheap and can be applied in a variety of contexts.

Future work

Now that the method is shown to be consistent with narrow-band and spectroscopic measurements at higher masses, to be consistent between fields and estimates the right values, while doing so very efficiently, there are a number of ways forward: to make it more reliable and flexible through better treatment of errors through addition of errors/lines to the SBMs (and other sets of models too) and attempting to recover the EWs. This might be a way to quantify how much of the EWs measured are due to nebular continuum and how fast this rises.

With better signal-to-noise, other emission lines might be found. The code can also be adapted to estimate Lα by an extrapolation baseline, but this is more uncertain because it relies on knowledge of the UV continuum.

A deeper 8.0μm or even 5.8μm would extend the method beyond z=5, with simultaneous [OIII] and Hα measurements at z=6 for measurement of the behaviour of the ionization parameter at z>2.4 and at z=8 for simultaneous coverage of all three lines.

It would also be interesting to divide the ELG population into subpopulations in PCA space and to look at the derived quantities over high-z.

This method would be even more powerful if applied to a multi-mediumband survey like SHARDS or using deep ZFOURGE bands or for handling at an early stage large numbers of ELGs in future new-generation deep wide-field high-z surveys from telescopes like EUCLID, WISH and EELT.

Improvement to the Method

ELG Morphologies by line

Throughout this thesis I have not used any galaxy morphologies, since the focus was on the multiwavelength data analysis. However, the aperture-limited HST resolution is one of the features of this catalogue and it is rich in information about the dynamical state of the gas in galaxies. After seeing this method work, it would be interesting to apply it pixel-by-pixel on a galaxy (see Fig. 5.1). This can be done now, but due to the different resolutions between IRAC and HST it might not resolve line emission. However, with the imminent launch of JWST it will be useful to have a quick tool to identify emission line properties down to the lowest masses quickly, since at those depths JWST is going to find far many more

galaxies than will be possible to track with slits or grism spectroscopy. This would provide a quick way to produce line emission morphologies and can be tested now in the CANDELS data. Furthermore, all mass/redshift estimations are already defined for each object and the decomposition would use those.

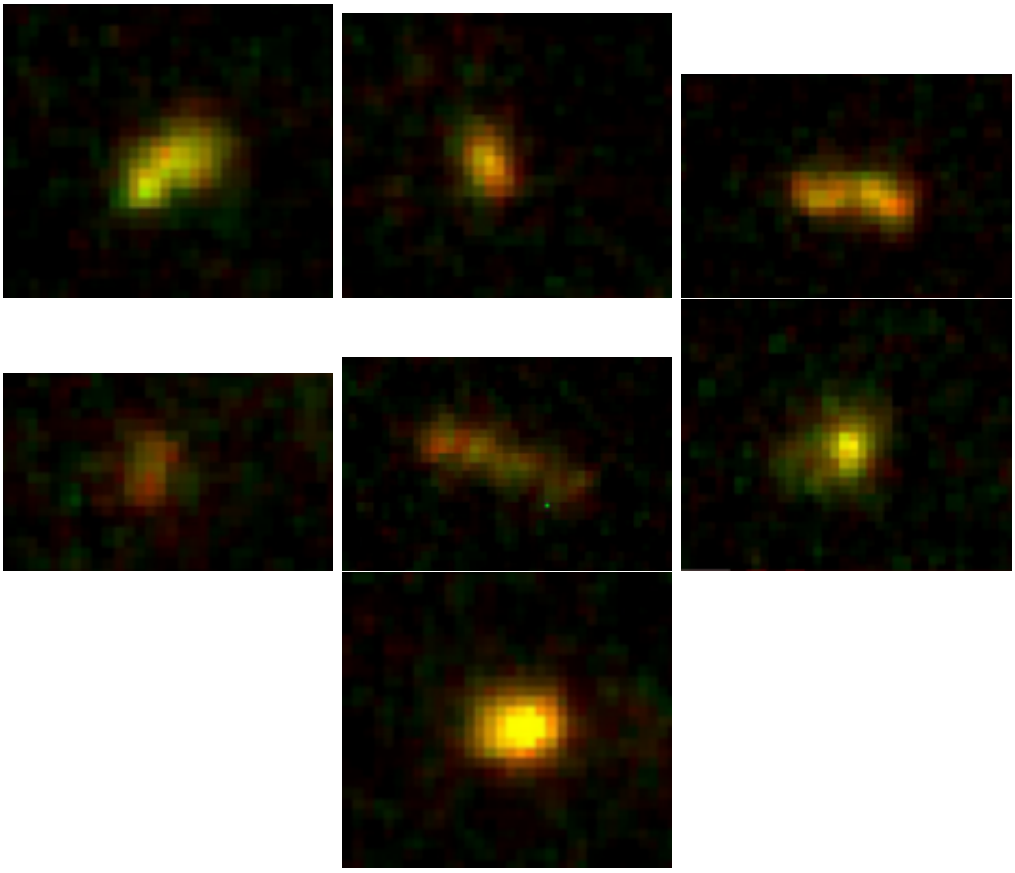

Figure 5.1: Red-green photometry maps of ELGs in CANDELS using J and H (try to use i814/K to make it RGB) for a number of the galaxies with the highest EWs measured around z=1.8. Some objects do not show colour gradients, others seem to be H or J enhanced. While some smaller fluctuations are due to shot noise, some galaxy regions clearly seem to be greener or redder and could be potentially due to localized emission lines.

Another simpler approach involving morphology would be to relate extracted ACS morphological parameters with emission-line luminosities and derived quantities.

Bibliography

Amorín R., et al., 2014, ApJ, 788, L4

Amorín R., et al., 2015, A&A, 578, A105

Anders P., Fritze-v. Alvensleben U., 2003, A&A, 401, 1063

Arnouts S., Ilbert O., 2011, LePHARE: Photometric Analysis for Redshift Estimate, Astrophysics Source Code Library (ascl:1108.009)

Ashby M. L. N., et al., 2013, ApJ, 769, 80

Ashby M. L. N., et al., 2015, ApJS, 218, 33

Atek H., et al., 2010, ApJ, 723, 104

Atek H., et al., 2011, ApJ, 743, 121

Atek H., et al., 2014, The Astrophysical Journal, 789, 96

Bacon R., et al., 2015, A&A, 575, A75

Baldwin J. A., Phillips M. M., Terlevich R., 1981, PASP, 93, 5

Barkana R., Loeb A., 2001, Phys. Rep., 349, 125

Beletic J. W., et al., 2008, in High Energy, Optical, and Infrared Detectors for Astronomy III. p. 70210H, doi:10.1117/12.790382

Bertin E., Arnouts S., 1996, A&AS, 117, 393

Bigiel F., Leroy A., Walter F., Brinks E., de Blok W. J. G., Madore B., Thornley M. D., 2008, AJ, 136, 2846

Blumenthal G. R., Faber S. M., Primack J. R., Rees M. J., 1984, Nature, 311, 517

Boulade O., et al., 2003, in Iye M., Moorwood A. F. M., eds, Proc. SPIEVol. 4841, Instrument Design and Performance for Optical/Infrared Ground-based Telescopes. pp 72–81, doi:10.1117/12.459890

Bournaud F., Elmegreen B. G., 2009, ApJ, 694, L158

Bournaud F., Elmegreen B. G., Teyssier R., Block D. L., Puerari I., 2010, MNRAS, 409, 1088

Bournaud F., et al., 2011a, ApJ, 730, 4

Bournaud F., Dekel A., Teyssier R., Cacciato M., Daddi E., Juneau S., Shankar F., 2011b, ApJ, 741, L33

Bower R. G., 1991, MNRAS, 248, 332

Brammer G. B., van Dokkum P. G., Coppi P., 2008, ApJ, 686, 1503

Bressan A., Marigo P., Girardi L., Salasnich B., Dal Cero C., Rubele S., Nanni A., 2012, MNRAS, 427, 127

Brinchmann J., Charlot S., White S. D. M., Tremonti C., Kauffmann G., Heckman T., Brinkmann J., 2004, MNRAS, 351, 1151

Brinchmann J., Kunth D., Durret F., 2008, A&A, 485, 657

Bruzual G., Charlot S., 2003, MNRAS, 344, 1000

Calzetti D., Armus L., Bohlin R. C., Kinney A. L., Koornneef J., Storchi-Bergmann T., 2000, ApJ, 533, 682

Cardamone C., et al., 2009, Monthly Notices of the Royal Astronomical Society, 399, 1191

Cava A., Pérez-González P. G., 2013, in Revista Mexicana de Astronomia y Astrofisica Conference Series. pp 79–80 (`arXiv:1201.2177`)

Chabrier G., 2003, PASP, 115, 763

Charlot S., Fall S. M., 1993, ApJ, 415, 580

Charlot S., Fall S. M., 2000, ApJ, 539, 718

Charlot S., Longhetti M., 2001, MNRAS, 323, 887

Coleman G. D., Wu C.-C., Weedman D. W., 1980, ApJS, 43, 393

Crowther P. A., 2007, ARA&A, 45, 177

Cucciati O., et al., 2012, A&A, 539, A31

Cullen F., Cirasuolo M., McLure R. J., Dunlop J. S., Bowler R. A. A., 2014, MNRAS, 440, 2300

Cullen F., Cirasuolo M., Kewley L. J., McLure R. J., Dunlop J. S., Bowler R. A. A., 2016, MNRAS, 460, 3002

Daddi E., Cimatti A., Renzini A., Fontana A., Mignoli M., Pozzetti L., Tozzi P., Zamorani G., 2004, ApJ, 617, 746

Daddi E., et al., 2007, ApJ, 670, 156

Dahlen T., et al., 2013, The Astrophysical Journal, 775, 93

Dalla Vecchia C., Schaye J., 2012, MNRAS, 426, 140

Dalton G. B., et al., 2006, in Society of Photo-Optical Instrumentation Engineers (SPIE) Conference Series. p. 62690X, doi:10.1117/12.670018

Dekel A., et al., 2009, Nature, 457, 451

Dib S., Piau L., Mohanty S., Braine J., 2011, MNRAS, 415, 3439

Dubois Y., Teyssier R., 2008a, A&A, 477, 79

Dubois Y., Teyssier R., 2008b, A&A, 482, L13

Dunlop J. S., 2013, in Wiklind T., Mobasher B., Bromm V., eds, Astrophysics and Space Science Library Vol. 396, The First Galaxies. p. 223 (`arXiv:1205.1543`), doi:10.1007/978-3-642-32362-1˙5

Einstein A., 1915, Sitzungsberichte der Königlich Preußischen Akademie der Wissenschaften (Berlin), Seite 844-847.,

Elbaz D., et al., 2007, A&A, 468, 33

Elmegreen B. G., 2000, ApJ, 530, 277

Elmegreen B. G., Falgarone E., 1996, ApJ, 471, 816

Elmegreen B. G., Scalo J., 2004, ARA&A, 42, 211

Evans C. J., et al., 2011, A&A, 530, A108

Faisst A. L., et al., 2016, preprint, (`arXiv:1601.07173`)

Fazio G. G., et al., 2004, ApJS, 154, 10

Ferguson H., et al., 1995, in American Astronomical Society Meeting Abstracts. p. 1294

Ferland G. J., et al., 2013, Rev. Mexicana Astron. Astrofis., 49, 137

Fioc M., Rocca-Volmerange B., 1997, A&A, 326, 950

Fontana A., et al., 2014, A&A, 570, A11

Friedmann A., 1922, Zeitschrift fur Physik, 10, 377

Fumagalli M., et al., 2012, ApJ, 757, L22

Galametz A., et al., 2013, The Astrophysical Journal Supplement Series, 206, 10

Goldsmith P. F., Langer W. D., 1978, ApJ, 222, 881

Grogin N. A., et al., 2011, ApJS, 197, 35

Groth E. J., Kristian J. A., Lynds R., O'Neil Jr. E. J., Balsano R., Rhodes J., WFPC-1 IDT 1994, in American Astronomical Society Meeting Abstracts. p. 1403

Guo Y., et al., 2013, ApJS, 207, 24

Hatton S., Devriendt J. E. G., Ninin S., Bouchet F. R., Guiderdoni B., Vibert D., 2003, MNRAS, 343, 75

Hayashi M., et al., 2015, PASJ, 67, 80

Holden B. P., et al., 2016, ApJ, 820, 73

Hopkins P. F., 2013, MNRAS, 430, 1653

Hopkins P. F., Quataert E., Murray N., 2012a, MNRAS, 421, 3488

Hopkins P. F., Quataert E., Murray N., 2012b, MNRAS, 421, 3522

Hopkins P. F., Kereš D., Oñorbe J., Faucher-Giguère C.-A., Quataert E., Murray N., Bullock J. S., 2014, MNRAS, 445, 581

Huang X., et al., 2015, ApJ, 801, 12

Hubble E., 1929, Proceedings of the National Academy of Science, 15, 168

Juneau S., et al., 2014, ApJ, 788, 88

Kajisawa M., et al., 2011, PASJ, 63, 379

Kennicutt Jr. R. C., 1998, ARA&A, 36, 189

Kennicutt R. C., Evans N. J., 2012, ARA&A, 50, 531

Kereš D., Katz N., Weinberg D. H., Davé R., 2005, MNRAS, 363, 2

Kewley L. J., Dopita M. A., 2002, ApJS, 142, 35

Kewley L. J., Geller M. J., Jansen R. A., 2004, AJ, 127, 2002

Kewley L. J., Dopita M. A., Leitherer C., Davé R., Yuan T., Allen M., Groves B., Sutherland R., 2013, ApJ, 774, 100

Kimm T., Cen R., Devriendt J., Dubois Y., Slyz A., 2015, preprint, (`arXiv:1501.05655`)

Kniazev A. Y., et al., 2009, MNRAS, 395, 1121

Knobel C., et al., 2012, ApJ, 753, 121

Koekemoer A. M., et al., 2011, ApJS, 197, 36

Kuhlen M., Faucher-Giguère C.-A., 2012, MNRAS, 423, 862

Kurucz R. L., 1993, VizieR Online Data Catalog, 6039

Lagos P., Telles E., Muñoz Tuñón C., Carrasco E. R., Cuisinier F., Tenorio-Tagle G., 2009, The Astronomical Journal, 137, 5068

Lagos C. d. P., et al., 2015, preprint, (arXiv:1503.04807)

Lawrence A., et al., 2007, MNRAS, 379, 1599

Le Fèvre O., et al., 2015, A&A, 576, A79

Leavitt H. S., Pickering E. C., 1912, Harvard College Observatory Circular, 173, 1

Luna A., Bronfman L., Carrasco L., May J., 2006, ApJ, 641, 938

Ly C., et al., 2007, ApJ, 657, 738

Ly C., Lee J. C., Dale D. A., Momcheva I., Salim S., Staudaher S., Moore C. A., Finn R., 2011, ApJ, 726, 109

Lynden-Bell D., 1967, MNRAS, 136, 101

Madau P., Dickinson M., 2014, preprint, (arXiv:1403.0007)

Mannucci F., Cresci G., Maiolino R., Marconi A., Gnerucci A., 2010, MNRAS, 408, 2115

Maraston C., 2005, MNRAS, 362, 799

Marmol-Queralto E., McLure R. J., Cullen F., Dunlop J. S., Fontana A., McLeod D. J., 2015, preprint, (arXiv:1511.01911)

Martizzi D., Faucher-Giguère C.-A., Quataert E., 2015, MNRAS, 450, 504

Maseda M. V., et al., 2013, The Astrophysical Journal, 778, L22

Matteucci F., Calura F., 2005, MNRAS, 360, 447

Matteucci F., Greggio L., 1986, A&A, 154, 279

McCracken H. J., et al., 2012, A&A, 544, A156

McCrea W. H., Milne E. A., 1934, The Quarterly Journal of Mathematics, 5

McKee C. F., Ostriker J. P., 1977, ApJ, 218, 148

Misiriotis A., Xilouris E. M., Papamastorakis J., Boumis P., Goudis C. D., 2006, A&A, 459, 113

Miyazaki S., et al., 2002, PASJ, 54, 833

Murray N., Quataert E., Thompson T. A., 2005, ApJ, 618, 569

Nakajima K., Ouchi M., 2014, MNRAS, 442, 900

Navarro J. F., Frenk C. S., White S. D. M., 1997, ApJ, 490, 493

Nayyeri H., et al., 2017, ApJS, 228, 7

Noeske K. G., et al., 2007, ApJ, 660, L43

Oke J. B., Gunn J. E., 1983, ApJ, 266, 713

Osterbrock D. E., Ferland G. J., 2006, Astrophysics of gaseous nebulae and active galactic nuclei

Pacifici C., Charlot S., Blaizot J., Brinchmann J., 2012, MNRAS, 421, 2002

Pacifici C., et al., 2015, MNRAS, 447, 786

Papovich C., et al., 2015, ApJ, 803, 26

Peacock J. A., 1999, Cosmological Physics

Peeples M. S., Pogge R. W., Stanek K. Z., 2009, ApJ, 695, 259

Pérez-González P. G., et al., 2013, ApJ, 762, 46

Pirard J.-F., et al., 2004, in Moorwood A. F. M., Iye M., eds, Proc. SPIEVol. 5492, Ground-based Instrumentation for Astronomy. pp 1763–1772, doi:10.1117/12.578293

Planck Collaboration et al., 2015, preprint, (`arXiv:1502.01589`)

Planck Collaboration et al., 2016, A&A, 594, A13

Press W. H., Schechter P., 1974, ApJ, 187, 425

Puget P., et al., 2004, in Moorwood A. F. M., Iye M., eds, Proc. SPIEVol. 5492, Ground-based Instrumentation for Astronomy. pp 978–987, doi:10.1117/12.551097

Reines A. E., Nidever D. L., Whelan D. G., Johnson K. E., 2010, ApJ, 708, 26

Riess A. G., et al., 1998, AJ, 116, 1009

Salpeter E. E., 1955, ApJ, 121, 161

Santini P., et al., 2015, ApJ, 801, 97

Sargent W. L. W., Searle L., 1970, The Astrophysical Journal, 162, L155

Schaerer D., 2002, A&A, 382, 28

Schaerer D., Vacca W. D., 1998, ApJ, 497, 618

Schaerer D., de Barros S., 2012, in Tuffs R. J., Popescu C. C., eds, IAU Symposium Vol. 284, IAU Symposium. pp 20–25 (arXiv:1111.6373), doi:10.1017/S1743921312008630

Schaye J., et al., 2010, MNRAS, 402, 1536

Schaye J., et al., 2015, MNRAS, 446, 521

Schenker M. A., Ellis R. S., Konidaris N. P., Stark D. P., 2013, The Astrophysical Journal, 777, 67

Scoville N., et al., 2007, ApJS, 172, 1

Sharples R., et al., 2013, The Messenger, 151, 21

Silk J., 1977, ApJ, 211, 638

Skelton R. E., et al., 2014, ApJS, 214, 24

Smit R., et al., 2014a, ApJ, 784, 58

Smit R., et al., 2014b, The Astrophysical Journal, 784, 58

Sobral D., et al., 2009, MNRAS, 398, 75

Sobral D., Smail I., Best P. N., Geach J. E., Matsuda Y., Stott J. P., Cirasuolo M., Kurk J., 2013, MNRAS, 428, 1128

Sobral D., Best P. N., Smail I., Mobasher B., Stott J., Nisbet D., 2014, MNRAS, 437, 3516

Somerville R. S., Kolatt T. S., 1999, MNRAS, 305, 1

Somerville R. S., Lemson G., Kolatt T. S., Dekel A., 2000, MNRAS, 316, 479

Somerville R. S., Hopkins P. F., Cox T. J., Robertson B. E., Hernquist L., 2008, MNRAS, 391, 481

Somerville R. S., Popping G., Trager S. C., 2015, MNRAS, 453, 4337

Speagle J. S., Steinhardt C. L., Capak P. L., Silverman J. D., 2014, ApJS, 214, 15

Spitler L. R., et al., 2012, ApJ, 748, L21

Spitzer Jr. L., 1942, ApJ, 95, 329

Springel V., et al., 2005, Nature, 435, 629

Stark D. P., Schenker M. A., Ellis R., Robertson B., McLure R., Dunlop J., 2013, ApJ, 763, 129

Steidel C. C., Giavalisco M., Pettini M., Dickinson M., Adelberger K. L., 1996, ApJ, 462, L17

Steidel C. C., et al., 2014, ApJ, 795, 165

Stott J. P., et al., 2013, MNRAS, 436, 1130

Straughn A., et al., 2010, in American Astronomical Society Meeting Abstracts #215. p. 463.25

Sutherland R. S., Dopita M. A., 1993, ApJS, 88, 253

Suzuki R., et al., 2008, PASJ, 60, 1347

Tacchella S., Dekel A., Carollo C. M., Ceverino D., DeGraf C., Lapiner S., Mandelker N., Primack J. R., 2015, preprint, (`arXiv:1509.02529`)

Terlevich R., 1988, in Kaiser N., Lasenby A. N., eds, Post-Recombination Universe. pp 69–83

Teyssier R., 2002, A&A, 385, 337

Teyssier R., Pontzen A., Dubois Y., Read J. I., 2013, MNRAS, 429, 3068

Toomre A., 1964, ApJ, 139, 1217

Vacca W. D., Garmany C. D., Shull J. M., 1996, ApJ, 460, 914

Vogelsberger M., et al., 2014, MNRAS, 444, 1518

Weiner B. J., et al., 2007, ApJ, 660, L39

Wild V., Charlot S., Brinchmann J., Heckman T., Vince O., Pacifici C., Chevallard J., 2011, MNRAS, 417, 1760

Wild V., et al., 2014, MNRAS, 440, 1880

Wilkins S. M., Hopkins A. M., Trentham N., Tojeiro R., 2008, MNRAS, 391, 363

Wilkins S. M., et al., 2013, MNRAS, 435, 2885

Wright G. S., et al., 2008, in Space Telescopes and Instrumentation 2008: Optical, Infrared, and Millimeter. p. 70100T, doi:10.1117/12.790101

Zackrisson E., Bergvall N., Olofsson K., Siebert A., 2001, A&A, 375, 814

Zackrisson E., Bergvall N., Leitet E., 2008, ApJ, 676, L9

van der Wel A., et al., 2011, ApJ, 742, 111

Publications

Ferreira, Dunlop, Wild - Emission Line Galaxies in CANDELS I: Hα, [OIII] and [OII] Equivalent Width Distributions from Panchromatic Broadband Photometry up to z=5 in UDS. In *MNRAS*, (in prep).

Ferreira, Dunlop - Emission Line Galaxies in CANDELS II: the Evolution of Cosmic Star Formation told by ELGs in Broadband. In *MNRAS*, (in prep).